

Dipl.-Ing. Andreas PETROVIC

# Signal modeling for quantitative magnetic resonance imaging

Dissertation

zur Erlangung des akademischen Grades eines Doktors der technischen  
Wissenschaften

Technische Universität Graz

Betreuer:

Univ.-Prof. Dipl.-Ing. Dr.techn. Rudolf Stollberger

Institut für Medizintechnik

Graz, im Juli 2020



## Eidesstattliche Erklärung

Ich erkläre an Eides statt, dass ich die vorliegende Arbeit selbständig verfasst, andere als die angegebenen Quellen/Hilfsmittel nicht benutzt, und die den benutzten Quellen wörtlich und inhaltlich entnommenen Stellen als solche kenntlich gemacht habe.

Melbourne, am 14.07.2020 .....


  
.....

(Unterschrift)

## Statutory Declaration

I declare that I have authored this thesis independently, that I have not used other than the declared sources/resources, and that I have explicitly marked all material which has been quoted either literally or by content from the used sources.

14/07/2020  
.....  
date

  
.....

(signature)



Für Mama und Papa



# Abstract

Quantitative magnetic resonance imaging (qMRI) attempts to determine physical and physiological parameters intrinsic to the body. This methodical approach allows for more objective medical analysis and diagnosis compared to the individual interpretation of conventional MR scans with a contrast that can substantially vary depending on the sequence and measurement parameters used. Furthermore, technical shortcomings, such as field inhomogeneity, can impair image contrast and obfuscate relevant details. Those limitations are alleviated using quantitative MRI but only inasmuch as the applied measurement and analysis techniques are accurate and precise. Since the sought physical parameters are mostly estimated from data using nonlinear models, the accuracy of those results is strongly dependent on the validity of the underlying model and its assumptions.

This thesis is dedicated to calculating, testing, and applying newly derived models for multi-echo spin-echo sequences for the quantification of the transverse relaxation time parameter  $T_2$  using the Generating Functions formalism (z-transform). To that end, existing formulas were extended and refined to incorporate RF field inhomogeneities and effects of non-ideal slice profiles into the parameter estimation process. Beyond that, a closed form time domain solution for the decay of transverse magnetization in multi-echo spin-echo sequences was derived. Furthermore, a closed form solution also for the longitudinal magnetization was found that can be applied in the simultaneous estimation of  $T_1$  and  $T_2$  with a modified multi-echo spin-echo sequence.

The presented models and their impact on the parameter estimation accuracy were tested using simulations and experiments on MR phantoms. In vivo measurements were conducted and the results were compared to gold standard and other methods, as well as literature values.

In conclusion, the newly developed signal models could in all cases outperform the established methods. Simulations proved a high accuracy and precision and data from measurements showed excellent agreement with the model computations.





# Zusammenfassung

Die quantitative Magnetresonanztomographie (qMRI) versucht physikalische und physiologische, dem Körper intrinsische, Parameter zu bestimmen. Im Vergleich zur individuellen Interpretation konventioneller MR Scans, deren Kontrast aufgrund unterschiedlicher Sequenzen, Messparameter und technischer Unzulänglichkeiten wie z.B. Feldinhomogenitäten stark variieren kann, erlaubt es dieser Ansatz im Prinzip objektive Daten zu erhalten und somit verbesserte medizinische Analysen und Diagnosen zu erstellen. Die Voraussetzung dafür ist jedoch, dass die verwendete Mess- und Auswertetechnik robust und präzise ist. Die gesuchten physikalischen Parameter werden in der Regel durch Anpassung von nichtlinearen Kurven an gemessene Daten ermittelt, daher ist die Genauigkeit der Resultate stark vom verwendeten Signalmodell und dessen Voraussetzungen abhängig.

Diese Dissertation beschäftigt sich mit der der Ableitung, dem Testen, und der Anwendung von neuen Signalmodellen zur Bestimmung der transversalen Relaxationszeit  $T_2$  mittels multi-echo Spin-Echo Sequenzen. Hierzu wurde der sogenannte Generating Functions Formalismus (äquivalent zur z-Transformation) verwendet und bestehende Formeln wurden verbessert und erweitert. Dadurch wurden Einflüsse wie RF Inhomogenitäten und Effekte des nicht idealen Schichtprofiles in das Signalmodell integriert. Des Weiteren konnte für den Zerfall der transversalen Magnetisierung eine geschlossene Signalformel im Zeitbereich abgeleitet werden. Zusätzlich wurde auch eine Formel für die longitudinale Magnetisierung bei repetitiver Anregung gefunden. Mithilfe der obengenannten Signalgleichungen und Modifikationen der multi-echo Spin-echo Sequenz konnten  $T_1$  und  $T_2$  in einer Messung bestimmt werden.

Die entwickelten Modelle und deren Auswirkungen auf die Parameterschätzung wurden durch Simulationen und Experimente an MR Phantomen getestet. Resultaten aus in vivo Scans wurden Messungen mittels "Gold-Standards", anderen Methoden, sowie Werten aus der Literatur gegenübergestellt.

Mit den neu entwickelten Modellen konnten in allen untersuchten Fällen bessere Ergebnisse erzielt werden als mit etablierten Methoden. Die Resultate der Simulationen ergaben eine hohe Genauigkeit und Präzision. Weiters zeigten gemessene Daten exzellente Übereinstimmung mit den Modellrechnungen.



# Contents

<b>1</b>	<b>Introduction</b>	<b>1</b>
1.1	Relaxation theory . . . . .	2
1.1.1	Principles of magnetic resonance . . . . .	2
1.1.2	Relaxation theory . . . . .	3
1.2	Relaxometry methods for $T_2$ . . . . .	8
1.2.1	Spin-echo sequences . . . . .	9
1.2.2	Multi-echo spin-echo (MSE) . . . . .	9
1.2.3	CPMG with stimulated echo correction . . . . .	14
1.2.4	Steady state free precession - SSFP . . . . .	14
1.2.5	$T_2$ -prepared methods . . . . .	15
1.2.6	Fast methods . . . . .	15
1.3	Why is mapping of MR relaxation times important? . . . . .	16
1.4	General considerations . . . . .	18
1.4.1	$B_{1+}$ mapping . . . . .	18
1.4.2	Computation of the slice profile . . . . .	21
	The forward SLR transform . . . . .	22
1.4.3	Additional considerations . . . . .	23
1.5	Dissertation outline . . . . .	30
<b>2</b>	<b>The Generating Functions approach</b>	<b>33</b>
2.1	The z-transform . . . . .	33
2.1.1	Properties of the z-transform . . . . .	34
2.1.2	Relation to discrete time Fourier transform and DFT . . . . .	36
2.1.3	Solving a simple difference equation . . . . .	36
2.2	The Bloch equations . . . . .	38
2.2.1	Solutions to Bloch equations . . . . .	41
	Relaxation . . . . .	41
	Free precession and relaxation . . . . .	41
2.2.2	From $M_x$ , $M_y$ , and $M_z$ to transverse and longitudinal magnetization $M_+$ and $M_z$ . . . . .	42
	Relaxation . . . . .	43
	Free precession and relaxation . . . . .	44
2.3	Generating functions for repetitive pulse sequences . . . . .	44
2.3.1	Alternative methods of signal computation . . . . .	46
2.3.2	The spoiled gradient echo sequence (SPGR) . . . . .	48

Contents

2.3.3	The CPMG and the CP sequence . . . . .	54
	Initial value and steady-state for CPMG sequence . . . . .	55
	Limiting cases . . . . .	58
2.3.4	The bSSFP and IR-bSSFP sequence . . . . .	59
<b>3</b>	<b>Accurate <math>T_2</math>-mapping for slice-selective MSE sequences</b>	<b>63</b>
3.1	Introduction . . . . .	63
3.2	Methods . . . . .	64
3.2.1	Simulations . . . . .	64
3.2.2	MR measurements . . . . .	66
3.2.3	Phantom measurements . . . . .	66
3.2.4	In-vivo validation . . . . .	67
3.3	Results . . . . .	68
3.3.1	Simulations . . . . .	68
3.3.2	Phantom measurements . . . . .	71
3.3.3	In-vivo results . . . . .	74
3.4	Discussion . . . . .	74
3.4.1	Application to model-based reconstruction . . . . .	78
<b>4</b>	<b>A time-domain MSE equation</b>	<b>81</b>
4.1	Theory . . . . .	81
4.1.1	Solution of Bloch equation . . . . .	81
4.1.2	z-transform of the difference equation . . . . .	83
4.1.3	Derivation of time domain formula . . . . .	88
4.2	Methods . . . . .	93
4.2.1	Simulations . . . . .	93
4.2.2	Comparison with measurements . . . . .	94
4.2.3	Fitting . . . . .	94
4.3	Results . . . . .	95
4.3.1	Simulations . . . . .	95
4.3.2	Comparison with measurements . . . . .	97
4.3.3	Fitting . . . . .	101
4.4	Discussion and Conclusion . . . . .	101
4.A	Code . . . . .	104
<b>5</b>	<b>Combined <math>T_1</math> and <math>T_2</math>-fitting using a modified MSE sequence (MOMSE)</b>	<b>111</b>
5.1	Introduction . . . . .	111

5.2	Theory . . . . .	114
5.2.1	Numerical computation . . . . .	116
5.3	Methods . . . . .	117
5.3.1	MR data acquisition . . . . .	117
5.3.2	Phantom measurements . . . . .	118
5.4	Results . . . . .	118
5.5	Discussion . . . . .	119
5.A	Time domain signal equation . . . . .	120
<b>6</b>	<b>Summary and Outlook</b>	<b>123</b>
6.1	Outlook . . . . .	125
6.2	Additional work . . . . .	126



# 1

## Introduction

Magnetic Resonance Imaging (MRI) today is one of the most versatile medical imaging modalities and is frequently used to detect and monitor disease. It provides distinct advantages compared to other imaging techniques. MRI, for instance, outperforms CT in terms of soft tissue contrast (whilst not involving ionizing radiation) and ultrasound in terms of resolution. Generally, its versatility is unbeaten including methods like functional and molecular imaging. However, it is still mainly used as a pure imaging method in contrast to a true measurement technique. As an image modality it produces scans with varying contrast and quality dependent on extrinsic factors such as scanner parameters, sequence and operator. As a measurement technique MRI aims to reconstruct quantitative maps of the underlying physical parameters thus rendering it independent from the aforementioned extrinsic factors. More or less, all the known and unknown extrinsic variables often make MR images not directly comparable to each other, especially in multi-center studies. Quantitative MRI (qMRI) aims at turning disease markers based on image contrast to real biomarkers that can be accurately measured and reflect a physical property, therefore allowing comparisons across different sites making multi-institutional studies possible [1]. Quantitative MRI means developing MRI from an imaging modality to a real measurement technique. However, the road is rocky, many of the available quantification methods lack accuracy and precision and there is still need for improvement.

In this thesis I want to summarize the developments I undertook during my PhD studies to improve qMRI, in particular, so-called  $T_2$  relaxometry. In the following chapters I will present methods to accurately model MR signals that are used for parameter estimation. To that end, I used the so-called Generating functions approach which yields closed-form solutions solutions, that can be efficiently implemented either directly, or using the fast Fourier transform, in contrast to other methods (e.g. EPG), that compute signals iteratively. Exact signal models that incorporate as many extrinsic measurement parameters as possible are a prerequisite for accurate quantification. Alongside with the derivation of various signal models for different MR sequences I will also show results from actual phantom and in-vivo measurements to corroborate the theoretical findings and to validate the methods.

## 1 Introduction

**Outline.** This chapter is aimed at introducing the reader to the principles of nuclear magnetic relaxation and the foundations of the so-called longitudinal and transverse relaxation times  $T_1$  and  $T_2$  (section 1.1). I will shortly cover the quantum physical origins of  $T_1$  and  $T_2$  in order to understand what physical properties of molecular dynamics are reflected in their values. In accordance with the methods developed in this work I will primarily focus on  $T_2$  relaxation. In section 1.2 the most common techniques to measure  $T_2$  are presented, including their pitfalls and sources of error. Section 1.3 is devoted to inform the reader about the relevance of relaxometry in the context of medical Magnetic Resonance Imaging and the detection, characterization and monitoring of disease and present some examples where  $T_2$  is used as a biomarker. These introductory sections are held as concise as possible and in order for the reader to fully comprehend them and the following chapters a basic knowledge of MRI, it's variety of sequences, like spin-echo and gradient echo, and the generation of images therewith is assumed.

Next, the reader will find general considerations that have to be kept in mind when MRI is used as a quantitative measurement technique (sec. 1.4), namely the mapping of the active RF transmit field  $B_{1+}$  in-vivo (sec. 1.4.1) and the numerical computation of the slice profile from the RF pulse shape (sec. 1.4.2). Furthermore, in 1.4.3 some additional considerations about  $T_2$  relaxometry are presented .

Finally, in section 1.5, I will shortly outline the topics covered in the following chapters of this dissertation.

## 1.1 Relaxation theory

### 1.1.1 Principles of magnetic resonance

The fundamental quantum mechanical property that altogether makes nuclear magnetic resonance (NMR) possible is the fact that atomic nuclei with spin quantum number  $I$  greater than 0 posses a magnetic moment  $\mu = \gamma\mathbf{I}$  which is coupled to its nuclear angular momentum  $\mathbf{I}$  and its gyromagnetic ratio  $\gamma$ . Moreover, the z-component (by convention) of the magnetic moment evaluates to  $\mu_z = \gamma I_z$ , or more precisely  $\mu_z = \gamma\hbar m$ , where  $m$  is the magnetic quantum number of the nucleus ( $m = [-I, -I + 1, \dots, I - 1, I]$ ) [2, pp. 2]. In magnetic resonance imaging (or NMR in general) a tiny excess (millions of times smaller than the total number of spins) of all those moments is aligned in the direction of a strong external static magnetic field  $B_0$  (pointing in z-direction also by convention). For spins with  $I = 1/2$ , such as protons, the quantity  $\Delta N$  of moments that are in excess aligned with  $B_0$ , i.e. those with  $m = +1/2$ , can be calculated statistically according to a Boltzmann distribution and is for  $N$  spins given by  $N \frac{\Delta E}{2kT}$  where the



energy difference between the stationary energy eigenstates is  $\Delta E = \hbar\gamma B_0$  [3]. As  $\Delta E$  is much smaller than  $kT$  the Boltzmann distribution can be linearized to obtain the above result. Despite being very small the integrated effect of these magnetic moments manifests itself as a measurable equilibrium magnetization  $M_0 = \frac{\Delta N}{V}\mu_z$ ,  $V$  being the volume. This is the quintessence of nuclear magnetism. For hydrogen atoms (i.e. protons) which we are mainly concerned with in magnetic resonance imaging this expression can be rewritten as  $M_0 = \frac{N}{V} \frac{\hbar^2 \gamma^2 B_0}{4kT}$ .

This tiny magnetization can be deflected from its equilibrium state. Specifically it can be brought into resonance by an external magnetic radio frequency (RF) field  $B_{1+}$  at the so-called Larmor frequency  $\omega_0 = \gamma B_0$ . This process is also called excitation. Once deflected from the equilibrium z-direction, the magnetic moments start to rotate just like a gyroscope around the static field also with the Larmor frequency giving rise to a detectable oscillating magnetic field. According to the law of induction this magnetic field induces a voltage  $U = -\frac{d\Phi}{dt} \propto -\frac{d \sin(\gamma B_0 t)}{dt}$  which is proportional to  $\omega_0 = \gamma B_0$  in a coil positioned in this very plane of precession. Putting everything together the overall measurable signal amplitude is proportional to  $\frac{\hbar^2 \gamma^3 B_0^2 \rho_0}{4kT}$ ,  $\rho_0 = N/V$  being the spin density of the sample. This is the basic principle of magnetic resonance.

Due to fact of the spins being driven out of their equilibrium state they of course tend to return there, as in physics all entities somewhen find their equilibrium state, which is the lowest energy level in their reach. Phenomenologically, the magnetization dynamics are governed by the *Bloch equations* which incorporate magnetic interaction between the magnetization  $\vec{M}$  and external magnetic fields  $\vec{B}$  as well as the regrowth of magnetization to equilibrium in the direction of  $B_0$  (longitudinal relaxation) and the vanishing of excited precessing magnetization components perpendicular to  $B_0$  (transverse relaxation). In the following paragraphs I will elucidate the basic physical principals of relaxation theory.

### 1.1.2 Relaxation theory

In principle, NMR relaxation is caused by stochastic fluctuations of the effective magnetic field at position of the nucleus. The fluctuations are caused by the random translational and rotational motion of the neighbouring nuclei that themselves exhibit a magnetic moment. The fields of these neighbouring nuclei fluctuate in the direction of the main field  $B_0$  as well as perpendicular to it. Fluctuations perpendicular to the main field cause transitions between energy eigenstates, are also called non-adiabatic, and require exchange of energy [2]. Due to these processes the longitudinal magnetization approaches a state of thermal equilibrium after some time. This phenomenon is called *longitudinal* relaxation and is quantified by the longitudinal relaxation time

## 1 Introduction

$T_1$ . Adiabatic processes due to magnetic fluctuations parallel to the static field cause dephasing of spins. This results in a shrinking of the measurable *transverse* magnetization as the ensemble of coherent spins begins to fan out right after excitation until the net transverse magnetization has decayed to zero. This process is quantified by the transverse relaxation time  $T_2$ .

### Adiabatic and non-adiabatic relaxation

The difference between adiabatic and non adiabatic relaxation can best be illustrated by having a look at the spin wave function

$$|\psi(t)\rangle = c_\alpha(t) |\alpha\rangle + c_\beta(t) |\beta\rangle \quad (1.1)$$

$$|\psi(t)\rangle = \begin{pmatrix} c_\alpha(t) \\ c_\beta(t) \end{pmatrix} \quad (1.2)$$

$$(1.3)$$

which is a weighted sum of the stationary basis wave function  $|\alpha\rangle$  and  $|\beta\rangle$ , usually being represented by a column vector  $|\psi\rangle(t)$ . For this wave function the Schrödinger equation has to be solved, whereas the Hamiltonian in this case only comprises the magnetic interaction.

$$\frac{d|\psi(t)\rangle}{dt} = -i\mathcal{H}(t) |\psi\rangle(t) \quad (1.4)$$

$$\mathcal{H}(t) = -\vec{\mu} \cdot \vec{B}(t) = -\gamma \vec{I} \cdot \vec{B}(t) \quad (1.5)$$

$$|\psi(t_1)\rangle = e^{-i\gamma \int_{t_0}^{t_1} \vec{I} \cdot \vec{B}(\tau) d\tau} |\psi_0\rangle \quad |\psi(t_0)\rangle = |\psi_0\rangle \quad (1.6)$$

Once solved, we see that the result is an exponential operator acting on the wave function at time  $t_0$ . Here,  $\vec{I} = (I_x, I_y, I_z)^T$  is the nuclear spin angular momentum operator. In matrix notation they are given by [4]

$$I_x = \frac{1}{2} \begin{pmatrix} 0 & 1 \\ 1 & 0 \end{pmatrix} \quad I_y = \frac{1}{2i} \begin{pmatrix} 0 & 1 \\ -1 & 0 \end{pmatrix} \quad I_z = \frac{1}{2} \begin{pmatrix} 1 & 0 \\ 0 & -1 \end{pmatrix} \quad \hat{1} = \begin{pmatrix} 1 & 0 \\ 0 & 1 \end{pmatrix} \quad (1.7)$$

For  $\vec{B} = (0, 0, B_0)$  and using  $\phi = \gamma B_0(t_1 - t_0)$  the matrix exponential can be expressed as a power series. Sorting out the terms and due to the fact that every angular momentum operator squared yields identity we find

$$\begin{aligned} e^{-i\phi I_z} &= \hat{1} \cos \frac{\phi}{2} + 2i I_z \sin \frac{\phi}{2} \\ &= \begin{pmatrix} e^{-i\phi/2} & 0 \\ 0 & e^{i\phi/2} \end{pmatrix} \\ &= \mathbf{R}_z(\phi) \end{aligned} \quad (1.8)$$

which is a complex rotation matrix. Applying equation 1.8 to  $|\psi\rangle$  gives

$$|\psi_1\rangle = \mathbf{R}_z(\phi/2) |\psi_0\rangle = \begin{pmatrix} c_{\alpha 0} e^{-i\phi/2} \\ c_{\beta 0} e^{i\phi/2} \end{pmatrix} \quad (1.9)$$

which is only changing the phase of the spin wave function but causes no mixing between the eigenstates. If the same procedure is done for  $I_x$  and  $I_y$  one ends up with

$$e^{-i\phi I_x} = \hat{1} \cos \frac{\phi}{2} - 2iI_x \sin \frac{\phi}{2} = \begin{pmatrix} \cos \frac{\phi}{2} & -i \sin \frac{\phi}{2} \\ -i \sin \frac{\phi}{2} & \cos \frac{\phi}{2} \end{pmatrix} = \mathbf{R}_x(\phi) \quad (1.10)$$

$$e^{-i\phi I_y} = \hat{1} \cos \frac{\phi}{2} - 2iI_y \sin \frac{\phi}{2} = \begin{pmatrix} \cos \frac{\phi}{2} & -\sin \frac{\phi}{2} \\ \sin \frac{\phi}{2} & \cos \frac{\phi}{2} \end{pmatrix} = \mathbf{R}_y(\phi) \quad (1.11)$$

Applying either 1.10 or 1.11 causes a mixing between  $|\alpha\rangle$  and  $|\beta\rangle$ , hence an exchange of energy. These matrices involve the so-called Cayley-Klein parameters and are the same as the SU(2) rotation matrices used in the Shinnar-Le Roux algorithm used to calculate the slice profile in section 1.4.2. Note that in the above used Schrödinger equation the definition in natural units was used so that the factor  $\hbar$  is missing.

**Relaxation mechanisms** Relaxation is caused by nuclear magnetic interactions between the spins with its surrounding and Brownian motion that causes the surrounding magnetic fields to fluctuate. The magnetic interactions can be of various forms: chemical shift, dipole-dipole, J-coupling, and quadrupole coupling. For isotropic liquids primarily dipole-dipole, chemical shift anisotropy, and spin-rotation are the mechanisms with their relative magnitude decreasing in the order they are listed here [4].

**Relaxation theories** In principal, the starting point for relaxation theories is the introduction of a time-varying fluctuating term in the nuclear spin Hamiltonian  $\mathcal{H}(t) = \mathcal{H}_0 + \mathcal{H}_1(t)$ . A thorough treatment of relaxation, therefore, requires a quantum mechanical approach involving the dynamics of the *density operator*, which is beyond the scope of this text. For a coarse review of the general approach see the box *Density matrix and master equation*. In the Bloch equations both longitudinal and transverse relaxation are treated in a phenomenological way as exponential decay constants (see section 2.2). The Solomon equations take into account a coupled system of two spins and the transition probabilities between those coupled spin states. With this approach one can derive longitudinal and transverse relaxation rates in dependence of these transition probabilities.

For dipolar coupling these probabilities are all dependent on the square of the dipolar coupling constant  $-\frac{\mu_0}{4\pi} \frac{\hbar\gamma^2}{r^3}$  and the so-called spectral density functions  $\mathcal{J}(\omega)$ . The density functions usually have a form of  $\mathcal{J}(\omega) = \frac{\tau_c}{1+\omega^2\tau_c^2}$  where  $\tau_c$  is the so-called

## 1 Introduction

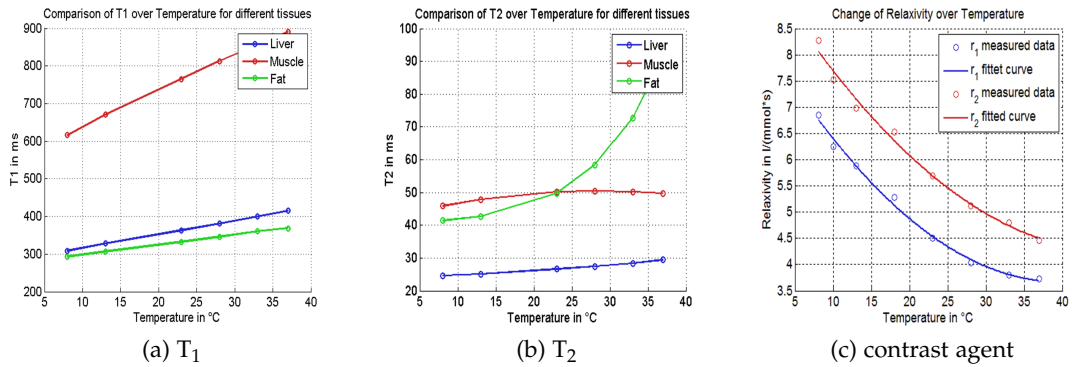


Figure 1.1: Temperature dependence of relaxation times  $T_1$  (a),  $T_2$  (b), and the relaxivities  $r_1$  and  $r_2$  of Gadovist (c) at 3T [5]. Interestingly,  $T_2$  of fat shows a remarkably strong dependence on temperature.

rotational correlation time [4, pp. 556]. Already we can see which molecular properties can be probed by measuring the relaxation time, as  $\tau_c$  is dependent on the size of the molecules and the viscosity, and the overall strength of the relaxation is dependent on the inverse sixth power of the distance  $r$  (for dipolar coupling) [4]. In fact  $\tau_c$  is connected to the rotational diffusion coefficient and the mean squared diffusion angle  $\langle \theta^2 \rangle$  by

$$2D_r\tau_c = \langle \theta^2 \rangle = 1, \quad (1.12)$$

$$D_r = \frac{k_B T}{8\pi\eta r^3}, \quad (1.13)$$

whereas the second equation is the famous Stokes-Einstein relation. One can now see explicitly the temperature dependence. Own data on the temperature dependence of

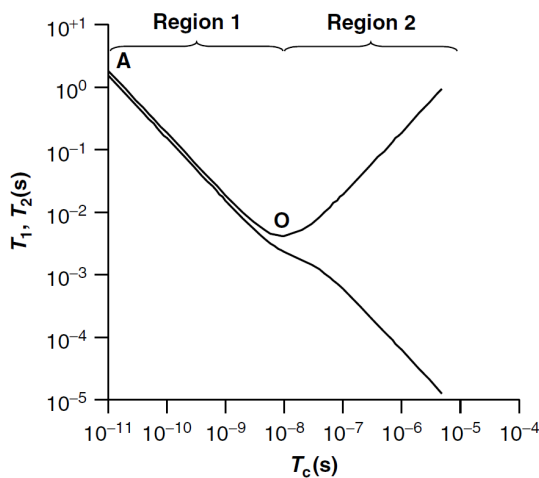


Figure 1.2:  $T_1$  and  $T_2$  dependence on correlation time  $\tau_c$ .  $T_2$  is long for short correlation times (water) and short for solid samples.  $T_1$  exhibits a minimum - it is long for fast rotating molecules but also long for solid samples (reprinted from [6]). At point A there is rapid molecular tumbling and the fluctuating fields average to zero. At point O the correlation time corresponds to the Larmor frequency and transitions between energy eigenstates is very effective. Therefore,  $T_1$  exhibits a minimum at this point.

relaxation times obtained in a experimental porcine model as well as contrast agent relaxivities are shown in figure 1.1. For the theoretical dependence of  $T_1$  and  $T_2$  on the correlation time see figure 1.2. A very useful semiclassical theory is the Bloch Wangsness Redfield (BWR) theory. A detailed discussion on relaxation theories can be found in [7, 8].

### Density matrix and master equation

The above presented formulas are valid for isolated spins. If one wants to describe the dynamics of a whole ensemble of spins the *spin density operator* comes into play. It is defined as

$$\rho(t) = |\psi(t)\rangle \langle \psi(t)| \quad (1.14)$$

and is a useful construct to calculate the expected value of a quantum mechanical operator  $\mathcal{I}$ .

$$\langle \mathcal{I} \rangle = \text{trace}\{\rho \mathcal{I}\} \quad (1.15)$$

The equation governing the dynamics of the spin density operator can be directly deduced by applying the chain rule and plugging in the Schrödinger equation,

$$\frac{d}{dt} |\psi(t)\rangle \langle \psi(t)| = \frac{d}{dt} |\psi(t)\rangle \langle \psi(t)| + |\psi(t)\rangle \frac{d}{dt} \langle \psi(t)| \quad (1.16)$$

$$= -i\mathcal{H}(t) |\psi(t)\rangle \langle \psi(t)| + i |\psi(t)\rangle \langle \psi(t)| \mathcal{H}(t). \quad (1.17)$$

Since the Hamiltonian is Hermitian (eigenvalues are real)

$$\frac{d}{dt} \langle \psi(t)| = \{-i\mathcal{H}(t) |\psi(t)\rangle\}^H = +i \langle \psi(t)| \mathcal{H}(t) \quad (1.18)$$

This yields the so-called master or Liouville-von Neumann equation for the density matrix

$$\frac{d\rho(t)}{dt} = -i(\mathcal{H}(t)\rho(t) - \rho(t)\mathcal{H}(t)) = -i[\mathcal{H}(t), \rho(t)] = -i\mathcal{L}(t)\rho(t) \quad (1.19)$$

where the square brackets denote the commutator and  $\mathcal{L}(t)$  the Liouville operator. The next step is to transform the equation in the so-called interaction frame to remove the explicit influence of  $\mathcal{H}_0$  [2, pp.351].

$$\rho^*(t) = e^{i\mathcal{H}_0 t} \rho(t) e^{-i\mathcal{H}_0 t} \quad \text{and} \quad \mathcal{H}_1^*(t) = e^{i\mathcal{H}_0 t} \mathcal{H}_1(t) e^{-i\mathcal{H}_0 t} \quad (1.20)$$

which yields the master equation in the interaction frame

$$\frac{d\rho^*(t)}{dt} = -i[\mathcal{H}_1^*(t), \rho^*(t)] \quad (1.21)$$

Solving equation 1.21 gives

$$\rho^*(t) = e^{-i \int_0^t \mathcal{L}^*(\tau) d\tau} \rho_0^* \quad (1.22)$$

$$\cong \rho_0^* - i \int_0^t \mathcal{L}^*(\tau) d\rho_0 \tau - \frac{1}{2} \int_0^t \int_0^{\tau'} \mathcal{L}^*(\tau') \mathcal{L}^*(\tau) \rho^*(\tau) \rho_0^* d\tau d\tau' \quad (1.23)$$

using the second order Taylor expansion for the operator exponential [7, pp. 276]. Taking the time derivative yields

$$\frac{d\rho^*(t)}{dt} = -i\mathcal{L}^*(t)\rho_0 - \frac{1}{2} \int_0^t \mathcal{L}^*(t) \mathcal{L}^*(\tau) \rho_0^* d\tau \quad (1.24)$$

$$= -i[\mathcal{H}_1^*(t), \rho_0^*] - \frac{1}{2} \int_0^t [\mathcal{H}_1^*(t), [\mathcal{H}_1^*(\tau), \rho_0^*]] d\tau \quad (1.25)$$

$$= -i[\mathcal{H}_1^*(t), \rho_0^*] - \frac{1}{2} \int_0^t [\mathcal{H}_1^*(t), [\mathcal{H}_1^*(t - \tilde{\tau}), \rho_0^*]] d\tilde{\tau} \quad (1.26)$$

The Hamiltonian  $\mathcal{H}_1^*(t)$  is a random variable so therefore the ensemble average has to be computed to arrive at a solution which gives (making some assumptions regarding the correlation between the density matrix and the Hamiltonian [2, p.352], as well as zero mean net fluctuations of  $\mathcal{H}_1^*(t)$ )

$$\frac{d\rho^*(t)}{dt} = - \int_0^\infty \overline{[\mathcal{H}_1^*(t), [\mathcal{H}_1^*(t - \tilde{\tau}), \rho^*(t)]]} d\tilde{\tau} \quad (1.27)$$

The solution to this equation is challenging and beyond the scope of this text. However, I want to point out here that inside the integral we can already see something looking like a correlation function, and indeed, the correlation functions and spectral densities often encountered in MR literature have their origin right there. For a detailed derivation the reader is referred to [7].

## 1.2 Relaxometry methods for $T_2$

MR relaxometry is devoted to measuring the relaxation time constants. The term *relaxometry* was first introduced by Koenig 1986 for the measurement of  $T_1$  dependence on magnetic field strength [1, 9]. Relaxation times not only are biological markers for physiological or pathological conditions, their measurement makes findings more comparable. In contrast to classical MRI, where images with arbitrary contrast depending on sequence parameters are produced, with relaxometry intrinsic physical quantities are measured. As with every measurement technique accuracy and precision of the measured values are important and differ by the methods used. In the following paragraphs I will give a short overview on the different methods, specifically on spin-echo methods as these are used mostly throughout this thesis.

### 1.2.1 Spin-echo sequences

The most obvious method to measure  $T_2$  is to deflect the equilibrium magnetization to the transverse plane (e.g. by a  $90^\circ$  pulse), let it evolve, and refocus it using for instance a  $180^\circ$  refocusing pulse to generate an echo at echo time TE, which is then  $T_2$ -weighted as the refocusing pulse eliminates effects of static dephasing ( $T_2'$ ). By repeating this experiment for different TEs one can fit the measured echo amplitudes to a mono-exponential (perhaps also multi-exponential) signal model  $S = M_0 e^{-TE/T_2}$  if the refocusing time TR is greater than 5 times  $T_1$  [6]. In this work this method is considered the gold standard for  $T_2$  mapping. The biggest drawback and reason why this method cannot be applied in clinical routine is clearly the duration of data acquisition due to the long TR requirement. This limitation can be addressed using multi-echo spin-echo sequences where a series of refocusing pulses are used to create multiple  $T_2$ -weighted echoes after a single excitation reducing the scan time by a factor equal to the number of acquired echoes. However, this approach introduces new difficulties. By the repetitive application of refocusing pulses with flip angles deviating from  $180^\circ$ , the signal decay is considerably altered, compared to a mono-exponential decay.

### 1.2.2 Multi-echo spin-echo (MSE)

*(adapted from [10])*

To acquire a series of images using multiple refocusing pulses a few considerations concerning image encoding have to be made to achieve images devoid of artifacts. Multi-echo sequences are in general subject to perturbations from  $B_{1+}$  and  $B_0$  inhomogeneities, which are exacerbated especially at high field strengths. Implementations using slice selective RF pulses are additionally disturbed by the non-ideal slice profile that usually tapers off at the borders producing much lower flip angles than prescribed. The consequences of  $B_{1+}$  and  $B_0$  inhomogeneities on  $T_2$  quantitation were extensively investigated by Majumdar et al [11–14] and others [15, 16].  $B_{1+}$  inhomogeneities cause inaccurate flip angles and, thus, cause an incomplete refocusing of magnetization. Furthermore, these perturbations convert certain parts of the excited magnetization into longitudinal magnetization and give rise to Hahn echoes and stimulated echoes. These so-called spurious echoes, which all have a different  $T_1$  and  $T_2$ -weighting, depending on the time they spent stored in the longitudinal plane, superimpose on the desired primary echoes, and produce a systematic error which accumulates and propagates throughout the echo train. Additionally, each spurious echo pathway experiences distinct imaging gradients which can cause signal cancellation and ghosting artifacts when the echoes are superimposed. This is true for MSE for the purpose of  $T_2$  mapping

## 1 Introduction

as well as in RARE sequences [17] for fast image acquisition.

The prerequisites for successful image generation can be subsumed as the so-called CPMG conditions [18]:

1. Refocusing pulse must be  $90^\circ$  out of phase with excitation pulse and the spacing between refocusing pulses must be twice the time as between excitation and first refocusing pulse.
2. The acquired phase of the spins must be equal between each refocusing pulse (which means in practice the encoding and crusher gradients have to have the same moment or have to be rewound within the precession interval as done with the phase encoding gradients).

The second condition on the one hand ensures the same encoding for all primary and spurious echoes to avoid ghosting but on the other hand increases the echo amplitudes and therefore alters the decay as all spurious echoes are added constructively to the signal. This is deliberately used in [19] where these principles are applied in conjunction with refocusing angles smaller than  $180^\circ$  to obtain images with still sufficient SNR. It's also possible to use crusher schemes that violate the CPMG conditions to suppress the unwanted echo pathways but at the price of substantial loss of signal to noise ratio (see also below).

In the original Carr-Purcell (CP) sequence [20] excitation and refocusing pulse had the same phase leading to the effect that errors due to incomplete refocusing were accumulated throughout the echo train. The Meiboom-Gill extension to the standard CP multiecho sequence (CPMG) enables a refocusing of magnetization previously converted into longitudinal magnetization for every second echo even if refocusing flip angles (FA)  $\alpha \neq 180^\circ$  [21]. However, this is only true up to FA deviations of the first order. Additionally, this modification does not eliminate stimulated echo contribution but rather prevents an accumulation of error throughout the echo train. In the presence of homonuclear J-coupling, this technique cannot compensate for errors [22]. More elaborate techniques such as composite refocusing pulses [22, 23] assure insensitivity to FA errors up to the second order. Robust variations of the CPMG phase conditions include the MLEV [24] and XY [25] approaches in which specific phase orders for subsequent refocusing pulses are repeated throughout the pulse sequence, and have shown to stabilize the echo train [26]. The approach of phase cycling proves useful in the cancelation of spurious echoes, however, at the cost of doubling scan duration [27]. Also a combination of both phase-cycling and composite pulses was proposed [28]. A comparison of several of these techniques by Bloch simulations is shown in fig. 1.3 and 1.4 for refocusing angles of  $150^\circ$  and  $120^\circ$ .



## 1.2 Relaxometry methods for $T_2$

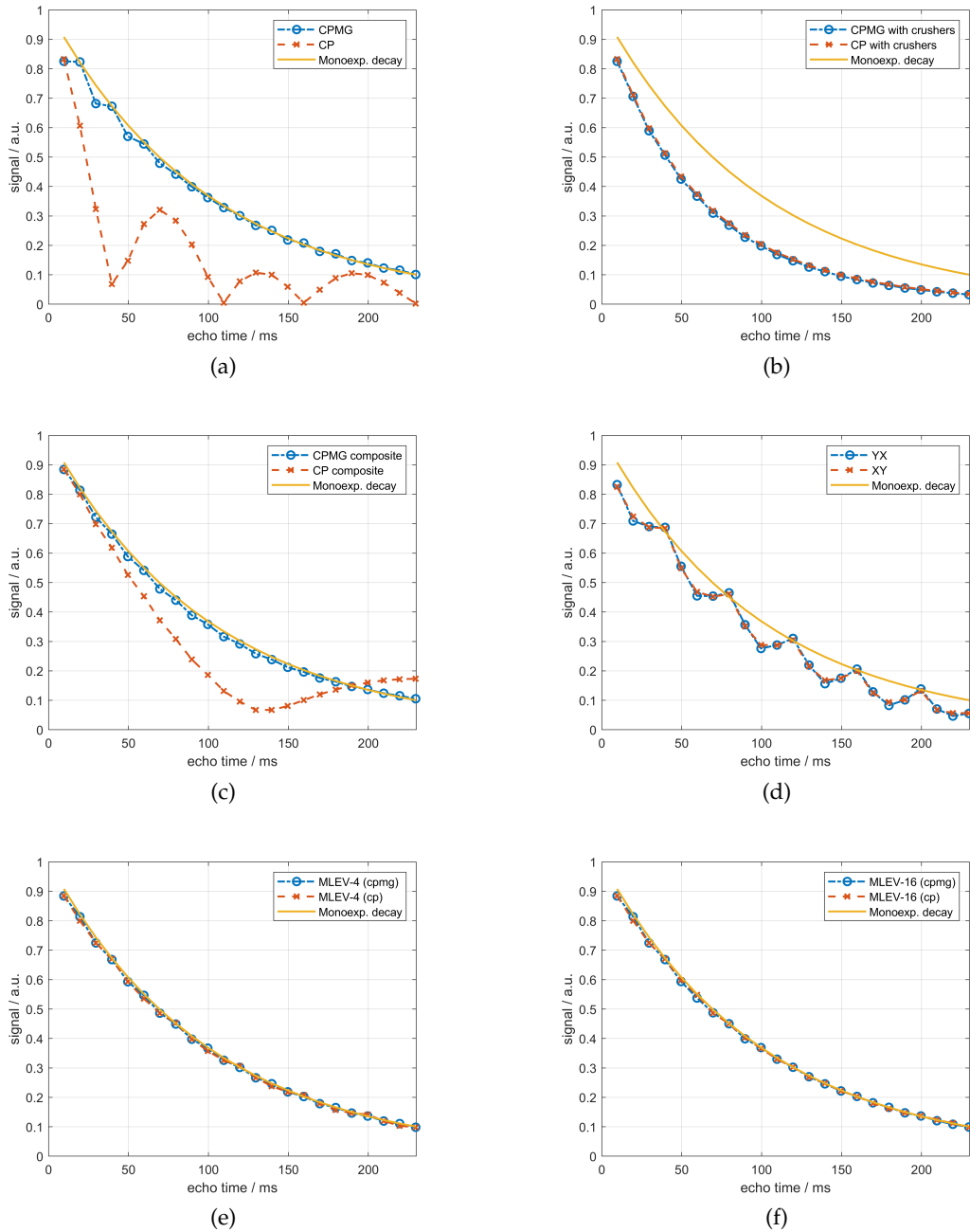


Figure 1.3: Comparison of different methods to stabilize the MSE echo train for a nominal refocusing FA of  $150^\circ$ ,  $T_1 = 2000$  ms,  $T_2 = 100$  ms, and echo spacing  $\tau = 10$  ms: (a) CPMG vs. CP - the CPMG sequence compensates for flip angle errors whereas the CP sequence accumulates the errors resulting in a severe signal loss, (b) CPMG with crushers vs. CP with crushers - due to the eliminations of all other than the primary echo pathways both sequences yield the same result, i.e. an artificially faster decay, (c) CPMG vs. CP with an  $\alpha/2 - \alpha - \alpha/2$  composite refocusing pulse - the CPMG signal is perfectly refocused, the CP signal is smooth but still deviates from mono-exponential decay, (d) XY vs. YX - both schemes can only perfectly refocus every fourth echo, and (e) and (f) the MLEV-4 and MLEV-16 phase cycling schemes (with composite pulse) perfectly refocus all echoes.

# 1 Introduction

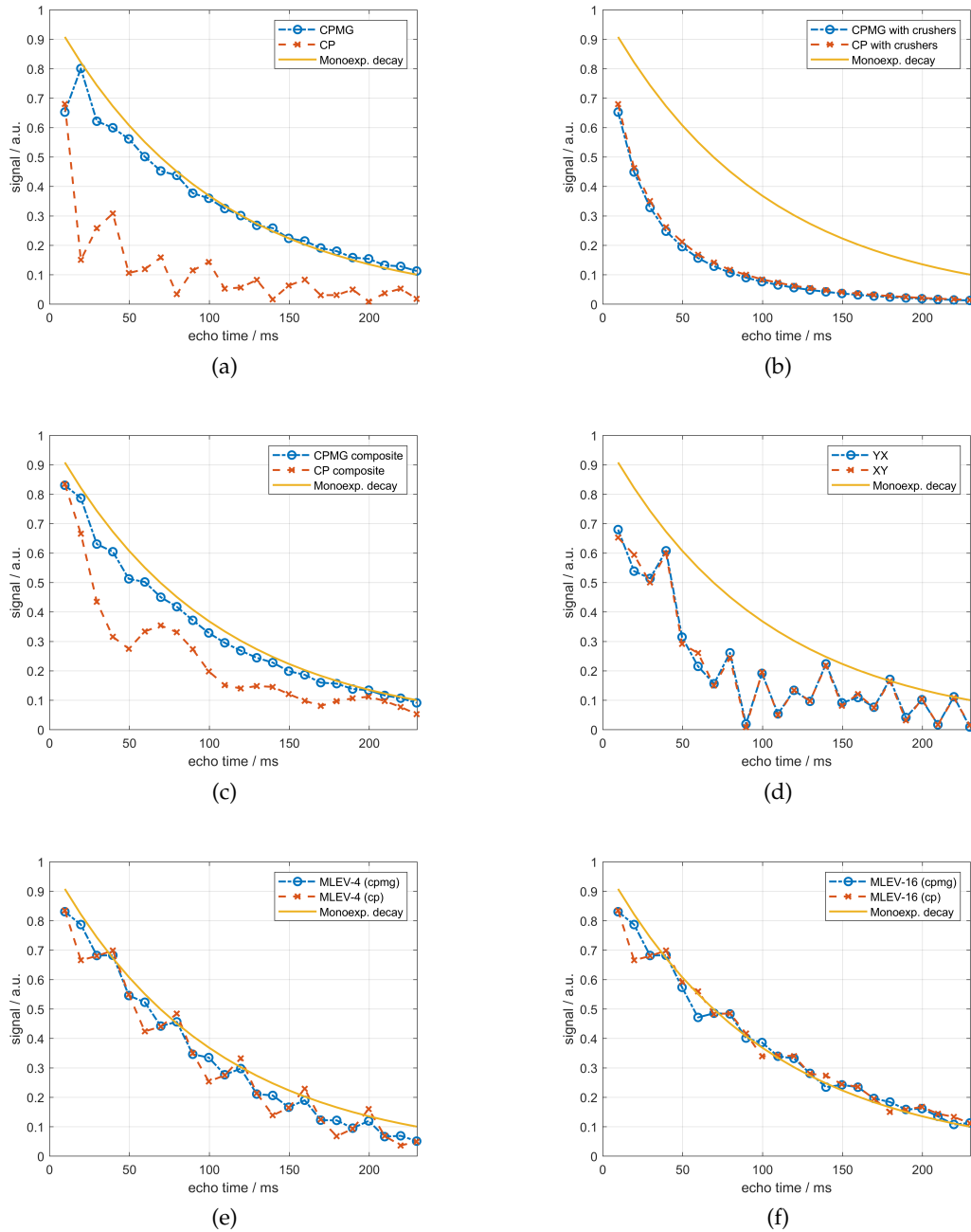


Figure 1.4: Comparison of different methods to stabilize the MSE echo train for a nominal refocusing FA of  $120^\circ$ ,  $T_1 = 2000$  ms,  $T_2 = 100$  ms, and echo spacing  $\tau = 10$  ms: (a) CPMG vs. CP - the CPMG sequence largely compensates for flip angle errors whereas the CP sequence accumulates the errors resulting in a severe signal loss, (b) CPMG with crushers vs. CP with crushers - due to the eliminations of all other than the primary echo pathways both sequences yield the same result, i.e. an artificially faster decay, also compared to fig. 1.3(b), (c) CPMG vs. CP with an  $\alpha/2 - \alpha - \alpha/2$  composite refocusing pulse - both variants cannot refocus the echoes, (d) XY vs. YX - these schemes do not seem to work for FA deviation of that size, and (e) and (f) the MLEV-4 and MLEV-16 phase cycling schemes (with composite pulse) still perform quite good, at least for every other echo.

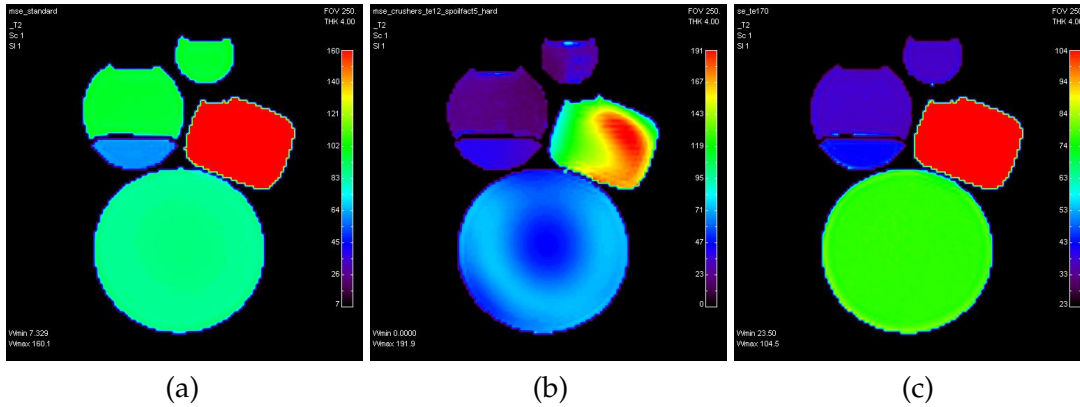


Figure 1.5: (a) is a mono-exponential fit to a standard CPMG sequence (b) a fit to a multi-echo spin-echo sequence with crushers, and (c) a fit to multiple single-echo spin-echo images. The estimated  $T_2$  values are substantially different for all approaches. In (b) also strong  $T_2$  variations can be seen which can be attributed to  $B_{1+}$  inhomogeneities. By crushing all non-essential echo pathways, a certain amount of magnetization is lost with every refocusing pulse, depending on the flip angle. This results in strong inhomogeneity and substantially shorter  $T_2$ . In contrast, in the CPMG sequence the magnetization is not crushed but stored, and eventually contributes to the echo train, whereas with a different weighting.

In the presence of non-ideal slice profiles and, thus, strong FA deviations across the slice, all above-mentioned approximations fail. To overcome this restriction, other techniques altering the pulse sequence and, thus, violating the CPMG conditions, by applying crusher gradients that eliminate all unwanted echoes in the echo train, have been developed [14, 15, 29, 30]. In these sequences the crusher gradient moment changes for every inter-pulse period throughout the RF train. However, the amplitude of the acquired echo train also has to be corrected by acquiring additional data (e.g.,  $B_{1+}$  maps) to account for the signal loss caused by the crushers. Fig. 1.5 shows a comparison of  $T_2$  maps of a CPMG, a crushed multi-echo, and a single-echo spin-echo sequence.

Other methods for improved  $T_2$  determination include broadening the refocusing slice profile [31], single-slice measurements (i.e. hard pulse refocusing) and multiple SE measurements (see above). Broadening the slice profile ensures an acceptable level of homogeneity of the profile at the position of the excited magnetization but has the shortcoming of limiting the number and distance of slices that can be acquired. The use of single-slice sequences and single SE measurements lead to excessively prolonged acquisition times, making them unusable in vivo, and still, stimulated echoes from  $B_{1+}$  inhomogeneities can also not be prevented in single slice measurements. Generally, single SE measurements also exhibit a stronger influence of diffusion effects and J-coupling. Adiabatic full-passage [32] pulses guarantee correct FAs and improved slice

## 1 Introduction

profiles but require long pulse durations and, thus, are associated with longer echo times. Additionally, the specific absorption rate is substantially increased for these pulses.

### 1.2.3 CPMG with stimulated echo correction

*(adapted from [10])*

Typically, in CPMG MSE sequences the mono-exponential decay is altered and accurate  $T_2$  quantification is impeded. Discarding the first echo in the calculation of  $T_2$  seems to be an established procedure in the processing of such data [33]. This approach will yield accurate  $T_2$  estimates if the ratio  $T_1/T_2$  is close to one [29]. However, for most biological tissues this is not the case. Generally, the usability of published  $T_2$  values is limited as the actual sequence design and fitting procedure are often not specified in sufficient detail. In general, there is a need for post-processing and fitting algorithms that accurately extract the  $T_2$  from the measured MSE decay. The approach presented in [34] demonstrated substantial improvements by using the extended phase graph (EPG) algorithm for the implementation of a more realistic model incorporating the slice profile based on the repeated multiplication of appropriate rotation matrices. The EPG was also used in [35, 36] whereas the slice profile was not explicitly incorporated but instead an optimized SLR refocusing pulse was used and an average FA was fitted from the data.

The Generating functions approach upon which this work is based on was introduced by Lukzen [37, 38] for MSE (and other repetitive) sequences, whereas only the signal equations were presented. A thorough investigation on the applicability to  $T_2$  mapping was missing to date and can be found in the remaining chapters of this thesis.

Bloch simulations in combination with a dictionary based approach has also been investigated [39].

However, if the right model is at hand and the equations are known one can make a feature out of the previous limitation, such as lowering the flip angle for SAR reduction whilst still computing accurate and comparable  $T_2$  values.

### 1.2.4 Steady state free precession - SSFP

A rapid method for simultaneous  $T_1$  and  $T_2$  mapping employs spoiled (SPGR,  $T_1$ ) and fully balanced (bSSFP,  $T_2$ ) gradient echo sequences. The SPGR signal is used to quantify  $T_1$  first as the bSSFP signal is dependent on both  $T_1$  and  $T_2$ . Relaxation parameters are then determined by fitting this signal equations to a series of images acquiring with varying FAs [40–42].

Another possibility using a bSSFP approach is the so-called inversion recovery (IR) bSSFP sequence where a bSSFP readout is preceded by an inversion pulse [43–45]. The acquired images can be fitted to a mono-exponential signal equation whereas the actual relaxation parameters can be calculated from the fitted values if the flip angle is known.

A further SSFP method is the triple echo steady-state (TESS) sequence [46] where a SSFP sequence is modified to acquire three differently weighted echoes in a single TR.  $T_1$  and  $T_2$  can then be estimated by a fitting dedicated equations to ratios of the acquired images.

In [47] a bSSFP sequence is used with a preceding  $T_2$  preparation module which leads to  $T_2$  prepared sequences described further in the next section.

### 1.2.5 $T_2$ -prepared methods

$T_2$  -prepared methods are constructed from a  $T_2$  preparation module followed by an imaging sequence. In [48] a CPMG preparation module is used followed by a FLASH readout, whereas an EPI readout after a spin echo preparation module is used in [49]. A saturation recovery module followed by a spin echo module and an EPI readout was used in [50] for simultaneous  $T_1$  and  $T_2$  quantification. The GESSE sequence [51] uses a gradient echo readout to sample a previously generated  $T_2$ -weighted spin echo.

### 1.2.6 Fast methods

As in every subarea of MR people have tried to make it faster. To give a few examples, e.g. compressed sensing was used to construct parameters maps in [52–55]. The approach of a model based reconstruction of MR images by iterative non-linear inversion [56, 57] directly reconstruct the parameter maps from the raw data [58, 59]. Just recently a model based approach including simultaneous multi-slice reconstruction was presented [60].

Further, [61] exploited the temporal correlation of the MR-signal in k-space for reconstruction. Another approach based on balanced SSFP employed a radial view sharing technique to quantify  $T_1$  and  $T_2$  [44]. Last but not least, MR fingerprinting is yet another approach where pseudo randomized sequences are used to generate a relaxometric fingerprint of the underlying spins [62]. Quantitation is then performed using a dictionary based approach.

Unlikely to be a complete list of available methods, the above section is aimed at giving the reader a coarse overview on the variety of methods that can be used for MR relaxometry.

### 1.3 Why is mapping of MR relaxation times important?

I've already mentioned in the very beginning of this thesis that the main advantage of qMRI is its ability to create reliable biomarkers that are only related to intrinsic tissue properties and not to external factors such as sequence, field homogeneity, or scanner. Hence, they are biomarkers that allow a direct comparison of results, for instance in multi-center or longitudinal studies.

A vast amount of literature exists investigating different parameters with respect to their suitability to reliably detect, grade, or monitor disease and to assess their predictive or discriminatory value. In this section I briefly present a few exemplary medical conditions in which qMRI was successfully applied.

**Brain.** Both  $T_1$  and  $T_2$  values, as well as proton density (PD), have been used in the characterization of multiple sclerosis [63] and a change of relaxation times can be observed in both white and gray matter [1]. An increase of  $T_1$  and PD were found in the cerebral cortex for MS patients in [64]. A multi-exponential  $T_2$  fit can be deployed to calculate the myelin water fraction which is a useful biomarker related to demyelination [65] also in the spinal cord [66]. In [67] a multi-parametric approach was used and a correlation between the evolution of lesions and  $T_1$  increase in normal appearing white matter over time was found. For more information on MR relaxometry in multiple sclerosis see reviews [68] and [69].

In brain tumors it was shown that  $T_1$  values are elevated with glioblastomas having the longest  $T_1$  values. Peritumoral edema in malignant gliomas was investigated with relaxometry in [70] and revealed tissue changes not visible on conventional MRI. [71] found promising results in glioblastoma monitoring in patients with anti-angiogenic therapy. Regarding vascularization, tumor perfusion and breakdown of the blood brain barrier relaxometry methods are indispensable for dynamic contrast enhanced (DCE) and dynamic susceptibility contrast (DSC) perfusion measurements.

Furthermore, in stroke one can observe an increase in  $T_1$  and  $T_2$  times [72] and also in diseases like autism, dementia and Parkinson's disease relaxation times are elevated [1].

**Body.** In osteoarthritis relaxation times are related to the biophysical and biochemical aspects of the disease. For instance, are changes in collagen content associated with changes in  $T_2$  and  $T_2^*$ , whereas  $T_2$  also reflects changes in collagen organization [1]. Furthermore, it was found that  $T_2$  map signal variation can predict symptomatic osteoarthritis progression and is possibly an early osteoarthritis imaging biomarker [73]. Relaxation time mapping proved useful in the differentiation of colon cancer metastases

### 1.3 Why is mapping of MR relaxation times important?

in the liver [74] or the distinction between benign and malignant hepatic lesion based on  $T_2$  times [75].  $T_2$  has shown to have predictive value in prostate cancers (Gleason  $\geq 7$ ) [76]. Quantitative  $T_2$  maps obtained in [77] allowed for high precision discrimination between the healthy and cancerous peripheral zone in the prostate. A significant difference between benign and malignant breast lesions could be established in [78]. Other applications include fatty liver disease, muscle inflammation and edema distinction [1]. Finally,  $T_1$  based MR thermometry can be used to monitor temperature in thermal ablation procedures [79].

**Blood (adapted from [80])** The idea of characterizing blood and its constituents using MRI is not new as show various studies of blood in vitro [81–89] and two case studies which investigated the changes of blood over time at 0.15 T and 0.47 T [90, 91]. It was shown that the oxygenation state of hemoglobin (Hb), the amount of different Hb metabolites such as methemoglobin (metHb), and the intactness of the cell membrane of the red blood cells (RBCs) play a key role in understanding hemorrhage behavior in MRI, as they affect both transversal and longitudinal relaxation times. According to the alteration of the relaxation times also the MRI signal is changed. These changes allow for a rough estimation of the age of intracranial hematomas. The literature largely agrees on the stages hyperacute, acute, early and late subacute, as well as chronic [92, 93]. While these stages might be sufficiently determined for a use in neuroradiology, they may not be transferable to subcutaneous hemorrhage which is of interest in forensic imaging due to the influencing factors of the surrounding tissue [94, 95]. Fig. 1.6 shows the time course of relaxation times changes of whole blood obtained in our in vitro study [80]. One can observe the initially high  $T_1$  values that start to decrease as soon as metHb is forming. For  $T_2$  a decrease is observed upon deoxygenation followed by a subsequent increase due to the homogenization of the sample as cells lysis occurs.

**Iron.** The condition of iron overload, whether in the brain or other organs, poses a severe problem to the affected person as it e.g. linked to cognitive dysfunction [96] or can even cause death after injuring body organs [1].  $T_2$  and  $T_2^*$  mapping methods produced very promising results for the purpose of iron content quantification as iron depositions directly affect these relaxation times. MR results were validated using biopsy or post-mortem analysis and calibration curves could be established [32, 96–99].

**Other.** Quantification of brain perfusion using methods as DCE or DSC MRI requires the measurement of relaxation times as they are altered by the administered contrast agent. Also in arterial spin labeling (ASL) both correction for  $T_1$  and  $T_2$  effects is

## 1 Introduction

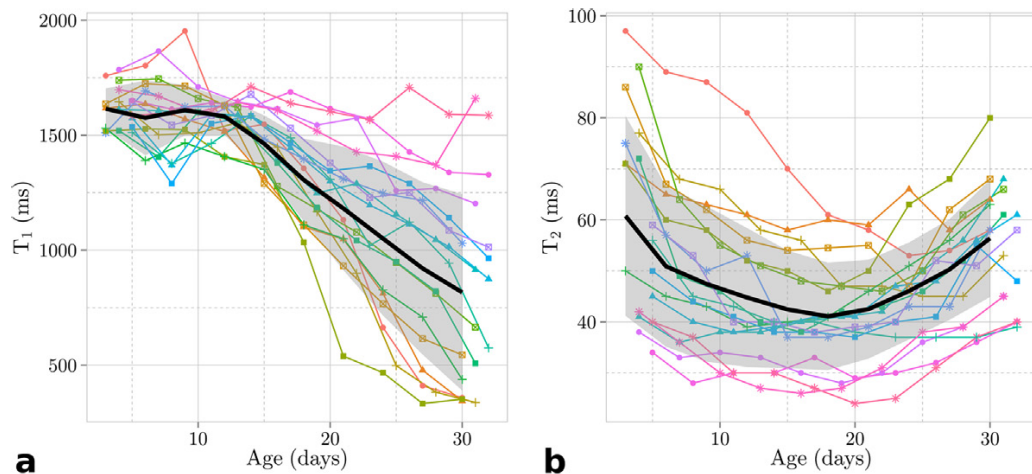


Figure 1.6:  $T_1$  and  $T_2$  changes during the aging of stationary blood. In this in-vitro study we investigated the systematic changes of the relaxation times during the degradation of whole blood samples at 3T (time axis stretched due to experimental design) [80].

necessary for an accurate quantification of cerebral blood flow [100]. Further, for quantitative BOLD (blood oxygenation level dependent) imaging and measurement of tissue oxygenation knowledge of  $T_2$  and  $T_2^*$  is necessary [101].

Synthetic MRI utilizes the knowledge of the relaxation parameters and proton density to be able to synthetically generate images with any desired contrast weighting any time after the scan [102].

All these results demonstrate the value accurate quantitative mapping techniques can provide in diagnosing and assessing disease. The alterations of relaxation times in diseased tissue are consequences of changes in physiology which in turn alter the physical properties in the affected tissues, such as viscosity and molecular mobility.

## 1.4 General considerations

### 1.4.1 $B_{1+}$ mapping

*"RF nonuniformity is the largest cause of error in qMRI"*<sup>1</sup>

Exact knowledge of the spatial distribution of the effective  $B_{1+}$  field is a key prerequisite for most quantitative MR techniques, namely those where either the excitation or refocusing flip angle enters the calculation of the final parameters or alters the signal such that it deviates from the applied signal model. This is for instance the case for

<sup>1</sup>Paul Tofts, Quantitative MRI of the brain, John Wiley and Sons Ltd., 2004 (chapter 2).



$T_2$  mapping with MSE sequences or  $T_1$  mapping with a variable flip angle method (VFA). However,  $T_2$  quantification using multiple single spin echo sequences (which is clinically infeasible) is not impeded because the flip angle enters the equation for every echo in the same way and is incorporated into  $M_0$  during data fitting.

The strength of the  $B_{1+}$  field in-vivo directly determines the flip angle that is achieved at this position given a certain transmit coil voltage. The reasons for  $B_{1+}$  inhomogeneities are manifold: (1) the transmit inhomogeneity of the coil itself which is strongly exacerbated for e.g. multi-array transmit coils compared to the body coil, (2) coil loading which requires the transmit voltage to be adjusted but varies from patient to patient, (3) dielectric resonance effects at higher field strengths (e.g. 3T) and (4) transmitter nonlinearity [103].

If accurate quantification with MRI is desired it's of paramount importance to know the exact value of the flip angle for each pixel. However, due to the very smooth and spatially slowly varying character of  $B_{1+}$ , a coarser resolution map is usually adequate which is then interpolated onto the image matrix [104]. The next paragraph shortly introduces some of the common methods for  $B_{1+}$  mapping.

**$B_{1+}$  mapping methods.** One of the most common methods is the so-called double angle method (DAM) [105] where two spin echo images  $I_1(\vec{x})$  and  $I_2(\vec{x})$  are acquired and the excitation flip angle is doubled for the second acquisition ( $\alpha_2 = 2\alpha_1$ ) or a variant thereof [106]. The  $B_{1+}$  spatial scaling factor  $\lambda(\vec{x})$  can be obtained using equation 1.28.

$$\alpha_1(\vec{x}) = \arccos \frac{I_2(\vec{x})}{2I_1(\vec{x})} \quad \lambda(\vec{x}) = \frac{\alpha_1(\vec{x})}{\alpha_1^{\text{nom}}} \quad (1.28)$$

Another common method is  $B_{1+}$  mapping by Bloch-Siegert (BS) shift [107] of which very fast implementations exist [108]. It consists of a standard spin-echo or SPGR sequence augmented by far off-resonant high flip angle pulses during the free precession times, once with a positive and once with a negative frequency offset  $\pm\omega_{RF}$ . Far off-resonant pulses exhibit a major component of their effective field in z-direction giving rise to accumulation of phase proportional to the  $B_{1+}$  field. The  $B_{1+}$  magnitude can be estimated from equation 1.29

$$\varphi_{BS} = \hat{B}_{1+}^2 \cdot \int_0^T \frac{(\gamma \bar{B}_{1+}(t))^2}{2\omega_{RF}} dt \quad B_{1+}(t) = \hat{B}_{1+} \cdot \bar{B}_{1+}(t) \quad (1.29)$$

where  $\hat{B}_{1+}$  is the peak amplitude,  $\bar{B}_{1+}(t)$  the normalized RF pulse shape, and  $T$  the pulse length. Another phase sensitive method uses a non-selective  $180_x^\circ$  followed by a  $90_y^\circ$  pulse. Flip angle deviations will produce transverse magnetization for the  $180_x^\circ$

## 1 Introduction

Figure 1.7: Severe  $B_{1+}$  inhomogeneities measured on a 3T scanner (Tim Trio, Siemens) in a homogeneous water phantom with regions of nominal flip angles confined to a thin ring. A comparison between the DA and BS methods demonstrates good agreement.

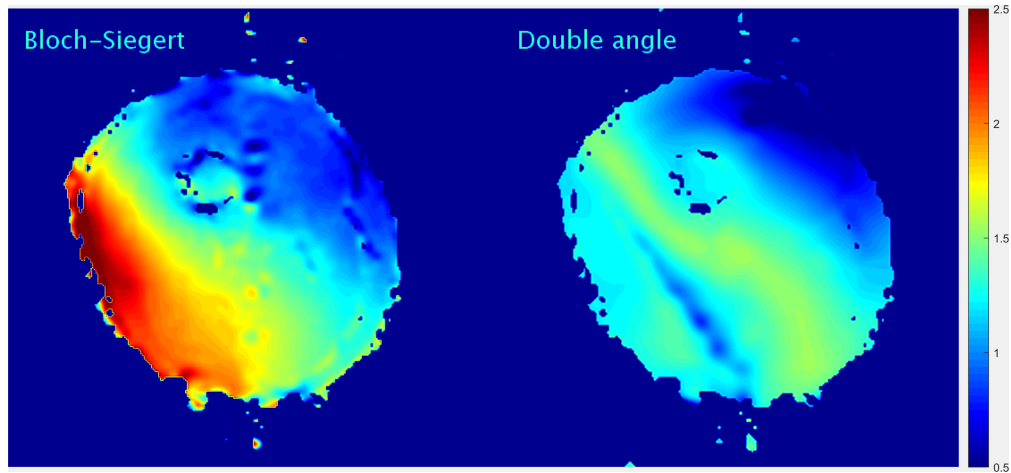


Figure 1.8: Strong  $B_{1+}$  inhomogeneities in the upper thigh. Left: GRE Bloch-Siebert map (8kHz off-resonant,  $700^\circ$  angle). Right: Spin echo double angle map (excitation angles  $60^\circ$  and  $120^\circ$ ). In areas of two times the nominal angle the spin echo sequence fails, as the refocusing angle is doubled to  $360^\circ$ .

pulse which is measured using the  $90_y^\circ$ .  $B_{1+}$  is then reflected in the phase of the acquired signal [109]. Actual flip angle imaging (AFI) operates in the pulsed steady state and employs a 3D SPGR sequence where TR is alternated between  $TR_1$  and  $TR_2$  for every other echo and the flip angle is computed from the two acquired images [110]. Yet another type of methods utilizes the fact that the signal is zero for a  $180^\circ$  excitation [111] [112]. Acquiring a set of images with angles around  $180^\circ$  and making a linear approximation of the signal equation permit to estimate the actual angle by linear regression.

Figure 1.7 shows  $B_{1+}$  maps of a large water phantom with quite severe radial inhomogeneities. The agreement between the DA and BS methods is quite good for large regions. In figure 1.8 an example of severe  $B_{1+}$  inhomogeneity in the human thigh is shown. In the left part of the thigh the FA is at some points twice as high as prescribed (Bloch-Siebert map, left side). In these regions the DA method fails, due to refocusing issues, i.e. the actual refocusing FA is  $360^\circ$  and no echo is produced. This issue is also nicely illustrated in figure 1.9 where an MSE and a GRE image of the same thigh are shown next to each other. The GRE images exhibits a rather homogeneous signal intensity whereas the MSE exhibits a complete signal void in the lower left area. This is due to the nature of the MSE sequence and the effects of severe  $B_{1+}$

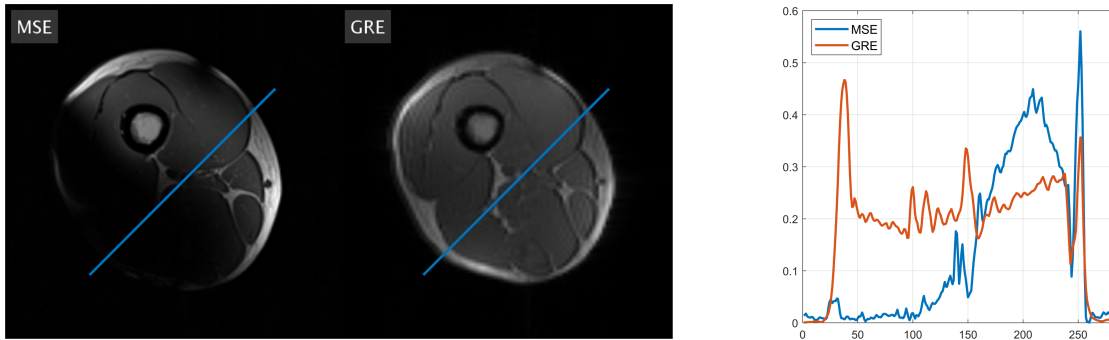


Figure 1.9: Strong  $B_{1+}$  inhomogeneities in the upper thigh. On the left a MSE and a GRE image of the same thigh are shown. On the right the cross sections are qualitatively compared.

inhomogeneities. In this area the MSE excites with  $180^\circ$ , i.e. it inverts, and refocuses by turning the magnetization one full time around. Hence, no signal can originate from these areas. For the GRE sequence the FA is much lower and even if doubled still produces acceptable images. In this thesis the DAM was used for  $B_{1+}$  mapping in phantom experiments and BS for in vivo measurements, respectively.

#### 1.4.2 Computation of the slice profile

Slice selective excitation and refocusing are the main sources of error for  $T_2$  quantification with MSE sequences, or generally for all quantification methods where the flip angle enters the calculation and must be known correctly. For instance, VFA methods are therefore mainly applied as 3D sequences. This problem becomes especially apparent for large flip angles as refocusing pulses are in MSE sequences. The reason for this is that in this regime the small flip angle approximation breaks down.

In principle, the slice profile can be computed by applying the Fourier transform on the pulse shape for small flip angles. For larger flip angles this approximation breaks down and the slice profile deteriorates, losing its sharp edges. That means that at the edge of a refocusing slice profile the nominal flip angle is not achieved, which is fundamentally equal to a severe  $B_{1+}$  inhomogeneity. For that reason accurate knowledge of the slice profiles of the applied pulses is essential.

In this work all slice profiles that were used were computed with the so-called forward Shinnar Le-Roux transform [113]. The SLR transform utilizes the so-called hard pulse approximation where the shaped RF pulse is subdivided in short but constant hard pulses each followed by a short period of precession due to the slice selection gradient. The rotations are computed using so-called spinors and  $2 \times 2$  complex rotation matrices (SU(2)) employing the Cayley-Klein parameters [114]. This method is closely related to

## 1 Introduction

the theory of quaternions and the Pauli spin matrices used in quantum mechanics. A SU(2) rotation is defined in matrix form as

$$\mathbf{Q} = \begin{bmatrix} \alpha & -\beta^* \\ \beta & \alpha^* \end{bmatrix} \quad (1.30)$$

with

$$\alpha = e^{i(\chi+\psi)/2} \cos \frac{\eta}{2}, \quad (1.31)$$

$$\beta = ie^{i(\chi-\psi)/2} \sin \frac{\eta}{2} \quad (1.32)$$

$\chi$ ,  $\psi$  and  $\eta$  being the Euler angles of rotation.

### The forward SLR transform

In terms of RF rotations the nutation and precession matrices can be written as [115]

$$\mathbf{N} = \begin{bmatrix} \cos \frac{\theta}{2} & ie^{-i\phi} \sin \frac{\theta}{2} \\ ie^{i\phi} \sin \frac{\theta}{2} & \cos \frac{\theta}{2} \end{bmatrix} \quad \mathbf{P} = \begin{bmatrix} e^{i\psi/2} & 0 \\ 0 & e^{-i\psi/2} \end{bmatrix} \quad (1.33)$$

$\theta$  and  $\phi$  being the nutation angle and phase, and  $\psi$  the precession angle  $\gamma\Delta B\Delta t = \gamma\vec{G}\vec{r}\Delta t$ .

The matrix  $\mathbf{P}$  can be rewritten as

$$\mathbf{P} = \begin{bmatrix} z^{1/2} & 0 \\ 0 & z^{-1/2} \end{bmatrix} = z^{1/2} \begin{bmatrix} 1 & 0 \\ 0 & z^{-1} \end{bmatrix} \quad (1.34)$$

In the SLR algorithm the initial spinor state is  $s_0 = [1 \ 0]^T$ . That yields after the first precession  $\mathbf{P}s_0 = z^{1/2}[1 \ 0]^T$  and after the first nutation  $\mathbf{N}$  the spinor  $s_1 = [\cos \frac{\theta}{2} \ ie^{i\phi} \sin \frac{\theta}{2}]^T$ . This procedure is carried out for the whole pulse with  $\mathbf{Q} = \mathbf{NP}$

$$s_n = z^{1/2}\mathbf{Q}_n s_{n-1} \quad (1.35)$$

The final spinor elements  $s_N = [\mathbf{a} \ \mathbf{b}]^T$  can afterwards be transformed to either a magnetization profile like for an inversion pulse  $M_z = M_0(1 - 2|\mathbf{b}|^2)$  or to the RF pulses' axis and angle parameters  $\alpha$  (rotation angle) and  $\theta$  and  $\phi$  (defining the rotation axis  $\vec{n}$ ) using the parameter relations given by Pauly [113].

$$\mathbf{a} = \cos \frac{\alpha}{2} - in_z \sin \frac{\alpha}{2} \quad \mathbf{b} = -i(n_x + in_y) \sin \frac{\alpha}{2} \quad (1.36)$$

The whole procedure might not seem very intuitive at first sight but the SU(2) rotations

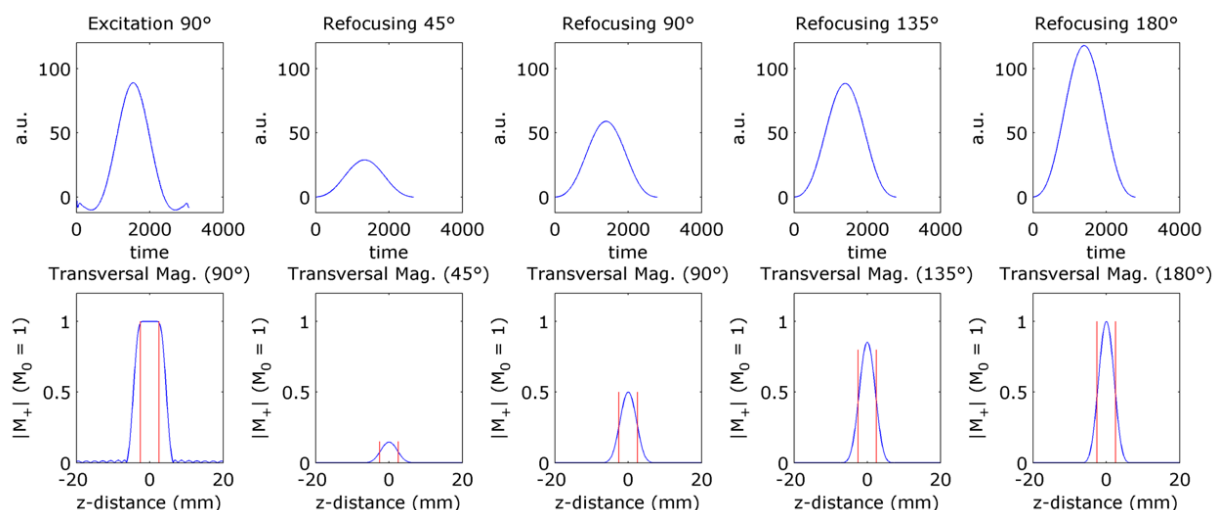


Figure 1.10: Qualitative comparison of slice profiles computed using the forward SLR algorithm for  $90^\circ$  excitation and subsequent refocusing with angles from  $45^\circ$  up to  $180^\circ$ . On the top row the actual pulse shapes are shown. (Pulse shapes were taken from vendor supplied multi-echo spin-echo sequence.)

reduce the effective number of mathematical operation, although it is not possible to account for relaxation effects during the RF pulse. Figure 4.5 gives an overview on how the slice profiles are shaped for given pulses and substantially degraded edges become apparent after refocusing.

### 1.4.3 Additional considerations

**Diffusion, J-coupling** J-coupling and diffusion pose a definite problem on  $T_2$  quantification with multi-echo spin-echo sequences that can not easily be remedied. Both effects are "hiding" in  $T_2$  and are dependent on the echo spacing whereby shorter echo spacing tendentially suppress the effects [116, 117]. Both influences cannot be totally refocused by RF pulses.

**Diffusion** Transverse magnetization (i.e. coherent spins) exposed to a magnetic field in  $z$ -direction will eventually accumulate phase  $\phi(t)$  according to

$$M_+(t) = M(0)e^{i\phi(t)} = M(0)e^{i\gamma \int_{\tau=0}^t B(\tau)d\tau} \quad (1.37)$$

Usually  $B(\tau)$  is deliberately altered for the purpose of image acquisition but there are also numerous reasons where field inhomogeneities will produce unwanted phase, especially in gradient echo sequences. For example, an unwanted constant field gradient in a voxel will produce phase dispersion that cannot be refocused in a gradient echo

## 1 Introduction

sequence and lets the magnetization decay faster with a sinc like behavior

When the signal of a voxel is measured a whole ensemble of spins has to be considered and the signal amounts to the integral over the whole spin ensemble. Furthermore, when it comes to diffusion or relaxation like processes the field  $B(t)$  is usually considered a stochastic variable, due to field fluctuations or diffusion of the spins through different field strengths. Generally, the expected value of the phase and magnetization can be expressed as:

$$\langle M(t) \rangle = \int_{\vec{x}} M(0) e^{i\gamma \int_0^t B(\vec{x}, \tau) d\tau} \cdot f(B(\vec{x}, t), \vec{x}) d\vec{x} \quad (1.38)$$

$$\langle \phi(t) \rangle = \int_{\vec{x}} i\gamma \int_0^t B(\vec{x}, \tau) d\tau \cdot f(B(\vec{x}, t), \vec{x}) d\vec{x} \quad (1.39)$$

where  $f(B(\vec{x}, \tau), \vec{x})$  denotes the probability density function that could be a function of the field or the spin position  $\vec{x}$ . Note that here we consider the spatial integral.

Let us now assume a linearly varying field in z-direction, i.e. a constant gradient,  $B(\vec{x}) = \vec{G} \cdot \vec{x}$  in the volume of interest which is not changing with time. The magnetization at time  $t$  then becomes

$$M_+(t) = M(0) e^{i\gamma \vec{G} \cdot \vec{x} t} \quad (1.40)$$

In the case of diffusion the random variable now is the position  $\vec{x}$  of each individual spin. For the sake of simplicity only one spatial coordinate is considered hereafter. The stochastic process at hand can now be modeled by a discrete random walk and the position of each spin at time  $\tau_j = j\tau_d$  ( $\tau_d$  being the diffusion time) will be expressed as

$$x_j = x_0 + \Delta_1 + \Delta_2 + \dots + \Delta_j = x_0 + \sum_{i=1}^j \Delta_i \quad (1.41)$$

where each  $\Delta_j$  is a distinct diffusion step width. All  $\Delta_j$ s are uncorrelated and normally distributed with  $\mathcal{N}(0, \sigma_\Delta)$ . The accumulation of phase can then be written as

$$\phi_k = \phi_{k-1} + \gamma G x_j \tau_d = \gamma G \tau_d \sum_{j=1}^k x_j \quad (1.42)$$

$$= \gamma G \tau_d \sum_{j=1}^k \left( x_0 + \sum_{i=1}^j \Delta_i \right). \quad (1.43)$$

Considering  $y_k = \sum_{j=1}^k \left( x_0 + \sum_{i=1}^j \Delta_i \right)$  a new random variable the magnetization after

G		$\Delta_1$	$\Delta_2$	$\Delta_3$	$\Delta_4$	$\Delta_5$	$\Delta_6$	$\Delta_7$	$\Delta_8$
+	$x_1$								
+	$x_2$								
+	$x_3$								
+	$x_4$								
+	$x_5$								
+	$x_6$								
+	$x_7$								
+	$x_8$								

Figure 1.11: Phase accumulation scheme for free diffusion:  $\Delta_i$  correspond to individual random jumps, whereas  $x_i$  denotes the position. The accumulated phase is indicated by the blue squares.

$k$  diffusion steps becomes

$$M_+(k \cdot \tau_d) = M(0)e^{i\gamma G y_k \tau_d}. \quad (1.44)$$

As  $y_k$  is a sum of normally distributed random variables and a constant  $x_0$  it will again be normally distributed with mean  $\mu_y$  and standard deviation  $\sigma_y$ . Computing the expectation value yields the general result

$$\langle M(k \cdot \tau_d) \rangle = M(0)e^{i\gamma G \tau_d \mu_y - \frac{1}{2}\gamma^2 G^2 \tau_d^2 \sigma_y^2} \quad (1.45)$$

where the first part of the exponent accounts for free precession of the whole spin ensemble if the mean position is not zero and the second part for signal decay due to diffusion in a constant gradient field. The exact values of  $\mu_y$  and  $\sigma_y$  depend on the MR sequence and still have to be calculated. I will now have a closer look at two distinct situations: Free diffusion through a constant gradient field and free diffusion through that field with refocusing.

**Free diffusion.** In fig. 1.11 the phase that accumulated after 8 time steps is marked in blue, whereas horizontally the individual uncorrelated jumps  $\Delta_i$  are indicated and vertically the actual positions, being the sum of the jumps marked in blue. The random

## 1 Introduction

phase accumulated after 8 jumps is just the some of all marked jumps. As we know from probability theory, the sum of normally distributed random variables is also normally distributed but with different mean and standard deviation. If the variables are uncorrelated, the individual variances sum up, if they are correlated an additional covariance term has to be included.  $Var(X, Y) = Var(X) + Var(Y) + 2Cov(X, Y)$ . Specifically if we have  $j$  times the same variable we get  $Var(jX) = j^2 Var(X)$  As we see from the columns in fig. 1.11 we have 8 times  $\Delta_1$ , 7 times  $\Delta_2$ , and so on. Furthermore, as every  $\Delta_i$  has the same standard deviation we can write the expected variance if  $\sigma_y^2$  after  $k$  jumps as

$$\sigma_y^2 = \sigma_\Delta^2 \sum_{j=1}^k j^2 = \sigma_\Delta^2 \left( \frac{k^3}{3} + \frac{k^2}{2} + \frac{k}{6} \right) \quad (1.46)$$

and the mean  $\mu_y = kx_0$ . For large  $k$  the term  $k^3/3$  dominates and we get

$$\langle M(k \cdot \tau_d) \rangle = M(0) e^{i\gamma G \tau_d k x_0 - \frac{1}{2} \gamma^2 G^2 \tau_d^2 \frac{k^3}{3} \sigma_\Delta^2} \quad (1.47)$$

or

$$\langle M(t) \rangle = M(0) e^{i\gamma G x_0 t - \frac{\gamma^2 G^2 \sigma_\Delta^2}{6 \tau_d} t^3} \quad (1.48)$$

$$= M(0) e^{i\gamma G x_0 t - \frac{\gamma^2 G^2 D}{3} t^3} \quad (1.49)$$

by considering  $t = k\tau_d$  and the diffusion constant being  $D = \sigma_\Delta^2 / (2\tau_d)$ . The expected magnetization value therefore decays with the third power of  $t$ .

**Free diffusion with refocusing.** From fig. 1.12 one can see that the situation is quite different when refocusing comes into play because after refocusing the accumulated phase needs to be subtracted and parts of the diffusion jumps cancel (marked with color). For each refocusing cycle with  $k$  steps (8 in the figure), the variance of  $\hat{y}_k$  is

$$\hat{\sigma}_y^2 = \sigma_\Delta^2 \left( \left( \frac{k}{2} \right)^2 + 2 \sum_j^{k/2-1} j^2 \right) = \sigma_\Delta^2 \left( \frac{k^3}{12} + \frac{k}{6} \right) \quad (1.50)$$

which linearly increases with echo number  $n$  (light red areas in figure 1.12).

$$\sigma_y^2 = n \sigma_\Delta^2 \left( \frac{k^3}{12} + \frac{k}{6} \right) \quad (1.51)$$



Introducing the echo spacing  $\tau$  with  $\tau = k\tau_d$  and  $t = n\tau$  one gets the following result ( $\mu_y = 0$ ):

$$\langle M(n) \rangle = M(0)e^{-\frac{1}{2}\gamma^2 G^2 \tau_d^2 \frac{nk^3}{12} \sigma_\Delta^2} \quad (1.52)$$

$$= M(0)e^{-\frac{\gamma^2 G^2 \sigma_\Delta^2}{24\tau_d} \tau^3 n} \quad (1.53)$$

$$= M(0)e^{-\frac{\gamma^2 G^2 D}{12} \tau^3 n} \quad (1.54)$$

The expected value of the magnetization now only decays linearly with echo number, but with the third power of echo spacing. This fact is reflected in the apparent  $T_2$  measured with multi-echo sequences and it's obvious that shorter echo spacing yields a slower decay.

**J-coupling** The effect of J-coupling, i.e. the electron mediated spin-spin coupling of neighbouring nuclei, manifests itself as a frequency difference resulting in a continuous phase accrual that cannot be reversed by  $180^\circ$  refocusing pulses. Principally, this results in a cyclic modulation of the spin echo signal. For complex spectra the summation of many of these oscillating signals yields a signal decay with apparently lower  $T_2$  which is also dependent on the echo spacing in multi-echo sequences. The shorter the echo time the higher the apparent  $T_2$  as the CPMG echo train decouples the spin system [118, 119]. Furthermore, if the echo spacing  $\tau$  is sufficiently small, i.e.

$$|J|\tau \ll 1 \quad \text{and} \quad |\Delta\delta|\tau \ll 1 \quad (1.55)$$

(where  $J$  is the coupling constant and  $\Delta\delta$  the chemical shift difference) the echo decay is unmodulated even when there is strong homonuclear coupling [117]. The effect of J-coupling is most prominent in oil or fatty tissue (see sec. 3.3) and is also the reason why fat appears brighter in TSE (RARE) sequences compared to SE sequences [119]. In [120] density matrix simulations were computed using the equations of Allerhand [117] to study the dependence of the CPMG echo amplitudes on J-coupling. The result was that the effect of J-coupling disappears when  $\tau$  is small. If  $\tau$  becomes too big a modulation of the echo train becomes visible. Furthermore, the relative signal amplitude at a specific echo time becomes unpredictable for larger  $\tau$  depending on the strength of the coupling. In fig. 1.13 these two findings are illustrated (reprinted from [120]).

A measurement of the J-coupling evolution and  $T_2$  values in oil phantoms and in vivo fatty tissue was performed in [121] once using broadband (565 Hz) and once narrow-band refocusing pulses (50 Hz, in the order of magnitude of the chemical

# 1 Introduction

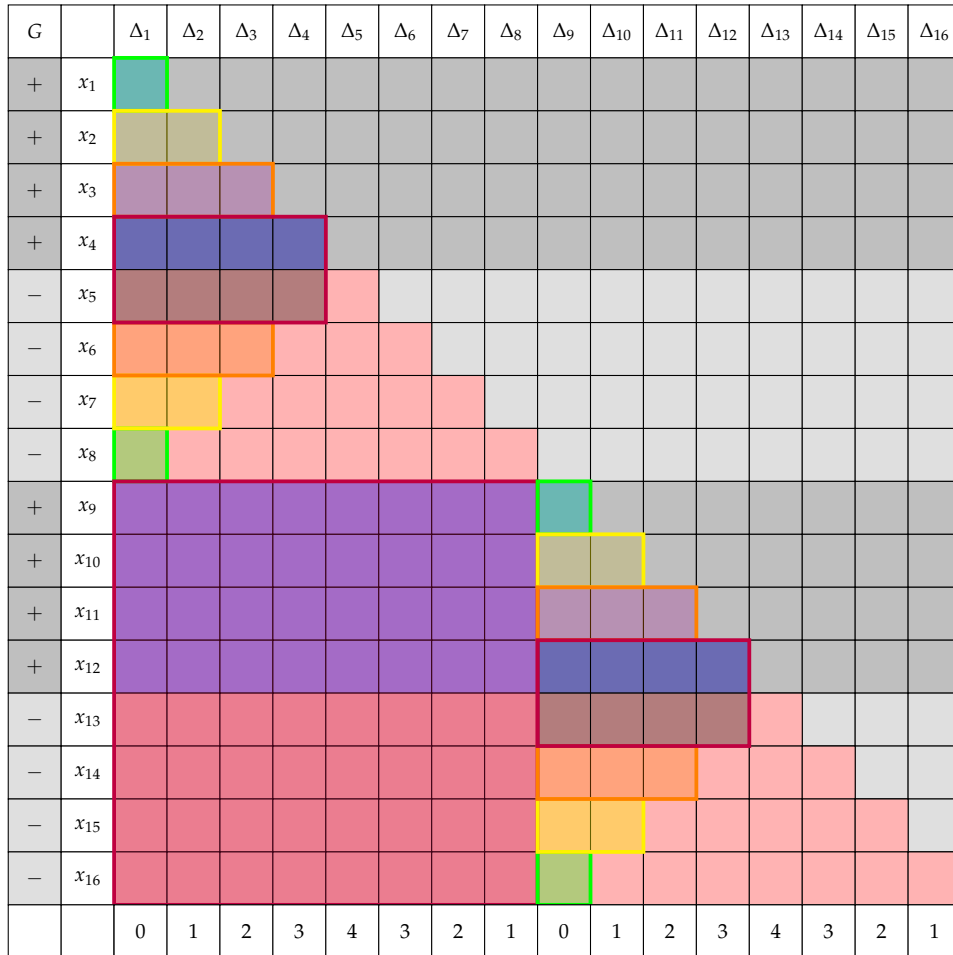


Figure 1.12: Phase accumulation scheme for a multi-echo spin-echo sequence:  $\Delta_i$  correspond to individual random jumps, whereas  $x_i$  denotes the position. The accumulated phase is indicated by the colored squares. The + and - signs in the leftmost column indicate the sign reversal due to refocusing pulses. This sign reversal yields to complete cancellation of parts of the accumulated phase (marked with colored boxes) leaving only the parts shaded in light red for each echo.

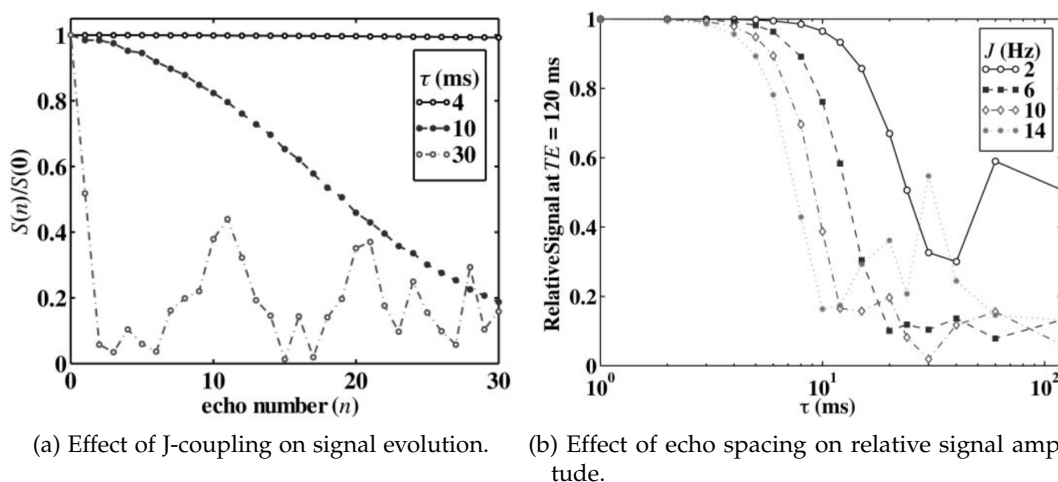


Figure 1.13: Illustration of the effect of J-coupling on a CPMG echo train. (a) Signal vs. echo number for different echo spacing ( $\Delta\delta = 40$  Hz and  $J = 6$  Hz), (b) relative echo amplitude vs. echo spacing for different J-couplings and  $\Delta\delta = 40$  Hz (reprinted from [120]).

shift difference of  $\text{CH}_2$  and  $\text{CH}_3$  protons) and a PRESS sequence. Only with narrow bandwidth pulses a meaningful  $T_2$  could be obtained as the J-coupling modulations disappear.

Considering the above results, one certainly has to pay attention when measuring and interpreting  $T_2$  values of J-coupled protons.

**Magnetization transfer and chemical exchange.** Off-resonant irradiation of macromolecular protons in adjacent slices poses a problem in slice selective MSE echo sequences. Additionally direct saturation effects due to overlapping slice profiles are present which can be minimized by introducing a larger slice gap between adjacent slices. Both mechanisms result in a loss of signal intensity. A slice gap of 100% was shown to be sufficient to mitigate these perturbations [118]. Allerhand et al. [116] investigated the behavior of the CPMG echo decay in relation to exchange processes between sites of different chemical shifts or  $T_2$  times. If the echo spacing is small enough exchange effects due to different chemical shift are eliminated, for large echo spacing the relaxation rate becomes a function of  $\tau$ . The general impact on the echo decay will also depend on the rate of exchange. The Luz-Meiboom equation is an example of a limiting case for a fast exchange process (detailed assumptions see [116]):

$$\frac{1}{T_2} = \frac{1}{T_2^0} + \tau_{ex} \left[ 1 - \frac{2\tau_{ex}}{\tau} \tanh \frac{\tau}{2\tau_{ex}} \right] \sum_j p_j (\Delta\omega_j)^2 \quad (1.56)$$

## 1 Introduction

One can readily see how the apparent transverse relaxation times is dependent on the exchange rate  $1/\tau_{ex}$  and the echo spacing  $\tau$  ( $p_j$  being the relative intensities and  $\Delta\omega$  the chemical shift for  $j$  different sites).

Furthermore, the signal in bSSFP sequences is also dependent on magnetization transfer [122] which has to be taken into account when used for MR relaxometry.

**Multi-compartment parameter estimation.** Several tissues in the human body exhibit a multi-compartment  $T_2$  characteristics with a short and a long  $T_2$  component, e.g. white brain matter where the short  $T_2$  component belongs to the myelin bound water. Clearly, the rules that are valid for multi-exponential fitting, which is inherently ill-posed [123, pp. 252], have also be regarded with more complicated models. Stimulated echo correction using the extended phase graph (EPG) was applied for multi-component  $T_2$  fitting and lead to an improved consistency and accuracy of the myelin water fraction [36]. In chapter 4 multi-compartment fitting was investigated too.

**Data fitting.** Most of the estimation techniques involve a non-linear parameter fit of which the goodness certainly has to be assessed as to confirm or disprove the applied model. Unfortunately, most measures of quality are derived for the linear case and are not or only partly applicable. However, measures like the residual, the coefficient of determination, the covariance matrix of the parameters, to name a few should be assessed (see [124, pp. 170]).

**Validation.** Validation is of paramount importance when new models are developed. First, simulations should be made, where the model is inspected and used in various test cases. Second, for  $T_2$ -reliable and stable phantoms are essential, preferably characterized with a "gold standard" sequence, if there is one. Third, in vivo measurements have to be conducted, and what is most often forgotten, repeated. No method should be compared to another unless it wasn't successfully compared to itself in a repeatability and reproducibility study.

I tried to adhere to these principles throughout the presented studies.

## 1.5 Dissertation outline

Throughout this thesis the following topics will be covered:

**Chapter 1** you've just read...

**Chapter 2** covers the z-transform, Bloch equations, the Generating functions formalism to calculate MR signals and a few illustrative examples

**Chapter 3** investigates the impact of the slice-profile on  $T_2$  -mapping with slice selective multi-echo spin-echo sequences

**Chapter 4** derives the Generating function for MSE sequences and a time domain version thereof

**Chapter 5** derives a signal equation for the longitudinal MSE magnetization and uses it to simultaneously estimate  $T_1$  and  $T_2$

**Chapter 6** shortly discusses the presented work



# 2

## The Generating Functions approach

The so-called *Generating Functions approach* (GF) as it was used by Lukzen et al. [37, 38] is an alternative name for the z-transform [125], specifically when ordinary GF are meant, and was originally introduced already 1730 by DeMoivre [126]. It can be used to compute solutions to *linear constant coefficient difference equations* and is often applied in signal processing for the analysis of linear time-invariant systems [127]. I will use the terms *Generating functions* and *z-transform* interchangeably throughout this text.

In multi-echo sequences in MRI the solution to the Bloch equation can be formulated by a recurrence relation, i.e. a system of linear constant coefficient difference equations provided the refocusing flip angle stays the same throughout the echo train. In this context, Lukzen et al. first developed a closed form solution for non-slice-selective CPMG sequences [37]. In their 2007 paper they describe an analytical formula for the echo amplitudes for spin-echo sequences with repetitive application of RF pulses.

In this chapter I will briefly outline some key properties of the z-transform and it's application to difference equations and, specifically, to the Bloch equation recurrence relation.

### 2.1 The z-transform

The z-transform is a transformation or series expansion that assigns in a certain domain a holomorphic function to a sequence of numbers [128]. It is formally equivalent to ordinary Generating Functions or the Laurent series [125]. It can be seen as Laplace transform for time discrete systems, and can be derived from applying the Laplace transform to signals passed through a sample and hold circuit [128]. Just as the Laplace transform can be used to solve differential equations, the z-transform can be used to solve difference equations, analogously.

There exist two different definitions for the z-transform  $\mathcal{Z}(x[n])$  of some time discrete function  $x[n]$ ; the version usually used in signal processing

$$\mathcal{Z}(x[n]) = X(z) = \sum_{n=-\infty}^{\infty} x[n]z^{-n}, \quad (2.1)$$

## 2 The Generating Functions approach

and the so called geophysical definition [129]

$$X(z) = \sum_{n=-\infty}^{\infty} x[n]z^n \quad (2.2)$$

which will be used throughout this text, mainly to be in accordance with the calculations done by Lukzen. For causal systems, i.e.  $x[n] = 0$  for  $n < 0$ , usually, the unilateral version of the z-transform is used which is defined by

$$X(z) = \sum_{n=0}^{\infty} x[n]z^n \quad (2.3)$$

### 2.1.1 Properties of the z-transform

Here, some properties of the z-transform and some essential correspondences  $x[n] \overset{z}{\circlearrowleft} X(z)$  that will be needed later in the text are given. The detailed description and proof of the stated properties is out of scope of this work and is to be found elsewhere [125, 127, 128].

**Time shifting property.** The time shifting property establishes a simple relation for the z-transform of  $x[n]$  and a time shifted version  $x[n + k]$ . This property will be used to solve the difference equations.

$$X(z) = \sum_{n=0}^{\infty} x[n]z^n = x[0] + x[1]z + x[2]z^2 + \dots \quad (2.4)$$

$$\hat{X}(z) = \sum_{n=0}^{\infty} x[n + 1]z^n = x[1] + x[2]z + x[3]z^2 + \dots \quad (2.5)$$

$$= z^{-1}X(z) - x_0z^{-1} \quad (2.6)$$

$$\text{or more generally } Y(z) = \sum_{n=0}^{\infty} x[n + k]z^n = z^{-k}\{X(z) - \sum_{n=0}^{k-1} x[n]z^n\} \quad (2.7)$$

**Final value theorem.** The final value of the sequence  $x[\infty]$  can be easily computed by eq. 2.8 and is very useful to calculate the steady state signal equation for certain MR sequences.

$$\lim_{z \rightarrow 1} (z^{-1} - 1)X(z) = \lim_{n \rightarrow \infty} x[n] = x[\infty] \quad (2.8)$$



**Initial value theorem.** The initial value  $x[0]$  can be readily computed from  $X(z)$  using the limit

$$\lim_{z \rightarrow 0} X(z) = \lim_{z \rightarrow 0} \sum_{n=0}^{\infty} x[n]z^n = \lim_{z \rightarrow 0} x[0] + x[1]z + x[2]z^2 + \dots + x[\infty]z^\infty = x[0]. \quad (2.9)$$

**Damping rule.** Multiplication of the original sequence  $x[n]$  with an exponential function  $a^n$  leads to the so called damping rule and can be used for apodization of signals so as to force them to zero for large  $n$ . This property is very useful when the original sequence is reconstructed from  $X(z)$  using the discrete Fourier transform (DFT) (see sec. 2.1.2).

$$X(az) = \sum_{n=0}^{\infty} x[n](az)^n = \mathcal{Z}(x[n]a^n) \quad (2.10)$$

**Region of convergence.** For sequences encountered throughout this text, i.e. causal or right-handed sequences that are zero for all  $n < 0$  the region of convergence (ROC) extends inwards from the innermost pole (for the geophysical definition). The ROC cannot contain any poles. If the unit circle lies within the ROC the relation of the z-transform to the DFT can be used to evaluate  $X(z)$  and successively compute  $x[n]$  numerically (sec. 2.1.2)

**Some correspondences.** In tab. 2.1 some correspondences are given, which will be used later on in this text, specifically to calculate limiting cases for the CPMG pulse sequence to validate the corresponding z-transform.

Function	Time domain	z-domain
Unit step	$u[n] = \begin{cases} 1 & n \geq 0 \\ 0 & n < 0 \end{cases}$	$U(z) = \frac{1}{1-z}$
Exponential	$x[n] = a^n u[n]$	$X(z) = \frac{1}{1-az}$
Alternating exponential	$x[n] = (-1)^n u[n]$	$X(z) = \frac{1}{1+z}$

Table 2.1: Time domain – z-domain correspondences

## 2 The Generating Functions approach

### 2.1.2 Relation to discrete time Fourier transform and DFT

One can easily see that, if  $z$  is confined to the unit circle, i.e.  $z = e^{i\psi}$ , the  $z$ -transform equation 2.2 reduces to the discrete time Fourier transform (DTFT).

$$X(z) = \sum_{n=-\infty}^{\infty} x[n]z^n \Big|_{z=e^{i\psi}} = \sum_{n=-\infty}^{\infty} x[n]e^{i\psi n} = X(e^{i\psi}) \quad (2.11)$$

If a signal has a finite number of samples  $N$ , the angle  $\psi$  can also be sampled at  $N$  discrete values,  $\psi_k = \frac{2\pi k}{N}$ , where  $k = 0 \dots N-1$ , and we get the well known DFT and inverse DFT (iDFT) formulas:

$$X[k] = \sum_{n=0}^{N-1} x[n]e^{\frac{2\pi i}{N}kn} \quad (2.12)$$

$$x[n] = \frac{1}{N} \sum_{k=0}^{N-1} X[k]e^{-\frac{2\pi i}{N}nk} \quad (2.13)$$

Note, that here again the minus sign in the exponent is switched between the two formulas compared to the classical definition of the DFT. If  $X(e^{i\psi})$  exists on the unit circle, i.e. the unit circle lies within the region of convergence, one can easily evaluate it and calculate  $x[n]$  numerically using the iDFT. However, care has to be taken when the sequence  $x[n]$  is truncated because so called truncation artifacts will arise. Sampling  $X[k]$  at a higher rate, e.g.  $4N$  points, can remedy the problem but increases computational cost. If one wishes to compute  $X[k]$  from  $x[n]$  for further processing the apodization property described previously comes in quite handy as multiplication with  $a^n$  ( $|a| < 1$ ) tapers off  $x[n]$  and reduces these artifacts.

### 2.1.3 Solving a simple difference equation

As mentioned at the beginning of this chapter the  $z$ -transform is often used to solve linear difference equations with constant coefficients. I will present here two simple examples to show the reader how this can be accomplished. The same principle is later used for a system of difference equations, namely the Bloch equations.

**Example 1 - homogeneous equation.** Given the simple difference equation  $x[n+1] = bx[n]$  with initial condition  $x[0] = \text{const.}$  one can easily obtain a transformed equation

$$z^{-1}X(z) - x[0]z^{-1} = bX(z) \quad (2.14)$$

$$X(z) = \frac{x[0]}{1 - bz} \quad (2.15)$$

From tab. 2.1 one can see by inspection that Eq. 2.15 corresponds to the time domain equation

$$x[n] = x[0]b^n \quad (2.16)$$

which equals the  $T_2$  decay if  $x = M_+$ , and  $b = e^{-\tau/T_2}$ .

**Example 2 - inhomogeneous equation.** Consider the inhomogeneous difference equation  $x[n+1] = ax[n] + (1-a)k$  with initial condition  $x[0] = \text{const}$ . Furthermore, assume our system is causal and recall that the z-transform of the unit step function equals  $1/(1-z)$ . Then the transformed equation is:

$$z^{-1}X(z) - x[0]z^{-1} = aX(z) + \frac{(1-a)k}{1-z} \quad (2.17)$$

$$X(z) = \frac{x[0]}{1-az} + \frac{(1-a)kz}{(1-z)(1-az)} \quad (2.18)$$

With partial fraction decomposition and inspection, the solution in the time domain can be obtained:

$$X(z) = \frac{x[0]}{1-az} + k \left( \frac{1}{(1-z)} - \frac{1}{1-az} \right) \quad (2.19)$$

$$x[n] = x[0]a^n u[n] + k(1-a^n)u[n] \quad (2.20)$$

Equation 2.20 actually resembles the formula for the longitudinal relaxation when  $a = e^{-\tau/T_1}$ ,  $x = M_z$ , and  $k = M_0$ .

#### Relation to differential equations.

In this excursion, the relation between continuous time differential and discrete time difference equations shall be demonstrated. Given the differential equation for longitudinal relaxation

$$\frac{dM_z(t)}{dt} = \frac{1}{T_1}(M_0 - M_z(t)) \quad (2.21)$$

one can approximate the differential quotient by the discrete time difference:

$$\frac{M_z(t+\tau) - M_z(t)}{\tau} = \frac{1}{T_1}(M_0 - M_z(t)) \quad (2.22)$$

$$M_z(t+\tau) = \frac{\tau}{T_1}M_0 - \frac{\tau}{T_1}M_z(t) + M_z(t) \quad (2.23)$$

## 2 The Generating Functions approach

Substituting for  $\tau/T_1$  a new expression  $(1 - \tilde{a})$  yields

$$M_z(t + \tau) = \tilde{a}M_z(t) - M_0(1 - \tilde{a}) \quad (2.24)$$

which closely resembles the previously solved difference equation. One can easily see that this substitution is related to the first order Taylor expansion of  $a = e^{-\tau/T_1}$  which is  $\tilde{a} = 1 - \frac{\tau}{T_1}$ .

## 2.2 The Bloch equations

In the most general form, the dynamics of the macroscopic magnetization vector  $\vec{M} = (M_x, M_y, M_z)^T$  is governed by the Bloch equations 2.25 [130, p. 27]

$$\frac{d\vec{M}}{dt} = \gamma\vec{M} \times \vec{B} - \frac{1}{T_2} \begin{pmatrix} M_x \\ M_y \\ 0 \end{pmatrix} + \frac{1}{T_1} \begin{pmatrix} 0 \\ 0 \\ M_0 - M_z \end{pmatrix}, \quad (2.25)$$

where  $\vec{B} = (B_x, B_y, B_z)^T$  is the total magnetic flux density (static, gradient, and RF fields) and  $T_1$  and  $T_2$  are the relaxation times. Note, that magnetization and field vectors,  $\vec{M} = \vec{M}(t)$  and  $\vec{B} = \vec{B}(t)$ , are generally functions of time, and, that the explicit notation of their time dependence is omitted here for the sake of legibility. Usually, these equations are transformed to the so-called rotating reference frame. In this reference frame which is rotating at the Larmor frequency around the z-axis, the magnetization vector is standing still if no additional magnetic field is applied. If an RF field at the Larmor frequency is applied, also this RF field vector is standing still. Let us first neglect relaxation and compute the spin dynamics under the influence of such a field. For the sake of convenience, the field vector,  $\vec{B}$ , is given in spherical coordinates as outlined in fig. 2.1.

The equation to be solved then is

$$\frac{d\vec{M}}{dt} = \gamma \begin{pmatrix} M_x \\ M_y \\ M_z \end{pmatrix} \times |B| \begin{pmatrix} \sin \theta \cos \phi \\ \sin \theta \sin \phi \\ \cos \theta \end{pmatrix} \quad (2.27)$$

Fig. 2.2 (a) illustrates the rotational effect of the magnetic field on the magnetization vector. The mathematical solution to the problem is given in eq. 2.29 where  $\alpha$  is the effective rotation angle and is given by  $\alpha = \gamma|B|\tau$ , and  $\tau$  is the time period the external field is switched on. This matrix and equivalent to a rotation matrix for a counter-clock-wise rotation around a normalized vector  $\vec{u} = -\vec{B}/|B|$  about an angle  $\alpha$

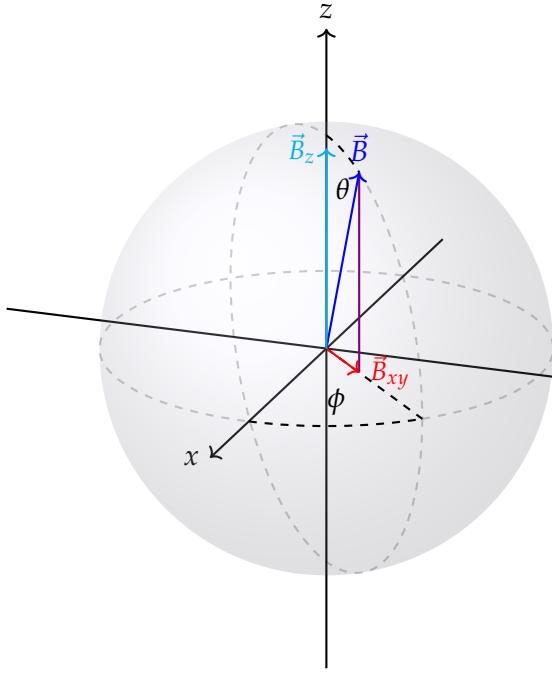


Figure 2.1: Definition of the spherical coordinates used in the calculations. Vector  $\vec{B}$  is given in terms of its length  $|B|$  and the polar and azimuthal angles  $\theta$  and  $\phi$ , respectively.

$$\vec{B} = |B| \begin{pmatrix} \sin \theta \cos \phi \\ \sin \theta \sin \phi \\ \cos \theta \end{pmatrix} \quad (2.26)$$

in the axis-angle-representation (see fig. 2.2 (b)). The solution after the application of a pulsed magnetic field of length  $\tau$  is then given by

$$\vec{M}^{(n+1)} = \mathbf{R}_{-\frac{\vec{B}}{|\vec{B}|}}(\gamma|\vec{B}|\tau) \vec{M}^{(n)} = \mathbf{R}_{\vec{u}}(\alpha) \vec{M}^{(n)} \quad (2.28)$$

where  $\vec{M}^{(n)}$  denotes the magnetization vector before the pulse and  $\vec{M}^{(n+1)}$  the magnetization after the  $n^{\text{th}}$  pulse.

$$\mathbf{R}_{-\frac{\vec{B}}{|\vec{B}|}}(\gamma|\vec{B}|\tau) = \begin{pmatrix} ((\cos(\alpha) - 1) \cos^2(\theta) + 1) \cos^2(\phi) + \cos(\alpha) \sin^2(\phi) & \sin^2(\frac{\alpha}{2}) \sin(2\phi) \sin^2(\theta) + \cos(\theta) \sin(\alpha) & \sin(\theta) (2 \cos(\theta) \cos(\phi) \sin^2(\frac{\alpha}{2}) - \sin(\alpha) \sin(\phi)) \\ \sin^2(\frac{\alpha}{2}) \sin^2(\theta) \sin(2\phi) - \cos(\theta) \sin(\alpha) & \sin^2(\theta) \sin^2(\phi) + \cos(\alpha) (\cos^2(\phi) + \cos^2(\theta) \sin^2(\phi)) & \sin(\theta) (\cos(\phi) \sin(\alpha) - (\cos(\alpha) - 1) \cos(\theta) \sin(\phi)) \\ \cos(\phi) \sin(2\theta) \sin^2(\frac{\alpha}{2}) + \sin(\alpha) \sin(\theta) \sin(\phi) & \sin(\theta) (-\cos(\phi) \sin(\alpha) - (\cos(\alpha) - 1) \cos(\theta) \sin(\phi)) & \cos^2(\theta) + \cos(\alpha) \sin^2(\theta) \end{pmatrix} \quad (2.29)$$

$$\mathbf{R}_{\vec{u}}(\alpha) = \begin{pmatrix} (1 - \cos(\alpha)) u_x^2 + \cos(\alpha) & u_x u_y (1 - \cos(\alpha)) - u_z \sin(\alpha) & u_x u_z (1 - \cos(\alpha)) + u_y \sin(\alpha) \\ u_x u_y (1 - \cos(\alpha)) + u_z \sin(\alpha) & (1 - \cos(\alpha)) u_y^2 + \cos(\alpha) & u_y u_z (1 - \cos(\alpha)) - u_x \sin(\alpha) \\ u_x u_z (1 - \cos(\alpha)) - u_y \sin(\alpha) & u_y u_z (1 - \cos(\alpha)) + u_x \sin(\alpha) & (1 - \cos(\alpha)) u_z^2 + \cos(\alpha) \end{pmatrix} \quad (2.30)$$

Generally, the RF field (also called  $B_{1+}$  field) is applied on-resonant in the  $x$ - $y$  plane and thus given by  $\vec{B}_{1+} = (B_{1+} \cos \phi, B_{1+} \sin \phi, 0)^T$ . An off-resonance  $B_{1+}$  field, however, produces an additional field component and, thus, rotation around the  $z$ -axis,

## 2 The Generating Functions approach

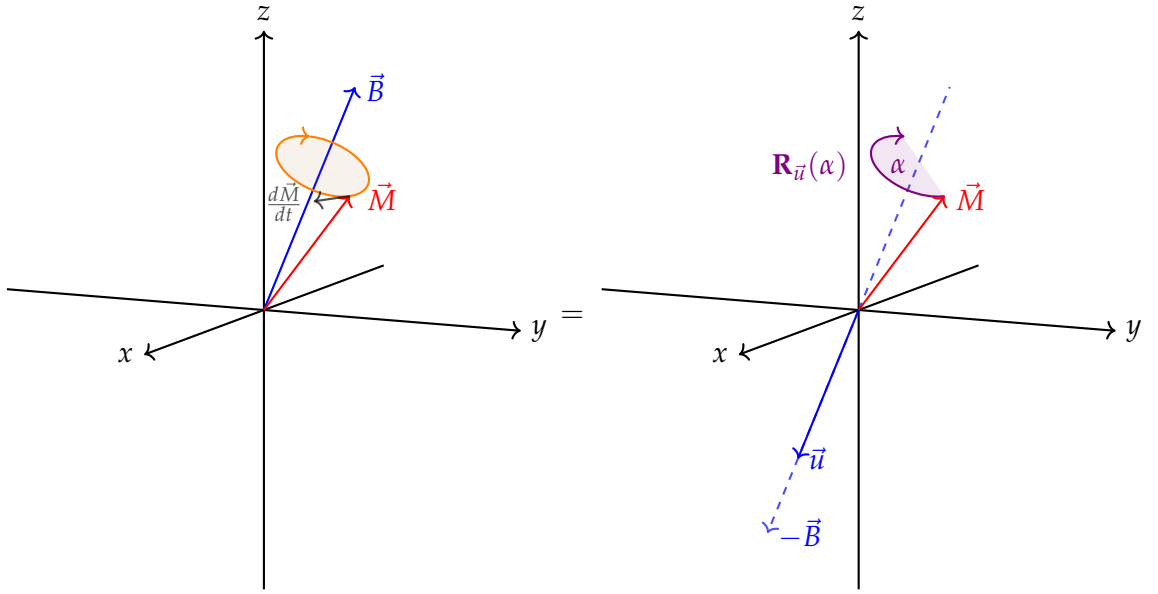


Figure 2.2: Equivalent description of the spin dynamics under an arbitrary magnetic field  $\vec{B}$ , (a) description by the Bloch equations and (b) equivalent description with a rotation matrix  $\mathbf{R}_{\vec{u}}(\alpha)$  around an arbitrary axis  $\vec{u} = -\vec{B}/|\vec{B}|$  by an angle of  $\alpha$ .  $\alpha$  is equivalent to  $\gamma|\vec{B}|\tau$  in the Bloch picture,  $\tau$  being the pulse duration.

and is denoted by  $\Delta B$  such that the effective field  $\vec{B}$  can also be written as  $\vec{B} = (B_{1+} \cos \phi, B_{1+} \sin \phi, \Delta B)^T$ . Equating this expression with eq. 2.26, one can compute the following relations:

$$\alpha = \gamma|\vec{B}|\tau = \gamma\tau\sqrt{|B_{1+}|^2 + \Delta B^2} \quad (2.31)$$

$$\frac{|B_{1+}|}{\Delta B} = \frac{\sin \theta}{\cos \theta} = \tan \theta \quad (2.32)$$

$$\theta = \arctan \frac{|B_{1+}|}{\Delta B} \quad (2.33)$$

### 2.2.1 Solutions to Bloch equations

For special cases, eq. 2.29 reduces to the well-known rotation matrices around x, y, and z-axis:

<span style="color: green;">x-axis: <math>\mathbf{R}_x(\alpha)</math></span> $\phi = 0, \theta = \frac{\pi}{2}$	<span style="color: purple;">y-axis: <math>\mathbf{R}_y(\alpha)</math></span> $\phi = \frac{\pi}{2}, \theta = \frac{\pi}{2}$	<span style="color: brown;">z-axis: <math>\mathbf{R}_z(\alpha)</math></span> $\theta = 0$
$\begin{pmatrix} 1 & 0 & 0 \\ 0 & \cos(\alpha) & \sin(\alpha) \\ 0 & -\sin(\alpha) & \cos(\alpha) \end{pmatrix}$	$\begin{pmatrix} \cos(\alpha) & 0 & -\sin(\alpha) \\ 0 & 1 & 0 \\ \sin(\alpha) & 0 & \cos(\alpha) \end{pmatrix}$	$\begin{pmatrix} \cos(\alpha) & \sin(\alpha) & 0 \\ -\sin(\alpha) & \cos(\alpha) & 0 \\ 0 & 0 & 1 \end{pmatrix}$
(2.34)		

#### Relaxation

The Bloch equations during periods of sole relaxation are written as

$$\frac{d\vec{M}}{dt} = - \begin{pmatrix} (1/T_2)M_x \\ (1/T_2)M_y \\ (1/T_1)(M_0 - M_z) \end{pmatrix} \quad (2.35)$$

with the solution being

$$\vec{M}(t) = \begin{pmatrix} M_x e^{-t/T_2} \\ M_y e^{-t/T_2} \\ M_z e^{-t/T_1} + (1 - e^{-t/T_1})M_0 \end{pmatrix} \quad (2.36)$$

$$= \begin{pmatrix} e^{-t/T_2} & 0 & 0 \\ 0 & e^{-t/T_2} & 0 \\ 0 & 0 & e^{-t/T_1} \end{pmatrix} \begin{pmatrix} M_x \\ M_y \\ M_z \end{pmatrix} + \begin{pmatrix} 0 \\ 0 \\ (1 - e^{-t/T_1})M_0 \end{pmatrix} \quad (2.37)$$

#### Free precession and relaxation

If only free precession around the z-axis and relaxation are considered the Bloch equations can be written as

$$\frac{d\vec{M}}{dt} = \gamma \begin{pmatrix} M_x \\ M_y \\ M_z \end{pmatrix} \times \begin{pmatrix} 0 \\ 0 \\ B_z \end{pmatrix} - \begin{pmatrix} (1/T_2)M_x \\ (1/T_2)M_y \\ (1/T_1)(M_0 - M_z) \end{pmatrix} \quad (2.38)$$

## 2 The Generating Functions approach

to which the solution is

$$\vec{M}(t) = \begin{pmatrix} (M_x \cos(B_z \gamma t) + M_y \sin(B_z \gamma t))e^{-t/T_2} \\ (M_y \cos(B_z \gamma t) - M_x \sin(B_z \gamma t))e^{-t/T_2} \\ M_z e^{-t/T_1} + (1 - e^{-t/T_1})M_0 \end{pmatrix} \quad (2.39)$$

$$= \begin{pmatrix} \cos(B_z \gamma t)e^{-t/T_2} & \sin(B_z \gamma t)e^{-t/T_2} & 0 \\ -\sin(B_z \gamma t)e^{-t/T_2} & \cos(B_z \gamma t)e^{-t/T_2} & 0 \\ 0 & 0 & e^{-t/T_1} \end{pmatrix} \begin{pmatrix} M_x \\ M_y \\ M_z \end{pmatrix} + \begin{pmatrix} 0 \\ 0 \\ (1 - e^{-t/T_1})M_0 \end{pmatrix} \quad (2.40)$$

### 2.2.2 From $M_x$ , $M_y$ , and $M_z$ to transverse and longitudinal magnetization $M_+$ and $M_z$

Often, the magnetization vector is given by defining the complex transverse magnetization  $M_+ = M_x + iM_y$  as

$$\vec{M} = \begin{pmatrix} M_+ \\ M_+^* \\ M_z \end{pmatrix} \quad (2.41)$$

where  $M_+^*$  is the complex conjugate of  $M_+$ .  $M_z$  stays as it is and denotes the longitudinal magnetization. As the new magnetization vector can be computed simply by applying the appropriate transformation matrix  $\mathbf{T}$

$$\begin{pmatrix} M_+ \\ M_+^* \\ M_z \end{pmatrix} = \mathbf{T} \begin{pmatrix} M_x \\ M_y \\ M_z \end{pmatrix} = \begin{pmatrix} 1 & i & 0 \\ 1 & -i & 0 \\ 0 & 0 & 1 \end{pmatrix} \begin{pmatrix} M_x \\ M_y \\ M_z \end{pmatrix} \quad (2.42)$$

the results obtained in the previous section can as easily be transformed, e.g. for a original rotation matrix  $\mathbf{R}$ :

$$\begin{pmatrix} M_+ \\ M_+^* \\ M_z \end{pmatrix} = \mathbf{TR}_{\vec{u}}(\alpha)\mathbf{T}^{-1} \begin{pmatrix} M_+ \\ M_+^* \\ M_z \end{pmatrix} = \mathbf{P} \begin{pmatrix} M_+ \\ M_+^* \\ M_z \end{pmatrix} \quad (2.43)$$

whereas

$$\mathbf{T}^{-1} = \begin{pmatrix} 1/2 & 1/2 & 0 \\ -i/2 & -i/2 & 0 \\ 0 & 0 & 1 \end{pmatrix} \quad (2.44)$$



When the formula for a rotation about an arbitrary axis,  $\mathbf{R}_{\vec{u}}(\alpha)$ , is transformed, one arrives at the following expression:

$$\mathbf{P}_{\vec{u}}(\alpha) = \begin{pmatrix} (\cos(\frac{\alpha}{2}) - i \cos(\theta) \sin(\frac{\alpha}{2}))^2 & e^{2i\phi} \sin^2(\frac{\alpha}{2}) \sin^2(\theta) & e^{i\phi} (-\cos(\alpha) \cos(\theta) + \cos(\theta) + i \sin(\alpha)) \sin(\theta) \\ e^{-2i\phi} \sin^2(\frac{\alpha}{2}) \sin^2(\theta) & (\cos(\frac{\alpha}{2}) + i \cos(\theta) \sin(\frac{\alpha}{2}))^2 & e^{-i\phi} (-\cos(\alpha) \cos(\theta) + \cos(\theta) - i \sin(\alpha)) \sin(\theta) \\ \frac{1}{2} e^{-i\phi} (-\cos(\alpha) \cos(\theta) + \cos(\theta) + i \sin(\alpha)) \sin(\theta) & -\frac{1}{2} e^{i\phi} ((\cos(\alpha) - 1) \cos(\theta) + i \sin(\alpha)) \sin(\theta) & \cos^2(\theta) + \cos(\alpha) \sin^2(\theta) \end{pmatrix} \quad (2.45)$$

or in short notation

$$\mathbf{P}_{\vec{u}}(\alpha) = \begin{pmatrix} \lambda & \chi & \nu e^{i\phi} \\ \chi^* & \lambda^* & \nu^* e^{-i\phi} \\ \frac{\nu}{2} e^{-i\phi} & \frac{\nu^*}{2} e^{i\phi} & \zeta \end{pmatrix} \quad (2.46)$$

$$\begin{aligned} \lambda &= (\cos \frac{\alpha}{2} - i \sin \frac{\alpha}{2} \cos \theta)^2, & \chi &= e^{2i\phi} \sin^2 \frac{\alpha}{2} \sin^2 \theta, \\ \nu &= 2 \sin \frac{\alpha}{2} \sin \theta (\sin \frac{\alpha}{2} \cos \theta + i \cos \frac{\alpha}{2}), & \zeta &= \cos \alpha \sin^2 \theta + \cos^2 \theta. \end{aligned} \quad (2.47)$$

For an off-resonant pulse around the  $x$ -axis one gets

$$\mathbf{P}_{xz}(\alpha) = \begin{pmatrix} \lambda & \mu & \nu \\ \mu & \lambda^* & \nu^* \\ \frac{\nu}{2} & \frac{\nu^*}{2} & \zeta \end{pmatrix} \quad (2.48)$$

as well as for an off-resonant pulse around  $y$  axis

$$\mathbf{P}_{yz}(\alpha) = \begin{pmatrix} \lambda & -\mu & i\nu \\ -\mu & \lambda^* & -i\nu^* \\ \frac{i\nu}{2} & \frac{-i\nu^*}{2} & \zeta \end{pmatrix}. \quad (2.49)$$

$\mathbf{P}_{xz}(\alpha)$  is exactly the same expression as derived by Lukzen [38] except for the fact that in the coordinate system used by Lukzen the  $z$ -component of the field vector is defined by the angle the vector has with the  $xy$ -plane (not like the polar angle  $\theta$  is defined). Therefore, in Lukzens work all  $\theta$ s are replaced by  $90 - \theta$  (Note that  $90 - \theta$  is denoted by  $\varphi$  in [38]).

## Relaxation

For pure relaxation, the solution of the Bloch equations in the complex domain is the same as in equation 2.37.

## 2 The Generating Functions approach

### Free precession and relaxation

For free precession and relaxation the solution in eq. 2.40 transforms to

$$\vec{M}(t) = \begin{pmatrix} M_+ e^{-t/T_2 + i\gamma B_z t} \\ M_+^* e^{-t/T_2 - i\gamma B_z t} \\ M_z e^{-t/T_1} + (1 - e^{-t/T_1}) M_0 \end{pmatrix} \quad (2.50)$$

$$= \begin{pmatrix} U e^{-t/T_2} & 0 & 0 \\ 0 & U^{-1} e^{-t/T_2} & 0 \\ 0 & 0 & e^{-t/T_1} \end{pmatrix} \begin{pmatrix} M_+ \\ M_+^* \\ M_z \end{pmatrix} + \begin{pmatrix} 0 \\ 0 \\ (1 - e^{-t/T_1}) M_0 \end{pmatrix} \quad (2.51)$$

with  $U = e^{i\gamma B_z t}$ .

## 2.3 Generating functions for repetitive pulse sequences

As we have seen in section 2.2, the Bloch equations can be solved for distinct events in a MR pulse sequence, such as RF pulses (nutating of magnetization), gradients or off-resonances (precession), and relaxation periods. Many MR sequences are repetitive in nature, i.e. certain parts of the sequence are repeated throughout the whole pulse sequence (with minor alterations between the distinct parts, e.g. different phase encoding gradients). Examples are spoiled, refocused or balanced GRE sequences, or multi-echo spin-echo sequences. If the Bloch equations are solved for one of these repetitive blocks, one can generally relate the magnetization vector (of one isochromat) before and after the block by a simple recurrence relation:

$$\vec{M}^{(n+1)} = \mathbf{A} \vec{M}^{(n)} + \vec{B} \quad (2.52)$$

where  $\mathbf{A}$  and  $\vec{B}$  account for the relaxation, precession, and nutation processes. If the changing elements of these blocks (e.g. phase encoding) do not have a net effect on the magnetization, which is the case for phase-encoding gradients that are often balanced and do not possess a net gradient moment, this relation is valid for each block within the whole sequence. In other words, the difference equation in eq. 4.2 accurately describes the whole sequence. If this is the case, one can use the methods from section 2.1.3 to derive a closed-form expression for the evolution of the magnetization vector, either in

the z-domain or even in the time domain.

$$\vec{M}^{(n+1)} = \mathbf{A}\vec{M}^{(n)} + \vec{B} \Rightarrow \vec{f}(z) = (\mathbf{I} - z\mathbf{A})^{-1} \left( \vec{M}^{(0)} + \frac{z}{1-z}\vec{B} \right)$$

$$f(\vec{z}) \bullet \circ \vec{M}[n] \tag{2.53}$$

where  $\vec{M}^{(0)}$  is the initial magnetization before the repetitive part of the sequence starts. This could be the magnetization after the excitation pulse in multi-echo spin-echo sequences, or the equilibrium magnetization, or the magnetization after some preparation pulse for GRE sequences.

**Methods of signal computation** If it is possible to inverse-transform  $\vec{f}(z)$  to the time domain, one can simply evaluate the resulting expression,  $\vec{M}[n]$ , for  $n = 0..N$  to obtain the desired echo amplitudes. In some cases the inverse transformation may not be straightforward and no explicit time domain solution can be calculated. However, in this case, one can still obtain the echo amplitudes by using the property that the z-transform corresponds to the discrete time Fourier transform for  $z = e^{i\psi}$  (see sec. 2.1.2). In that way, one can compute the DFT of the signal evolution by evaluation of  $\vec{f}(z)$  for  $z$  on the unit circle. Furthermore, by applying the inverse DFT to the values computed in such a way, one again obtains the echo amplitudes in the time domain.

This method generally works well if the magnetization tends towards zero throughout the echo train. There are two cases where exactly this prerequisite is not fulfilled: (1) the signal generally tends towards zero, but within the time of acquisition this is not the case and a finite amount of magnetization is still remaining (e.g. long  $T_2$ -components in multi-echo spin-echo sequences, and (2) the sequence produces a steady-state different from zero (e.g. GRE sequences). In the first case, one deals with so called leakage or truncation effects of the DFT. In the second, case the discrete time Fourier series just does not exist (i.e. does not converge as the time domain sequence is not absolutely summable). In other words, the resultant z-transform has poles on the unit circle and therefore cannot be evaluated everywhere around the unit circle. However, in that case one can use the apodization property and obtain a time domain signal. The effects of apodization are the following: (1) in the time-domain, multiplication with an apodization function makes the signal taper off to zero for large  $n$ , and, thus, eliminates leakage effects. (2) in the z-domain, multiplication of  $z$  by an apodization factor results in a stretching or squeezing of the unit circle, such that, no poles are encountered when computing the DFT. Following the second approach, the apodization clearly has to

be undone in the time-domain after signal evaluation by dividing by an apodization function.

**Averaging over isochromats** The difference equation 4.2 only describes the signal evolution for a single isochromate. However, in unbalanced sequences different isochromats experience different magnetic fields and hence acquire different phase during a sequence block. With the GF formalism one can easily arrive at the overall signal amplitudes by averaging over all isochromats, i.e. by integrating over the phase angle  $\psi$  from  $0 \dots 2\pi$ . In the formulation with complex magnetization  $M_+$ , each isochromat's phase appears in a phase factor  $U = e^{i\psi}$ . That means that averaging over all isochromates involves a contour integral where  $U$  is integrated around the unit circle. As known from complex analysis, this problem can readily be solved by employing the residue theorem. A detailed example outlining this procedure is presented in chapter 4.

### 2.3.1 Alternative methods of signal computation

The method outlined in previous paragraphs is not the only method to compute echo amplitudes for MR sequences. Iterative solution of the Bloch equations or the extended phase graph (EPG) algorithm constitute two other methods with their distinct advantages and disadvantages and will be shortly reviewed in the following paragraphs.

**Bloch equations** Simulations using the Bloch equations are directly utilizing the above presented relaxation and rotation matrices (real or complex). The MRI sequence is simulated by consecutively applying the relaxation and precession matrices, followed by an instantaneous RF pulse (although also relaxation effects during the pulse can be implemented), and again followed by relaxation and precession. The exact values of the matrices are of course dependent on the sequence at hand, e.g. for a SPGR sequence an additional spoiling matrix that nulls the transverse components would be applied. For a balanced sequence the described procedure already yields the desired echo amplitudes. For a multi-echo spin-echo sequence, on the other hand, an additional fact has to be taken in to account. Since the the gradient moment between two consecutive pulses is not zero, one actually does not rotate a single magnetization vector, but a disc of vectors with each vector having a distinct phase (due to the read out gradient). So, the simulation of the entire sequence has to be carried out for each single isochromat and finally the magnetization vectors can be added together. The procedure is outlined in algorithm 1.

---

**Algorithm 1:** Bloch simulation algorithm:  $\mathbf{m}_{(n,k)}$  denotes the magnetization vector at the time of echo number  $n$ ;  $\mathbf{m}_{(n,k)}^-$  and  $\mathbf{m}_{(n,k)}^+$  correspond to the magnetization vector right before and after the RF pulse, respectively.  $E_1$  is the longitudinal relaxation term,  $\mathbf{e}_z$  the unit vector in  $z$ -direction,  $m_0$  the equilibrium magnetization, and  $\mathbf{P}_k$  the precession matrix, depending on isochromate index  $k$ .

---

initialize relaxation matrix  $\mathbf{E}$   
 initialize rotation matrix  $\mathbf{R}$   
 initialize  $\mathbf{m}_{0,k} = m_0[1 \ 1 \ 0]^T$  // exciting rotation around negative  $y$ -axis

**Result:**  $\mathbf{m}_n$

```

for  $n=1$ :Echoes do
    for  $k=1$ :Isochromates do
         $\mathbf{m}_{(n-1,k)}^- \leftarrow \mathbf{P}_k \mathbf{E} \mathbf{m}_{(n-1,k)} + \mathbf{e}_z (1 - E_1) m_0$ 
         $\mathbf{m}_{(n-1,k)}^+ \leftarrow \mathbf{R} \mathbf{m}_{(n-1,k)}^-$ 
         $\mathbf{m}_{(n,k)} \leftarrow \mathbf{P}_k \mathbf{E} \mathbf{m}_{(n-1,k)}^+ + \mathbf{e}_z (1 - E_1) m_0$ 
    end
end
 $\mathbf{m}_{(n)} = \sum_k \mathbf{m}_{(n,k)}$ 
    
```

---

**Extended phase graph** In the extended phase graph formalism the spins are decomposed into so-called configurations which actually correspond to the various echo pathways that are created by successive application of RF pulses and encoding gradients. RF pulses are represented by rotation matrices whereas precession is implemented by a shift operator. If we recall the complex precession matrix and look at its effect on  $\vec{M}$  we find

$$\begin{pmatrix} e^{-i\phi} & 0 & 0 \\ 0 & e^{i\phi} & 0 \\ 0 & 0 & 1 \end{pmatrix} \begin{pmatrix} M_+ \\ M_+^* \\ M_z \end{pmatrix} = \begin{pmatrix} M_+ e^{-i\phi} \\ M_+^* e^{i\phi} \\ M_z \end{pmatrix} = \begin{pmatrix} M_{+z} \\ M_{*z}^{-1} \\ M_z \end{pmatrix}. \quad (2.54)$$

Rotation matrices on the other hand mix these configurations. Repeated application of the shift and rotation operators thus creates a power series in  $z$ . However, the only configuration that creates a measurable signal is the 0th power  $F_0$  state. One can think

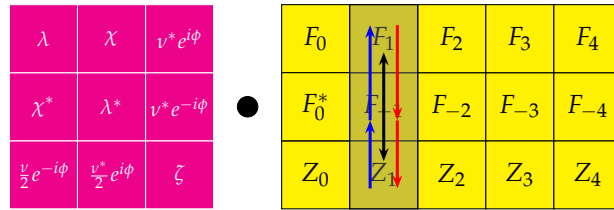


Figure 2.3: Effect of an RF pulse in the EPG algorithm demonstrated on the first configuration.

---

**Algorithm 2:** EPG algorithm

---

**Result:**  $\mathbf{m}_n$

```

initialize relaxation matrix E
initialize rotation matrix R
initialize  $\mathbf{m}_0 = m_0[1\ 1\ 0]^T$  // exciting rotation around negative y-axis

initialize configurations matrix  $\mathbb{F}_0 = \mathbf{m}_0$ 
for  $n=1$ :Echoes do
    extend  $\mathbb{F}_n$  with zeros
    right/left shift top/bottom row
    set  $F_0 \leftarrow F_0^*$ 
    multiply  $\mathbb{F}_n = \mathbf{E}\mathbf{R}\mathbb{F}_{n-1}$ 
    do shift procedure again
    save  $\mathbf{m}_n \leftarrow \mathbb{F}_0$ 
end

```

---

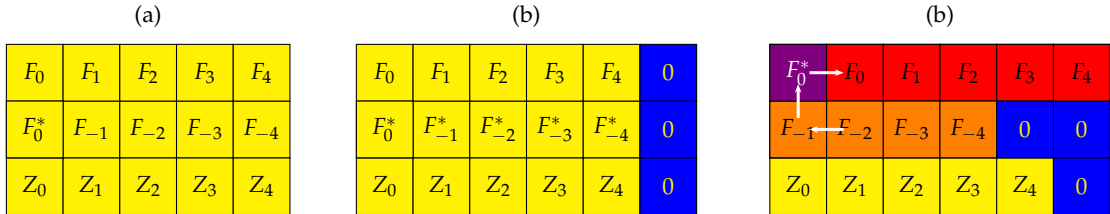


Figure 2.4: Schematics of the EPG shift operation. (a) The state of the EPG matrix after 4 shift operations. (b) A column of zeros is appended to the end of the EPG matrix. (c) Free precession: The top row is shifted to the right, the middle row to the left (with one more zero inserted at the end). The bottom row is left unchanged by free precession.

of precession as a right shift, i.e. multiplication by  $z$  (this is the only operation the first element of  $\vec{M}$  experiences during precession). Multiplication by  $z$  corresponds to a dephasing and by  $z^{-1}$  to a rephasing gradient. Algorithm 2 lists the procedure and figures 2.4 and 2.3 illustrate the effects of the gradient and the RF operator on the individual configurations, respectively.

### 2.3.2 The spoiled gradient echo sequence (SPGR)

The standard spoiled gradient echo sequence provides a nice and easy example to show the derivation of a quite tractable generating function which also offers the possibility to simply inversely z-transform and therewith compute a closed form solution in the time domain. In SPGR sequences the transverse magnetization is spoiled for each repetition, and, hence, transverse magnetization can essentially be neglected in the signal computation. It is, therefore, quite easy to derive signal equations solely in the

### 2.3 Generating functions for repetitive pulse sequences

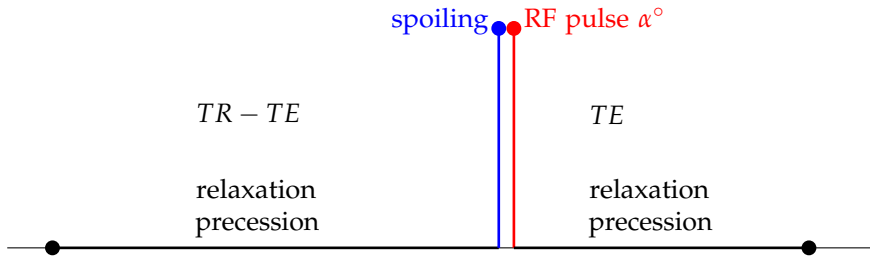


Figure 2.5: Elementary building block for a SPGR sequence.

time domain as well. However, to give the reader an idea of how to use the GF method, the strict application of the z-transform will be used to arrive at equations for both the longitudinal and transverse magnetization.

**Recursive signal model and generating function** First, the sequence diagram in fig. 2.5 is analyzed to arrange the appropriate nutation, precession, and relaxation matrices. A sequence subunit for the SPGR sequence consists of a time  $TR - TE$  for precession (off-resonance  $\Delta\omega$ ) and relaxation, then an instantaneous excitation, and subsequently another precession and relaxation period of length  $TE$  until the echo is acquired. The combined relaxation and precession matrices before (pre) and after (post) the pulse are given by:

$$\mathbf{Q}_{pre} = \begin{pmatrix} e^{\frac{-(TR-TE)}{T_2^*} + i(TR-TE)\Delta\omega} & 0 & 0 \\ 0 & e^{\frac{-(TR-TE)}{T_2^*} - i(TR-TE)\Delta\omega} & 0 \\ 0 & 0 & e^{\frac{-(TR-TE)}{T_1^*}} \end{pmatrix} \quad (2.55)$$

$$\mathbf{Q}_{post} = \begin{pmatrix} e^{\frac{-TE}{T_2^*} + iTE\Delta\omega} & 0 & 0 \\ 0 & e^{\frac{-TE}{T_2^*} - iTE\Delta\omega} & 0 \\ 0 & 0 & e^{\frac{-TE}{T_1^*}} \end{pmatrix} \quad (2.56)$$

The nutation matrix can be directly taken from [38]:

$$\mathbf{P} = \begin{pmatrix} \lambda & \mu & \nu \\ \mu & \lambda^* & \nu^* \\ \frac{\nu}{2} & \frac{\nu^*}{2} & \zeta \end{pmatrix} \quad (2.57)$$

$$(2.58)$$

## 2 The Generating Functions approach

Assuming perfect spoiling, the transverse magnetization is totally dephased by the spoiler gradients before each excitation pulse. This can be accounted for in this derivation by the introduction of a spoiler matrix,  $\mathbf{S}$ , that only preserves the z-component of the magnetization.

$$\mathbf{S} = \begin{pmatrix} 0 & 0 & 0 \\ 0 & 0 & 0 \\ 0 & 0 & 1 \end{pmatrix} \quad (2.59)$$

$$(2.60)$$

The recursion formula for the magnetization is then given by:

$$\vec{M}[n+1] = \mathbf{Q}_{post} \mathbf{P} \mathbf{S} \mathbf{Q}_{pre} \vec{M}[n] + \mathbf{Q}_{post} \mathbf{P} \vec{S}_{eq,pre} + \vec{S}_{eq,post} \quad (2.61)$$

whereas  $\vec{S}_{eq,pre} = [0, 0, (1 - e^{-\frac{(TR-TE)}{T1}})M_0]^T$  and  $\vec{S}_{eq,post} = [0, 0, (1 - e^{-\frac{TE}{T1}})M_0]^T$ . The Generating function for the SPGR sequence can now be obtained by solving the difference equation 2.61 in the z-domain, i.e. by evaluating the following formula. For initial magnetization  $\vec{M}[0] = [0, 0, K]^T$ ,  $\vec{F}(z)$  becomes

$$\vec{F}(z) = (\mathbf{I} - z\mathbf{Q}_{post} \mathbf{P} \mathbf{S} \mathbf{Q}_{pre})^{-1} \left( M_0 \begin{pmatrix} 0 \\ 0 \\ K \end{pmatrix} + \frac{z}{1-z} (\mathbf{Q}_{post} \mathbf{P} \vec{S}_{eq,pre} + \vec{S}_{eq,post}) \right) \quad (2.62)$$

$$\vec{F}(z) = \begin{pmatrix} \frac{M_0 v z e^{-\frac{TE}{T2} + i\Delta\omega TE} \left( (1-K)(1-z)e^{\frac{TE}{T1}} - e^{\frac{TR}{T1}} + z \right)}{(1-z) \left( \zeta z - e^{\frac{TR}{T1}} \right)} \\ \frac{M_0 v^* z e^{-\frac{TE}{T2} - i\Delta\omega TE} \left( (1-K)(1-z)e^{\frac{TE}{T1}} - e^{\frac{TR}{T1}} + z \right)}{(1-z) \left( \zeta z - e^{\frac{TR}{T1}} \right)} \\ \frac{e^{-\frac{TE}{T1}} \left( M_0 e^{\frac{TR}{T1}} \left( (\zeta-1)z + (-Kz+K+z)e^{\frac{TE}{T1}} \right) - \zeta M_0 z e^{\frac{TE}{T1}} \right)}{(z-1) \left( \zeta z - e^{\frac{TR}{T1}} \right)} \end{pmatrix} \quad (2.63)$$

**Steady state SPGR signals** To obtain a steady state solution for the SPGR signal one can use the final value theorem of the z transform by computing the limit  $\lim_{z \rightarrow 1} F(z)(z^{-1} - 1)$ . This gives the following expressions for transversal magnetization  $M_+$  and  $M_+^*$  and



### 2.3 Generating functions for repetitive pulse sequences

longitudinal magnetization  $M_z$

$$\vec{M}_{SS} = \begin{pmatrix} M_0 \nu \frac{1-e^{-TR/T_1}}{1-\zeta e^{-TR/T_1}} e^{\frac{-TE}{T_2^*} + iTE\Delta\omega} \\ M_0 \nu^* \frac{1-e^{-TR/T_1}}{1-\zeta e^{-TR/T_1}} e^{\frac{-TE}{T_2^*} - iTE\Delta\omega} \\ (1 - e^{-TE/T_1})M_0 + e^{-TE/T_1} \zeta \frac{1-e^{-TR/T_1}}{1-\zeta e^{-TR/T_1}} M_0 \end{pmatrix} \quad (2.64)$$

Note that the steady state expression is independent of the initial magnetization preparation value  $K$ . If an on-resonant excitation around the x-axis is considered parameters  $\nu$  and  $\zeta$  reduce to  $\nu = i \sin \alpha$  and  $\zeta = \cos \alpha$  with  $\alpha$  being the flip angle. The third component of the steady state vector is the longitudinal component at the time of the echo. The longitudinal component right after and right before the RF pulse can be extracted from this formula by setting the echo time  $TE = 0$  as  $\zeta \frac{1-e^{-TR/T_1}}{1-\zeta e^{-TR/T_1}}$  (where  $\zeta$  is just the amount of magnetization that is left in the z-direction directly after applying the RF pulse) or setting  $TE = TR$  giving  $\frac{1-e^{-TR/T_1}}{1-\zeta e^{-TR/T_1}}$ , which is the well known steady state expression of the longitudinal magnetization for SPGR sequences.

#### Signal equation for SPGR with off-resonances

Plugging in the most general values for  $\nu$  and  $\zeta$ , one arrives at the time domain signal equation for SPGR sequences with off-resonance effects:

$$S = 2M_0 \sin \frac{\alpha}{2} \sin \theta \left( \cos \frac{\alpha}{2} - i \sin \frac{\alpha}{2} \cos \theta \right)^2 \cdot \frac{1 - e^{-TR/T_1}}{1 - (\cos \alpha \sin^2 \theta + \cos^2 \theta) e^{-TR/T_1}} e^{\frac{-TE}{T_2^*} + iTE\Delta\omega + i\phi} \quad (2.65)$$

$$\theta = \arctan \frac{|B_{1+}|}{\Delta B} \quad (2.66)$$

$$\phi = \arctan \frac{B_{1y}}{B_{1x}} \quad (2.67)$$

$$\Delta\omega = \gamma\Delta B \quad (2.68)$$

**Transient SPGR signals** The SPGR transient can be obtained by transformation of equation 2.63 to the time domain. For arbitrary initial  $M_z$  preparation, e.g.  $K = -1$  for inversion or  $K = 0$  for saturation, flip angle  $\alpha$ ,  $\cos \alpha_e = \cos \alpha \sin^2 \theta + \cos^2 \theta$  and

## 2 The Generating Functions approach

$\kappa_1 = e^{-TR/T_1}$ , this yields:

$$M_+[n] = -2M_0 e^{-\frac{TE}{T_2} + i(TE\Delta\omega + \phi)} \left( \cos\theta + i \cos\frac{\alpha}{2} \right) \sin\frac{\alpha}{2} \sin\theta \cdot \frac{1 - \kappa_1 - \kappa_1^{-n} \cos\alpha_e - \kappa_1 \cos^{n-1}\alpha_e (\kappa_1(K-1) [\kappa_1 - \cos\alpha_e] + \kappa_1 \cos\alpha_e)}{\cos\alpha_e - \kappa_1}$$

(2.69)

Curves in figure 2.6 are computed with this formula and show SPGR transients for different angles  $\theta$  and  $\alpha$ . For  $K = 1$  and  $\theta = \pi/2$ , i.e. completely on-resonant, it simplifies to

$$M_+[n] = iM_0 e^{-\frac{TE}{T_2} + i(TE\Delta\omega + \phi)} \frac{1 - \kappa_1 + \kappa_1^{-n} \cos^n\alpha}{1 - \kappa_1 \cos\alpha} \sin\alpha \quad (2.70)$$

The interesting part of this equation is that there are additional imaginary parts in addition to  $e^{i\phi}$  when the rotation axis is tilted away from the  $x$ - $y$ -plane. This makes sense since rotation around an axis, e.g. somewhere in the  $x$ - $z$ -plane will produce magnetization that lies outside of the  $y$ - $z$ -plane (as we would expect after pure rotation around the  $x$ -axis). Some examples of the steady state limit, derived with this method, underpin the validity of equation 2.69. For  $\alpha = 90^\circ$  and  $\theta = 45^\circ$ , the magnetization is split equally between real and imaginary part.

$$M_+^{SS} = M_0 e^{-\frac{TE}{T_2} + i(TE\Delta\omega + \phi)} \frac{\sqrt{2}(1+i)(1-\kappa_1)}{1-2\kappa_1} \quad (2.71)$$

For  $\alpha = 180^\circ$  and  $\theta = 45^\circ$ , the magnetization is in fact rotated  $90^\circ$  down to the  $x$ -axis

$$M_+^{SS} = M_0 e^{-\frac{TE}{T_2} + i(TE\Delta\omega + \phi)} (1 - \kappa_1) \quad (2.72)$$

and for  $\theta = 0^\circ$  which corresponds to a rotation around the  $z$ -axis the result is

$$M_+^{SS} = 0 \quad (2.73)$$

for all times.

**Transient SPGR signals - Look-Locker** In the Look-Locker approach for  $T_1$ , several SPGR acquisitions are made after an initial  $180^\circ$  inversion pulse, such that the recovery

### 2.3 Generating functions for repetitive pulse sequences

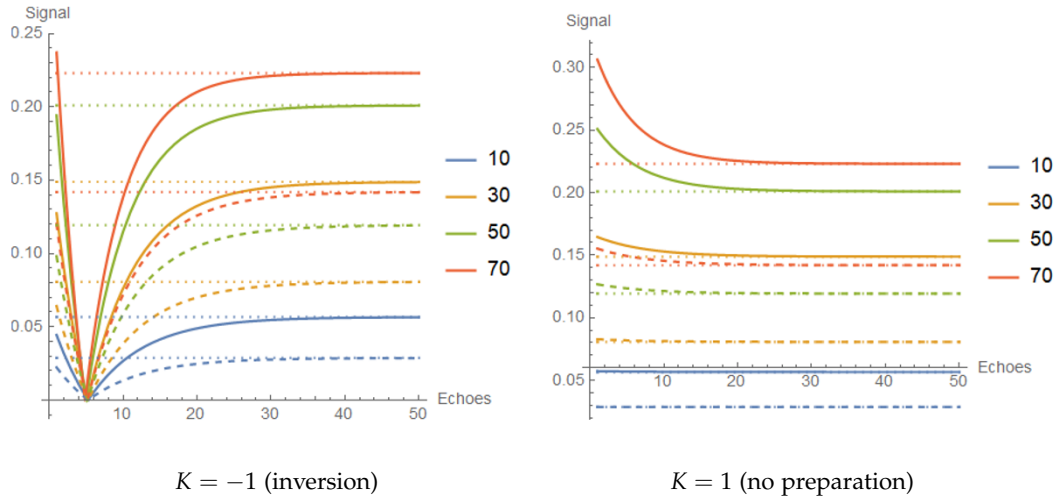


Figure 2.6: Transient of SPGR signals computed with the GF approach for different off-resonance angles  $\theta = \arctan(|B_{1+}|/\Delta B)$  ( $10^\circ$  to  $70^\circ$ ) and  $M_z$  preparation (left  $K = -1$ , right  $K = 1$ ). Solid lines are with flip angle  $\alpha = 20^\circ$ , dashed lines with  $\alpha = 10^\circ$ , dotted are steady state solutions.

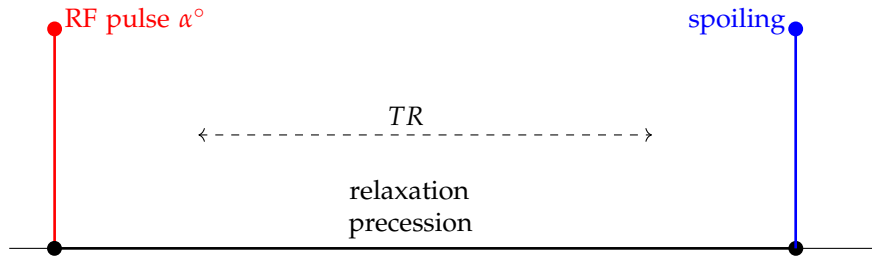


Figure 2.7: Elementary building block for a Look-Locker sequence.

of the longitudinal magnetization is sampled at multiple points along the relaxation curve. As with every SPGR excitation, a small fraction of the longitudinal magnetization is lost, the signal recovery is different from pure  $T_1$ -relaxation. To accurately model the signal amplitudes, one is interested in the longitudinal magnetization prior to each  $\alpha^\circ$  excitation pulse. The actual sequence unit to be used within the GF framework is shown in fig. 2.7.

$$\mathbf{Q} = \begin{pmatrix} e^{\frac{-TR}{T_2^*} + iTE\Delta\omega} & 0 & 0 \\ 0 & e^{\frac{-TR}{T_2^*} - iTE\Delta\omega} & 0 \\ 0 & 0 & e^{\frac{-TE}{T_1}} \end{pmatrix} \quad (2.74)$$

$\mathbf{P}$  and  $\mathbf{S}$  are the same as in the previous section. The recurrence relation for this sequence unit is then  $\vec{M}^{(n+1)} = \mathbf{SQP}\vec{M}^{(n)} + \mathbf{S}[0, 0, M_0(1 - e^{-TR/T_1})]^T$ . With the initial

## 2 The Generating Functions approach

magnetization being  $\vec{M}^{(0)} = M_0[0, 0, K]^T$  the GF is

$$\vec{F}(z) = \begin{pmatrix} 0 \\ 0 \\ M_0 \frac{K+z(1-K-e^{-TR/T_1})}{(1-z)(1-z\zeta e^{-TR/T_1})} \end{pmatrix} \quad (2.75)$$

With this setup of the sequence building block, the magnetization right after the spoiling gradients is computed. Therefore, the transverse components of the GF are zero. The longitudinal component can be back-transformed to the time domain yielding the following formula for the magnetization transient (for  $\zeta = \cos \alpha$ ):

$$M_z[n] = M_0 \frac{1 - e^{-TR/T_1}}{1 - \cos \alpha e^{-TR/T_1}} + M_0 e^{-nTR/T_1} \cos^n \alpha \frac{-1 + K + e^{-TR/T_1} - K \cos \alpha e^{-TR/T_1}}{1 - \cos \alpha e^{-TR/T_1}} \quad (2.76)$$

$$= M_0 \frac{1 - e^{-TR/T_1}}{1 - \cos \alpha e^{-TR/T_1}} - M_0 e^{-nTR/T_1} \cos^n \alpha \frac{1 - e^{-TR/T_1}}{1 - \cos \alpha e^{-TR/T_1}} + \quad (2.77)$$

$$M_0 e^{-nTR/T_1} \cos^n \alpha \frac{K(1 - \cos \alpha e^{-TR/T_1})}{1 - \cos \alpha e^{-TR/T_1}} \quad (2.78)$$

$$M_z[n] = M_0 \frac{1 - e^{-TR/T_1}}{1 - \cos \alpha e^{-TR/T_1}} \left( 1 - e^{-nTR/T_1} \cos^n \alpha \right) + M_0 K e^{-nTR/T_1} \cos^n \alpha \quad (2.79)$$

### 2.3.3 The CPMG and the CP sequence

A CPMG sequence consists of an excitation pulse (usually  $90^\circ$ ), a time  $\tau/2$  of free precession, and a train of refocusing pulses (usually  $180^\circ$ ), spaced by  $\tau$ , and which are  $90^\circ$  out of phase with the excitation pulse. As already pointed out in the introduction, the  $90^\circ$  phase difference between excitation and refocusing is very beneficial when refocusing pulses are not exactly  $180^\circ$ . The imperfections of the pulses are then inherently compensated for every second echo. Unfortunately, this is only true for small FA deviations. However, compared to the CP sequence where both excitation and refocusing are around the same axis, a lot more signal can be retained throughout the echo train with this approach. Principally, when slice-selective pulses are used, each CPMG sequence has some CP characteristics, and vice versa. Figures 2.8 to 2.11 illustrate the differences between CPMG and CP refocusing.

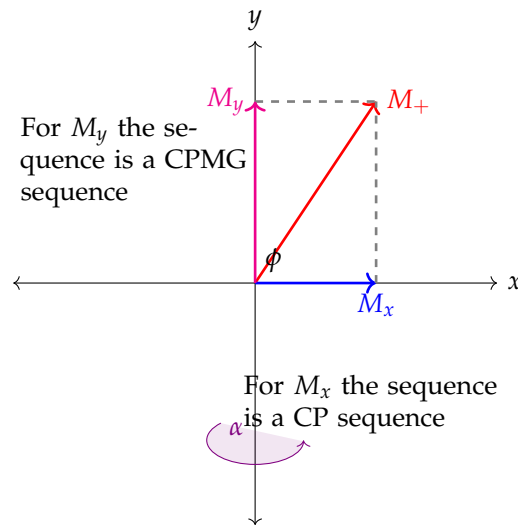


Figure 2.8: The transversal magnetization can be split in two perpendicular parts of which one experiences a CPMG sequence (here  $M_y$  as the rotation is performed around the  $y$ -axis), and one part that experiences a CP sequence. Basically, this scenario can be found when slice-selective pulses are used, since they always produce some magnetization perpendicular to the intended direction.

**Generating functions for CP and CPMG** In principle, the GF for the transverse magnetization, as derived in [37] takes the following form,

$$F(z) = \frac{M_0}{2} \left( 1 + \sqrt{\frac{(1 + z\kappa_2)(1 - z \cos \alpha(\kappa_1 + \kappa_2) + z^2\kappa_1\kappa_2)}{(1 - z\kappa_2)(1 - z \cos \alpha(\kappa_1 - \kappa_2) - z^2\kappa_1\kappa_2)}} \right), \quad (2.80)$$

for an on-resonant CPMG sequence with excitation of  $90^\circ$  around the  $y$ , and refocusing with  $\alpha^\circ$  around the  $x$ -axis, respectively. Here,  $\kappa_1$  and  $\kappa_2$  denote the relaxation terms. A detailed derivation of the GF  $F(z)$  for CP and CPMG sequences and combinations thereof can be found in chapter 4. For the evolution of the longitudinal magnetization  $L(z)$  the reader is referred to chapter 5.

#### Initial value and steady-state for CPMG sequence

By applying the initial and final value theorem of the  $z$ -transform, the initial and steady state value of the CPMG sequence can be computed (Tab. 2.2). Obviously, the initial values are equal to the initial value that was given prior to computing the Generating function  $\vec{F}(z)$ , i.e.  $\vec{M}^{(0)} = [M_0 \sin \beta, M_0 \sin \beta, M_0 \cos \beta]^T$ , where  $\beta$  is the excitation flip angle. The steady state expression for the transverse magnetization reduces to zero, which is not surprising, as we know it is decaying to zero. The longitudinal component,

## 2 The Generating Functions approach

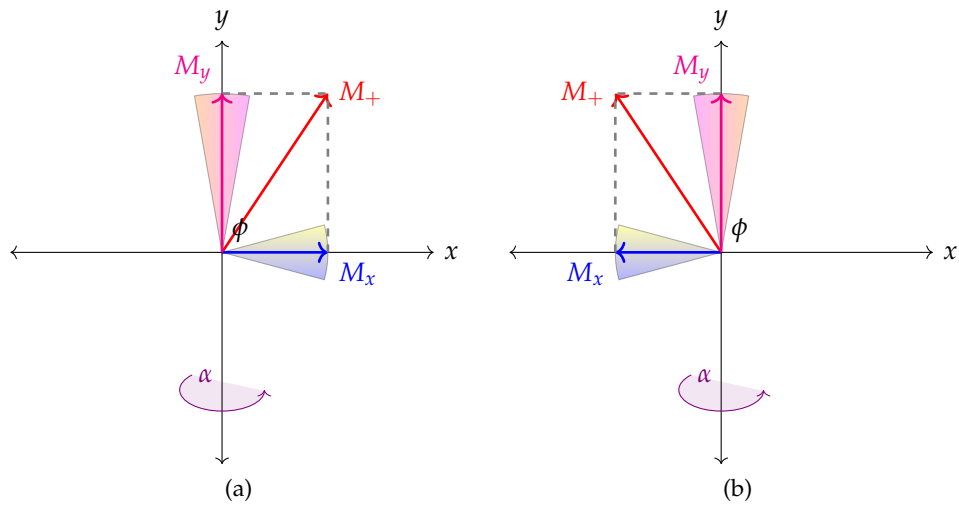


Figure 2.9: Effect of refocusing pulse for  $M_x$  and  $M_y$  components. (a) before, and (b) after refocusing: lets suppose the magnetization vectors rotate counter-clockwise. For  $M_x$  the yellow shaded part is rotating faster than the blue part, and after refocusing the phase state of the yellow and blue spins is inverted, and the yellow part will eventually "catch up" with the blue for all isochromates to refocus at time  $\tau$ . Note that after refocusing, the sign of  $M_x$  is reversed. For  $M_y$ , the orange part is rotating faster, then set behind the pink shaded spins by the refocusing pulse, so that they will finally refocus along the  $y$ -axis without changing sign.

however, approaches a defined steady state value  $M_z^{ss}$  which is independent of the initial excitation pulse angle  $\beta$ . For complete refocusing with  $\alpha = 180^\circ$ , a simple-steady state signal expression can be obtained from  $L(z)$  and is given below (Eq. 2.83) with  $E_1 = e^{-\tau/T1}$  and  $\tau$  being the echo spacing:

	Transverse magnetization	Longitudinal magnetization
Initial value	$\lim_{z \rightarrow 0} F(z) = M_0 \sin \beta$	$\lim_{z \rightarrow 0} L(z) = M_0 \cos \beta$
Steady state	$\lim_{z \rightarrow 1} (z^{-1} - 1)F(z) = 0$	$\lim_{z \rightarrow 1} (z^{-1} - 1)L(z) = M_z^{ss}$

Table 2.2: Initial and steady state values for the transverse and longitudinal magnetization of a CPMG sequence computed via the  $z$ -transform.

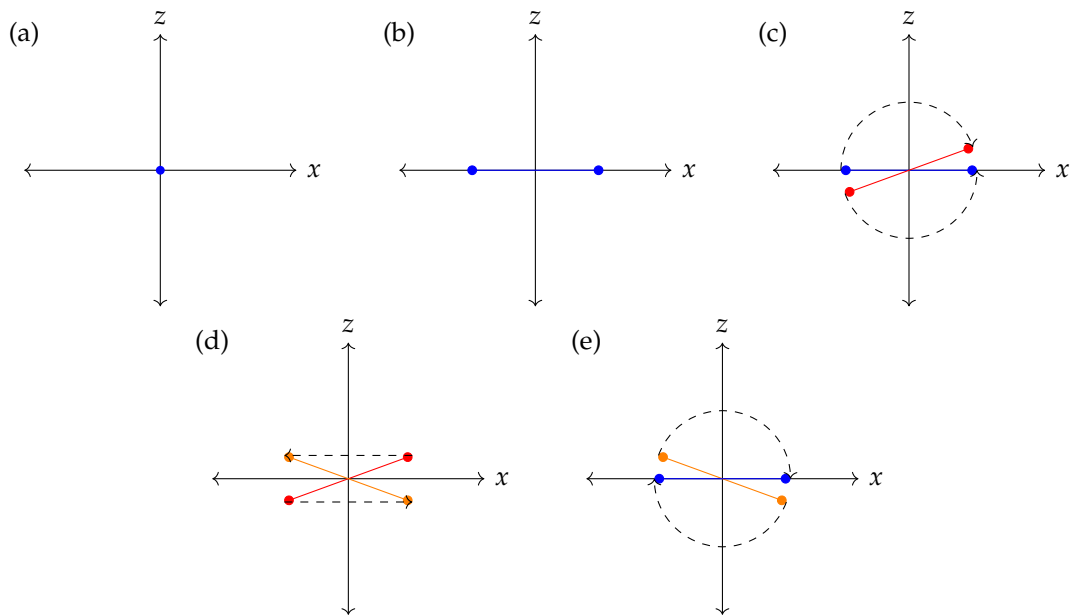


Figure 2.10: Imperfect refocusing in a CPMG sequence seen from the  $x$ - $z$ -plane: (a) all spins are coherent, (b) the spins dephase with time (blue), (c) the imperfect refocusing pulse is unable to rotate the "spin-fan" back to the  $x$ - $y$ -plane (red), (d) with time the spins refocus and dephase in the other direction since fast and slow spins have changed position (orange), (e) the second refocusing pulse, although imperfect, puts the spins back in the  $x$ - $y$ -plane (blue) and thereby compensates its own imperfection.

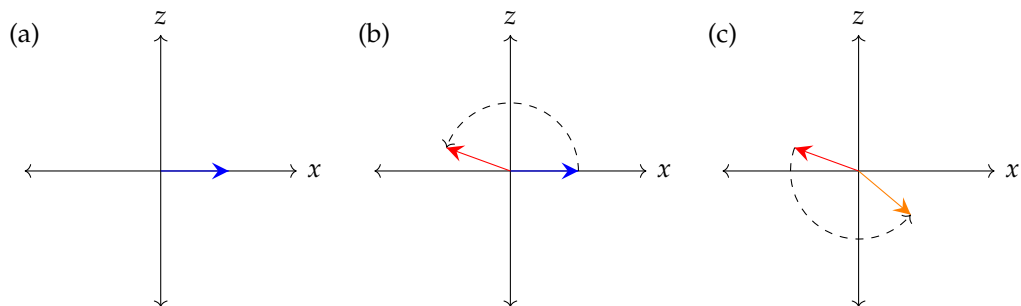


Figure 2.11: Imperfect refocusing in a CP sequence seen from the  $x$ - $y$ -plane: (a) all spins are aligned with the  $x$ -axis and start to dephase (not seen), (b) the imperfect refocusing pulse is unable to put the "spin-fan" in the direction of the  $-x$ -axis, then the spins refocus and dephase again, (c) the second refocusing pulse is again not rotating enough and since there was a small gap to the  $y$ -axis before, there's now twice the gap to the  $x$ -axis. The error due to the imperfect pulse is thus accumulating.

## 2 The Generating Functions approach

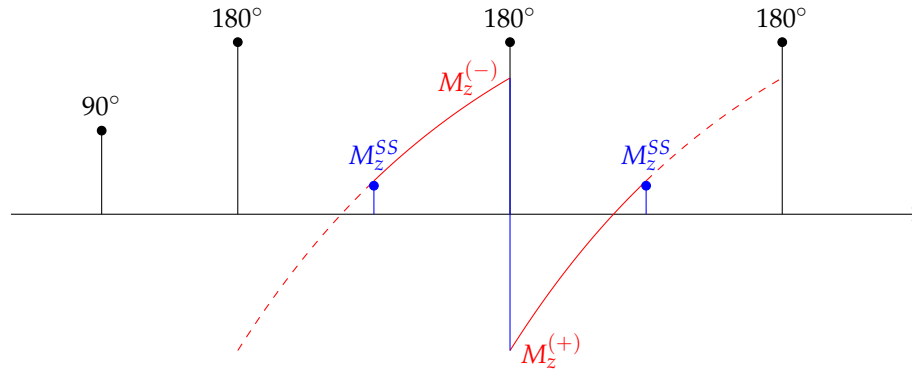


Figure 2.12: Calculation of the steady state for the longitudinal magnetization.

$$\lim_{z \rightarrow 1} (z^{-1} - 1)L(z) = M_0 \left( 1 + \frac{2\sqrt{E_1}\sqrt{(1+E_1)^2}}{(1+E_1)^2} \right) \quad (2.81)$$

$$= M_0 \left( 1 \pm \frac{2\sqrt{E_1}(1+E_1)}{(1+E_1)^2} \right) \quad (2.82)$$

$$= M_0 \left( 1 - \frac{2\sqrt{E_1}}{(1+E_1)} \right) \quad (2.83)$$

For this special case the same expression can be computed from equations derived from the diagram in fig. 2.12 and the solution to the Bloch equations:

$$M_z^{(-)} = M_z^{SS} \sqrt{E_1} + M_0(1 - \sqrt{E_1}) \quad (2.84)$$

$$M_z^{(+)} = M_z^{(-)} \cos \pi = -M_z^{(-)} \quad (2.85)$$

$$M_z^{SS} = M_z^{(+)} \sqrt{E_1} + M_0(1 - \sqrt{E_1}) = -M_z^{(-)} \sqrt{E_1} + M_0(1 - \sqrt{E_1}) \quad (2.86)$$

$$M_z^{SS} = M_0 \frac{(1 - \sqrt{E_1})^2}{(1 + E_1)} = M_0 \frac{1 - 2\sqrt{E_1} + E_1}{1 + E_1} = M_0 \left( 1 - \frac{2\sqrt{E_1}}{(1 + E_1)} \right) \quad (2.87)$$

### Limiting cases

In table 2.3 some more limiting cases regarding the excitation and refocusing angles are given, whereas for rows 1. and 2. the well-known expressions for a saturation and an inversion recovery experiment are obtained, respectively. In row 6., the transverse magnetization evolution becomes a simple mono-exponential decay as would be expected for optimal pulse parameters.



### 2.3 Generating functions for repetitive pulse sequences

Table 2.3: Limiting cases for  $F(Z)$  and  $L(z)$ .

	Limiting case	$F(z)$	$M_+[n]$	$L(z)$	$M_z[n]$
1.	$\beta = \pi/2, \alpha = 0$	0	0	$\frac{M_0}{1-z} - \frac{M_0}{1-E_1z}$	$M_0(1-E_1^n)u[n]$
2.	$\beta = \pi, \alpha = 0$	0	0	$\frac{M_0}{1-z} - \frac{2M_0}{1-E_1z}$	$M_0(1-2E_1^n)u[n]$
3.	$\beta = 0, \alpha = 0$	0	0	$\frac{M_0}{1-z}$	$M_0u[n]$
4.	$\beta = 0, \alpha = \pi, T_1 \rightarrow \infty$	0	0	$\frac{M_0}{1+z}$	$M_0(-1)^nu[n]$
5.	$\beta = \pi, \alpha = \pi, T_1 \rightarrow \infty$	0	0	$-\frac{M_0}{1+z}$	$-M_0(-1)^nu[n]$
6.	$\beta = \pi/2, \alpha = \pi$	$\frac{M_0}{1-E_2z}$	$M_0E_2^n$	(0 for $E_1 = 1$ )	(0 for $E_1 = 1$ )

#### 2.3.4 The bSSFP and IR-bSSFP sequence

The elementary sequence block for a balanced gradient-echo sequence is shown in figure 2.13. It consists of a precession period,  $TR/2$ , an RF pulse, and another precession period,  $TR/2$ , such that the echo is always appearing just in the middle between two RF pulses. Further, the net gradient area between two RF pulses is zero, i.e. all phase-encoding and readout-gradients are rewound prior to the next RF pulse (in contrast to SSFP-FID and SSFP-Echo). Right before every RF pulse, the spins are totally refocused, such that a single magnetization vector is rotated by the pulse, in contrast to the "spin pancake" that is flipped in the MSE sequence. Unfortunately, if the spins experience some off-resonance, the refocusing is not effective any more, the extreme being an off-resonance angle of  $90^\circ$  which prevents refocusing by the RF pulse at all. This is the reason for the so-called banding artifacts that are often seen with bSSFP sequences.

In the publication by Lukzen [38] a GF formula for bSSFP is provided that can readily be used to compute the echo amplitudes (eq. 2.88).

$$F(z) = \frac{M_0\sqrt{\kappa_2}(1-z\kappa_1)\left(U_0^{1/2}\nu + z\kappa_2U_0^{-1/2}\nu^*\right)}{(1-z)[1-z^3\kappa_1\kappa_2^2 + z\cos\alpha_e \cdot (z\kappa_2^2 - \kappa_1) - z\kappa_2(1-z\kappa_1)(\lambda^*U^{-1} + \lambda U)]} \quad (2.88)$$

Care must be taken because of the factor  $(1-z)$  in the denominator. In the foremen-

## 2 The Generating Functions approach

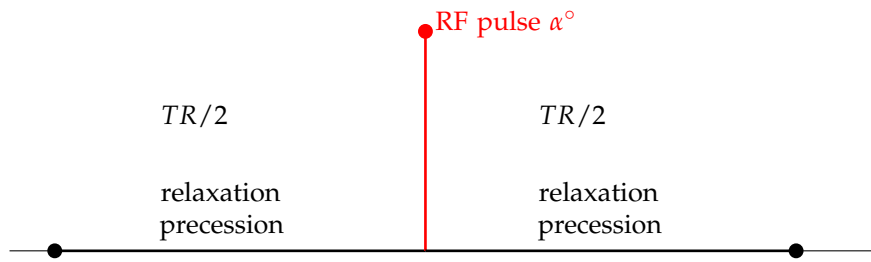


Figure 2.13: Elementary bSSFP building block.

tioned publication also formulas for SSFP-FID and SSFP-Echo can be found.

In figure 2.14, the evolution of an IR-bSSFP slice profile computed with this approach is shown. The formula is not given here due to its resistance to simplification and therefore unhandiness, but it can easily be derived and used by symbolic mathematics programs such as Mathematica. Figure 2.15 shows some data acquired with 3 variants

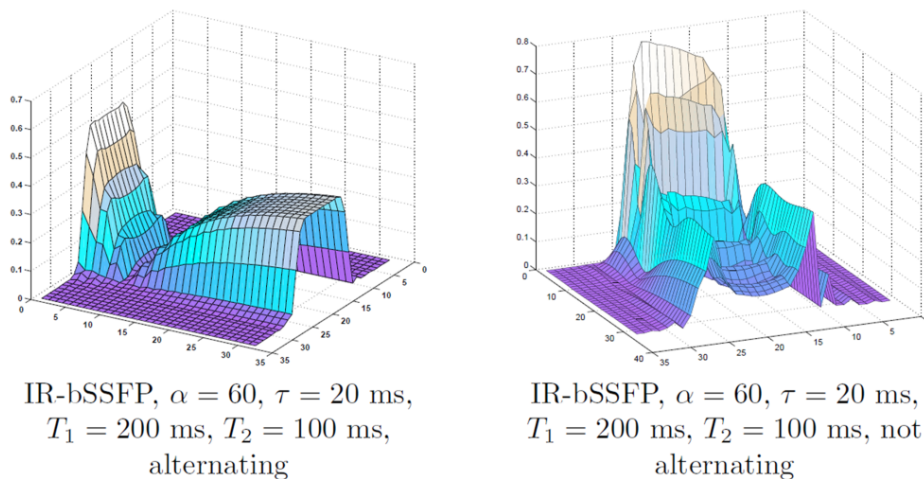


Figure 2.14: Evolution of the slice profile for an inversion recovery bSSFP sequence with alternating (left) and non-alternating phase of the RF pulse. In the alternating sequence the phase of the RF pulse is changed between  $\pi$  and  $-\pi$  for every second echo, whereas in the non-alternating version the RF phase stays the same throughout the echo train.

of the bSSFP sequence: on the left is the non-alternating bSSFP sequence which is flipping always in the same direction, in the middle the variant where the phase of the RF pulse is alternated between  $0^\circ$  and  $180^\circ$ , and to the right an IR recovery bSSFP with alternating phase of the flip angle. The alternating nature of the latter two is also reflected in the corresponding phases. For each sequence, signal evolution for flip angles between  $10^\circ$  and  $90^\circ$  are displayed. It still has to be shown to what extent eq.

### 2.3 Generating functions for repetitive pulse sequences

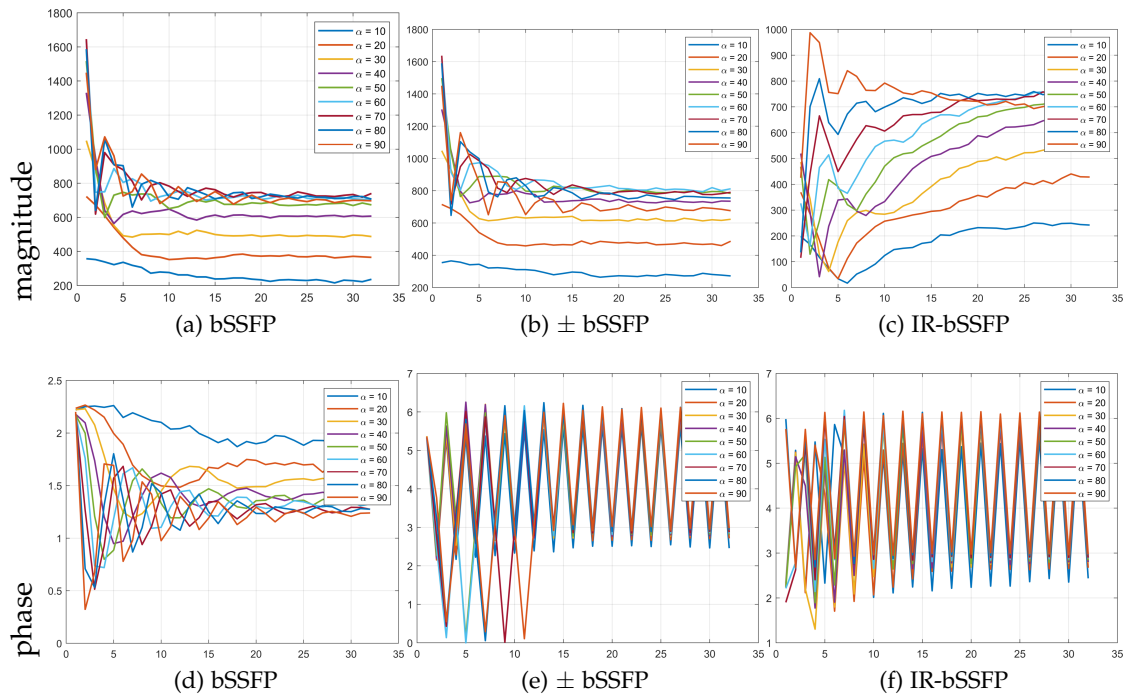


Figure 2.15: Transient MR signals acquired with balanced SSFP sequences (top: magnitude, bottom: phase).

2.88 can be used to describe or fit these data.



# 3

## Accurate $T_2$ -mapping for slice-selective MSE sequences

*This chapter is adopted from "Closed-Form Solution for  $T_2$ -Mapping with Nonideal Refocusing of Slice-Selective CPMG Sequences" [10].*

### 3.1 Introduction

In clinical practice,  $T_2$ -quantification, is usually performed using slice-selective MSE sequences (sec. 1.2.2). For this reason, the GF formalism was extended by incorporating the slice profile to improve the accuracy of the computed  $T_2$ -maps. The goal of the study was to investigate the behavior and validity of different models for  $T_2$ -fitting under various experimental conditions. To demonstrate the applicability of the proposed approach, Monte Carlo simulations and validation by measurements in phantoms and in-vivo were performed. Additionally, the fitting algorithm was evaluated with regard to the estimation of additional parameters, e.g.,  $B_{1+}$ . These experiments shall demonstrate how an advanced signal model can improve  $T_2$ -mapping results obtained with the widely used standard CPMG multi-echo sequences.

As we have seen in the previous chapter (eq. 2.80) the transverse magnetization for a CPMG sequence can be expressed using a Generating function,

$$F(z, M_0, T_1, T_2, \alpha, \tau) = \frac{M_0}{2} \left( 1 + \sqrt{\frac{(1 + z\kappa_2)(1 - z \cos \alpha (\kappa_1 + \kappa_2) + z^2 \kappa_1 \kappa_2)}{(1 - z\kappa_2)(1 - z \cos \alpha (\kappa_1 - \kappa_2) - z^2 \kappa_1 \kappa_2)} \right), \quad (3.1)$$

with  $\kappa_1 = e^{-\tau/T_1}$ ,  $\kappa_2 = e^{-\tau/T_2}$ , and  $\alpha$  is the effective flip angle. This expression can now be used to calculate the entire evolution of a whole slice profile, given the RF pulse shapes are known. One way to do this is to discretize the slice profile  $\mathbf{q}$  in  $j = 1 \dots Q$  parts corresponding to flip angles  $q_j \alpha$ . The sum of all contributions is considered the

### 3 Accurate $T_2$ -mapping for slice-selective MSE sequences

averaged generating function  $F_q(z)$

$$F_q(z, M_0, T_1, T_2, \alpha, q, \tau) = \frac{1}{Q} \sum_{j=1}^Q F(z, M_0, T_1, T_2, \alpha \cdot q_j, \tau) \quad (3.2)$$

For convenience, we further refer to the GF as  $F_q(z, \mathbf{p})$ , introducing the various known and unknown parameters in the parameter vector  $\mathbf{p} = [M_0, T_1, T_2, \tau, \alpha, q] = [\mathbf{p}_k, \mathbf{p}_u]$  (size  $1 \times (5 + Q)$ ).  $\mathbf{p}_k$  denotes the parameters that are known a priori, and  $\mathbf{p}_u$  the parameters that need to be estimated by fitting, respectively. The slice profile is considered as a row vector  $\mathbf{q}$  ( $1 \times Q$ ). The size of these vectors varies according to how many parameters are fitted. The data fitting is then performed by minimizing expression

$$\min \|\mathbf{y} - \mathbf{W} \text{abs}(DFT_K\{\mathbf{F}_q(\mathbf{z}, \mathbf{p})\})\|_2^2 \quad (3.3)$$

where  $\mathbf{y}$  (length  $N$ ) is the acquired data vector,  $DFT_K$  denotes the  $K$ -point discrete Fourier transform,  $z = e^{i\psi}$  with  $\psi = 2\pi k/K$  and  $k = -K/2 \dots K/2 - 1$ , and  $\mathbf{W} = (\mathbf{Z}^{N \times 1}, \mathbf{I}^{N \times N}, \mathbf{Z}^{N \times K - N - 1})$  is a rectangular matrix selecting only the data points 2 to  $N + 1$  ( $\mathbf{Z}$  zero matrix,  $\mathbf{I}$  identity matrix). This is necessary because  $K$  is usually much larger than the number of measured samples,  $N$ , to avoid leakage effects (and the first computed sample corresponds to the equilibrium magnetization). Eq. 3.3 poses a nonlinear optimization problem that cannot be linearized and solved by computation of the pseudoinverse. Hence, minimization by means of nonlinear least squares algorithms has to be used to obtain optimal estimates for the parameters  $\mathbf{p}_u$ .

The second possibility to fit the data to the GF model is by first transforming the data to the  $z$ -domain and then fitting to the original GF formula  $F_q(z)$ . However, usually the decay is not entirely sampled to the point where the signal reaches the noise level. Therefore, transforming the data introduces truncation errors, as the decay is cut off at the last sample point. Suitable apodization of the acquired decay, i.e., multiplication by a decaying exponential  $a^{-n\tau}$  ( $a > 1$ ), is necessary. The apodization is easily incorporated into the GF formula by applying the damping rule of the  $z$ -transform and fitting to  $F(za^{-1})$ .

## 3.2 Methods

### 3.2.1 Simulations

Ground truth signals for simulation purposes were generated using Eq. 3.2 (256 data points) and subsequent application of the DFT. After transformation, only 32 data samples, as in standard clinical imaging protocols, were considered. For all simulations

$M_0$  was set to 1. Refocusing slice profiles were calculated from sinc and Gaussian shaped pulses using the forward Shinnar-Le-Roux transform [113]. Slice profiles were sampled at 90 points.

Several forward simulations were computed for different combinations of parameters to qualitatively visualize their influence on the effective signal: (i) Signals for various tissue types ( $T_1$  and  $T_2$  from the literature [85, 87, 131, 132]) at refocusing FA  $\alpha = 144^\circ$  (at the center of the slice profile), inter-echo spacing  $\tau = 10$  ms, and with a Gaussian slice profile, were generated. (ii) The flip angle  $\alpha$  was varied from  $18^\circ$  to  $180^\circ$  to assess its influence on the signal ( $T_1 = 1000$  ms,  $T_2 = 100$  ms,  $\tau = 10$  ms, ideal slice profile). (iii) The influence of different slice profiles was visualized by simulating signals for ideal, Gaussian, and sinc-pulse profiles ( $T_1 = 1000$  ms,  $T_2 = 100$  ms,  $\tau = 10$  ms,  $\alpha = 144$ ). (iv) Signal dependence on the relaxation times was investigated by varying  $T_1$  from 100 to 3400 ms with a fixed  $T_2 = 100$  ms and by varying  $T_2$  from 40 to 200 ms with a fixed  $T_1 = 1000$  ms ( $\tau = 10$  ms,  $\alpha = 90$  for both).

The performance of the fitting algorithm was evaluated using simulated signals with additionally added Rician noise according to a predefined SNR. The SNR was defined as the equilibrium signal ( $M_0$ ) divided by the standard deviation ( $\sigma$ ) of the noise. For fitting purposes, the slice profile was sampled at 5 sample points to assure adequate fitting speed. Two fitting approaches were compared, i.e., fitting to a mono-exponential decay function, discarding the first echo of the generated signal, and fitting to the GF formalism 3.3. The comparison was performed using Monte-Carlo methods with 10,000 trials per experiment and assessment of the fitted parameters. Median values, and upper and lower quartiles of all trials were plotted and judged concerning accuracy and precision of the  $T_2$  estimates.

The Monte-Carlo simulations consisted of the following experiments: (i) the refocusing FA  $\alpha$  was varied between  $90^\circ$  and  $270^\circ$  ( $\tau = 10$  ms,  $T_1 = 1000$  ms,  $T_2 = 100$  ms, SNR = 80, ideal profile), (ii)  $\alpha$  was varied between  $90^\circ$  and  $180^\circ$  assuming Gaussian slice profile ( $\tau = 10$  ms,  $T_1 = 1000$  ms,  $T_2 = 100$  ms, SNR = 80). In this case,  $B_{1+}$  and  $T_1$  were further estimated from the data ( $\mathbf{p}_u = [M_0, T_2, \alpha, T_1]$ ). (iii)  $T_1$  was varied between 100 and 3000 ms ( $\tau = 10$  ms,  $T_2 = 100$  ms,  $\alpha = 144^\circ$ , SNR = 80, Gaussian profile), (iv)  $T_2$  was varied between 20 and 300 ms ( $\tau = 10$  ms,  $T_1 = 1000$  ms,  $\alpha = 144^\circ$ , SNR = 80, Gaussian profile), and (v) SNR was varied between 20 and 160 ( $\tau = 10$  ms,  $T_1 = 1000$  ms,  $T_2 = 100$  ms,  $\alpha = 144^\circ$  Gaussian profile).

Fitting was always performed for the unknowns  $\mathbf{p}_u = [M_0, T_2]$  unless otherwise stated;  $M_0$ ,  $T_1$  and  $T_2$  were required to be positive;  $\alpha$  was restricted to  $0 \leq \alpha \leq 180$ . All simulations were performed using Matlab (Natick, MA). Curve fitting was achieved using least squares minimization with the constrained nonlinear optimization function,

### 3 Accurate $T_2$ -mapping for slice-selective MSE sequences

fmincon.

To illustrate that fitting can also be accomplished in the  $z$ -domain, an additional experiment was performed. Simulated relaxometry data ( $\tau = 10$  ms,  $T_1 = 1000$  ms,  $\alpha = 144^\circ$ , Gaussian profile) with added noise (SNR = 80, 1000 realizations) was fitted in the  $z$ -domain for a varying range of  $T_2$  values (50 – 300 ms). The apodization factor  $a$  was 1.13.

#### 3.2.2 MR measurements

All measurements were performed on a 3 Tesla (T) Magnetom Tim Trio System (Siemens, Erlangen, Germany). All sequences, except the Bloch-Siegert  $B_{1+}$  mapping sequence, were vendor supplied.

#### 3.2.3 Phantom measurements

As phantoms, 50 mL tubes with  $MnCl_2 \cdot 4H_2O$  and tap water in various concentrations were used to simulate  $T_1$ , and  $T_2$ -values in a physiological range (Table 3.2, column 1). Additionally, one phantom consisted of water doped with Gadobutrol (Bayer Healthcare, Berlin, Germany) (4.04 mM) to achieve  $T_1$ , and  $T_2$ -values of a comparable scale. A corn oil phantom was included to assess the influence of J-coupling.  $T_2$  was measured using an MSE sequence with a repetition time repetition time TR = 7000 ms, echo spacing  $\tau = 12$  ms, 32 echoes, field of view (FOV)  $210 \times 110$  mm<sup>2</sup>, resolution  $1.1 \times 1.1 \times 7$  mm<sup>3</sup> and a bandwidth of 200Hz/ pixel. Nominal excitation and refocusing angles were  $\beta = 90^\circ$  and  $\alpha = 180^\circ$ , respectively.  $T_1$ -measurements were obtained using a turbo inversion-recovery sequence (TIR, TR=7000 ms, echo time TE = 7.8 ms, inversion times TI = 25, 50, 100, 200, 400, 800, 1600, 3200 ms). The turbo inversion-recovery sequence consisted of an inversion module, followed after time TI by a RARE sequence for image acquisition.  $B_{1+}$  was measured using a double angle (DA) method (36) with flip angles  $\alpha_{nom} = 60^\circ$  and  $120^\circ$ , and TR = 10 s.

Reference  $T_2$ -values (“gold standard”) of the different samples were determined by single-voxel spectroscopy (voxel  $12 \times 12 \times 28$  mm<sup>3</sup>, excitation angle  $90^\circ$ , sample points 1024, and bandwidth 1200 Hz). Echo times were equally spaced but calculated separately for each sample ranging from the lowest possible (30 ms) up to a value where the signal had decayed to approximately 10% of its supposed equilibrium magnitude. In this way, sampling of the decay in a wide range for each sample, despite their different  $T_2$  times, was ensured. Additionally, data from SE experiments with varying TEs (12, 24, 36, 48, 72, 144, 288 ms) were collected for comparison (other parameters were the same as for MSE sequence). All measurements were performed with a single



channel circularly polarized head coil.

A second experiment was carried out on a bottle filled with Manganese doped water to check the influence of in-plane  $B_{1+}$  inhomogeneities (0.11 mM). An MSE (TR = 7000 ms,  $\tau = 10$  ms, 32 echoes, FOV  $300 \times 134$  mm<sup>2</sup>, resolution  $1.6 \times 1.6 \times 7$  mm<sup>3</sup>, bandwidth = 200 Hz/pixel,  $\beta = 90^\circ$  and  $\alpha = 180^\circ$ ), a SE (equal parameters as above, TE = 12, 24, 48, 72, 144, and 288 ms), a TIR (TR = 7000 ms, TE = 7.4 ms, TI = 100, 200, 400, 800, 1600, and 3200 ms, other parameters as above), and a DA sequence for  $B_{1+}$  mapping were used (TR=10 s, TE=12 ms,  $\alpha_{\text{nom}} = 60^\circ$ ). Unknown parameter values  $\mathbf{p}_u = [M_0, T_2]$  were calculated for the MSE sequence using the slice selective GF fitting including measured  $B_{1+}$ , and  $T_2$ -values, and by fitting to a mono-exponential decay model while excluding the first echo. The SE data were fitted to a mono-exponential decay model. For the acquired spectra, monoexponential fitting was performed to the maximum values of the water peaks.

For visual comparison,  $T_2$ -maps were calculated for the large phantom using the same fitting procedures as described above. Additionally, fitting was also performed for the extended unknown parameter set  $\mathbf{p}_u = [M_0, T_2, T_1, \alpha]$ .  $T_2$ -maps were median filtered (kernel  $2 \times 2$ ) to remove outliers.

### 3.2.4 In-vivo validation

In vivo validation and comparison of single-voxel spin-echo spectroscopy and MSE sequences was carried out for brain tissue of six healthy male volunteers (age 26–38; median, 30 years) using a 12-channel head coil.  $T_2$ -decay was sampled using an MSE sequence (TR=4000 ms,  $\tau = 10$  ms, 25 echoes, FOV =  $300 \times 213$  mm<sup>2</sup>, resolution  $1.6 \times 1.6 \times 4$  mm<sup>3</sup>, bandwidth 200 Hz/pixel) and a single-voxel spectroscopy SE sequence. The voxels for the spectroscopy sequence (voxel  $8 \times 8 \times 8$  mm<sup>3</sup> or  $8 \times 5 \times 14$  mm<sup>3</sup>, 5 echoes) were each placed in frontal white matter (WM), caudate nucleus, putamen, and globus pallidus. Additionally, images with a spin-echo variant, where short TRs are permissible by holding TR-TE constant [133], were acquired (TR=400 + TE ms, TE=[10, 58, 107, 155, 204, 253] ms, other parameters as above).

The DA method for  $B_{1+}$  mapping is not applicable in vivo due to its inherently long scan times. Therefore, the FA distribution was measured using the  $B_{1+}$  mapping method by Bloch- Siegert shift [107] (GRE, TR=73 ms, TE=12 ms,  $\alpha = 15^\circ$ , FOV  $300 \times 206$  mm<sup>2</sup>, resolution  $4.7 \times 4.7 \times 4$  mm<sup>3</sup>, Gaussian off-resonance pulse with  $B_{1,\text{peak}} = 0.11G$ , KBS = 21.3 rad/G<sup>2</sup>/ms, duration 8000 ms and  $f_{\text{OR}} = 8$  kHz). Two parameter fits for  $\mathbf{p}_u = [M_0, T_2]$  were calculated using the GF approach and mono-exponential fitting for MSE as well as SE data. Resulting  $T_2$ -maps were median filtered (kernel  $2 \times 2$ ) to remove outliers.

### 3 Accurate $T_2$ -mapping for slice-selective MSE sequences

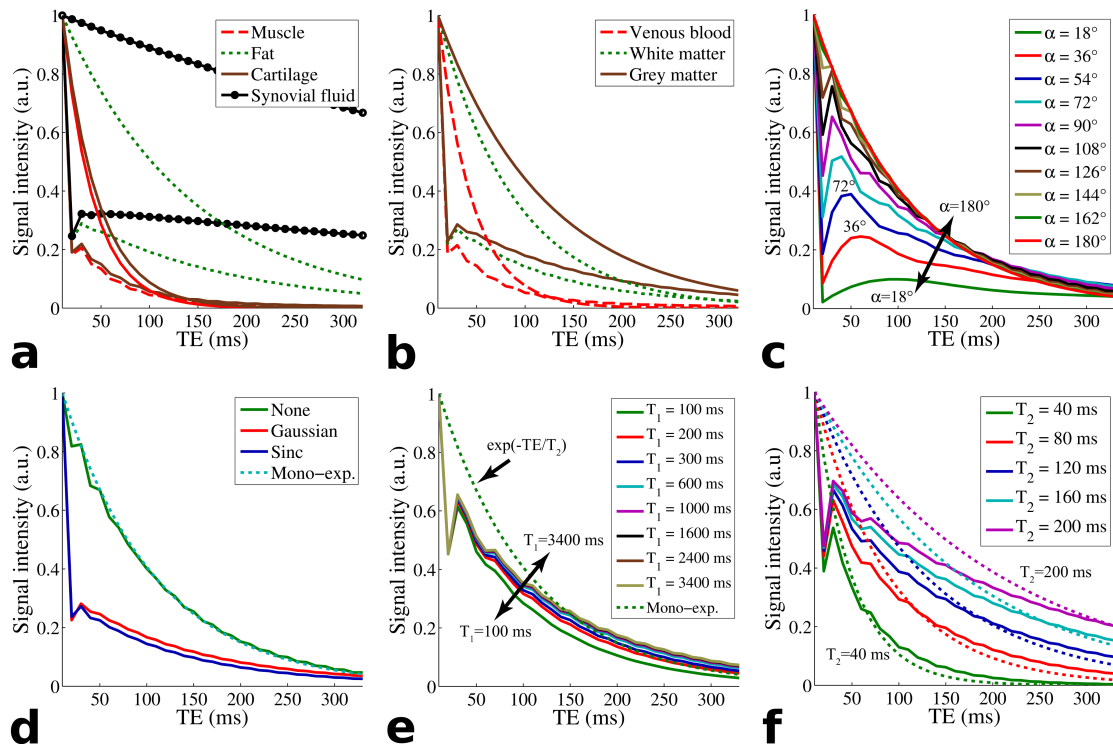


Figure 3.1: Forward simulations of the signal decay starting at the equilibrium magnetization  $M_0$  as a function of different parameters. a,b: Signal decay according to two different signal models, i.e., mono-exponential decay (continuously decreasing curve) and GF model (curve characterized by an initial sharp bend,  $\alpha = 144^\circ$ , Gaussian slice profile) for different tissues. The influence of the refocusing flip angle (from  $18^\circ$  to  $180^\circ$ , ideal slice profile,  $T_1 = 1000$  ms,  $T_2 = 100$  ms) on the signal decay (c), influence of slice profiles versus mono-exponential decay (dotted curve) and ideal slice profile ( $T_1 = 1000$  ms,  $T_2 = 100$  ms,  $\alpha = 144^\circ$ ) (d). In (e) and (f), the effects of varying  $T_1$ , and  $T_2$ -values on the decay are illustrated ( $\alpha = 90^\circ$ , ideal slice profile) and compared with the mono-exponential decay (dotted curves).

## 3.3 Results

### 3.3.1 Simulations

Figure 3.1a and b show simulated decay curves for different tissue types and signal models. Compared with the mono-exponential decay, a large decrease in signal intensity of the first echo can be observed for the GF model in all tissues. The deviation from pure exponential decay is obvious as the second echo is higher than the first, resulting in a spike of the curve. The strong dependence of the signal on the actual refocusing FA is shown in Figure 3.1c. For FAs between  $180^\circ$  and approximately  $135^\circ$  the signal can still be fitted to a mono-exponential model when using only the even echoes. For smaller angles, the signal decay is not exponential. While for these simulations the slice

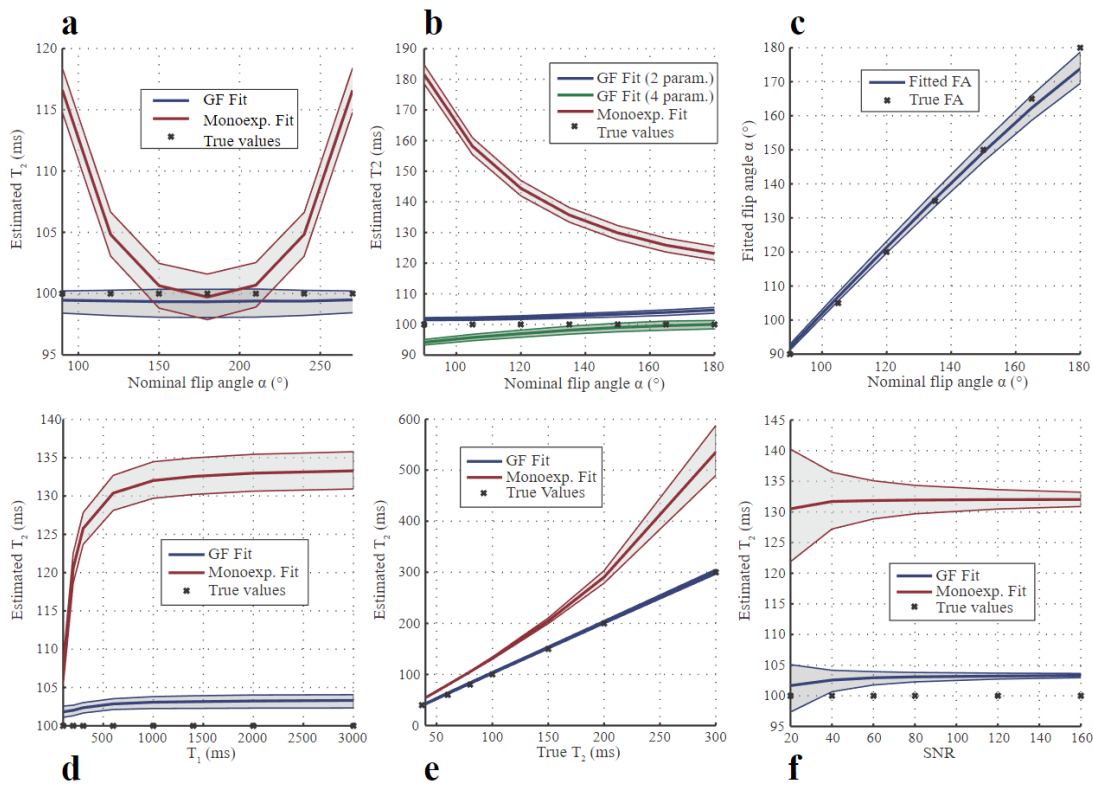


Figure 3.2: Results of the Monte Carlo simulation. Estimated  $T_2$ -times are shown for the GF formalism (dark curves) and a mono-exponential model (bright curves), and are compared with true  $T_2$ -values (cross symbols). Shaded areas represent the range from lower to upper quartile. All results are from the two-parameter fit unless otherwise stated. Influence of varying flip angles assuming ideal slice profile (a), and Gaussian slice profile (b) using a two-parameter (with prior knowledge of  $B_{1+}$  and  $T_1$ ) and a four-parameter fit ( $B_{1+}$  and  $T_1$  both included in the fitting procedure). (c) Fitting results of  $B_{1+}$  (four-parameter fit). Influence of varying  $T_1$  (d),  $T_2$ -values (e), and SNR (f).

profile was considered ideal, the influence of two different slice profiles is illustrated in Figure 3.1d. It demonstrates the large effect of the slice profile compared with sole FA deviations. Figure 3.1e displays the effect of varying  $T_1$ -times on the signal decay. The GF model curves for the different  $T_1$ s show a very similar decay, indicating that there is hardly any influence of  $T_1$  on the signal. Only for  $T_1 = T_2 = 100$  ms a slightly faster decay can be observed. The influence of  $T_2$  on the decay is shown in Figure 3.1f, comparing the GF formalism to the mono-exponential model. For short  $T_2$ -times, and starting at the second echo, the decay using the GF formalism deviates only slightly from the pure exponential decay. However, for longer  $T_2$ -times, the decay is considerably slower.

Figure 3.3: Data fitting in the z-domain. Real and imaginary part of transformed data (and) and corresponding fits (solid and dashed lines) in the z-domain. Simulation parameters were  $T_1 = 1000$  ms,  $T_2 = 150$  ms,  $\alpha = 144^\circ$ ,  $\tau = 10$  ms,  $SNR = 80$ , Gaussian profile, apodization factor 1.13.

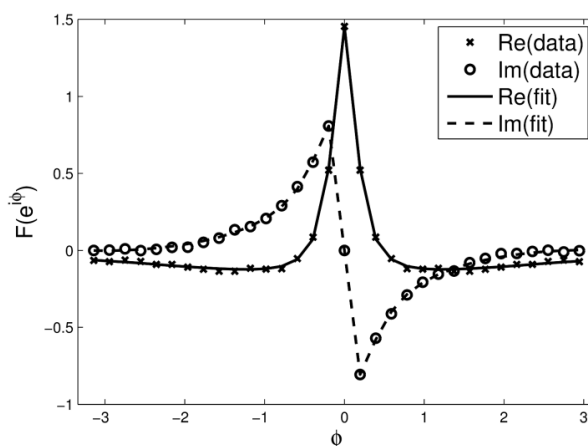


Table 3.1: Comparison of original and estimated  $T_2$ -values via z-domain fitting (mean  $\pm$  SD)

$T_2$ (ms)	$T_2$ (ms) [fit]	Rel. Error %
50	$50.1 \pm 1.5$	$0.16 \pm 2.89$
70	$70.0 \pm 2.0$	$0.10 \pm 2.81$
90	$90.2 \pm 0.12$	$0.12 \pm 2.92$
120	$119.9 \pm 3.4$	$0.15 \pm 2.85$
150	$150.4 \pm 4.8$	$0.13 \pm 3.20$
200	$200.3 \pm 7.2$	$0.00 \pm 3.58$
300	$299.9 \pm 13.5$	$0.24 \pm 4.52$

180°. The GF approach is robust for flip angle variations, with the mean of the fitting results close to the true values of  $T_2$  over the entire range of flip angles. When a Gaussian slice profile is used (Fig. 3.2b), the error for mono-exponential fitting is still greater with deviations of 25% to 80% for flip angles from 180° to 80°. For both fits, the GF formalism, i.e., a two-parameter (with prior knowledge of  $B_{1+}$  and  $T_1$ ) and a four-parameter fit ( $B_{1+}$  and  $T_1$  included in the fitting procedure), yields accurate and precise results with a negligible error compared with the mono-exponential approach.  $B_{1+}$  was reliably estimated using the GF formalism (Fig. 3.2c), however, with a tendency of underestimation for nominal flip angles close to 180°.  $T_1$  could not be reliably estimated in any of the cases that were investigated (data not shown). Figure 3.2d shows that the influence of  $T_1$  on mono-exponentially estimated  $T_2$ -values results in a constant overestimation of approximately 32% for  $T_1 / T_2$  ratios higher than 5. Below that ratio, the error is smaller with a minimum for  $T_1 / T_2 = 1$ . Using the GF approach,  $T_2$ -values are slightly overestimated (error  $< 4\%$ ). For increasing  $T_2$ -values, mono-exponentially estimated  $T_2$ -values deviate progressively, whereas the

The results of the Monte Carlo simulations are presented in Figure 3.2a–f. The simulations for flip angles varying from 80° to 280° using an ideal slice profile (Fig. 3.2a) show a marked increase of estimated  $T_2$ -times for the mono-exponential model if the flip angle deviates more than  $\pm 30^\circ$  from the ideal value of

Table 3.2: Measured relaxation times for doped water phantoms and corn oil.

Conc (mM)	$T_1$	$T_2$ SP <sup>a</sup>	$T_2$ SE <sup>b</sup>	dev.	$T_2$ MSE <sup>c</sup>	dev.	$T_2$ GF <sup>d</sup>	dev.	
<b>MnCl<sub>2</sub></b>									
1	0.02	2331.1 ± 32.0	407.7	443.6 ± 48.5	8.8	459.5 ± 17.6	12.7	368.3 ± 6.3	-9.7
2	0.08	1213.0 ± 10.2	119.2	114.1 ± 1.8	<b>-4.3</b>	137.9 ± 0.9	15.7	113.7 ± 13.6	<b>-4.6</b>
3	0.10	1066.3 ± 9.1	96.0	93.8 ± 1.4	<b>-2.3</b>	114.4 ± 0.8	19.2	91.3 ± 0.4	<b>-4.9</b>
4	0.15	767.0 ± 5.2	61.8	60.8 ± 0.7	<b>-1.6</b>	75.6 ± 0.4	22.3	59.9 ± 0.2	<b>-3.1</b>
5	0.21	616.8 ± 3.6	46.9	46.1 ± 0.5	<b>-1.7</b>	58.8 ± 0.4	25.4	47.1 ± 2.5	<b>0.4</b>
6	0.38	366.8 ± 3.1	25.5	24.8 ± 0.4	<b>-2.7</b>	33.1 ± 0.3	29.8	26.3 ± 0.2	<b>3.1</b>
<b>Gadovist</b>									
7	4.04	40.9 ± 0.7	35.3	34.0 ± 0.5	-3.7	36.2 ± 0.3	2.5	37.4 ± 12.6	6.0
<b>Corn Oil</b>									
8		291.1 ± 2.0	64.4	43.4 ± 0.6	32.6	96.9 ± 9.7	-50.4	78.2 ± 9.8	-21.4

<sup>a</sup>Spectroscopy sequence, mono-exponential fit.

<sup>b</sup>Single-echo spin-echo sequence, mono-exponential fit.

<sup>c</sup>Multiple-echo spin-echo sequence, mono-exponential fit.

<sup>d</sup>Multiple-echo spin-echo sequence, generating functions fit.

GF approach yields values close to the true value (Fig. 3.2e). The effect of the SNR on  $T_2$ -estimation (Fig. 3.2f) shows that the GF approach is less influenced by noise than the mono-exponential model. In the worst case of SNR= 20, the interquartile range was 7.8 ms (GF) compared with 18.3 ms (mono-exponential) for a true  $T_2$  of 100 ms. For the monoexponential fit, the systematic bias was approximately 30% compared with less than 4% for the GF approach. Figure 3.3 illustrates a fit to real and imaginary parts of transformed data obtained in the GF domain. Detailed results on the performed simulations are given in Table 3.1. The mean relative error is less than 0.3% in all simulated cases with standard deviations varying between 2.81 and 4.52%.

### 3.3.2 Phantom measurements

In table 3.2, measured  $T_1$ , and  $T_2$ -values for different sequences and fitting models in various phantoms are presented. The  $T_1$ -values of the MnCl<sub>2</sub> solutions (phantoms 1–6) were considerably longer than the corresponding  $T_2$  values. The deviations of  $T_2$  using the SE approach, compared with the spectroscopic measurements, were very small (< 5%) except for phantom 1 with a relative error of 8.8%. Higher errors of 15.7 to 29.8% were observed using MSE data with a mono-exponential fit with a slightly lower error for phantom 1. Using the GF model for  $T_2$ -estimation resulted in deviations between 0.4 and 9.7%, i.e. similar to the SE approach. In the Gadolinium phantom,  $T_1$  and  $T_2$

### 3 Accurate $T_2$ -mapping for slice-selective MSE sequences

Table 3.3: Measured  $T_2$ -values for brain tissue compared to values from the literature (in ms). Additional data of the knee from one volunteer is also shown.

Region	$T_2$ SP <sup>a</sup>	$T_2$ MSE <sup>b</sup>	$T_2$ GF <sup>c</sup>	$T_2$ SE	Literature
Samples	$n = 6$	$n = 6$	$n = 6$	$n = 1$	
Frontal WM	$68 \pm 6$	$71 \pm 2$	$53 \pm 8$	50	$79.6 \pm 0.6^d, 53 \pm 3^e, 69 \pm 3^f, 50 \pm 2^g, 100^h, 53 \pm 2^i$
Caudate nucleus	$69 \pm 10$	$81 \pm 2$	$63 \pm 5$	60	$60 \pm 3^e, 82 \pm 3^g, 77^h, 56 \pm 3^i$
Putamen	$56 \pm 5$	$72 \pm 1$	$57 \pm 3$	55	$55 \pm 3^e, 69 \pm 3^g, 66^h, 50 \pm 3^i$
Globus pallidus	$48 \pm 4$	$56 \pm 2$	$45 \pm 1$	37	$38 \pm 2^e, 63^h, 38 \pm 3^i$
Samples		$n = 1$	$n = 1$	$n = 1$	
Muscle		$37 \pm 1$	$30 \pm 1$	$28 \pm 2$	
Subcutaneous fat		$101 \pm 2$	$84 \pm 2$	$44 \pm 1$	
Bone marrow		$116 \pm 1$	$95 \pm 2$	$44 \pm 1$	

<sup>a</sup>Spectroscopy sequence, mono-exponential fit; <sup>b</sup>Multiple-echo spin-echo sequence, mono-exponential fit; <sup>c</sup>Multiple-echo spin-echo sequence, generating functions fit; <sup>d</sup>Multiple-echo spin-echo [131]; <sup>e</sup>Extended phase graph, compensating stimulated echoes [34]; <sup>f</sup>Multiple-echo spin-echo [134]; <sup>g</sup>DESPOT2 [42]; <sup>h</sup>Multi-echo spin-echo (post-mortem) [96]; <sup>i</sup>Adiabatic pulses at 4.7T (MASE) [135].

were similar, and  $T_2$  could be estimated with a good accuracy with all methods. For the corn oil phantom large  $T_2$ -discrepancies between the investigated methods were observed. Refocusing flip angles were close to  $180^\circ$  in all cases.

$T_2$ -maps computed with different models (Fig. 3.4a–c) illustrate the combined influence of the actual FA and the slice profile in a homogenous manganese doped water phantom. Compared with the “gold standard” mono-exponential fit to SE data (Fig. 3.4b), the GF approach (Fig. 3.4a) results in a homogenous and unbiased map with minimal residual modulation. In contrast, a large modulation of  $T_2$  resulting from  $B_{1+}$ -inhomogeneity and a substantial bias due to slice profile effects were observed for a mono-exponential fit to MSE data (Fig. 3.4c). A flip angle map of the phantom (Fig. 3.4d) indicates deviations of 50% to 130% of the nominal flip angle. A horizontal cross-section of the different approaches is presented in Figure 3.4e showing that the error becomes minimal for flip angles of  $180^\circ$ . Median estimated  $T_2$ -values across the entire slice were 84.6 ms for the SE measurement, 83.7 ms and 82.1 ms for the GF approach (two-parameter fit and four-parameter fit, respectively), and 104.1 ms for mono-exponential fitting to MSE data corresponding to relative errors of 1.1, 2.9, and 23.0%, respectively (relative to the SE measurement). The possibility to estimate the FA distribution directly from MSE data (four-parameter fit) is demonstrated in Figure 3.5a and is compared with the DA method for  $B_{1+}$  mapping (Fig. 3.5b). Due to the symmetry of the MSE signal intensities around  $180^\circ$ , only deviations from the nominal

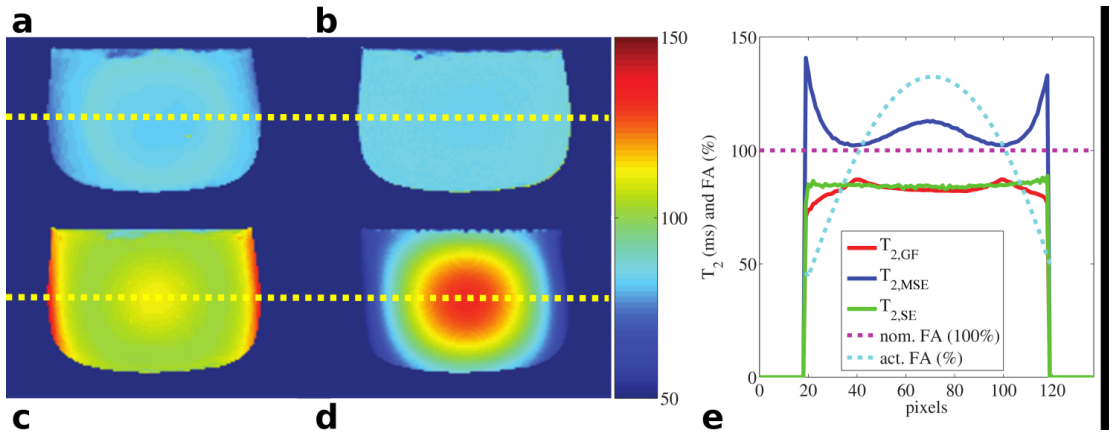


Figure 3.4:  $T_2$ -maps scaled in ms of manganese-doped water phantom. a:  $T_2$ -map calculated using the GF approach (a), "gold standard" mono-exponential fit to SE data (b), mono-exponential fit to MSE data (without first echo) (c), and  $B_{1+}$ -map scaled in % (d), 100% correspond to a flip angle of  $180^\circ$  e: Cross-sectional  $T_2$  and FA distributions, respectively, for the maps a–d. Note that in (e), two different quantities are plotted and thus two different scales are used. The solid lines correspond to  $T_2$ -values in ms, the dotted lines to nominal and actual FA in % (of the nominal angle).

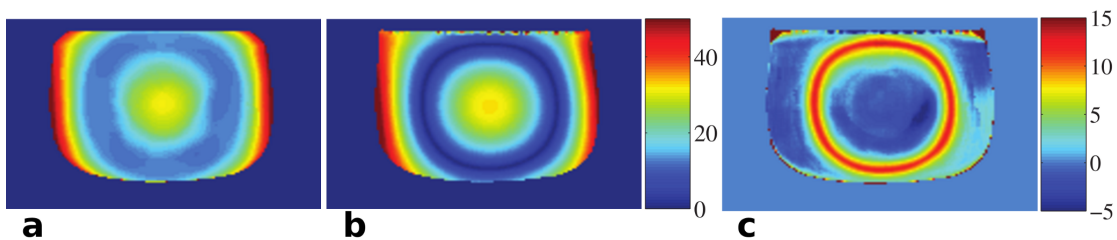


Figure 3.5: Absolute deviations from a nominal flip angle of  $180^\circ$ , scaled in degrees. a: Estimation by the GF fitting approach using a four-parameter fit, after filtering with a  $15 \times 15$  kernel median filter, In areas of  $180^\circ$  (zero deviation) the GF approach cannot accurately determine the flip angle. b: Estimation by  $B_{1+}$  mapping (DA method). c: Difference image between the GF approach (a) and  $B_{1+}$  mapping (b).

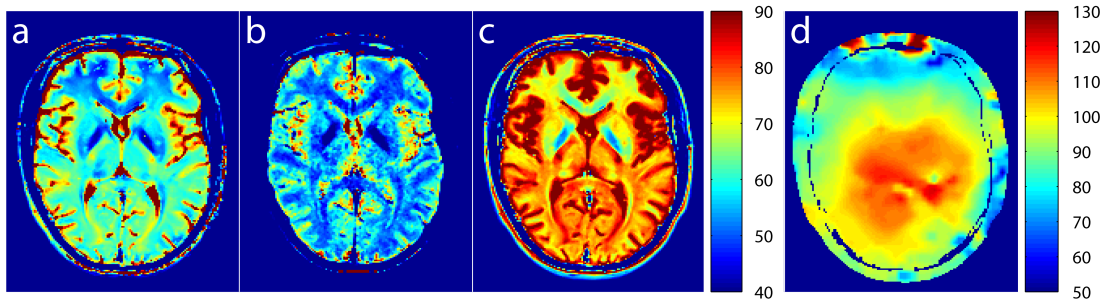


Figure 3.6: Maps of estimated  $T_2$  (a,b,c, scaled in ms) and  $B_{1+}$  (d) of a human brain in vivo.  $T_2$ -map calculated using the GF formalism (a), calculated by mono-exponential fitting to single echo data using the method in [133] (b), and using mono-exponential fitting to MSE data (c).  $B_{1+}$  map acquired with the Bloch-Siegert method, scaled in % of nominal FA. All images are median filtered with a  $2 \times 2$  kernel.

angle could be calculated. Refocusing FAs that substantially deviate from the nominal angle could accurately be estimated by GF fitting. However, in areas close to  $180^\circ$  this process fails because there, the MSE decay is insensitive to FA deviations. Additionally, in these regions the density of outliers produced by the fitting routine was higher.

### 3.3.3 In-vivo results

In figure 3.6, maps of estimated  $T_2$  of an in vivo human brain are presented. While the monoexponential fitting to MSE data tended to overestimate  $T_2$  (Fig. 3.6c), the GF approach (Fig. 3.6a) and spectroscopic measurements provided similar results. The method of [133] generally produced quite noisy results. Results of the ROI analysis in comparison with spectroscopic  $T_2$ -data are given in Table 3.3. Additionally, reported values from the literature are listed for comparison. For subcutaneous fatty tissue and bone marrow in the knee (case study) major differences are found comparing the different techniques (see table 3.3 and figure 3.7 for details).

## 3.4 Discussion

Accurate measurement of transverse relaxation times is a difficult task if FA deviations of the refocusing pulses from  $180^\circ$  cannot be excluded. Generally, this is the case for slice-selective pulses and in most in-vivo situations at high field strength. In this study, a method to circumvent these major limitations is presented. The proposed method identifies the underlying  $T_2$  of the signal-decay of a CPMG MSE sequence by fitting a new signal equation that includes the contribution of the stimulated echoes generated



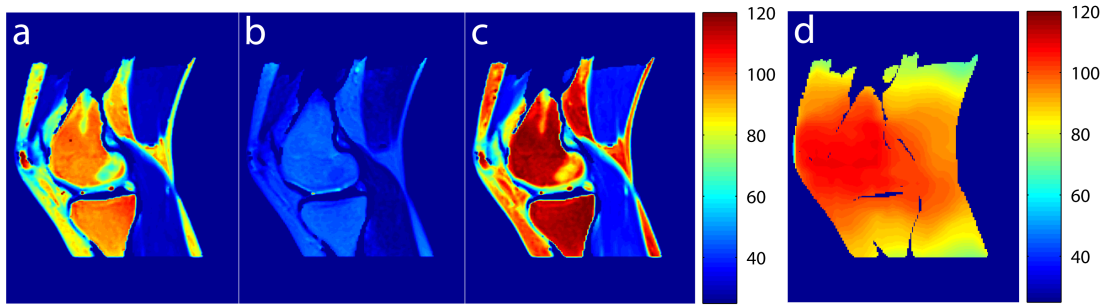


Figure 3.7:  $T_2$ -maps (a-c) and  $B_{1+}$ -map (d) of a human knee joint in-vivo. (a) is the  $T_2$ -map calculated with the GF formalism, (b) calculated by mono-exponential fitting to single echo data [133], and (c) by mono-exponential fitting to multi-echo data, all scaled in ms. (d) is a  $B_{1+}$  acquired with the Bloch-Siegert method (scaled in % of nominal FA). All images are median filtered with a  $2 \times 2$  kernel.

from non-ideal refocusing pulses. The presented approach was assessed and validated by computer simulations, phantom experiments, and in vivo investigations.

The simulations performed underpin that the signal acquired with a standard CPMG MSE sequence cannot be described by an exponential decay model, due to its substantial error in  $T_2$ -estimation. The MSE signal is a complex function depending on various factors, i.e.

$$S = f(M_0, T_1, T_2, FA, \text{slice profiles}, J, B_0, MT, \text{diffusion}, TE, TR, \text{chemical exchange, sensitivity}), \quad (3.4)$$

some of which influence the signal as multiplicative coefficients while others confound signal generation in a more complicated way. Thus, two strategies can be pursued to deal with this problem, i.e. to account for the effects with an appropriate model or to avoid them to measure the pure  $T_2$ . In accordance with previous studies [11, 13], two major influences were identified that alter the signal decay substantially and introduce " $T_1$ -mixing" into the signal. The simulations performed suggest that typical deviations from an ideally rectangular slice-profile, resulting in substantially reduced FAs at the borders, dominate over global  $B_{1+}$ -inhomogeneities with deviations in the range  $\pm 30\%$  from the nominal value. However, there will most likely be a combination of both effects in virtually all cases at high field strength (Figs. 3.2a, b). To account for  $B_{1+}$ -inhomogeneities, it is either necessary to use the actual FA distribution from additional measurements or to fit the refocusing pulse angle as additional parameter in the GF approach. Simulations and phantom measurements showed that near  $180^\circ$ ,

### 3 Accurate $T_2$ -mapping for slice-selective MSE sequences

$\alpha$  cannot be reliably fitted with the GF approach, as the influence of the FA on the MSE signal disappears. However, for substantial FA deviations from 180, the angle can be determined directly from the MSE data (Figs. 3.2c, 3.5a). The variation of  $T_1$  (Fig. 3.2d) did not show a considerable influence on the estimated  $T_2$ -values for a large range of  $T_1$ , particularly for relaxation times with a high ratio of  $T_1 / T_2$ . However, for a small  $T_1 / T_2$  ratio, the knowledge of the  $T_1$  has a critical influence on accuracy. If  $T_1$  equals  $T_2$ , the resulting signal decay ensures accurate estimates even for the mono-exponential fit [136]. This phenomenon has been described as purely accidental [29], and was validated here for the gadolinium-doped phantom and in the simulations. Also, from the four-parameter fit it can be seen that the signal is not very sensitive to  $T_1$ . For future applications, we therefore suggest two- or three-parameter fits. An analysis of the influence of  $T_2$  on the signal decay (Fig. 3.2e) showed that the deviation for mono-exponential fitting is proportional to the actual  $T_2$ . Beyond 200 ms the error increased, most likely because the inter-echo spacing was too small for large  $T_2$ -values and, thus, the decay was inefficiently sampled. This effect was also observed for the first Manganese phantom, where the error was higher in contrast to the error for the phantoms with  $T_2$ -values <120 ms. However, the GF approach produced accurate values throughout the investigated  $T_2$ -range in the simulations.

To avoid any influence of TR, the TR was chosen long enough for the longitudinal magnetization to fully recover. Influences of diffusion, homonuclear J-coupling and chemical exchange are judged to be minimal, because the MSE approach with short echo times is inherently robust against these influences compared with the SE technique (6–8) [20, 116, 117]. The signal of fatty tissue or the oil phantom, where J-coupling seems to have a stark effect, is an exception to these observations. Additionally, diffusion effects from imaging gradients were prevented by keeping readout bandwidth low, and were confirmed by calculation of the sequences' b-values. For our phantom data,  $T_2$ -estimations based on SE and GF measurements agreed much better with the spectroscopic measurements than with MSE data as they did not suffer from stimulated, and higher order echoes. Overall, this was also true for the in-vivo data, however, larger deviations were observed for frontal WM.  $T_2$  measured by spectroscopy tended to be slightly higher than when using a SE sequence, probably because two refocusing pulses have to be applied. Magnetization transfer and direct saturation via slice cross talk can also alter the signal intensity in multi-echo sequences [118]. However, when slice gaps of at least 2 mm are used, as in our experiments, the cross talk is negligible [136]. Magnetization transfer effects can be excluded in our experiments on water phantoms but might play a role in our in-vivo experiments, especially in white matter.

Rather different  $T_2$ -values were obtained for the corn oil phantom. In the spec-

troscopic measurement of  $T_2$ , only the decay of the largest peak in the spectrum was considered. However, in MRI imaging, a mean  $T_2$ -value of all separate peaks is measured. For SE measurements, estimated  $T_2$ -values are a lot smaller than for MSE, due to stronger J-coupling influence. The GF approach yields values between these two by correcting for stimulated echoes while being inherently robust to J-coupling. These findings were also confirmed by the in-vivo results for subcutaneous fat and bone marrow.

The presented method has similarities to the recently published approach by Lebel and Wilman [34]. However, this method follows an iterative scheme of the extended phase graph algorithm whereas the GF approach uses a closed form solution. This solution is obtained by using the z-transform for solving the recurrence relation for the magnetization vector of a whole inter-echo period. This strategy is often used to solve difference equation describing linear time-invariant systems in signal processing [137] and can theoretically be applied for any echo train sequence in MRI. The solution can be given as a simple formula and can be very efficiently implemented using the fast Fourier transform compared with the EPG where iterative application of rotation matrices is necessary. Furthermore, non-ideal slice profiles are readily incorporated by a summation that can be performed in the z-domain due to the linearity of the underlying transform, making necessary only one final Fourier transform.

For the EPG, the total number of real multiplications is  $N/2(N+1)36Q$  where  $N$  is the number of echoes, and  $Q$  is the number of sample points for the slice profile. In contrast, the number of multiplications for the GF approach is  $P(8+25Q)$  for function evaluation and  $(K2^K)4$  for the FFT ( $K = \log_2(P)$ ). Here,  $P$  is the number of sample points in the z-domain. One can readily observe that the computational cost of the EPG is quadratically dependent on the number of echoes, whereas for the GF there is a linear (function evaluation) and linearithmic (FFT) dependence. Therefore, the GF approach is more efficient especially, for longer echo trains.

Finally, it is also possible to Fourier transform the measured data and fit to the GF in the z-domain (Fig. 3.3) which speeds up the computation considerably by requiring only  $N(8+25Q)$  multiplications ( $N$  is number of echoes). However, proper apodization of the data will then be necessary to avoid leakage effects. The simulation results also indicate excellent accuracy with this approach. Our results are in excellent agreement with the brain  $T_2$ -values by Lebel, and also with  $T_2$ -values acquired using adiabatic pulses [135]. Clearly,  $T_2$ -values acquired with other sequences differ from our values, as presented in Table 3.3 [42, 96, 131, 134].

Limitations of this study are that we assume that the excitation FA is  $90^\circ$  and the excitation slice profile is homogeneous. Additionally, the influence of off-resonance

effects was not included in the signal model. As the phantom measurements were all carried out in the isocenter of the magnet,  $B_0$  inhomogeneities played a minor role. The additive noise bias in the mono-exponential model is not the most accurate way to model the influence of noise in magnitude MR data. However, because we were using images with a high SNR ( $> 3$ ) we do not expect a large effect [138]. Furthermore, the slice-profile was only calculated for a single FA and, subsequently, was only scaled by the actual FA scaling factor to save computation time. Recomputing the profile for each FA would have been more exact and, thus, probably would have removed the residual modulation in the  $T_2$ -maps.

### 3.4.1 Application to model-based reconstruction

In a cooperative effort it was possible to improve model-based  $T_2$ -estimation [59] by incorporating the presented model in the reconstruction framework of [58].

**Theory** Following the approach described in [58, 139] the parameter maps for  $M_0$  and  $T_2$  (here represented as vectors  $\mathbf{M}_0$  and  $\mathbf{T}_2$  since estimation is performed not pixel-wise but for the whole image at once) were estimated by minimizing the following cost function  $\Phi(\mathbf{p}_u)$  that measures the squared distance between the acquired k-space data  $\mathbf{k}_c$  and the simulated data calculated from the forward model  $\mathcal{M}(\mathbf{p}_u)$  and the current parameter estimates  $\mathbf{p}_u$ , i.e. the data fidelity term.

$$\Phi(\mathbf{p}_u) = \frac{1}{2} \sum_c \|\mathcal{M}(\mathbf{p}_u) - \mathbf{k}_c\|_2^2 \quad (3.5)$$

The subscript  $c$  accounts for the different coil channels. In the order applied, the forward model consists of the CPMG signal model  $F_q(\mathbf{p}_u)$ , a 1-dimensional DFT to get from the  $z$  domain to the time domain, multiplication by the individual coil sensitivities, subsequent 2D DFT to produce k-space data, and finally an undersampling operator  $\mathcal{P}$  to blank out the k-space lines, not acquired by the sequence.

$$M(\mathbf{p}_u) = P\mathcal{F}_{xy}C_c\mathcal{F}_\omega F(\mathbf{p}) \quad (3.6)$$

$$\mathbf{p}_u = [\mathbf{M}_0, \mathbf{T}_2]^T \quad (3.7)$$

$$\Phi(\mathbf{p}) = \frac{1}{2} \sum_c \|P\mathcal{F}_{xy}C_c\mathcal{F}_\omega W(\mathbf{p}) - \mathbf{k}_c\|_2^2 \quad (3.8)$$

Regularization was necessary due to the fact that high values for  $T_2$  lead to large outliers and was done by adding  $L^2$ -regularization terms penalizing the distance from

TABLE I  
T2 RELAXATION TIMES OF A PHANTOM FOR DIFFERENT FITTING METHODS

Compartment	1	2	3	4	5	6
SE Reference	46 ± 2	81 ± 3	101 ± 2	132 ± 5	138 ± 4	166 ± 5
Mono-Exp	59 ± 4	101 ± 5	117 ± 4	161 ± 5	170 ± 4	205 ± 7
	28.3%	24.7%	15.8%	22.0%	23.2%	23.5%
GF	46 ± 3	81 ± 4	100 ± 3	131 ± 4	137 ± 3	165 ± 5
	0.0%	0.0%	-1.0%	-0.8%	-0.7%	-0.6%
GF, const T1	44 ± 3	79 ± 4	93 ± 3	130 ± 4	138 ± 3	168 ± 6
	-4.3%	-2.5%	-7.9%	-1.5%	0.0%	1.2%

Absolute values represent a ROI analysis and are given in ms (mean ± SD).  
Relative values for T2 estimates represent the deviation to the reference.

Figure 3.8: Summary of the result of an MR phantom measured with different undersampling factors. The GF approach agrees very well with the spin-echo gold standard (reprinted from [59]).

the initial guesses  $\mathbf{M}_0^0$  and  $\mathbf{T}_2^0$ .

$$\Phi(\mathbf{p}) = \frac{1}{2} \sum_c \|P\mathcal{F}_{xy}C_cF_\omega W(\mathbf{p}) - \mathbf{k}_c\|_2^2 + \lambda_{M_0} \|\mathbf{M}_0 - \mathbf{M}_0^0\| + \lambda_{T_2} \|\kappa_2 - \kappa_2^0\| \quad (3.9)$$

where  $\kappa_2 = e^{-\tau/T_2}$

**Methods.** Cartesian undersampling was performed in phase-encoding direction, which facilitates the reconstruction process.  $\Phi(\mathbf{p}_u)$  was minimized using a conjugate gradient descent algorithm [140]. Data were acquired with the same parameters as in section 3.2. Undersampling was done retrospectively using a block-pattern with undersampling factors up to  $R = 12$ .

**Results.** The findings were quite similar to and in good agreement with the ones presented above as shorter  $T_2$ -times were observed with using the GF model. Phantom experiments yielded accurate values for undersampling factors up to  $R = 6$ , in vivo, even factors up  $R = 12$  produced reasonable  $T_2$ -maps. Figure 3.8 shows the table from the publication, summarizing the phantom experiments for different fitting methods and undersampling factors. In-vivo results of a human brain for a standard mono-exponential fit and the GF approach are shown in figure 3.9. The good performance of the method presented, even for large undersampling factors, is remarkable.

### 3 Accurate $T_2$ -mapping for slice-selective MSE sequences

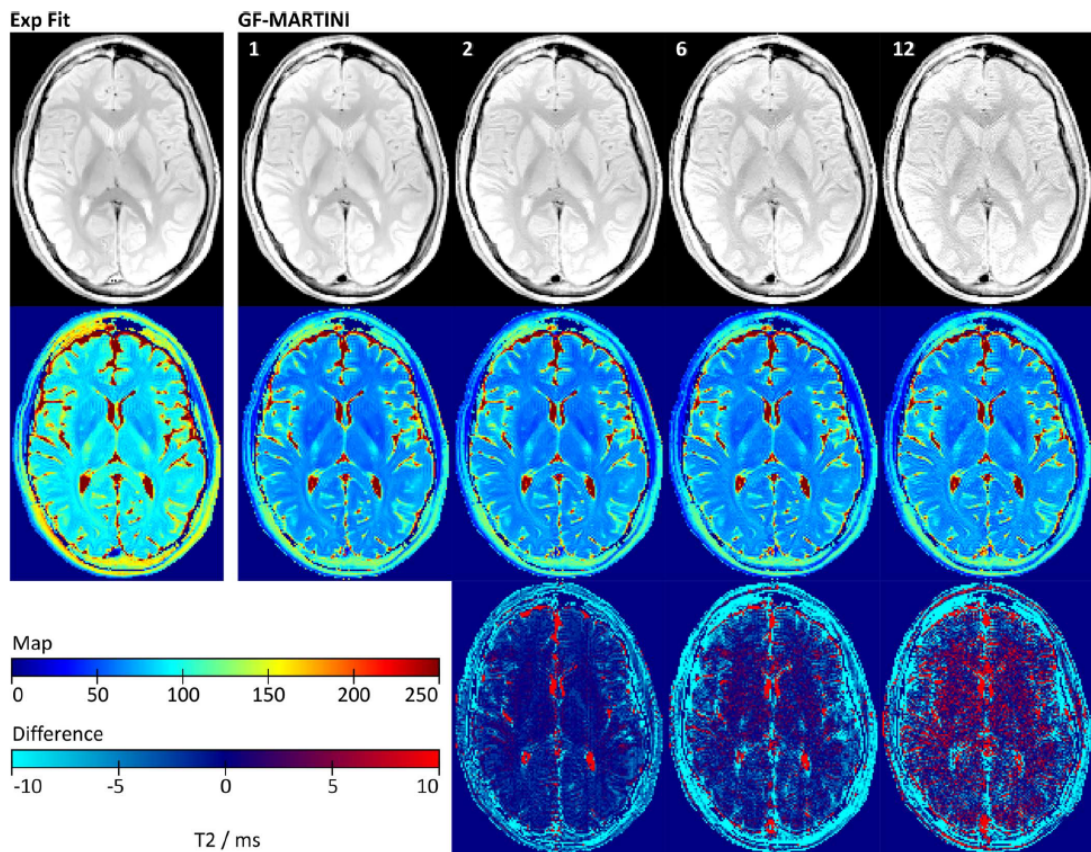


Figure 3.9: In vivo results of a human brain for different undersampling factors (reprinted from [59]).

# 4

## A-time domain signal equation for multi-echo spin-echo sequences with arbitrary excitation and refocusing angle and phase

*This chapter is adopted from "A time domain signal equation for multi-echo spin-echo sequences with arbitrary excitation and refocusing angle and phase" [141].*

### 4.1 Theory

The derivation of the time-domain formula consists of three main parts: (1) solution of the Bloch equations for the elementary sequence building blocks (fig. 4.1, shaded area) with arbitrary refocusing and excitation pulse parameters, (2) derivation of the z-transform/GF of the signal evolution, and (3) the inversion of the z-transform in order to arrive at an analytical solution in the time domain. In this chapter, a detailed derivation of the time-domain formula will be presented.

#### 4.1.1 Solution of Bloch equation

In a MESE sequence the elementary sequence block that is repeating throughout the sequence, after the initial excitation, consists of a free precession period,  $\tau/2$ , including relaxation and a dephasing (readout) gradient followed by the refocusing pulse (hard pulse approximation) and another free precession period including the rephasing (readout) gradient (see Fig. 4.1). The spin dynamics during these periods is governed by the Bloch equation in the case of uncoupled spins with spin quantum number 1/2. It can be solved piecewise for these relaxation, precession, and rotation periods. The evolution of the complex magnetization vector  $\vec{M} = [M_+, M_+, M_z]^T$  (where  $M_+ = M_x + iM_y$ ) during such a block is then given by the difference equation

#### 4 A time-domain MSE equation

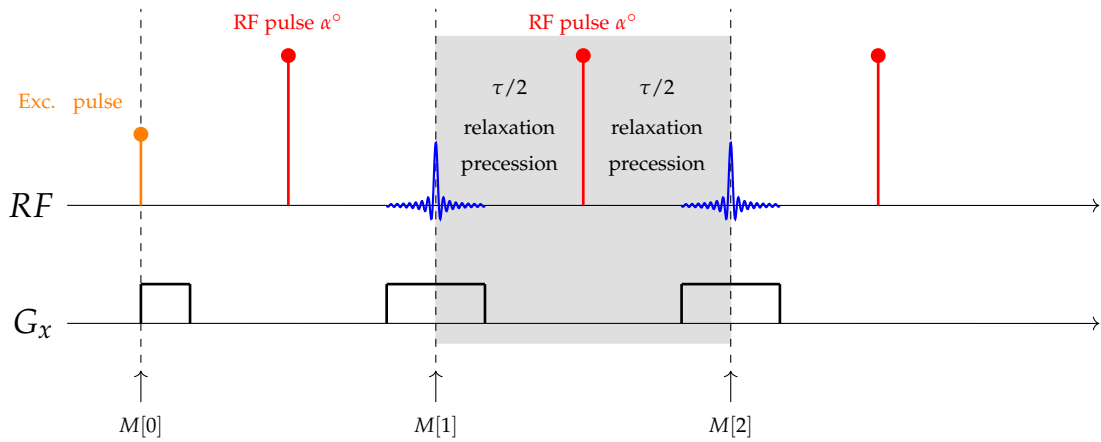


Figure 4.1: Sequence diagram for a MESE sequence: The shaded area corresponds to the repeating sequence building blocks that stay the same from one echo to another. Phase-encoding and slice-selection gradients are omitted as they are balanced throughout the sequence.

[38]

$$\vec{M}[n+1] = \mathbf{QPQ}\vec{M}[n] + (\mathbf{QP} + \mathbf{I})\vec{S}_{eq} \quad (4.1)$$

$$\vec{M}[0] = [M_+[0], M_+^*[0], M_z[0]]^T \quad (4.2)$$

where  $\mathbf{Q}$  is a complex matrix accounting for relaxation ( $\kappa_1$  and  $\kappa_2$ ) and free precession  $U = e^{i\psi}$  about the z-axis where  $\psi$  denotes the phase acquired during precession due to the readout gradient (and other off-resonance effects).

$$\mathbf{Q} = \begin{pmatrix} U\sqrt{\kappa_2} & 0 & 0 \\ 0 & U^{-1}\sqrt{\kappa_2} & 0 \\ 0 & 0 & \sqrt{\kappa_1} \end{pmatrix}, \quad \begin{aligned} \kappa_1 &= e^{-\tau/T_1}, \\ \kappa_2 &= e^{-\tau/T_2}, \\ U &= e^{i\psi}, \end{aligned} \quad (4.3)$$

$\mathbf{I}$  is the unit matrix, the vector  $S_{eq}$  accounts for longitudinal relaxation towards equilibrium and is given by  $\vec{S}_{eq} = [0, 0, M_0(1 - \sqrt{\kappa_1})]^T$ , and  $\tau$  is the inter-echo period.  $\mathbf{P} = \mathbf{P}_{\vec{u}}(\alpha)$  is a complex rotation matrix around an arbitrary rotation axis  $\vec{u} = [\cos\phi \sin\theta, \sin\phi \sin\theta, \cos\theta]^T$  ( $\phi$  azimuthal angle,  $\theta$  polar angle, see Fig.4.2) about an effective flip angle  $\alpha$  and is given by

$$\mathbf{P}_{\vec{u}}(\alpha) = \begin{pmatrix} \lambda & \chi & v e^{i\phi} \\ \lambda^* & \lambda^* & v^* e^{-i\phi} \\ \frac{v}{2} e^{-i\phi} & \frac{v^*}{2} e^{i\phi} & \zeta \end{pmatrix} \quad (4.4)$$



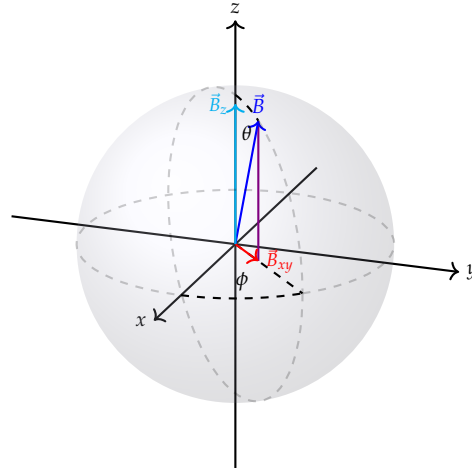


Figure 4.2: Definition of coordinate system and angles for the  $\vec{B}$  field used in the derivation. The same angles are used for the initial magnetization  $\vec{M}[0]$  ( $\theta_e$  and  $\phi_e$ ).

with

$$\begin{aligned} \lambda &= \left( \cos \frac{\alpha}{2} - i \sin \frac{\alpha}{2} \cos \theta \right)^2, & \chi &= e^{2i\phi} \sin^2 \frac{\alpha}{2} \sin^2 \theta, \\ \nu &= 2 \sin \frac{\alpha}{2} \sin \theta \left( \sin \frac{\alpha}{2} \cos \theta + i \cos \frac{\alpha}{2} \right), & \zeta &= \cos \alpha \sin^2 \theta + \cos^2 \theta. \end{aligned} \quad (4.5)$$

In general, for repetitive MR sequences, the recurrence relation can be written as

$$\vec{M}[n+1] = \mathbf{A}\vec{M}[n] + \vec{B} \quad (4.6)$$

whereas in this special case  $\mathbf{A} = \mathbf{QPQ}$  and  $\vec{B} = (\mathbf{QP} + \mathbf{I})\vec{S}_{eq}$  [38].

#### 4.1.2 z-transform of the difference equation

Introducing the z-transform  $\vec{f}(z) = \mathcal{Z}(\vec{M}[n]) = \sum_{n=0}^{\infty} \vec{M}[n]z^n$  and using the shifting property [142], one obtains an expression for the z-transformed difference equation,  $\vec{M}[n+1] = \mathbf{A}\vec{M}[n] + \vec{B}$  as follows: The z-transform of  $\vec{M}[n+1]$  can be easily obtained as

$$\mathcal{Z}(\vec{M}[n+1]) = \sum_{n=0}^{\infty} \vec{M}[n+1]z^n = \vec{M}[1] + \vec{M}[2]z + \dots + \vec{M}[\infty]z^\infty = \quad (4.7)$$

$$= z^{-1} \left( \sum_{n=0}^{\infty} \vec{M}[n]z^n - \vec{M}[0] \right) = z^{-1} \left( \mathcal{Z}(\vec{M}[n]) - \vec{M}[0] \right) \quad (4.8)$$

As the sequence is causal and all values for negative  $n$  are zero, the additive factor  $\vec{B}$  can be thought of as a function  $\vec{B}[n] = \vec{B}u[n]$ , where  $u[n]$  is the unit step function.

#### 4 A time-domain MSE equation

Transforming this expression yields the sum of the geometric series (requiring  $|z| < 1$  for convergence)

$$\sum_{n=0}^{\infty} \vec{B}u[n]z^n = \frac{1}{1-z}\vec{B} = \frac{z^{-1}}{z^{-1}-1}\vec{B} \quad (4.9)$$

Putting all this together, one arrives at the z-transformed difference equation:

$$z^{-1}(\mathcal{Z}(\vec{M}[n]) - \vec{M}[0]) = \mathbf{A}\mathcal{Z}(\vec{M}[n]) + \frac{z^{-1}}{z^{-1}-1}\vec{B}. \quad (4.10)$$

$\vec{M}[0]$  is the initial magnetization (i.e. after excitation)

$$\vec{M}[0] = M_0[\cos \phi_e \sin \theta_e, \sin \phi_e \sin \theta_e, \cos \theta_e]^T \quad (4.11)$$

and  $M_0$  the equilibrium magnetization. Solving for  $\vec{f}(z)$  gives a closed form solution for the z-transform of the magnetization evolution

$$\vec{f}(z) = \mathcal{Z}(\vec{M}[n]) = [F(z), F^*(z), L(z)]^T = (\mathbf{I} - z\mathbf{A})^{-1} \left( \vec{M}[0] + \frac{z}{1-z}\vec{B} \right) \quad (4.12)$$

Evaluating this expression gives a vector of three rational functions, of which only the first  $F(z)$  is of interest concerning the transverse magnetization.  $F(z)$  accounts for the magnetization evolution for every single isochromate. Next, it is useful to group the terms in numerator and denominator in  $F(z)$ , according to the powers of  $U$ , as we now have to average over all individual isochromates to obtain an expression that accurately models the evolution of the signal in a MESE sequence. After collecting the terms, we end up with the following expression:

$$F(z) = \frac{c_0 + c_1U + c_2U^2 + c_3U^3}{d_0 + d_1U^2 + d_2U^4} \quad (4.13)$$

with coefficients

$$\begin{aligned}
c_0 &= -M_+ z \kappa_2 (1-z)(1-z\kappa_1) \left( \cos \theta \sin \frac{\alpha}{2} - i \cos \frac{\alpha}{2} \right)^2, \\
c_1 &= -2e^{i\phi} z^2 \kappa_2^{3/2} (M_z \sqrt{\kappa_1} (1-z) + M_0 (1 - \sqrt{\kappa_1}) (1 + z\sqrt{\kappa_1})) \sin \frac{\alpha}{2} \sin \theta \left( \cos \theta \sin \frac{\alpha}{2} - i \cos \frac{\alpha}{2} \right), \\
c_2 &= -(1-z) \left( M_+ - M_+ z \kappa_1 \cos^2 \theta + z \sin^2 \theta \left( M_+^* e^{2i\phi} \kappa_2 (1 + z\kappa_1) \sin^2 \frac{\alpha}{2} - M_+ \kappa_1 \cos \alpha \right) \right), \\
c_3 &= -2ze^{i\phi} \sqrt{\kappa_2} (M_z \sqrt{\kappa_1} (1-z) + M_0 (1 - \sqrt{\kappa_1}) (1 + z\sqrt{\kappa_1})) \sin \frac{\alpha}{2} \sin \theta \left( \cos \theta \sin \frac{\alpha}{2} + i \cos \frac{\alpha}{2} \right), \\
d_0 &= -z\kappa_2 (1-z)(1-z\kappa_1) \left( \cos \theta \sin \frac{\alpha}{2} - i \cos \frac{\alpha}{2} \right)^2, \\
d_1 &= -(1-z) \left( 1 + (\kappa_2^2 z^2 - \kappa_1 z) \left( \cos^2 \frac{\alpha}{2} + \cos(2\theta) \sin^2 \frac{\alpha}{2} \right) - \kappa_1 \kappa_2^2 z^3 \right), \\
d_2 &= -z\kappa_2 (1-z)(1-z\kappa_1) \left( \cos \theta \sin \frac{\alpha}{2} + i \cos \frac{\alpha}{2} \right)^2.
\end{aligned} \tag{4.14}$$

The coefficients  $c_i$  and  $d_i$  are equivalent to those published by Lukzen [38] for the special case of a  $90^\circ$  excitation around the y-axis and arbitrary refocusing around the x-axis. In this case,  $\phi = 0$ ,  $M_+ = M_0$ , and  $M_z = 0$ . Furthermore, to be consistent with [38], the polar angle  $\theta$  has to be replaced with  $\pi/2 - \theta$ . Expression 4.13 now is the z-transform of the magnetization evolution for a single isochromate and needs to be averaged to model the signal in a MESE sequence.

Averaging over isochromates can be achieved utilizing the residue theorem of complex analysis [38] yielding an averaged function  $\vec{f}_0(z) = [F_0, F_0^*, L_0]^T$  with the relevant component  $F_0$  accounting for the transverse magnetization ( $L_0$  models the evolution of the longitudinal magnetization). First, it is best to consider the approach of decomposing the total magnetization into the configurations [37, 143]

$$S(n, U) = \sum_{n=-\infty}^{\infty} \mathbb{F}_k(n) e^{ik\psi} = \sum_{n=-\infty}^{\infty} \mathbb{F}_k(n) U^k \tag{4.15}$$

I.e. the total magnetization,  $S(n, U)$ , is nothing else but a Laurent series with the configurations as coefficients whereas for every  $n$  only the zeroth configuration gives rise to an echo. However, the total magnetization is also modelled by  $F(z)$  and so  $S(n, U)$  can be expressed as the inverse z-transform thereof:

$$S(n, U) = \mathcal{Z}^{-1}\{F(z)\} \tag{4.16}$$

Equating eqns. (4.15) and (4.16), subsequent z-transform and exploiting linearity of the

#### 4 A time-domain MSE equation

z-transform,

$$\mathcal{Z}\{S(n, U)\} = F(z) = \mathcal{Z}\left\{\sum_{k=-\infty}^{\infty} \mathbb{F}_k(n)U^k\right\} = \sum_{k=-\infty}^{\infty} \mathcal{Z}\{\mathbb{F}_k(n)\}U^k, \quad (4.17)$$

shows that  $F(z)$  is simply the Laurent series of the z-transformed configurations. One now needs to extract the z-transform of the zeroth configuration, i.e. the zeroth coefficient of the Laurent series. As known from complex analysis, the closed line integral of a function around a pole gives the coefficient  $F_{-1}$  of the corresponding Laurent series:  $F_{-1} = 1/(2\pi i) \oint F(U)dU$  [144]. Thus, dividing  $F(z, U)$  by  $U$  yields the zeroth coefficient of the Laurent series.

$$F_0(z) = \mathcal{Z}\{\mathbb{F}_0(n)\} = \frac{1}{2\pi i} \oint_{|U|=1} \frac{F(z, U)}{U} dU \quad (4.18)$$

The evaluation of the integral can be elegantly accomplished using the residue theorem, [144]

$$F_0(z) = \sum_{m=1}^M \text{Res}\left(\frac{F(z, U)}{U}, U_m\right), \quad (4.19)$$

where  $U_m$  are the poles of  $F(z, U)/U$  that lie inside the unit circle. If  $U_m$  is a single pole and  $F(z, U)/U$  is of the form  $h(z, U)/g(z, U)$ , then the residue at  $U_m$  can be calculated as

$$\text{Res}\left(\frac{F(z, U)}{U}, U_m\right) = \frac{g(z, U_m)}{h'(z, U_m)}. \quad (4.20)$$

By calculating the roots of the denominator in (4.13), the poles are given as

$$U_0 = 0, \quad (4.21)$$

$$U_{1,2,3,4} = \frac{\mp \sqrt{-\frac{d_1 \mp \sqrt{d_1 - 4d_0 d_2}}{d_2}}}{\sqrt{2}}. \quad (4.22)$$

Following the method of Lukzen [37] only the poles inside of the unit circle ( $U_0, U_3, U_4$ ) are used to yield the averaged GF:

$$F_0(z) = \frac{g(z, 0)}{U_1 U_2 U_3 U_4} + \frac{g(z, U_3)}{U_3(U_3 - U_1)(U_3 - U_2)(U_3 - U_4)} + \frac{g(z, U_4)}{U_4(U_4 - U_1)(U_4 - U_2)(U_4 - U_3)} \quad (4.23)$$

Carrying out these steps gives

$$F_0(z) = \frac{-2c_2d_0\sqrt{d_1^2 - 4d_0d_2} + c_0\left(4d_0d_2 + d_1\left(-d_1 + \sqrt{d_1^2 - 4d_0d_2}\right)\right)}{2d_0\left(-d_1^2 + 4d_0d_2\right)} \quad (4.24)$$

and finally

$$F_0(z) = e^{i\phi} \left[ \frac{M_x \cos \phi + M_y \sin \phi}{2} \left( 1 + \sqrt{\frac{X_+(z)}{X_-(z)}} \right) + i \frac{M_y \cos \phi - M_x \sin \phi}{2} \left( 1 + \sqrt{\frac{X_-(z)}{X_+(z)}} \right) \right] \quad (4.25)$$

$$X_+(z) = (1 + z\kappa_2)(1 - z(\cos \alpha \cos^2 \theta + \sin^2 \theta)(\kappa_1 + \kappa_2) + z^2\kappa_1\kappa_2) \quad (4.26)$$

$$X_-(z) = (1 - z\kappa_2)(1 - z(\cos \alpha \cos^2 \theta + \sin^2 \theta)(\kappa_1 - \kappa_2) - z^2\kappa_1\kappa_2) \quad (4.27)$$

If furthermore the initial magnetization is given in spherical coordinates  $\vec{M}[0] = M_0[\cos \phi_e \sin \theta_e, \sin \phi_e \sin \theta_e, \cos \theta_e]^T$ , one arrives at the final result given in eq. 4.28.

$$F_0(z) = \frac{M_0 e^{i\phi} \sin \theta_e}{2} \left[ \cos(\phi_e - \phi) \left( 1 + \sqrt{\frac{X_+(z)}{X_-(z)}} \right) + i \sin(\phi_e - \phi) \left( 1 + \sqrt{\frac{X_-(z)}{X_+(z)}} \right) \right] \quad (4.28)$$

The first term in the square brackets describes the signal for a CPMG sequence and the second one for a CP sequence, respectively (see also ref. [38]). The factor  $\cos(\phi_e - \phi)$  is the amount of initial magnetization that is projected onto the orientation of the refocusing  $B_1+$  field in the  $xy$ -plane, and  $\sin(\phi_e - \phi)$  the amount that is projected onto the perpendicular orientation. This is not surprising since the magnetization that is aligned with the refocusing rotation axis experiences a CPMG sequence and perpendicular magnetization experiences a CP sequence. The polar angle of the refocusing axis,  $\theta$ , enters the equation through the effective flip angle which is defined by  $\cos \alpha_e = \cos \alpha \sin^2 \theta + \cos^2 \theta$  [38]. After computation of the signal evolution, the previous projection has to be undone by rotating the resulting transverse magnetization back to its original orientation by multiplying by  $e^{i\phi}$ .  $M_0 \sin \theta_e$  is exactly the amount of magnetization converted to transversal magnetization by the excitation pulse (for previously fully relaxed equilibrium magnetization). The reader should not confuse the specific angles for excitation and refocusing pulse, namely the excitation pulse profile expressed in polar coordinates  $\theta_e$  and  $\phi_e$ , and the rotation axis  $\theta$  and the phase  $\phi$  of the refocusing pulse, respectively. The former describe the excited magnetization in spheric coordinates, whereas the latter define the rotation axis of the refocusing pulse. The expression incorporating the excited magnetization in Cartesian coordinates can be found in the appendix.

Principally, equation 4.28 can already be used to calculate the echo amplitudes

#### 4 A time-domain MSE equation

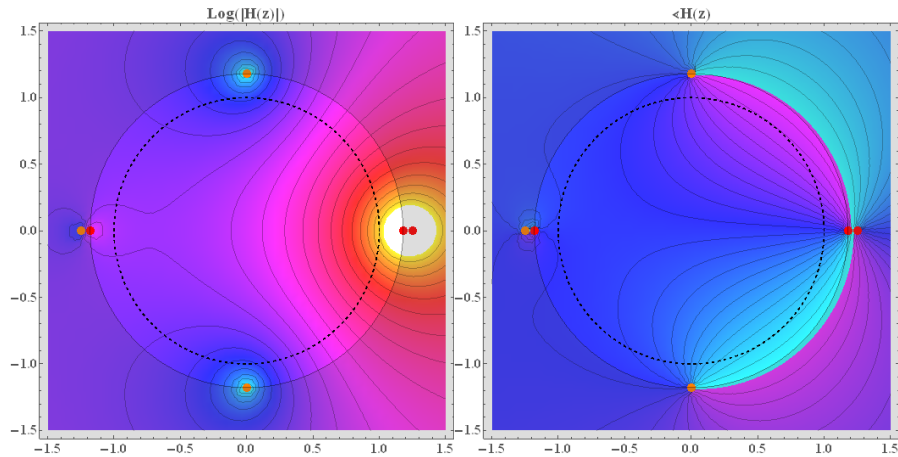


Figure 4.3: Roots and poles of  $Y_{\perp}(z)$  in the complex plane. Poles are indicated in red, roots in orange color, respectively. The inner dashed circle corresponds to the unit circle. The outer circle was drawn at the position of the innermost pole.

for a MESE sequence. Bearing in mind that the  $z$ -transform reduces to the discrete time Fourier transform (if it exists) for  $z = e^{i\varphi}$ , and moreover to the discrete Fourier transform (DFT) for equidistantly sampled values of  $\varphi$ , i.e.  $\varphi_k = \frac{2\pi k}{K}$  and  $k = 0, \dots, K-1$ , the echo amplitudes are obtained using the inverse DFT of  $F_0(e^{i\varphi_k})$  evaluated around the unit circle. However, the DFT can cause problems through truncation/leakage effects which results in flawed echo amplitudes [10]. Therefore, a method to analytically transform  $F_0(z)$  to the time domain is desirable.

#### 4.1.3 Derivation of time domain formula

For inverse  $z$ -transform of (4.28) first the arguments of the square roots are treated. Here we obtain rational functions  $Y_{\perp}(z) = X_{+}(z)/X_{-}(z)$ , indicating the CPMG part, and  $Y_{\parallel}(z) = X_{-}(z)/X_{+}(z)$ , indicating the CP part, that can be inversely transformed using e.g. Mathematica. Doing that, one arrives at a time domain expression  $\eta[n]$ , which is a convolution of the inverse  $z$ -transform of the root itself according to the convolution property ( $x[n] * x[n] \stackrel{z}{\circlearrowleft} X(z)^2$ ). Thus,

$$Y_{\perp}(z) \stackrel{z^{-1}}{\circlearrowleft} \eta_{\perp}[n] = g_{\perp}[n] * g_{\perp}[n] \quad \text{and} \quad Y_{\parallel}(z) \stackrel{z^{-1}}{\circlearrowleft} \eta_{\parallel}[n] = g_{\parallel}[n] * g_{\parallel}[n]. \quad (4.29)$$

The actual time domain contribution of both magnetization components  $g_{\perp}[n]$  and  $g_{\parallel}[n]$  experiencing a CPMG and a CP sequence, respectively, can subsequently be obtained by deconvolution of the corresponding functions  $\eta_{\perp}[n]$  and  $\eta_{\parallel}[n]$ .

**Check poles of  $Y_{\perp}(z)$  and  $Y_{\parallel}(z)$ .** To do that one has to first have a look at the roots  $z_{+k}$  and poles  $z_{-k}$  of  $Y_{\perp}(z)$  (the roots of  $Y_{\perp}(z)$  are the poles of  $Y_{\parallel}(z)$ ). From the definition of the z-transform used in this work, the positioning of all poles outside the unit circle corresponds to a stable and causal system. The poles of  $Y_{\perp}(z)$  all lie on the real axis and are given by the following equations:

$$z_{-1} = \frac{\left( (\kappa_2 - \kappa_1) \cos \alpha_e - \sqrt{4\kappa_1\kappa_2 + (\kappa_1 - \kappa_2)^2 \cos^2 \alpha_e} \right)}{2\kappa_1\kappa_2}, \quad (4.30)$$

$$z_{-2} = \frac{\left( (\kappa_2 - \kappa_1) \cos \alpha_e + \sqrt{4\kappa_1\kappa_2 + (\kappa_1 - \kappa_2)^2 \cos^2 \alpha_e} \right)}{2\kappa_1\kappa_2}, \quad (4.31)$$

$$z_{-3} = \frac{1}{\kappa_2}, \quad (4.32)$$

where the abbreviation  $\cos \alpha_e = \cos \alpha \sin^2 \theta + \cos^2 \theta$  is used. Given the fact that  $0 < \kappa_2 < \kappa_1 < 1$ , one can calculate the minimum values for the poles of  $Y_{\perp}(z)$ , which are given for all possible values of  $\alpha$  by

$$\min z_{-1} = -1/\kappa_2 \quad (4.33)$$

$$\min z_{-2} = 1/\kappa_1 \quad (4.34)$$

$$\min z_{-3} = 1/\kappa_2 \quad (4.35)$$

We can see that all poles lie outside the unit circle and, hence, conclude the system  $Y_{\perp}(z)$  is both causal and stable for the region of convergence (ROC) being the disk inside the innermost pole [137] (causality being a logical prerequisite for every MR sequence, as no magnetization can be measured before the first RF pulse).

Considering the poles of  $Y_{\parallel}(z)$ , the result is similar (whereas the poles can be complex in this case)

$$z_{+1} = \frac{(\kappa_1 + \kappa_2) \cos \alpha_e - \sqrt{-4\kappa_1\kappa_2 + (-\kappa_1 - \kappa_2)^2 \cos^2 \alpha_e}}{2\kappa_1\kappa_2} \quad (4.36)$$

$$z_{+2} = \frac{(\kappa_1 + \kappa_2) \cos \alpha_e + \sqrt{-4\kappa_1\kappa_2 + (-\kappa_1 - \kappa_2)^2 \cos^2 \alpha_e}}{2\kappa_1\kappa_2} \quad (4.37)$$

$$z_{+3} = -\frac{1}{\kappa_2} \quad (4.38)$$

#### 4 A time-domain MSE equation

with the minimum values also being all outside the unit circle.

$$\min z_{+1} = -\frac{1}{\kappa_2} \quad (4.39)$$

$$\min z_{+2} = -\sqrt{\frac{1}{\kappa_1 \kappa_2}} \quad (4.40)$$

$$\min z_{+3} = -\frac{1}{\kappa_2} \quad (4.41)$$

**Inverse transform of  $Y_{\perp}(z)$ .** Upon calculating the inverse transform of  $Y_{\perp}(z)$  we see that the resulting function  $\eta_{\perp}[n]$  is a sum of weighted and shifted versions of another function  $\zeta_{\perp}[n]$ .

$$\begin{aligned} \eta_{\perp}[n] = & \zeta_{\perp}[n] + (\kappa_2 - \kappa_p \cos \alpha_e) \zeta_{\perp}[n-1] + \\ & \kappa_2 (\kappa_1 - \kappa_p \cos \alpha_e) \zeta_{\perp}[n-2] + \kappa_1 \kappa_2^2 \zeta_{\perp}[n-3] \end{aligned} \quad (4.42)$$

$\zeta_{\perp}[n]$  in turn is a weighted sum of three exponential functions.

$$\kappa_1 = e^{-\tau/T_1} \quad (4.43)$$

$$\kappa_2 = e^{-\tau/T_2} \quad (4.44)$$

$$\kappa_m = \kappa_1 - \kappa_2 \quad (4.45)$$

$$\cos \alpha_e = \cos \alpha \sin^2 \theta + \cos^2 \theta \quad (4.46)$$

$$S_m = \sqrt{4\kappa_1 \kappa_2 + \kappa_m^2 \cos^2 \alpha_e} \quad (4.47)$$

$$W_{(m,p)} = (\kappa_m \cos \alpha_e + S_m)/2 \quad (4.48)$$

$$W_{(m,m)} = (\kappa_m \cos \alpha_e - S_m)/2 \quad (4.49)$$

$$w_{m,m} = \kappa_1 (-2\kappa_2 + S_m) - \kappa_m \cos \alpha (\kappa_1 - S_m + \kappa_m \cos \alpha_e) \quad (4.50)$$

$$w_{m,p} = \kappa_1 (2\kappa_2 + S_m) + \kappa_m \cos \alpha (\kappa_1 + S_m + \kappa_m \cos \alpha_e) \quad (4.51)$$

$$\zeta_{\perp}[n] = \frac{\sec^2(\alpha_e/2)}{4\kappa_m S_m} \cdot [-2\kappa_2 S_m \kappa_2^n + w_{m,m} W_{(m,m)}^n + w_{m,p} W_{(m,p)}^n] \quad (4.52)$$

$$g_{\perp}[n] = \frac{\eta_{\perp}[n] - \sum_{k=1}^{n-1} g_{\perp}[k] g_{\perp}[n-k]}{2\sqrt{\eta_{\perp}[0]}} \quad n \geq 1 \quad (4.53)$$



Since the system is causal ( $\eta_{\perp,\parallel} = 0$  for all  $n < 0$ ), the deconvolution is given recursively as

$$g_{\perp}[n] = \begin{cases} \sqrt{\eta_{\perp}[0]} & n = 0 \\ \frac{\eta_{\perp}[n] - \sum_{k=1}^{n-1} g_{\perp}[k]g_{\perp}[n-k]}{2\sqrt{\eta_{\perp}[0]}} & n \geq 1 \end{cases} \quad (4.54)$$

with  $\eta_{\perp}[0] = 1$ .

**Inverse transform of  $Y_{\parallel}(z)$ .** The results of  $\eta_{\parallel}[n] \bullet^{\overset{z^{-1}}{\circ}} Y_{\parallel}(z)$  are structurally very similar and given by

$$\eta_{\parallel}[n] = \zeta_{\parallel}[n] - (\kappa_2 + \kappa_m \cos \alpha) \zeta_{\parallel}[n-1] - \kappa_2(\kappa_1 - \kappa_m \cos \alpha) \zeta_{\parallel}[n-2] + \kappa_1 \kappa_2^2 \zeta_{\parallel}[n-3] \quad (4.55)$$

The formulas for  $\zeta_{\parallel}[n]$  are as follows:

$$\kappa_p = \kappa_1 + \kappa_2 \quad (4.56)$$

$$S_p = \sqrt{-4\kappa_1\kappa_2 + \kappa_p^2 \cos^2 \alpha_e} \quad (4.57)$$

$$W_{(p,p)} = (\kappa_p \cos \alpha_e + S_p) / 2 \quad (4.58)$$

$$W_{(p,m)} = (\kappa_p \cos \alpha_e - S_p) / 2 \quad (4.59)$$

$$w_{p,p} = \kappa_1(-2\kappa_2 + S_p) + \kappa_p \cos \alpha_e(\kappa_1 + S_p + \kappa_p \cos \alpha_e) \quad (4.60)$$

$$w_{p,m} = \kappa_1(2\kappa_2 + S_p) - \kappa_p \cos \alpha_e(\kappa_1 - S_p + \kappa_p \cos \alpha_e) \quad (4.61)$$

$$\zeta_{\parallel}[n] = \frac{\sec^2(\alpha_e/2)}{4\kappa_p S_p} \cdot [2\kappa_2 S_p (-\kappa_2)^n + w_{p,p} W_{(p,p)}^n + w_{p,m} W_{(p,m)}^n] \quad (4.62)$$

In contrast to  $S_m$ , for CPMG part, the terms of  $S_p$  under the square root can get negative, resulting in a complex value for  $S_p$ . Since  $g_{\parallel}[n]$  models the magnitude for the CP part of the magnetization, it has to be a real number. In order to assure that, this special case was examined closer.

**Case  $-4\kappa_1\kappa_2 + \kappa_p^2 \cos^2 \alpha < 0$**  In this case,  $S_p$  is purely imaginary, and it turns out that  $w_{p,p} = -\overline{w_{p,m}} = w_p$ . Furthermore,  $W_{(p,p)} = \overline{W_{(p,m)}} = W_{(p)}$ . Then,  $\zeta_{\parallel}[n]$  is equal to

#### 4 A time-domain MSE equation

$$\zeta_{\parallel}[n] = \frac{\sec^2(\alpha/2)}{4\kappa_p S_p} \cdot [2\kappa_2 S_p (-\kappa_2)^n + w_p W_{(p)}^n - \overline{w_p W_{(p)}^n}] \quad (4.63)$$

$$= \frac{\sec^2(\alpha/2)}{4\kappa_p S_p} \cdot [2\kappa_2 S_p (-\kappa_2)^n + w_p W_{(p)}^n - \overline{w_p W_{(p)}^n}] \quad (4.64)$$

$$= \frac{\sec^2(\alpha/2)}{4\kappa_p i \sqrt{-\cdot}} \cdot [2\kappa_2 i \sqrt{-\cdot} (-\kappa_2)^n + i 2\Im(w_p W_{(p)}^n)] \quad (4.65)$$

$$(4.66)$$

As the  $i$ 's in this expression cancel, the resulting function is always a real function. Finally, the deconvolution formula for  $g_{\parallel}[n]$  is essentially the same as for  $g_{\perp}[n]$

$$g_{\parallel}[n] = \begin{cases} \sqrt{\eta_{\parallel}[0]} & n = 0 \\ \frac{\eta_{\parallel}[n] - \sum_{k=1}^{n-1} g_{\parallel}[k] g_{\parallel}[n-k]}{2\sqrt{\eta_{\parallel}[0]}} & n \geq 1 \end{cases} \quad (4.67)$$

with  $\eta_{\parallel}[0] = 1$ .

**Complete formula.** To arrive at the complete time domain formula, one must not forget the constant terms 1 in (4.28), which inversely transform to a Dirac delta function  $\delta[n]$ . In summary, the combined and actually measured signal, i.e. the  $n^{\text{th}}$  echo at echo time  $n \cdot \tau$ , can be computed as

$$M_+[n] = \frac{M_0 e^{i\phi} \sin \theta_e}{2} [\cos(\phi_e - \phi)(g_{\perp}[n] + \delta[n]) + i \sin(\phi_e - \phi)(g_{\parallel}[n] + \delta[n])] \quad n \geq 0. \quad (4.68)$$

For  $n = 0$ , this reduces to the magnetization directly after the excitation pulse,  $M_+[0] = M_0 e^{i\phi_e} \sin \theta_e$ .

**Special case for  $\alpha_e = \pi$ .** In case the refocusing angle  $\alpha_e = \pi$  the  $\sec(\alpha_e/2)$  becomes infinity. Computing the limit for both  $\eta_{\perp}$  and  $\eta_{\parallel}$  yields

$$\lim_{\alpha_e \rightarrow \pi} \eta_{\perp}[n] = 4n\kappa_2^n \quad (4.69)$$

$$\lim_{\alpha_e \rightarrow \pi} \eta_{\parallel}[n] = 4n(-\kappa_2)^n, \quad (4.70)$$

which are the convolution of an exponential decay and an alternating-sign exponential decay function, respectively:

$$g_{\perp}[n] = 2\kappa_2^n \quad (4.71)$$

$$g_{\parallel}[n] = 2(-\kappa_2)^n \quad (4.72)$$

This is exactly what would be expected for a  $180^\circ$  pulse for a CPMG and CP sequence. Putting it all together, the evolution of the magnetization for this limiting case is given by

$$M_+[n] = M_0 e^{i\phi} \sin \theta_e [\cos(\phi_e - \phi) \kappa_2^n + i \sin(\phi_e - \phi) (-\kappa_2)^n] \quad n \geq 0. \quad (4.73)$$

For the purpose of data fitting, it's necessary to check the value of  $\alpha_e$  and branch to a code using the simple exponential decay if  $\alpha_e \approx \pi$ . Experiments have shown, that a branching condition of  $0.999\pi < \alpha < 1.001\pi$  is sufficient, when working with double-precision numbers.

## 4.2 Methods

### 4.2.1 Simulations

**Signal evolution for CPMG, CP, and mixed type MESE sequences.** Six signal evolutions for various parameter combinations were simulated and plotted. Parameters were chosen as (a) excitation around x-axis, refocusing around y-axis (CPMG sequence), (b) excitation around y-axis, refocusing around x-axis (CPMG sequence), (c) excitation and refocusing around y-axis (CP sequence), (d) excitation around an axis of  $45^\circ$ , refocusing around  $-45^\circ$  (CPMG sequence with additional phase), (e) excitation around an axis of  $135^\circ$ , refocusing around x-axis (mixed CP and CPMG sequence), (f) excitation around y-axis and refocusing around an axis of  $45^\circ$  (mixed CP and CPMG sequence). The other parameters were fixed for all simulations  $M_0 = 1$  a.u.,  $T_1 = 1000$  ms,  $T_2 = 100$  ms, echo-spacing  $\tau = 10$  ms, excitation angle  $\theta_e = 90^\circ$ , refocusing angle  $\alpha = 180^\circ$ , and polar angle of the refocusing axis  $\theta = 90^\circ$ .

**Simulation of the evolution of the slice profile.** In this experiment the evolution of a whole slice profile was computed. The numerical waveforms of RF amplitude and phase and the slice-selection gradient were fed into the forward Shinnar-Le Roux (SLR) algorithm [113] to compute the corresponding final Cayley-Klein parameters  $\mathbf{a}$  and  $\mathbf{b}$  for the accumulated effect of the RF pulse.

#### 4 A time-domain MSE equation

For the excitation pulse, the excitation magnetization profile was computed using  $M_+ = 2ab^*$  (assuming initially fully relaxed magnetization  $\vec{M} = [0, 0, M_0]^T$ ). This profile was then converted to spherical coordinates, and parameters  $\theta_e(z)$  and  $\phi_e(z)$  were extracted ( $z$  denoting the spatial coordinate in slice direction).

For the refocusing pulse, the computation of the actual refocusing profile is not necessary. Instead the relations between the parameters  $\mathbf{a}$  and  $\mathbf{b}$  and the parameters  $\alpha$ ,  $\theta$ , and  $\phi$  given in the publication by Pauly [113] were inverted.

$$\alpha = 2 \arccos \Re(\mathbf{a}) \quad (4.74)$$

$$\phi = \arctan -\frac{\Re(\mathbf{b})}{\Im(\mathbf{b})} \quad (4.75)$$

$$\theta = \arctan \frac{-\mathbf{b}e^{-i\phi}/i}{-\Im(\mathbf{a})} \quad (4.76)$$

This yields the spatially dependent parameters  $\alpha(z)$ ,  $\phi(z)$ , and  $\theta(z)$  that can be directly inserted in the previously derived formula ( $z$  again denoting the spatial coordinate). Care must be taken implementing the arctan functions, e.g. for the simulations in this publication the Matlab (Mathworks Inc., Natick, MA) function `atan2` was used. The remaining parameters used in the simulations were  $M_0 = 1$  a.u.,  $T_1 = 137$  ms  $T_2 = 111$  ms (in accordance with the phantoms used), and  $\tau = 12$  ms. The results were plotted in a 3D plot to illustrate the alterations of the signal decay when moving through the slice profile.

#### 4.2.2 Comparison with measurements

To compare the signals computed with the derived formula, the simulated and measured evolution of the slice profile were compared. Therefore, data for a CPMG (excitation y-axis, refocusing x-axis) and a CP sequence (both excitation and refocusing y-axis) were measured in a Gadolinium doped water phantom ( $T_2 = 111$  ms and  $T_1 = 137$  ms) on a 3T scanner (Skyra, Siemens). Pulse sequence parameters were: echo spacing  $\tau = 12$  ms, TR=1000 ms, nominal excitation flip angle  $\beta = 90^\circ$  and nominal refocusing flip angle  $\alpha = 180^\circ$ . The standard Siemens MESE sequence was modified such that the read out gradients were applied in the slice-direction to obtain the slice signal evolution across the slice profile.

#### 4.2.3 Fitting

The superior performance of models including  $B_{1+}$ -inhomogeneities and slice profiles for  $T_2$ -mapping using the GF approach [38] was already demonstrated in [10]. To

asses the accuracy and precision of the algorithm applied to least squares fitting of "bi-exponential" relaxation data with two  $T_2$  components  $T_{2s}$  (short) and  $T_{2l}$  (long), the following experiments were performed.

1. Fitting of simulated data to assess accuracy and precision of the model:  $T_2$ -values were chosen to mimic normal white brain matter [145]. Complex MSE data were simulated with parameters  $\tau = 10$  ms for  $T_{2l} = 100$  ms ( $M_{0l} = 40$  a.u.) and  $T_{2s} = 15$  ms ( $M_{0s} = 10$  a.u.), and  $T_1 = 1000$  ms. Both decay curves were added together and Gaussian noise was added to the real and imaginary part of the data. Noise standard deviation was computed to achieve 3 different SNRs (SNR=80, 60, 40). For each SNR level, the fitting was repeated  $N = 200$  times, with individually generated noise for each fitting. Median values, and the 25% and 75% quantiles of the fitted parameters were evaluated.
2. Fitting of acquired white matter data to assess feasibility in brain  $T_2$ -mapping: For 183 white matter pixels  $T_2$ -values were estimated using our method, bi-exponential and mono-exponential least-squares fitting. Mean values and standard deviations were compared between the methods. The CPMG sequence parameters were TR=4000 ms,  $\tau = 10$  ms, 25 echoes, matrix 192, voxel size  $1.3 \times 1.3 \times 4$  mm<sup>3</sup>. The  $B_{1+}$  map was acquired with a sequence employing the Bloch-Siegert shift [107].

## 4.3 Results

### 4.3.1 Simulations

**Signal evolution for CPMG, CP, and mixed type MESE sequences.** In Fig. 4.4 the results of the simulations for CPMG, CP, and mixed type MESE sequences are shown. (a) corresponds to a standard CPMG sequence. As the excitation is carried out around the x-axis, only  $M_y$  (i.e. negative imaginary part) is present. This magnetization is refocused around the y-axis and therefore doesn't oscillate but stays negative while decaying. (b) is basically the same scenario as in (a) with the only difference that excitation and refocusing axis are switched. This results in a decaying positive real component  $M_x$  without oscillations. Fig. 4.4 (c) corresponds to a classic CP sequence with excitation and refocusing around the y-axis. The resulting decay has only a real component  $M_x$  but oscillates between positive and negative values after every refocusing pulse. In (d) the phase between excitation and refocusing pulse is  $90^\circ$  (i.e. CPMG) but both rotation axes are turned  $-45^\circ$ . This results in a CPMG like decay

#### 4 A time-domain MSE equation

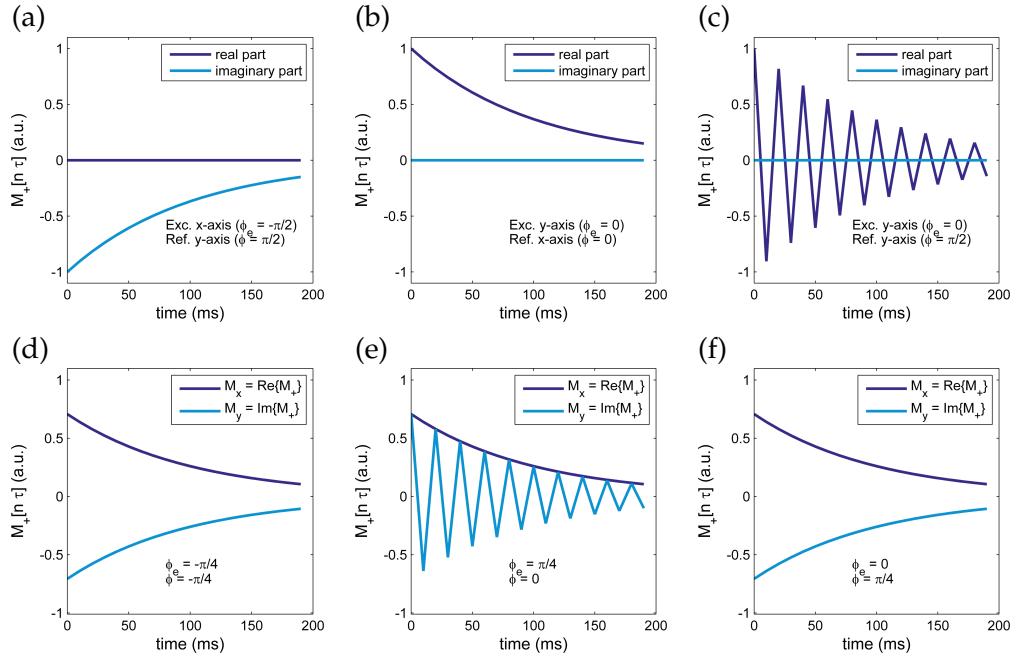


Figure 4.4: Simulation of signal evolution for (a) excitation around x-axis, refocusing around y-axis (CPMG sequence), (b) excitation around y-axis, refocusing around x-axis (CPMG sequence), (c) excitation and refocusing around y-axis (CP sequence), (d) excitation around an axis of  $45^\circ$ , refocusing around  $-45^\circ$  (CPMG sequence with additional phase), (e) excitation around an axis of  $135^\circ$ , refocusing around x-axis (mixed CP and CPMG sequence), (f) excitation around y-axis and refocusing around an axis of  $45^\circ$  (mixed CP and CPMG sequence).

(no oscillations) with the overall magnetization split into a positive real and negative imaginary part with initial magnitude of  $1/\sqrt{2}$ . Fig. 4.4 (e) shows the magnetization decay after an excitation around an axis of  $135^\circ$  (resulting in magnetization aligned  $\phi_e = 45^\circ$  between x and y-axis). Refocusing is performed around the x-axis, so that the magnetization amount along the x-axis (real part) experiences a CPMG sequence (no oscillations), and the amount along the y-axis a CP sequence (oscillations). Finally, in (f) also a mixed-type sequence is shown with excitation around the y-axis (resulting in  $\phi_e = 0^\circ$ ) and refocusing around a  $\phi = 45^\circ$  axis. The difference compared to (e) is that here the different magnetization amounts experiencing a CP or CPMG sequence are mixed together when they are read out, giving rise to oscillations in both the real and imaginary part. These intuitive test cases all support the validity of the presented formula.

**Simulation of the evolution of the slice profile.** In Fig. 4.5 the RF pulses used and their corresponding slice profiles or pulse parameters  $\alpha$ ,  $\theta$ , and  $\phi$  are shown. In (a) and (b), the excitation and refocusing pulses are displayed. Fig. 4.5 (c) illustrates the magnitude as well as  $x$  and  $y$  components of the transverse magnetization after a  $90^\circ$  excitation using the pulse in (a) computed with the forward SLR algorithm. Excitation was obviously carried out around the  $y$ -axis as the main component of the magnetization is aligned with the  $x$ -axis thereafter. However, some residual magnetization is left along the  $+$  and  $-y$  axes. The parameters  $\alpha$ ,  $\phi$ , and  $\theta$  for the refocusing pulse were extracted from the SLR parameters **a** and **b** and are displayed in Fig. 4.5 (d)-(f).

In Fig. 4.6 the simulated evolution of the magnetization for a CPMG (exc.  $y$ -axis, refoc.  $x$ -axis) are plotted. In (a) and (b) the whole slice profile and selected decay curves (1 = middle . . . 4 = edge) are given for  $M_x$ , and in (c) and (d) for  $M_y$ , respectively. In (b) it can be seen that most decay curves exhibit a large magnetization drop already after the first refocusing pulse when the flip angle is not  $180^\circ$  (curves 2-4). The subsequent decay is also slower, as described previously [10]. In (d), the signal curve 1 is zero at all times because the excitation pulse did not produce magnetization in the middle of the slice profile along the  $y$ -axis. The other curves (3-4) alternate between positive and negative values.

### 4.3.2 Comparison with measurements

In Fig. 4.7, simulated (top row) and measured (bottom row) signals for a CP (left) and CPMG (right) sequence are plotted. For each plot, the horizontal position corresponds to a position across the slice profile and the vertical position to the time evolution of the signal, respectively. First of all, by comparing simulation and measurement (top

#### 4 A time-domain MSE equation

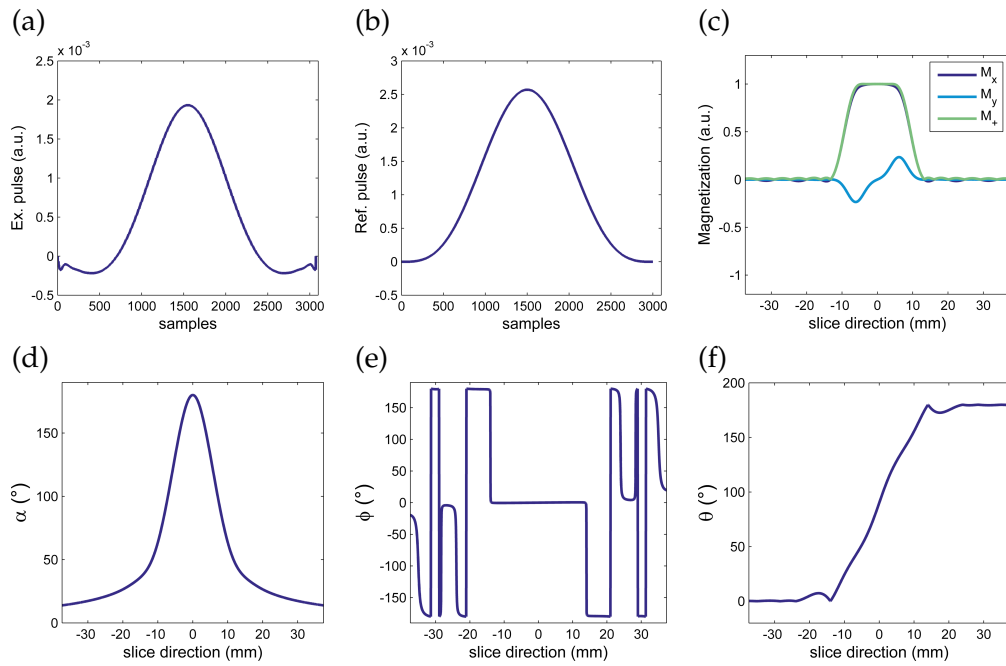


Figure 4.5: (a) RF waveform of excitation pulse, (b) RF waveform of refocusing pulse, (c) excitation pulse profile, (d) refocusing angle profile, (e) refocusing azimuthal angle (i.e. refocusing phase) profile, and (f) refocusing polar angle (i.e. refocusing axis) profile, all computed using forward SLR algorithm.



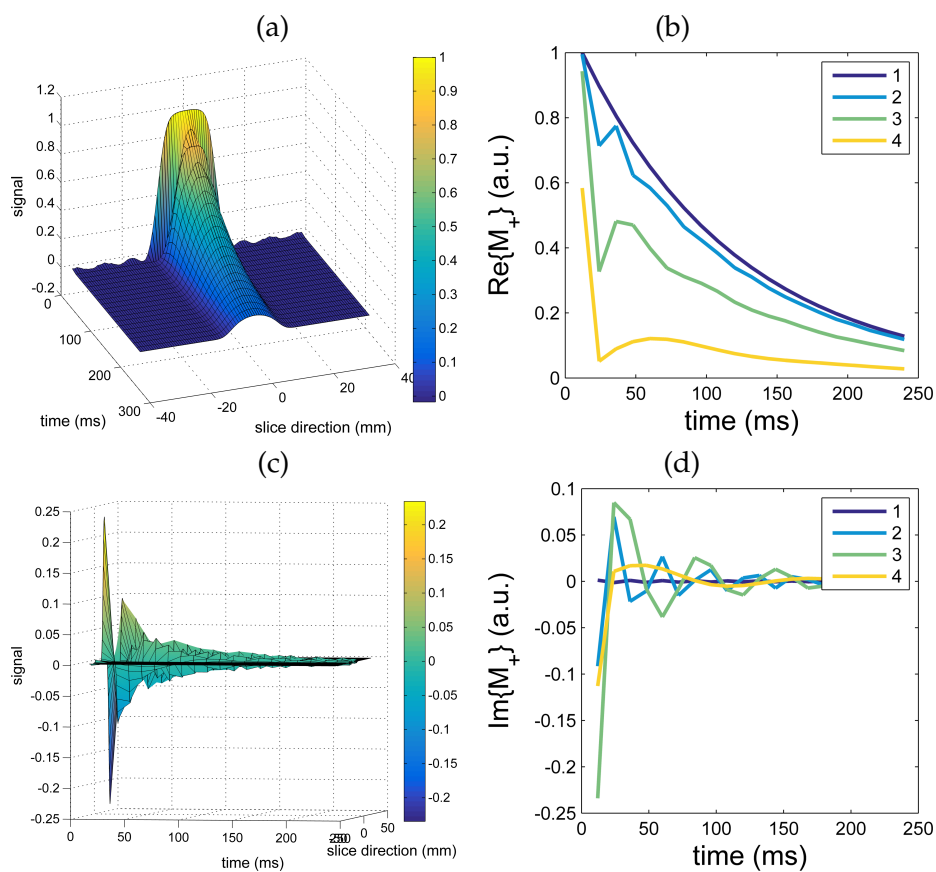


Figure 4.6: (a) Evolution of the slice profile for  $M_x$ , (b) selected  $M_x$  decay curves, (c) evolution of the slice profile for  $M_y$ , (d) selected  $M_y$  decay curves. For (b) and (d) numbers 1 correspond to the middle of the slice profile going to 4 at the edge of the profile.

#### 4 A time-domain MSE equation

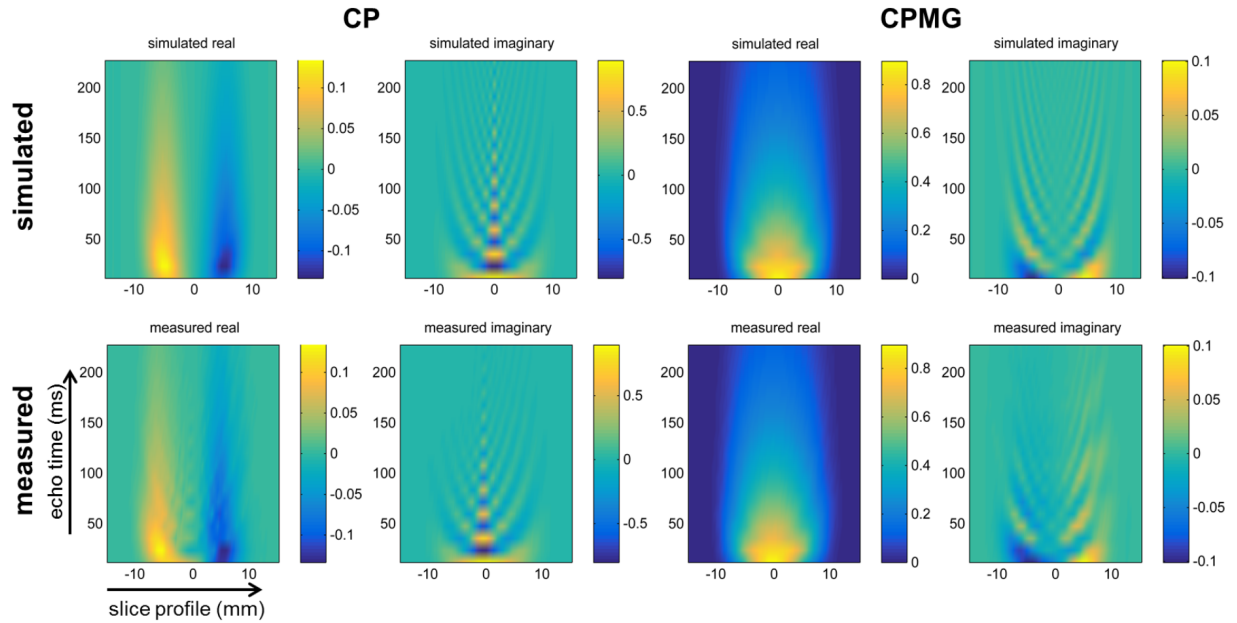


Figure 4.7: Comparison between simulation and measurements: The top row are simulations, the bottom row the corresponding measurements. On the left hand side the signals for a CP sequence are compared, on the right hand side signals for a CPMG sequence, respectively. For each sequence type both real and imaginary part show excellent agreement between simulation and measurement.

and bottom row), one can observe excellent agreement between those two. For the CP sequence with excitation around the  $x$ -axis the major part of the magnetization is flipped to the  $-y$ -axis (imaginary part) and a smaller portion with negative parts on the left and positive parts on the right of the slice profile is flipped to the  $-x/x$ -axis (real part). The real part then experiences a CPMG sequence and therefore keeps its sign throughout the echo evolution, whereas the imaginary part has alternating sign. Both have in common that the magnetization is decaying. The imaginary part decays with  $T_2$  in the center, where the flip angle is close to  $180^\circ$ , but faster than  $T_2$  at the border of the slice due to imperfect refocusing. The pure  $T_2$ -decay cannot be seen in the real part, as there is no initial magnetization at the center of the slice. For the CPMG sequence, the main part of the magnetization is aligned along the  $x$ -axis after excitation. It is refocused around this axis and therefore keeps its sign and again decays with  $T_2$  in the middle of the slice and faster at the edges. The part of the magnetization that is initially aligned along the  $-y/y$ -axis experiences a CP sequence and therefore changes sign after a couple of pulses.

### 4.3.3 Fitting

The results for the fitting simulation are summarized in table 4.1 where median values and upper and lower quantiles are compared to the simulation ground truth values. For the long  $T_2$ -species both  $M_0$  and  $T_2$  were fitted with good accuracy and precision. For the short  $T_2$ -species deviations were bigger, but still acceptable, especially for the  $T_{2s}$ -value. The estimations generally tend to get worse with decreasing SNR level.

For the fitting to acquired MR data of normal white matter the following results were obtained for the proposed model compared to conventional bi-exponential fitting (subscript  $bi$ ) and mono-exponential fitting (subscript  $T_{2,mo}$ ):  $T_{2s} = 27.8 \pm 5.4$  ms vs.  $T_{2s,bi} = 43.1 \pm 6.4$  ms and  $T_{2l} = 87.2 \pm 5.8$  ms vs.  $T_{2l,bi} = 121.5 \pm 8.5$  ms, and  $T_2 = 96.6 \pm 3.0$  (all values are mean  $\pm$  standard deviation). This observation that  $T_{2,bi}$  is longer than  $T_2$  coincides with the results for mono-exponential fitting [10] where  $T_2$ -values are usually overestimated using the standard mono-exponential approach. Mono-exponential fitting yields a result located in-between  $T_{2s,bi}$  and  $T_{2l,bi}$ . Standard deviations are in a reasonable range for all methods.

Values for  $M_0$  are not given here as they are influenced by the slice profile incorporation as well as the local sensitivity of the receive coils.

## 4.4 Discussion and Conclusion

In this work, we present a time-domain formula for the evolution of the transverse magnetization in multi-echo spin-echo sequences. The formula derived is a continuation and generalization of the Generating functions method first published by Lukzen [37, 38]. For a repetitive sequence building block, a solution of the Bloch equation is computed and, subsequently, the established recurrence relation is solved by using the

Table 4.1: Results of the bi-exponential fitting simulations. In comparison to the ground truth median values and 25% and 75% quantiles are given for 3 different SNR values (N=200).

	ground truth	SNR = 80			SNR = 60			SNR = 40		
		0.25	0.5	0.75	0.25	0.5	0.75	0.25	0.5	0.75
$M_{0s}$ (a.u.)	10	9.7	10.6	11.9	9.4	10.8	12.1	10.3	12.7	16.1
$M_{0l}$ (a.u.)	40	39.3	39.9	40.7	38.4	39.9	40.7	38.2	39.9	41.1
$T_{2s}$ (ms)	15	11.9	15.2	18.1	12.2	16.1	20.1	9.1	14.0	21.2
$T_{2l}$ (ms)	100	98.5	100.0	101.7	98.8	100.4	103.0	97.8	100.6	103.5

#### 4 A time-domain MSE equation

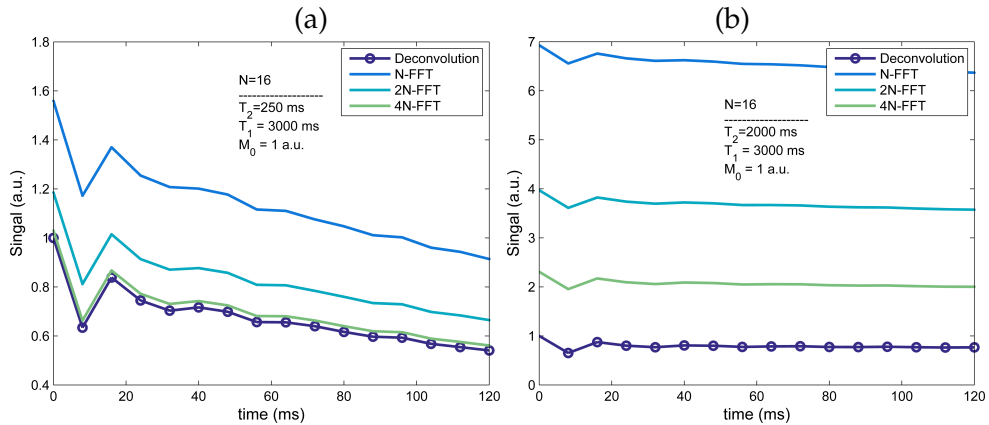


Figure 4.8: Illustration of leakage effect using the DFT approach compared to the presented method for (a) blood ( $T_2 \approx 250$  ms) and (b) CSF ( $T_2 \approx 2000$  ms) for different DFT lengths. Other simulation parameters where  $M_0 = 1$  a.u.,  $T_1 = 3000$  ms,  $\tau = 8$  ms, 16 echoes. The shorter the computed DFT, the more the deviation from the actual signal decay becomes apparent.

z-transform. This method works for all sequences that consist of repeating building blocks. Theoretically, the method can be extended also to coupled or exchanging spins using, e.g. the Bloch-McConnell equation. For spins  $> 1/2$ , one could also use the master equation of the density matrix, although the equations might quickly get intractable.

Simulations for test cases are all in agreement with the expected signal decay. Furthermore, when compared to measurements, also excellent congruence between simulation and measurement could be observed. The formula provided contains all relevant excitation and refocusing parameters that are used in the MESE sequence. First, the initial excitation profile is incorporated with the flip angle  $\theta_e$  and the phase angle  $\phi_e$ , and, second, the refocusing axis and angle by the parameters  $\theta$ ,  $\phi$ , and  $\alpha$ . Using  $\theta_e$  and  $\phi_e$ , an arbitrary magnetization preparation preceding the refocusing train can be used. Naturally, also the equilibrium magnetization,  $M_0$ , relaxation parameters,  $T_1$ , and  $T_2$ , as well as sequence timing,  $\tau$ , are included. Compared to the generating functions approach, where the z-transform is evaluated at points around the unit circle,  $z = e^{i\phi_k}$ , and subsequently the inverse DFT is applied, no leakage effects from the transformation are possible, which is especially relevant for long  $T_2$  such as observed in blood [134], peritumoral edema [70] or CSF [146] (see fig. 4.8). The derived formula is an exact solution without any approximations. In the limiting case of a  $180^\circ$  refocusing pulse, the formula degenerates to a simple and an alternating sign exponential decay, for CPMG and CP type sequences, respectively. It is readily implemented and evaluated by the computation of the sum of 3 exponential functions, and a discrete deconvolution step

which can also be exactly calculated due to the causal nature of the signals. Compared to other methods, such as Bloch matrices or EPG, no consecutive multiplication of nutation and precession matrices is necessary, and additionally the formula inherently keeps track of all relevant isochromats, as the averaging over all isochromats has already been performed analytically in the derivation of the formula.

In the case of 2D  $T_2$ -mapping, the knowledge of the actual angle and phase of the pulses across the slice is crucial. All pulse parameters are discretized along the slice direction giving a vector  $\alpha_j$ , and equivalently for  $\theta_j$  and  $\phi_j$ , where subscript  $j$  accounts for discretization across the slice profile. This gives the following expression for the measured signal pixelwise integrated across the slice profile:

$$M_+^{\text{SP}}[n] = \frac{1}{Q} \sum_{j=1}^Q \frac{M_0 e^{i\phi_j} \sin \theta_{e,j}}{2} \left[ \cos(\phi_{e,j} - \phi_j)(g_{\perp}[n,j] + \delta[n]) + i \sin(\phi_{e,j} - \phi_j)(g_{\parallel}[n,j] + \delta[n]) \right] \quad n \geq 0, \quad (4.77)$$

where SP denotes integration across the slice and  $Q$  is the number of discretization points. Basically,  $\alpha_j$ ,  $\theta_j$ , and  $\phi_j$  are computed from the refocusing pulse shape ( $\theta_e$  and  $\phi_e$  for the excitation pulse, respectively) using the SLR algorithm, which takes the actual  $B_{1+}$  and  $B_0$  values as input values for every pixel. Therefore,  $B_{1+}$ -mapping, e.g. by [105] is necessary beforehand. However, it was also shown in [10] that the  $B_{1+}$ -map can be fitted itself under certain conditions.  $B_0$ -inhomogeneities slightly alter the flip angle and deform the slice. It is our experience, that this effect is negligible and, therefore, no additional  $B_0$ -mapping is required.

$T_2$ -fitting is then for example accomplished by least-squares minimization of the following functional when magnitude image data  $d[n]$  are used:

$$\hat{M}_0, \hat{T}_2 = \arg \min_{M_0, T_2} \|d[n] - |M_+^{\text{SP}}[n]|\|_2^2 \quad (4.78)$$

In the case of a long and short  $T_2$ -species, such as free and myelin-bound water, usually bi-exponential fits are computed. Bi-exponential fitting itself is an ill-posed problem [123] and a sufficiently high SNR, in combination with a substantial difference between  $T_{2s}$  and  $T_{2l}$ , is required to obtain reliable results. In a simulation experiment, we demonstrated the feasibility of the proposed model for multi-parameter estimation and presented values on the accuracy and precision of the method for different SNRs. For the fitting of acquired brain data, the incorporation of the slice-profile yielded lower values for  $T_2$  as was already demonstrated for the case of a single  $T_2$ -species [10]. Mono-exponential fitting yielded results between the bi-exponential  $T_2$ -values and, although this is certainly the wrong model, a reasonably good fit was achieved. The values obtained by our method tend to approach the values Whittall et al. presented in [145]. This is good evidence for the effectiveness of our method as these authors employ

## 4 A time-domain MSE equation

a single-slice CPMG sequence with rectangular (hard) refocusing pulses to eliminate slice profile effects. Furthermore, they report a generally larger standard deviation for  $T_{2s}$  in simulation experiments, which is also reflected in our observations.

We believe this approach is a valuable and ready-to-use method that can be used for more accurate and comparable  $T_2$ -quantification and will be of great value for model-based MRI reconstruction techniques in the future. Therefore, we also decided to make a C/C++ version of the core algorithm available to the scientific community. The source files will be for download under <http://www.t2mapping.rocks>.

### 4.A Code

```
1  /*
2  * Computes a multi-echo spin-echo train with the deconvolution algorithm
3  * (c) Andreas Petrovic, 2020
4  */
5  #include "math.h"
6  #include "cpmg_decon.h"
7
8  #define PI 3.141592653589793238463
9
10 namespace my {
11 template <typename T>
12 struct complex {T re; T im;};
13 }
14
15 template <typename T>
16 inline my::complex<T> complexMult(my::complex<T> u, my::complex<T> v);
17
18 template <typename T>
19 inline my::complex<T> complexAdd(my::complex<T> u, my::complex<T> v);
20
21
22 template <typename T>
23 void getEchoTrain(T M0, T T1, T T2, T tau, T alpha, T theta, T phi, T phie, T thetae, ←
    const int Nechoes, T *outr, T* outi)
24 {
25 // convert to radians
26 alpha = alpha/180*PI;
27 theta = theta/180*PI;
28 phi = phi/180*PI;
29 phie = phie/180*PI;
30 thetae = thetae/180*PI;
31
32 // compute effective flip angle
33 double alphae = acos(cos(alpha)*pow(sin(theta),2.0)+pow(cos(theta),2.0));
34
35 // make sure flip angle is not too close to PI (results in a division by 0)
```

```

36 if (alphae > 0.999*PI && alphae <= PI) alphae = 0.999*PI;
37 if (alphae < 1.001*PI && alphae > PI) alphae = 1.001*PI;
38
39 // set up frequently used parameters
40 double k1 = exp(-tau/T1);
41 double k2 = exp(-tau/T2), k22 = k2*k2, k2acc=1.0, k2macc=1.0;
42 double twoacc=1.0, twom2acc= 1.0/4;
43 double cosa = cos(alphae), cosa2 = cosa*cosa;
44 double secah = 1/cos(alphae/2);
45 double secah2 = secah*secah;
46 double km = k1 - k2, km2 = km*km;
47 double kp = k1 + k2, kp2 = kp*kp;
48 double Sm;
49 double Wmp, Wmpacc=1.0;
50 double Wmm, Wmmacc=1.0;
51
52 Sm = sqrt(4*k1*k2+km2*cosa2);
53 Wmp = (km*cosa+Sm)/2;
54 Wmm = (km*cosa-Sm)/2;
55
56 my::complex<double> Wpp, Wppacc, Wpm, Wpmacc, Sp;
57 Wppacc.re = 1.0;
58 Wppacc.im = 0.0;
59 Wpmacc.re = 1.0;
60 Wpmacc.im = 0.0;
61
62 // handle complex numbers if term under square root is < 0 !!
63 double Sp2 = -4*k1*k2+kp2*cosa2;
64
65 if (Sp2 >= 0)
66 {
67 Sp.re = sqrt(Sp2);
68 Sp.im = 0.0;
69 }
70 else
71 {
72 Sp.re = 0.0;
73 Sp.im = sqrt(-Sp2);
74 }
75
76 Wpp.re = (kp*cosa+Sp.re)/2;
77 Wpp.im = (Sp.im)/2;
78
79 Wpm.re = (kp*cosa-Sp.re)/2;
80 Wpm.im = (-Sp.im)/2;
81
82
83 int length = Nechoes + 3;
84 double *zetacpmg, *gammaacpmg, *fcpmg;
85 double *zetacp, *gammaacp, *fcpc;
86
87 // -----
88 // CPMG sequence

```

#### 4 A time-domain MSE equation

```
89 zetacpmg = (double*) malloc(sizeof(double)*length);
90 zetacpmg[0] = 0;
91 zetacpmg[1] = 0;
92 zetacpmg[2] = 0;
93
94 gammacpmg = (double*) malloc(sizeof(double)*Nechoes);
95 fcpmg = (double*) malloc(sizeof(double)*Nechoes);
96 // -----
97
98 // -----
99 // CP sequence
100 zetacp = (double*) malloc(sizeof(double)*length);
101 zetacp[0] = 0;
102 zetacp[1] = 0;
103 zetacp[2] = 0;
104
105 gammacp = (double*) malloc(sizeof(double)*Nechoes);
106 fcp = (double*) malloc(sizeof(double)*Nechoes);
107 // -----
108
109 // -----
110 my::complex<double> dummy1, dummy2, dummy3, dummy4, dummy5;
111 my::complex<double> oneOverSp;
112
113 oneOverSp.re = Sp.re / (Sp.re*Sp.re + Sp.im*Sp.im);
114 oneOverSp.im = -1*Sp.im / (Sp.re*Sp.re + Sp.im*Sp.im);
115
116 dummy3.re = sechah2/kp * oneOverSp.re * 0.25;
117 dummy3.im = sechah2/kp * oneOverSp.im * 0.25;
118 // -----
119
120 // -----
121 // W factors
122 double Wmmfac = k1*(-2*k2+Sm) - km*cosa*(k1-Sm+km*cosa);
123 double Wmpfac = k1*(2*k2+Sm) + km*cosa*(k1+Sm+km*cosa);
124
125 my::complex<double> Wppfac, Wpmfac;
126 Wppfac.re = k1*(-2*k2+Sp.re)+kp*cosa*(k1+Sp.re+kp*cosa);
127 Wppfac.im = k1*(Sp.im)+kp*cosa*(Sp.im);
128
129 Wpmfac.re = k1*(2*k2+Sp.re) - kp*cosa*(k1-Sp.re+kp*cosa);
130 Wpmfac.im = k1*(Sp.im) - kp*cosa*(-Sp.im);
131 // -----
132
133 // -----
134 // COMPUTE ZETA CP/CPMG
135 // -----
136 int i;
137 for (i=0; i<Nechoes; i++)
138 {
139 // CPMG sequence, just one line because everything is real
140 zetacpmg[i+3] = sechah2/km/Sm*0.25 * (-2*k2*k2acc*Sm + Wmmfac*Wmmacc + Wmpfac*Wmpacc);
```



```

141 //      zetacpmg[i+3] = sech2/km*0.25 * (-2*k2*k2acc*Sm + Wmmfac*Wmmacc + Wmpfac*←
      Wmpacc);
142
143 // CP sequence, here we deal with complex values
144 dummy4 = complexAdd(complexMult<double>(Wppfac,Wppacc),complexMult<double>(Wmpfac,←
      Wmpacc));
145 dummy4.re += 2*k2*k2acc*Sp.re;
146 dummy4.im += 2*k2*k2acc*Sp.im;
147
148 dummy5 = complexMult<double>(dummy3,dummy4);
149
150 zetacp[i+3] = dummy5.re;
151
152 // Accumulators
153 twom2acc*=0.5;
154 twoacc*=2.0;
155
156 Wmmacc*=Wmm;
157 Wmpacc*=Wmp;
158 Wmpacc = complexMult<double>(Wmpacc, Wpm);
159 Wppacc = complexMult<double>(Wppacc, Wpp);
160
161 k2acc*=k2;
162 k2macc*= -k2;
163 }
164
165 // -----
166 // COMPUTE GAMMA CP/CPMG
167 // -----
168 for (i=0; i < Nechoes; i++)
169 {
170 gammacpmg[i]=(zetacpmg[i+3] + (k2-kp*cosa)*zetacpmg[i+2] + k2*(k1-kp*cosa)*zetacpmg[i←
      +1] + k1*k22*zetacpmg[i]);
171
172 gammacp[i]=(zetacp[i+3] - (k2+km*cosa)*zetacp[i+2] - k2*(k1-km*cosa)*zetacp[i+1] + k1←
      *k22*zetacp[i]);
173 }
174
175 // -----
176 // COMPUTE F CP/CPMG
177 // -----
178 int j;
179 double sf=0;
180
181 fcpmg[0] = sqrt(gammacpmg[0]);
182 fcpmg[1] = gammacpmg[1]/(2*fcpmg[0]);
183
184 fcp[0] = sqrt(gammacp[0]);
185 fcp[1] = gammacp[1]/(2*fcp[0]);
186
187 for (i=2; i < Nechoes; i++)
188 {
189 sf = 0;

```

#### 4 A time-domain MSE equation

```
190 for (j=1;j<=(i-1);j++)
191 {
192 sf+=fcpmg[j]*fcpmg[i-j];
193 }
194 fcpmg[i] = (gamma_cpmg[i] - sf)/(2*fcpmg[0]);
195
196 sf = 0;
197 for (j=1;j<=(i-1);j++)
198 {
199 sf+=fcp[j]*fcp[i-j];
200 }
201 fcp[i] = (gamma_cp[i] - sf)/(2*fcp[0]);
202 }
203 fcpmg[0]*=2;
204 fcp[0]*=2;
205
206 double cphi = cos(phi)*sin(thetae);
207 double sphi = sin(phi)*sin(thetae);
208
209 //-----
210 // fill output arrays
211 for (i=0; i < Nechoes; i++)
212 {
213 fcpmg[i]*= 0.5*M0*cos(phi_e-phi);
214 fcp[i]*= 0.5*M0*sin(phi_e-phi);
215
216 outr[i] += (cphi*fcpmg[i]-sphi*fcp[i]);
217 outi[i] += (cphi*fcp[i]+sphi*fcpmg[i]);
218 }
219
220 // free dynamic memory
221 free(zetacpmg);
222 free(gamma_cpmg);
223 free(fcpmg);
224
225 free(zetacp);
226 free(gamma_cp);
227 free(fcp);
228
229 }
230
231 template <typename T>
232 inline my::complex<T> complexMult(my::complex<T> u, my::complex<T> v)
233 {
234 my::complex<T> dummy;
235 dummy.re = u.re*v.re - u.im*v.im;
236 dummy.im = u.re*v.im + u.im*v.re;
237 return dummy;
238 }
239
240 template <typename T>
241 inline my::complex<T> complexAdd(my::complex<T> u, my::complex<T> v)
242 {
```

```
243 my::complex<T> dummy;
244 dummy.re = u.re + v.re;
245 dummy.im = u.im + v.im;
246 return dummy;
247 }
248
249 // explicit template instantiation
250 template void getEchoTrain<float>(float M0, float T1, float T2, float tau, float ↵
    alpha, float theta, float phi, float phie, float thetai, int Nechoes, float *↵
    outr, float* outi);
251 template void getEchoTrain<double>(double M0, double T1, double T2, double tau, ↵
    double alpha, double theta, double phi, double phie, double thetai, int Nechoes,↵
    double *outr, double* outi);
```



# 5

## Combined $T_1$ and $T_2$ -fitting using a modified MSE sequence (MOMSE)

*This chapter is adapted from "Simultaneous  $T_1$  and  $T_2$  mapping using a modified multi-echo spin-echo sequence (MOMSE)" [147].*

### 5.1 Introduction

Quantitative MRI techniques are usually very time-consuming, e.g. CPMG for  $T_2$  or turbo inversion recovery (TIR) for  $T_1$ -measurements. Therefore, the development of multi-parametric qMRI techniques (e.g. MR fingerprinting and model-based reconstruction) has gained more and more interest. Simultaneous quantification of proton density and both relaxation times already offers great advantage. As shown in chapters 3 and 4 imperfect  $B_{1+}$ -fields and slice-selective refocusing pulses lead to longitudinal magnetization components and stimulated echoes that alter the mono-exponential signal decay. On the one hand, this poses a problem for accurate  $T_2$ -quantification, on the other hand, one can think of utilizing this artifact and make it a feature. During the CPMG echo-train with refocusing pulses  $< 180^\circ$ , longitudinal magnetization is building up again by  $T_1$ -relaxation and can be used for  $T_1$ -estimation.

The CPMG decay itself is already dependent on  $T_1$  (" $T_1$ -mixing") but the effect is

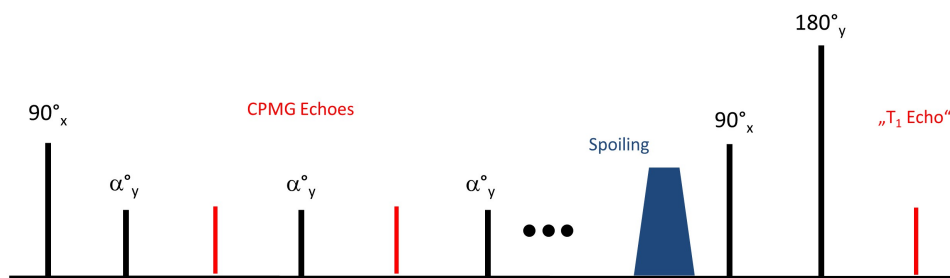


Figure 5.1: RF sequence diagram for the MOMSE sequence.

## 5 Combined $T_1$ and $T_2$ -fitting using a modified MSE sequence (MOMSE)

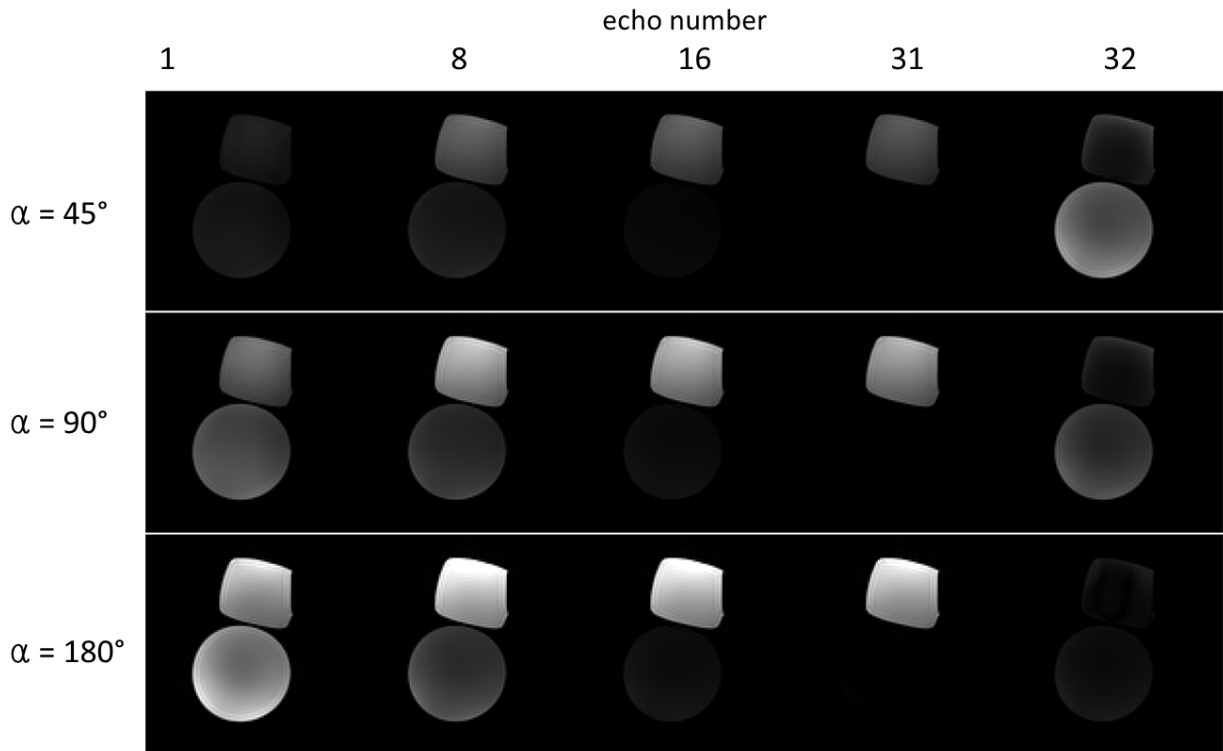


Figure 5.2: Examples of a round phantom with  $T_1 = 103$  ms  $T_2 = 81$  ms, and a square phantom  $T_1 = 3000$  ms  $T_2 = 2500$  ms, images not scaled to a fixed scale. Echo 32 is the  $T_1$ -weighted echo.

small ( $T_1 \gg \tau$ ) and the sensitivity is not large enough to directly fit  $T_1$  from MSE data (see section 3.3). However, the basic idea of this method is to deliberately lower the refocusing angle and acquire a long echo train such that a substantial amount of  $M_z$  is recovering during the CPMG train. That very magnetization can be used to create an additional  $T_1$ -weighted echo at the end. After the last CPMG echo the transverse magnetization is spoiled, whereas  $M_z$  stays untouched by the spoilers and is read out by a  $90^\circ$ - $180^\circ$  spin-echo block. The sequence diagram for the RF pulses is shown in figure 5.1.

The evolution of  $M_z$  is not a purely mono-exponential function as in an IR experiment but can be described by a Generating Function, analogously to  $F_0(z)$ . Section 5.2 is devoted to outlining the derivation of the longitudinal GF  $L_0(z)$ . The following sections show the applicability of the developed method by comparing measured and simulated data, and multi-parametric fitting results. In appendix 5.A, a time-domain solution to  $L_0(z)$  is derived.

Fig 5.2 shows images measured with the proposed sequence (excitation angle  $90^\circ$ , refocusing angle  $45^\circ$ ,  $90^\circ$ ,  $180^\circ$ ). From left to right, different echo times are shown,

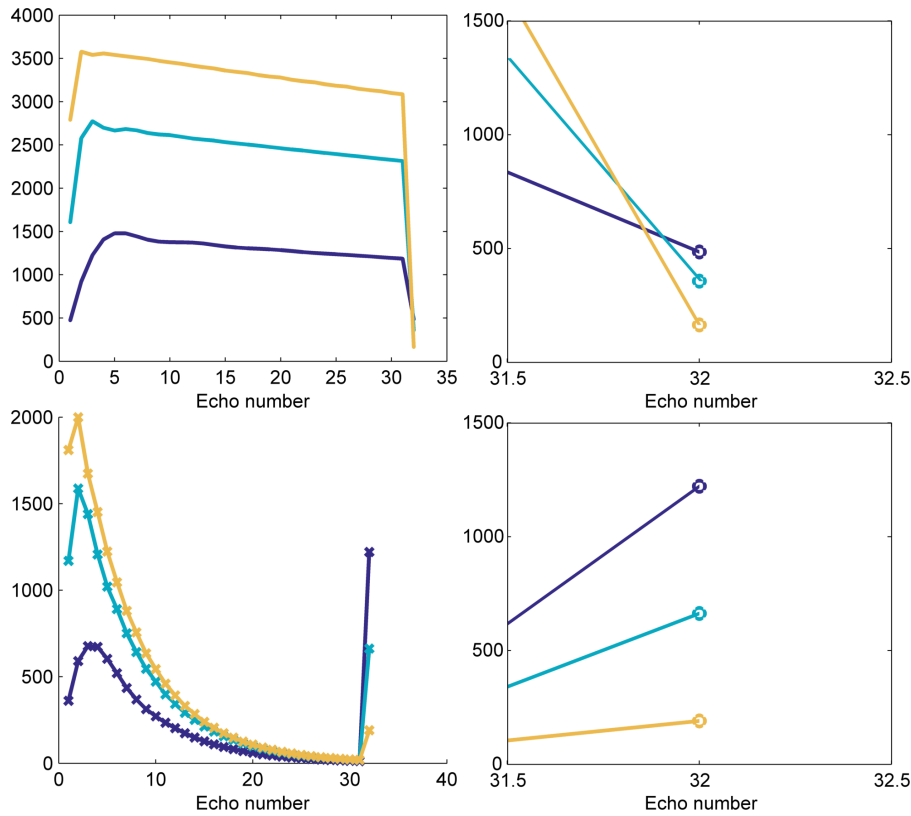


Figure 5.3: Bottom row: round tap water phantom  $T_1 = 103$  ms  $T_2 = 81$  ms. Top row: square Gd-doped phantom  $T_1 = 3000$  ms  $T_2 = 2500$  ms. Sequence parameters: excitation angle  $\theta_e = 90^\circ$ , refocusing angle  $\alpha = [45^\circ, 90^\circ, 180^\circ]$ ,  $\tau = 13.2$  ms,  $TR=3000$  ms, 32 echoes. On the right side a close-up view of the last echo is displayed.

whereas on the far right the "T<sub>1</sub>-echo" is displayed which has a fundamentally different contrast, namely T<sub>1</sub>-weighting. The square phantom is filled with tap water and has therefore long T<sub>1</sub>, and T<sub>2</sub>-times and exhibits bright signal in the T<sub>2</sub>-weighted MSE echoes, whereas rather low signal intensity in the T<sub>1</sub>-weighted image, as expected. Looking at the last column from bottom to top, it is obvious that the signal intensity increases. This is due to the lower refocusing flip angle, which allows more magnetization to recover, or, put differently, more excited magnetization is brought back to the longitudinal direction during the sequence because of incomplete refocusing. The round phantom is doped with gadolinium and one can observe a quite opposite behavior. The signal is quickly decaying during the MSE part, but the last echo exhibits a clearly perceptible signal, especially for the lower refocusing angles.

In fig 5.3, all acquired echoes are shown, in the top row for the water phantom, in the bottom row for the Gd-doped phantom. One can easily observe the fundamentally different evolution curves caused by the different relaxation times. The close up view

## 5 Combined $T_1$ and $T_2$ -fitting using a modified MSE sequence (MOMSE)

of the last echo shall visualize the difference in signal intensity that is achievable (right side). However, one must not overlook that the lower the refocusing angle, the lower the overall signal intensity one can observe.

Combining both Generating functions for  $T_1$  and  $T_2$  and non-linear parameter estimation enables simultaneous quantification of  $T_1$  and  $T_2$ .

## 5.2 Theory

The formula for the time evolution of the longitudinal magnetization can be computed analogously as in section 4.1.2 for the transverse magnetization. To this end, one has to analyze the rational function  $L(z)$  contained in  $\vec{f}(z) = \mathcal{Z}(\vec{M}[n]) = [F(z), F^*(z), L(z)]^T$ .  $L(z)$  has quite a similar form as  $F(z)$  and can be expressed as polynomials in  $U$  in the numerator and in the denominator, respectively.

$$L(z) = \frac{m_0 + m_1U + m_2U^2 + m_3U^3 + m_4U^4}{n_0 + n_1U^2 + n_2U^4} \quad (5.1)$$

with coefficients

$$m_0 = \frac{1}{4} e^{i\phi} \kappa_2 z (M_z(1-z) + M_0 z(1-\kappa_1)) \left( \cos \theta \sin \frac{\alpha}{2} - i \cos \frac{\alpha}{2} \right)^2, \quad (5.2)$$

$$m_1 = \frac{1}{4} \sqrt{\kappa_1} \sqrt{\kappa_2} (1-z) z \left( e^{2i\phi} M_+^* + \kappa_2 M_+ z \right) \sin \frac{\alpha}{2} \sin \theta \left( \cos \theta \sin \frac{\alpha}{2} - i \cos \frac{\alpha}{2} \right), \quad (5.3)$$

$$m_2 = \frac{1}{4} e^{i\phi} \left( (M_z(1-z) + M_0 z(1-\kappa_1)) (1 + \kappa_2^2 z^2) - 4z \left( -\kappa_1 M_0 + \kappa_2^2 z (M_z(1-z) + M_0 z) + \sqrt{\kappa_1} M_0 (1 - \kappa_2^2 z^2) \right) \right) \sin^2 \frac{\alpha}{2} \sin^2 \theta, \quad (5.4)$$

$$m_3 = \frac{1}{4} \sqrt{\kappa_1} \sqrt{\kappa_2} (1-z) z \left( M_+ + e^{2i\phi} \kappa_2 M_+^* z \right) \sin \frac{\alpha}{2} \sin \theta \left( \cos \theta \sin \frac{\alpha}{2} + i \cos \frac{\alpha}{2} \right), \quad (5.5)$$

$$m_4 = \frac{1}{4} e^{i\phi} \kappa_2 z (M_z(1-z) + M_0 z(1-\kappa_1)) \left( \cos \theta \sin \frac{\alpha}{2} + i \cos \frac{\alpha}{2} \right)^2 \quad (5.6)$$

$$n_0 = \frac{1}{4} e^{i\phi} z \kappa_2 (1-z)(1-\kappa_1 z) \left( \cos \theta \sin \frac{\alpha}{2} - i \cos \frac{\alpha}{2} \right)^2, \quad (5.7)$$

$$n_1 = \frac{1}{4} e^{i\phi} (1-z) \left( (1-\kappa_1 z)(1+\kappa_2^2 z^2) + 2z(\kappa_1 - \kappa_2^2 z) \sin^2 \frac{\alpha}{2} \sin^2 \theta \right), \quad (5.8)$$

$$n_2 = \frac{1}{4} e^{i\phi} z \kappa_2 (1-z)(1-\kappa_1 z) \left( \cos \theta \sin \frac{\alpha}{2} + i \cos \frac{\alpha}{2} \right)^2. \quad (5.9)$$

Again, the poles of  $L(z)$  have to be computed and the residue theorem is used to integrate  $L(z)/U$  around the unit circle to average over the individual isochromates. The poles have the exact same form as for  $F(z)$  except that they are functions of  $n_i$



instead of  $d_i$ :

$$U_0 = 0, \quad (5.10)$$

$$U_{1,2,3,4} = \frac{\pm \sqrt{-\frac{n_1 \mp \sqrt{n_1^2 - 4n_0 n_2}}{n_2 \pm}}}{\sqrt{2}}. \quad (5.11)$$

Computing the sum of the residues of  $L(z, U)/U$  yields the desired GF  $L_0(z)$ :

$$L_0(z) = \text{Res} \left( \frac{L(z, U)}{U}, 0 \right) + \text{Res} \left( \frac{L(z, U)}{U}, U_3 \right) + \text{Res} \left( \frac{L(z, U)}{U}, U_4 \right) \quad (5.12)$$

Upon plugging in the coefficients and simplification (best done with programs like Mathematica), one arrives at the following expression for  $L_0(z)$ .

$$L_0(z) = \frac{M_0}{1-z} - \frac{M_0 - M_z}{1 - \kappa_1 z} + \frac{C(z)}{(1-z)(1 - \kappa_1 z)} \frac{1}{\sqrt{X_+(z)X_-(z)}} \quad (5.13)$$

$$C(z) = \sqrt{\kappa_1} z (1 - \kappa_2^2 z^2) [M_z \sqrt{\kappa_1} (1-z) + M_0 (1 - \sqrt{\kappa_1}) (1 + \sqrt{\kappa_1} z) (1 - \cos \alpha_e)] \quad (5.14)$$

$$X_+(z) = (1 + z\kappa_2)(1 - z \cos \alpha_e (\kappa_1 + \kappa_2) + z^2 \kappa_1 \kappa_2) \quad (5.15)$$

$$X_-(z) = (1 - z\kappa_2)(1 - z \cos \alpha_e (\kappa_1 - \kappa_2) - z^2 \kappa_1 \kappa_2) \quad (5.16)$$

$$\cos \alpha_e = \cos \alpha \sin^2 \theta + \cos^2 \theta \quad (5.17)$$

What becomes apparent first is the appearance of the functions  $X_+(z)$  and  $X_-(z)$ , and the effective flip angle  $\cos \alpha_e$  that are already contained in  $F_0(z)$ . Next, we find the first two terms modeling solely longitudinal relaxation and a factor  $C(z)$  containing relaxation and refocusing parameters. At a closer look, one also notices that all phase parameters have vanished, which makes sense as there is no phase for longitudinal magnetization. Explicitly,  $\phi$  and all occurrences of the transverse magnetization component  $M_+ = M_0 e^{i\phi_e} \sin \theta_e$  (containing  $\phi_e$  in polar coordinates) are now missing. Expressing the initially excited magnetization in polar coordinates,  $M_z = M_0 \cos \theta_e$ , yields:

$$L_0(z) = \frac{M_0}{(1-z)(1 - \kappa_1 z)} \left( z - \kappa_1 z + (1-z) \cos \theta_e + \frac{\tilde{C}(z)}{\sqrt{X_+ X_-}} \right) \quad (5.18)$$

$$\tilde{C}(z) = \sqrt{\kappa_1} z (1 - \kappa_2^2 z^2) (1 - \cos \alpha_e) [(1 - \sqrt{\kappa_1})(1 + \sqrt{\kappa_1} z) + \sqrt{\kappa_1} (1-z) \cos \theta_e] \quad (5.19)$$

Just like for  $F_0(z)$ , also for  $L_0(z)$ , a time-domain expression can be derived. In appendix 5.A, the detailed calculations starting from equation 5.18 are presented. The resulting

## 5 Combined $T_1$ and $T_2$ -fitting using a modified MSE sequence (MOMSE)

signal equation,  $M_z[n]$ , takes the form of

$$M_z[n] = I[n] = M_0 \{ (1 - (1 - \cos \theta_e) \kappa_1^n) + w[n] * \zeta_{\parallel}[n] * g_{\perp}[n] \}. \quad (5.20)$$

One can readily see, the two main components of  $I[n]$ , namely a pure longitudinal relaxation part plus a second more complicated part accounting for flipping of the magnetization due to the refocusing pulses. For  $\alpha_e = 0^\circ$ , i.e. no refocusing at all, the equation reduces to  $M_0(1 - (1 - \cos \theta_e) \kappa_1)$  and specifically for an "excitation" of  $90^\circ$  or  $180^\circ$ , it yields the well-known saturation and inversion recovery curves  $M_0(1 - \kappa_1^n)$  and  $M_0(1 - 2\kappa_1^n)$ , respectively.

The part  $w[n] * \zeta_{\perp}[n] * g_{\perp}[n]$  is not that easy to interpret. It is a convolution sum of a new function  $w[n]$  with two functions  $\zeta_{\parallel}[n]$  and  $g_{\perp}[n]$  found previously in the computation of the CPMG signal. More precisely,  $g_{\perp}[n]$  is (almost) the CPMG signal itself (the only difference is lacking a Dirac delta function,  $\delta[n]$ ). This is rather advantageous numerically when  $M_z[n]$  is implemented in conjunction with  $M_+[n]$  as it saves computational cost.

**Complete formula for the longitudinal magnetization in the time domain** The computation of the convolution sum can be expressed by a double sum:

$$I[n] = M_0(1 - (1 - \cos \beta) \kappa_1^n) + \sum_{q=0}^Q w[q] \sum_{m=0}^M \zeta_{\parallel}[m] g_{\perp}[n - q - m] \quad (5.21)$$

### 5.2.1 Numerical computation

The longitudinal signal evolution can be calculated using the Generating function  $L_0(z)$ , which provides a closed form solution in the  $z$ -domain. The signal in the time domain can then be computed thereof by evaluating the  $L_0(z)$  for  $z = e^{i\varphi_k}$  around the unit circle in the complex plane and subsequent inverse DFT. A clear difference to the evaluation of  $F_0(z)$  is that for  $L_0(z)$ , appropriate apodization, i.e. computing  $L_0(az)$ , is necessary in any case. This is due to the fact, that it contains the factor  $1/(1 - z)$  in two of its terms creating a pole at  $z = 1$ . This is not surprising since the longitudinal magnetization is approaching a non-zero steady state. The Fourier sum therefore does not converge and the DFT does not exist. Evaluating  $L_0(az)$  creates a time-domain signal that is multiplied by a decaying exponential  $a^n$  that certainly has to be undone by multiplying the result with  $a^{-n}$ . The magnitude of  $a$  depends on the number of evaluated points. It can usually be found by trying out a range of values close to one were  $L_0(z)$  stays

stable, and picking one value in this stable range. If  $|a|$  is too small and  $a^n$  approaches 0 too quickly, it kills the signal and apodization cannot be undone as it would mean a division by zero.

If, like in the proposed method,  $M_z[n]$  is only desired at the very last position in the echo train, not all of the inverse DFT has to be computed.  $M_z[N]$  can be found by computing the scalar product  $[L_0, L_1, \dots, L_K] \cdot [1, e^{\frac{2\pi i N}{K}}, \dots, e^{2\pi i N}]^T$ . Another alternative, lacking the apodization problem, is using the time-domain formula  $l[n]$ . However, the computational effort for the double convolution is for the  $N^{\text{th}}$  echo  $N^2/2$ .

The so obtained value  $M_z[n]$  is not yet the magnetization that is measured in the proposed sequence since another spin-echo has to be produced using 2 RF pulses. During the spoiling period  $\tau_s$  prior to the spin-echo sequence,  $M_z$  is experiencing further longitudinal relaxation,

$$\hat{M}_z[N] = M_z[N]e^{-\frac{\tau_s}{T_1}} + M_0 \left(1 - e^{-\frac{\tau_s}{T_1}}\right). \quad (5.22)$$

$\hat{M}_z[N]$  is the magnetization right before the first spin-echo pulse. The transverse magnetization that is ultimately being measurable [3] is

$$M_+[N_{SE}] = \left[ M_z[N]e^{-\frac{\tau_s}{T_1}} + M_0 \left(1 - e^{-\frac{\tau_s}{T_1}}\right) \right] \sin \beta_e \sin^2 \frac{\beta_r}{2} e^{-\frac{TE}{T_2}}, \quad (5.23)$$

where  $TE$  is the echo time and  $\beta_e$  and  $\beta_r$  are the excitation and refocusing pulse angle, respectively. In slice-selective sequences, clearly, also the slice-profiles of these two pulses have to be considered in the calculations.

## 5.3 Methods

### 5.3.1 MR data acquisition

For data acquisition, the vendor-provided MSE (CPMG) sequence was extended to collect an additional "T<sub>1</sub>-echo" after the CPMG echo train (fig. 5.1). Basically, the modification consists of a strong spoiling block followed by a traditional spin-echo. Data were acquired on a 3T Skyra (Siemens) using an echo-spacing of  $\tau = 13$  ms, TR=5000 ms, 32 echos,  $2 \times 2 \times 4$  mm<sup>3</sup> voxel size. Excitation flip angles  $\theta_e$  and  $\beta_e$  where both 90°, whereas the refocusing angle was either 90° or 45° for different experiments. Refocusing angle for the last spin echo was  $\beta_r = 180^\circ$ .

Reference values were obtained using a MSE sequence with a GF fit with TR=4000 ms,  $\tau = 15$  ms, 32 echoes, and, for T<sub>1</sub>-mapping, a turbo inversion recovery (TIR) sequence with TR=12 s, TE=9.6 ms, and 6 different inversion times TI=[50, 200, 600, 1000, 2000,

## 5 Combined $T_1$ and $T_2$ -fitting using a modified MSE sequence (MOMSE)

4000] ms.

### 5.3.2 Phantom measurements

First, a large gadolinium-doped water phantom was measured to assess the performance of the method with respect to the slice profile of the pulses used. For this purpose, the direction of the sequence's phase-encoding gradients were changed to the z-direction (slice direction) to resolve the slice profile. Measured data was then compared to simulated data.

**Multi-parametric fitting.**  $M_0$ ,  $T_1$ , and  $T_2$  were fitted for 6 phantoms (Water, Agarose, Gadolinium doped) and compared to reference values acquired with a MSE and a TIR sequence.

## 5.4 Results

Figure 5.4 displays a comparison of measured and simulated data of the time evolution of a slice profile in a  $90^\circ$  (left side) and a  $45^\circ$  (right side) MOMSE acquisition. The simulations were in excellent agreement with the measured data, especially for the "regular" echoes. One can see that initially the  $90^\circ$  acquisition has more signal and decays until the 32<sup>st</sup> echo. For the  $45^\circ$  acquisition signal is quite low already in the beginning, slightly increases for echo 5 and then decays. However, this acquisition exhibits a much larger signal for the  $T_1$ -echo compared to the  $90^\circ$  acquisition (left), although with a worse slice profile. In general, the measured  $T_1$ -echo profiles showed slight deviations from the measured data, probably due to a timing error. The excellent

$T_1$ (TIR)	$T_1$ ( $45^\circ$ )	<i>err</i> %	$T_1$ ( $90^\circ$ )	<i>err</i> %	$T_2$ (MSE)	$T_2$ ( $45^\circ$ )	<i>err</i> %	$T_2$ ( $90^\circ$ )	<i>err</i> %
1938	1677	-13.4	1780	-8.1	138	125	-9.4	127	-7.9
617	589	-4.5	572	-7.2	110	104	-5.4	110	0
285	233	-18.2	226	-20.7	88	84	-4.5	85	-3.4
603	687	12.0	709	15.6	39	39	0	40	2.5
975	834	-14.4	792	-18.7	373	413	10.7	413	10.7
380	391	2.8	376	-1.0	98	86	12.2	92	-6.1
1890	1550	-17.9	3195	69.0	34	39	14.7	31	-8.8

Table 5.1: Comparison of "gold standard" sequences and MOMSE. All values are in ms.

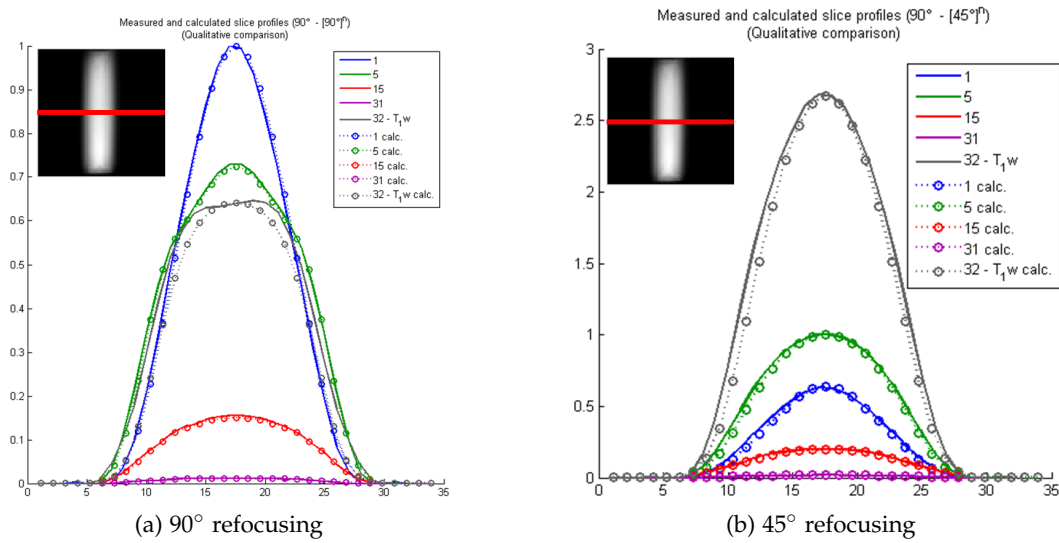


Figure 5.4: Time evolution of the slice profile using a MOMSE sequence for selected echoes. Echoes 1-31 are classical CPMG echos, echo 32 is the additional  $T_1$ -echo. Solid lines are measurements, dotted lines simulations.

data fits achieved with this method, even for the  $T_1$ -echo, are shown in figure 5.5 for 3 selected phantoms in a  $\alpha = 45^\circ$  acquisition. Table 5.1 lists the reference values and MOMSE estimates for  $T_1$  and  $T_2$  of 6 phantoms. Good agreement was found for  $T_2$  values, whereas for  $T_1$  a higher uncertainty was observed. For  $T_2$ , the  $90^\circ$  acquisitions seem to be more accurate; for  $T_1$ , the  $45^\circ$  acquisition.

## 5.5 Discussion

In this work we presented a modified MSE sequence and derived the corresponding signal model using the GF formalism. The agreement of simulated and measured data is excellent; however, from the estimated  $T_1$ -values it seems that the  $T_1$ -sensitivity is still not entirely sufficient. This suggests imaging at even lower flip angle to intensify the influence of longitudinal relaxation, given the SNR is high enough. However, a systematic investigation of the sensitivity is desired. Further, we think the presented model is very suitable for under-sampled acquisition schemes with varying TR and a model-based reconstruction. Possibly a combination of different TRs and flip angles in combination with a direct parameter map reconstruction, using an iterative optimization algorithm, could improve this method. Because of the spin-echo character of the sequence, it is robust against  $B_0$ -inhomogeneities. Furthermore, due to the lower flip angles used, the SAR is substantially reduced. This, however, comes at the price of

## 5 Combined $T_1$ and $T_2$ -fitting using a modified MSE sequence (MOMSE)

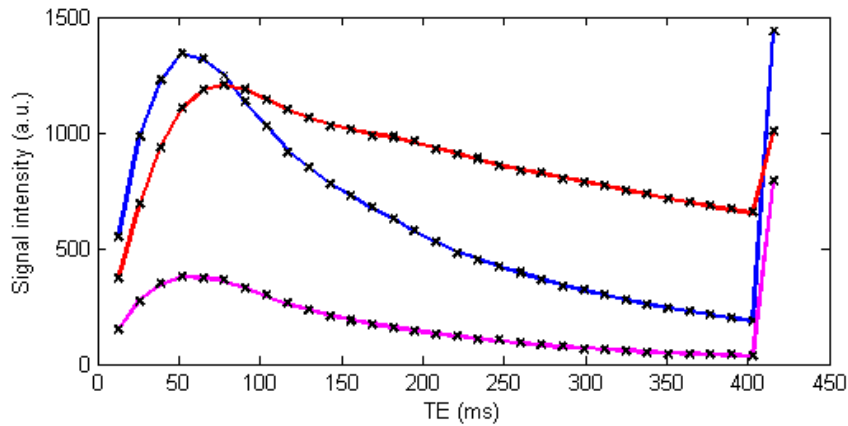


Figure 5.5: Measured signal evolution and corresponding multi-parametric fit for 3 selected phantoms acquired with refocusing angle  $\alpha = 45^\circ$

somewhat lower SNR. These features render this sequence absolutely applicable at high field scanners.

### 5.A Time domain signal equation

In order to transform  $L_0(z)$  to the time-domain it is beneficial to split the expression in additive and multiplicative parts. The first two parts that can be easily separated are

$$L_{0,1}(z) = M_0 \frac{(z - \kappa_1 z + (1 - z) \cos \theta_e)}{(1 - z)(1 - \kappa_1 z)}, \quad (5.24)$$

$$L_{0,2}(z) = M_0 \frac{\tilde{C}(z)}{(1 - z)(1 - \kappa_1 z)} \frac{1}{\sqrt{X_+ X_-}}, \quad (5.25)$$

$$(5.26)$$

whereas the first part  $L_{0,1}(z)$  again governs the pure longitudinal relaxation and the second part is sequence dependent. Inverse z-transform of  $L_{0,1}(z)$  yields

$$l_1[n] = M_0 \cdot (1 - (1 - \cos \theta_e) \kappa_1^n) \quad n \geq 0 \quad (5.27)$$

$$(5.28)$$

$L_{0,2}(z)$  is a little bit more cumbersome because of the square root term. However, the square roots contains the same polynomials  $X_+(z)$  and  $X_-(z)$ , but now in a multiplicative form. Simple rearrangement of  $1/\sqrt{X_+ X_-}$  as  $1/X_+ \cdot \sqrt{X_+/X_-}$  yields a

very tractable form consisting of 3 factors.

$$L_{0,2}(z) = M_0 W(z) \frac{1}{X_+} \sqrt{\frac{X_+}{X_-}} \quad (5.29)$$

$W(z)$  incorporates  $\tilde{C}(z)$  and some polynomial in the denominator,  $\sqrt{X_+(z)/X_-(z)}$  is the same expression as in the CPMG sequence, and  $1/X_+(z)$  transforms back to function  $\zeta_{\parallel}[n]$ , which we already encountered in the derivation of the CP sequence. Multiplicative factors in the  $z$ -domain transform to convolutions in the time domain, so that  $l_2[n]$  is given by

$$l_2[n] = M_0 \cdot w[n] * \zeta_{\perp}[n] * g_{\perp}[n] \quad (5.30)$$

As mentioned before, the expressions for  $\zeta_{\parallel}[n]$  and  $g_{\perp}[n]$  can be found in chapter 4.  $W(z)$  corresponds to the following function in the time domain:

$$w[n] = \begin{cases} 0 & n < 0 \\ (1 - \cos \alpha_e)(\sqrt{\kappa_1} - \kappa_1(1 - \cos \theta_e)) & n = 0 \\ (1 - \cos \alpha_e)(\sqrt{\kappa_1} - \kappa_1^2(1 - \cos \theta_e)) & n = 1 \\ (1 - \cos \alpha_e)(\sqrt{\kappa_1}(1 - \kappa_2^2) - \kappa_1^{n-2} \kappa_m \kappa_p (1 - \cos \theta_e)) & n > 2 \end{cases} \quad (5.31)$$

It certainly does not make sense to try to analytically calculate this convolution. In fact, it is better to compute the convolution sum numerically, especially since for most applications the transverse magnetization is desired as well and already pre-computed. Finally,  $M_z[n]$  is given by

$$\begin{aligned} M_z[n] &= l[n] = l_1[n] + l_2[n] \\ &= M_0 \cdot (1 - (1 - \cos \theta_e) \kappa_1^n) + M_0 \cdot w[n] * \zeta_{\perp}[n] * g_{\perp}[n] \end{aligned} \quad (5.32)$$





# 6

## Summary and Outlook

This thesis provides an extensive treatment of the application of the Generating functions formalism (z-transform), in order to compute accurate signal formulas for quantitative MRI. To that end, the GF formalism was thoroughly analyzed and tested for a variety of sequences, with particular focus on multi-echo spin-echo (CPMG) sequences. In the very beginning of my PhD program I was conducting my first relaxometry study, which was aimed at measuring the relaxation times  $T_1$ ,  $T_2$ , and  $T_2^*$  of human whole blood samples [80]. Not soon after acquiring the first data, I recognized the discrepancy between signal decay and the mono-exponential signal model, that is commonly used to generate  $T_2$ -maps. This problem soon caught my interest, and I started looking for solutions. Furthermore, it was the beginning of my intensive studies of relaxometry methods, the corresponding signal models, as well as their limitations, which lay the foundation of this thesis.

The aim of this thesis was to accurately model the multi-echo spin-echo signal decay, and to estimate  $T_2$ -values in vivo as accurate and precise as possible. Additionally, to enable multi-parameteric qMRI, a formula for the  $T_1$ -recovery in multi-echo sequences was sought. Furthermore, another goal was the application of the GF formalism on other pulse sequences.

To that end, I hypothesized, that is possible to use the Generating functions formalism to (1) incorporate as many relevant sequence parameters in signal modeling as possible, (2) to compute realistic signals and accurate  $T_1$  and  $T_2$ -estimates, (3) provide a ready-to-use solution that is easy to implement and not computationally costly, and (4) extend it to for multi-parametric mapping.

Relaxometry methods should be able to generate comparable measurements, used as biomarkers, and further improve MR as a diagnostic tool. These methods should be free of bias introduced by sequence or scanner, and images should be acquired in a reasonable amount of time. Relaxometry methods lose their value, if they generate inaccurate parameter values, or if data acquisition is not clinically feasible due to time constraints. Therefore, the above posed questions are of high relevance.

To test the hypothesis, different methods have been used and various experiments

have been conducted. First, formulas for the signal evolution were analytically derived by using the GF formalism and step-by-step expanded by complexity. Second, the obtained formulas were checked for plausibility by looking at limiting cases (regarding certain parameters) for which closed-form solutions are already known. Further, these formulas were used to numerically generate signal decays, which then were compared to Bloch equations, to verify their validity. To assess their applicability for parameter estimation, usually Monte Carlo simulations of the fitting process for a multitude of parameter settings were performed. Those results were analyzed regarding accuracy and precision. Next, to test the estimation performance with acquired data, experiments with various kinds of well defined homogenous MR phantoms were conducted and compared to "gold-standard" techniques (which are usually not feasible in vivo due to long scan times). Finally, the methods were also tested in vivo, and results were compared to values acquired with other techniques, as well as literature values.

The results obtained could all corroborate the hypothesis. It was possible to compute a solution for multi-echo spin-echo sequences incorporating all relevant measurement parameters. A closed-form solution could even be found in the time domain, alleviating the shortcoming of leakage effects, sometimes encountered, when the z-domain model is used directly. A significantly improved accuracy could be found in simulations, phantom, and in vivo experiments.

The formulas derived are easy to implement numerically, especially the z-domain versions. Alternative algorithms, such as Bloch simulations or the EPG algorithm, first need some effort to fully understand them, to be implemented thereafter. Time-domain solutions are bit more cumbersome, but still straight-forward to implement in scientific computing languages. A C/C++ version of the time-domain formula for  $T_2$ -fitting can be found under [www.t2mapping.rocks](http://www.t2mapping.rocks). Regarding the computational cost, the GF approach in the z-domain outperforms Bloch simulations, and performs better than the EPG for long echo trains. The computational performance for the time-domain solutions has yet to be investigated.

In the direction of multi-parametric mapping first steps could be made by deriving a closed-form solution for the longitudinal magnetization in multi-echo spin-echo experiments. This formula was successfully applied in simultaneous  $T_1$  and  $T_2$ -mapping by using a modified multi-echo sequence, and yielded  $T_1$  values with reasonable accuracy. Most of the results obtained indicate that the presented solutions incorporate all essential sequence parameters necessary to achieve good measurement accuracy. Certainly, one could try to extend these methods by considering more intrinsic processes influencing the MR signal, such as diffusion and magnetization transfer. Errors due to  $B_{1+}$ -inhomogeneities could be corrected, and, especially, effects of non-ideal slice

profiles, which exhibit by far the greatest influence on the signal, could be accounted for. The presented methods are the next step for improving qMRI by making it more robust and accurate, and allow for direct comparison of MR data.

The publications produced during my PhD studies are also dedicated to exploring the above formulated question. In [10] I investigated the applicability of the GF approach for in vivo  $T_2$ -mapping. After that, to improve fitting accuracy, I extended the equations for the excitation profile and derived a time domain solution [141]. To address multi-parametric mapping, I extended the method by formulas for the longitudinal magnetization [147]. Finally, to reduce scan time, I tried to apply my methods in model-based reconstruction [59].

There are also several limitations regarding this work. The GF formalism can only be used for repetitive pulse sequences, rendering it inapplicable for sequences with varying parameters. The more parameters included in the derivation, the more complex, and at some point intractable, the signal equations get. In this case simplifications of the model have likely to be made. Though, incorporation of diffusion and J-coupling effects, as well as magnetization transfer (by using the Bloch-McConnell equations) would be interesting. Further, the number of in vivo experiments is limited, or even missing for the modified spin-echo method. For the modified spin-echo method a systematic investigation of different parameter combinations, or even slice profiles, could be beneficial in improving  $T_1$  accuracy. Generally, more in vivo experiments throughout the whole body are needed to determine confounding factors, such as J-coupling and magnetization transfer, for different tissues. Finally, also the computational performance in relation to the EPG should be investigated further.

## 6.1 Outlook

The exact knowledge of the evolution of the magnetization due to *intrinsic* as well as *extrinsic* factors might be useful for other purposes than sole relaxation mapping. With little experimental background to date, I dare to envision a scenario where deliberately imperfect pulse sequences are used as a tool to manipulate, i.e. encode, magnetization. To put it differently, knowing how to exactly calculate the signal evolution for a given sequence parameter set, one could use RF pulses as a means of encoding, in addition to gradient encoding. For instance, in simultaneous multislice imaging the individual slices can be refocused with different flip angle and phase so as to leave a footprint that helps to separate the individual signals during reconstruction. Another possibility would be to excite a 3D slab with a systematically varying flip angle and phase. Spins at a certain position will experience a certain RF pulse, which manifests itself in an

individually shaped signal evolution. By application of several encoding cycles these systematic signal variations could be used for reconstruction.

In order not to prolong the scan time, this might be especially useful for model-based reconstruction, where only a subset of k-space is measured. As, with this method, spatial, as well, as  $T_1$  and  $T_2$  information would be encoded in the echo train in a specific manner, direct reconstruction of parameter maps from raw k-space data might be feasible by using model-based reconstruction.

Furthermore, I think that multi-parametric imaging will benefit from exact models, especially to save acquisition time, to provide reliable and comparable physical information of the tissue, and, if at all necessary, to synthetically create all desired contrast weightings from a single scan. Chapter 5 is already a step in this direction, whereas the accuracy must be significantly improved. A possible further development in this direction could also be for model-based reconstruction. For example, if another scan using a modified spin-echo sequence with a different TR is acquired,  $T_1$  accuracy could be substantially increased. Also, an interleaved approach with different TRs for every other excitation could be envisioned. Again, not to prolong scan time, an iterative model-based approach, employing the appropriate models and an elaborate variational regularization technique, could be very beneficial.

The above mentioned ideas could also easily be applied on other imaging sequences, such as steady-state free precession methods. Finally, it would be interesting to investigate if the presented methods can be extended by other intrinsic parameters, to measure them all simultaneously in one measurement.

## 6.2 Additional work

Here, I would like to give a short insight into the projects that happened besides quantitative MRI and  $T_2$ -mapping during my PhD studies. As I already pointed out, my interest in accurate and detailed modeling of relaxation curves emerged from the need to actually apply  $T_2$ -mapping in another project. This project, which was funded by the Ludwig Boltzmann Institute for Clinical Forensic Imaging (LBI-CFI), was dedicated to explore if MR relaxometry was an option to improve the unsolved problem of staging of bruises. In a forensic context, the knowledge of the age of subcutaneous bleedings is of utmost importance as it provides evidence in court. This is especially important if the victim cannot give information, like small children, or probably deliberately falsely testifies to protect him or herself.

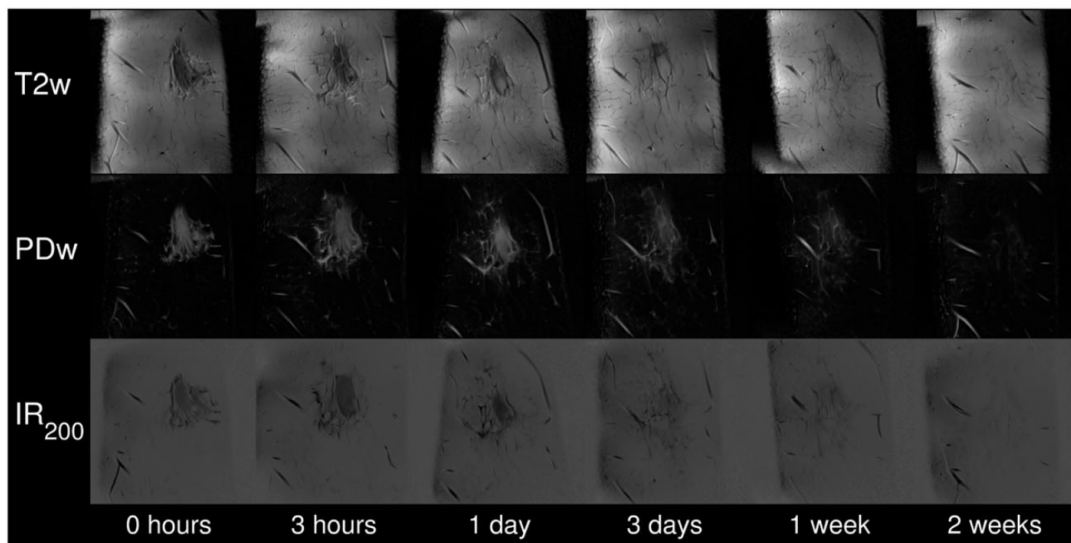


Figure 6.1: Time course of the resorption of an artificially created hematoma in-vivo. PDw with fat suppression clearly gives the best contrast [148].

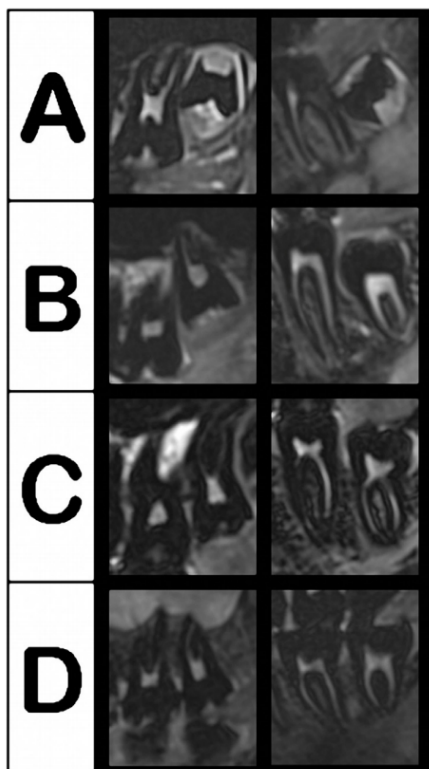


Figure 6.2: Four stages of root channel development of the third molars used in a forensic context for age estimation [149]

The results of my first study concerned with blood in MRI was an investigation of the alteration of  $T_1$  and  $T_2$  of stationary blood samples over a period of time in-vitro. The results are published in [80]. The dissatisfaction about the MSE data not really fitting to the exponential model triggered my interest in MR signal modeling.

Further, I would like to mention some other projects I carried out with my colleagues from the LBI, of which many are somehow connected to quantification using MRI. The logical continuation of the in-vitro blood study was an in-vivo study investigating the degradation of experimentally created subcutaneous hematomas published in [148, 150]. Located in the same area of forensic imaging was a study investigating the accuracy and reliability of volume estimation of bruises in the subcutaneous fatty tissue in an experimental pork-belly setup [151]. Another quite exotic topic I worked on was the depiction of the dental pulpa by MRI [149, 152]. In a forensic context, this is of relevance as the development of the root canals

## 6 Summary and Outlook

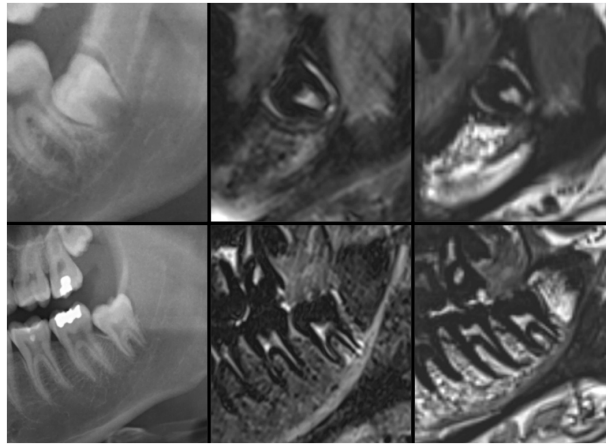


Figure 6.3: Comparison of MR images of the pulpa with an orthopantomogram ("gold standard", left column). The dental pulpa appears bright in PD-weighted TSE (middle column) and CISS (right column) sequences.

is an indicator related to the age of the subject and is used to assess asylum seekers. Another quite contrary topic, but still somehow connected to relaxation, was the development of a new class of MR contrast agents based on quadrupolar cross relaxation. The idea was submitted as an "Future and Emerging Technologies" project and funded by the EU (FET-Open, Horizon 2020). I was involved in several publications connected to the project [153–156].

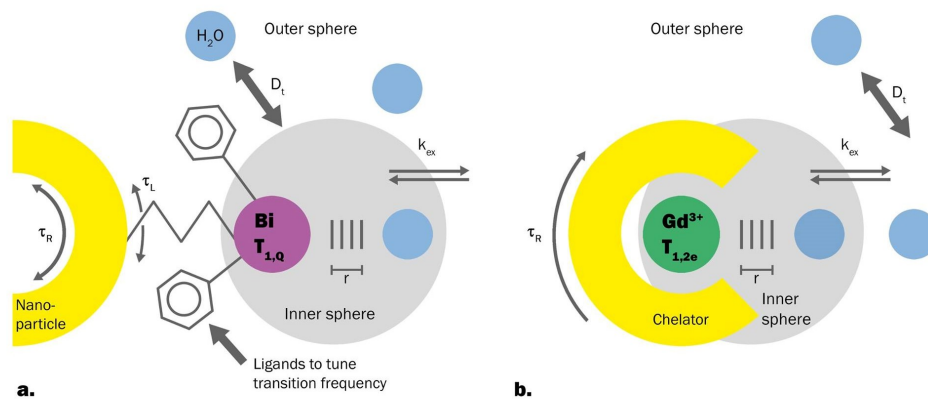


Figure 6.4: Mode of operation of the envisioned Bismuth based quadrupolar contrast agent on the left opposed to that of conventional paramagnetic contrast agents.

# Publications

## Publications directly related to this dissertation

### Peer-reviewed Papers

1. A. Petrovic, C. S. Aigner, A. Rund, R. Stollberger, **A time domain signal equation for multi-echo spin-echo sequences with arbitrary excitation and refocusing angle and phase.** *Journal of Magnetic Resonance* 309, 106515 (2019).
2. T.J. Sumpf, A. Petrovic, M. Uecker, F. Knoll, J. Frahm, **Fast T<sub>2</sub> Mapping with Improved Accuracy Using Undersampled Spin-echo MRI and Model-based Reconstructions with a Generating Function.** *IEEE Transactions on Medical Imaging* 33(12):2213-22 (2014).
3. A. Petrovic, E. Scheuer, R. Stollberger, **Closed form solution for T<sub>2</sub> mapping with non-ideal refocusing of slice selective CPMG sequences.** *Magnetic Resonance in Medicine* 73(2):818-827 (2014).

### Conference abstracts

1. A. Petrovic, R. Stollberger, **Simultaneous T<sub>1</sub> and T<sub>2</sub> mapping using a modified multi-echo spin-echo sequence (MOMSE).** *Proc. Intl. Soc. Mag. Reson. Med.* 23, Toronto, 1671 (2015).
2. A. Petrovic, E. Scheurer, K. Yen, R. Stollberger, **Improved T<sub>2</sub>-Quantification with Slice Selective MSE-Sequences.** *Proc. Intl. Soc. Mag. Reson. Med.* 19, p. 2749 (2011).
3. A. Petrovic, E. Scheurer, K. Yen, R. Stollberger, **Monte Carlo analysis of T<sub>1</sub>-mixing errors for MSE T<sub>2</sub> mapping.** *Proc. Intl. Soc. Mag. Reson. Med.* 19 p. 2760 (2011).

## Further Publications

### Patent

1. Fischer R., Kruk D., Petrovic A, Spirk S., Scharfetter H., **Novel Compounds for Use as Contrast Agents in Magnetic Resonance Imaging.** (EP 3 292 876 A1 (application filed)).

### Peer-reviewed Papers

4. D. Kruk, E. Masiewicz, E. Umut, A. Petrovic, R. Kargl, H. Scharfetter, **Estimation of the magnitude of quadrupole relaxation enhancement in the context of magnetic resonance imaging contrast.** *Journal of Chemical Physics* 150, 184306 (2019).
5. T. Widek, P. Genet, H. Merkens, J. Boldt, A. Petrovic, J. Vallis, E. Scheurer, **Dental age estimation: The chronology of mineralization and eruption of male third molars with 3T MRI.** *Forensic Science International* 297:228–235 (2019).
6. C. Gösweiner, P. Lantto, R. Fischer, C. Sampl, E. Umut, P.O. Westlund, D. Kruk, M. Bödenler, S. Spirk, A. Petrovic, H. Scharfetter, **Tuning Nuclear Quadrupole Resonance: A Novel Approach for the Design of Frequency-Selective MRI Contrast Agents.** *Physical Review X* 8(2):021076-1–20 (2018).
7. M. Bödenler, M. Basini, M.F. Casula, E. Umut, C. Gösweiner, A. Petrovic, D. Kruk, H. Scharfetter, **R<sub>1</sub> dispersion contrast at high field with fast field-cycling MRI.** *Journal of Magnetic Resonance* 290:68-75 (2018).
8. K. Ogris, A. Petrovic, S. Scheicher, H. Sprenger, M. Urschler, E. Hasler, K. Yen, E. Scheurer, **Detection and volume estimation of artificial hematomas in the subcutaneous fatty tissue: comparison of different MR sequences at 3.0 T.** *Forensic Science, Medicine, and Pathology* 13(2):135-144 (2017).
9. P. Baumann, T. Widek, H. Merkens, J. Boldt, A. Petrovic, M. Urschler, B. Kernbauer, N. Jakse, E. Scheurer, **Dental age estimation of living persons: comparison of MRI with OPG.** *Forensic Science International* 253:76-80 (2015).



10. A. Petrovic, E. Hassler, A. Krauskopf, R. Stollberger, E. Scheurer, **Time related changes of  $T_1$ ,  $T_2$ , and  $T_1^*$  of human blood in-vitro.** *Forensic Science International* accepted (2016).
11. B. Webb, A. Petrovic, E. Scheurer, **Assessment of fiducial markers to enable the co-registration of photographs and MRI data.** *Forensic Science International* 248:148-153 (2014).
12. E.M. Hassler, K. Ogris, A. Petrovic, B. Neumayer, T. Widek, K. Yen, E. Scheurer, **Contrast of artificial subcutaneous hematomas in MRI over time.** *International Journal of Legal Medicine* 129(2):317-24 (2014).
13. B. Neumayer, E. Hassler, A. Petrovic, T. Widek, K. Ogris, E. Scheurer, **Age determination of soft tissue hematomas.** *NMR in Biomedicine* 27(11):1397-1402 (2014).
14. H. Scharfetter, A. Petrovic, H. Eggenhofer, R. Stollberger, **A no-tune no-match wideband probe for nuclear quadrupole resonance spectroscopy in the VHF range.** *Measurement Science and Technology* 25(12):125501 (2014).

#### Conference abstracts

4. T. Widek, E. Hassler, A. Petrovic, B. Neumayer, K. Ogris, E. Scheurer, **Analysis of possible impact factors on the regeneration of hematomas in the subcutaneous fatty tissue.** *Proceedings of the 32nd Annual Scientific Meeting ESMRMB, Edinburgh*, 434 (2015).
5. B. Webb, A. Petrovic, T. Schwark, E. Scheurer, **Characterisation and systematic selection of MRI phantoms for implementation as novel knee-based reference standards.** *Proceedings of the 32nd Annual Scientific Meeting ESMRMB, Edinburgh*, 782 (2015).
6. A. Lesch, A. Petrovic, T.J. Sumpf, C. Aigner, R. Stollberger, **Fast and Accurate Quantification of  $T_1$ ,  $T_2$  and Proton Density Using IR BSSFP with Slice Profile Correction and Model Based Reconstruction.** *Proc. Intl. Soc. Mag. Reson. Med.* 23, Toronto, 1676 (2015).

## 6 Summary and Outlook

7. A. Lesch, A. Petrovic, R. Stollberger, **Robust Implementation of 3D Bloch Siebert B1 Mapping**. *Proc. Intl. Soc. Mag. Reson. Med. 23, Toronto*, 2381 (2015).
8. S. Grasseger, T. Ehammer, T. Widek, A. Petrovic, P. Baumann, E. Scheurer, **Native 3T MRI for skeletal age assessment of the hand and wrist: a comparison of two methods**. *Proc. Intl. Soc. Mag. Reson. Med. 23, Toronto*, 4193 (2015).
9. Webb, **Co-registration of photographs and MRI data: Evaluation and application of external fiducial markers in the forensic investigation of subcutaneous hematomas**. *ISFRI* (2015).
10. B. Webb, A. Petrovic, E. Scheurer, **Correlation of MRI and Externally Visible Findings by External Fiducial Markers**. *Proc. Intl. Soc. Mag. Reson. Med. 22, Milano*, 1574 (2014).
11. K. Ogris, E. Hassler, A. Petrovic, B. Neumayer, T. Widek, E. Scheurer, **Evaluation of Impact Factors in the Regeneration Process of Hematomas in the Subcutaneous Fatty Tissue**. *Proc. Intl. Soc. Mag. Reson. Med. 22, Milano*, 2237 (2014).
12. H. Scharfetter, A. Petrovic, R. Stollberger, **Wideband Probe for Magnetic Quadrupole Resonance Spectroscopy**. *Biomedizinische Technik* 58 (Suppl. 1) (2013).
13. B. Webb, A. Petrovic, E. Scheurer, **Correlation of Macroscopic and Histopathologic Findings with MRI in Forensic Examinations**. *Biomedizinische Technik* 58 (Suppl. 1) (2013).
14. P. Baumann, T. Widek, H. Merkens, J. Boldt, A. Petrovic, M. Urschler, B. Kirnbauer, N. Jakse, E. Scheurer, **Dental age estimation of living persons: Comparison of dental MRI with conventional orthopantomogram**. *International Congress of I.O.F.O.S., Firenze* (2013).
15. S. Grassegger, T. Ehammer, T. Widek, A. Petrovic, P. Baumann, E. Scheurer, **Comparison of two methods for the assessment of skeletal age using MRI of the hand**. *Proceedings of the 30th Annual Scientific Meeting ESMRMB*, 135 (2013).

16. J. Krusz, A. Petrovic, R. Stollberger, E. Scheurer, **Investigation of temperature dependence of tissue relaxation parameters for post-mortem imaging.** *Proc. Intl. Soc. Mag. Reson. Med 21, Salt Lake City*, p. 2469 (2013).
17. B. Neumayer, A. Petrovic, T. Widek, C. Boesch, E. Scheurer, **Reproducibility of 1H MR Spectroscopy of Human Lumbar Vertebrae at 3 Tesla.** *Proceedings of the 30th Annual Scientific Meeting ESMRMB*, 631 (2013).
18. A. Petrovic, C. Diwojky, E. Hassler, K. Ogris, E. Scheurer, **IDEAL fat-water separation for the detection and characterization of soft tissue hematomas.** *Proc. Intl. Soc. Mag. Reson. Med. 21, Salt Lake City*, p. 2420 (2013).
19. A. Petrovic, F. Schweser, A. Deistung, E. Scheurer, J.R. Reichenbach, **Longitudinal investigation of diffuse hemorrhagic lesions using using Quantitative Susceptibility Mapping (QSM).** *Proc. Intl. Soc. Mag. Reson. Med. 21, Salt Lake City*, p. 2488 (2013).
20. E. Scheurer, T. Widek, P. Baumann, A. Petrovic, H. Merkens, S. Grassegger, **Forensic age estimation of living adolescents using MRI of wisdom teeth, wrist and clavicles.** *Proc. Intl. Soc. Mag. Reson. Med. 21*, p. 1686 (2013).
21. P. Baumann, T. Widek, H. Merkens, J. Boldt, A. Petrovic, B. Krinbauer, N. Jakse, E. Scheurer, **Dental age estimation of living persons: comparison of MRI with the gold standard, the orthopantomogram.** *Proc. Intl. Soc. Mag. Reson. Med. 20*, p. 1421 (2012).
22. E. Hassler, B. Neumayer, A. Petrovic, K. Ogris, T. Widek, K. Yen, E. Scheurer, **Contrast evaluation of artificial hematomas in different MRI sequences over time.** *Proceedings of the 29th Annual Scientific Meeting ESMRMB*, 364 (2012).
23. B. Neumayer, E. Hassler, T. Widek, A. Petrovic, E. Scheurer, **Modelling of Contrast Changes in Soft Tissue Hematomas.** *Proceedings of the 29th Annual Scientific Meeting ESMRMB*, 643 (2012).

24. T. Sumpf, F. Knoll, J. Frahm, R. Stollberger, A. Petrovic, **Nonlinear inverse reconstruction for  $T_2$  mapping using the generating function formalism on undersampled Cartesian data**. *Proc. Intl. Soc. Mag. Reson. Med.* 20, p. 2398 (2012).
25. A. Petrovic, K. Ogris, E. Hassler, R. Stollberger, E. Scheurer, **Characterization of the time course of MR relaxation parameters for ageing blood**. *Proc. Intl. Soc. Mag. Reson. Med.* 20, p. 1441 (2012).
26. A. Petrovic, R. Stollberger, E. Scheurer, **Optimization of MRI sequences for the assessment of dental age**. *Proceedings of the 29th Annual Meeting ESMRMB*, 129 (2012).
27. K. Ogris, M. Urschler, A. Petrovic, K. Yen, E. Scheurer, **Artificial hematomas in subcutaneous fatty tissue: volume estimation by using different MR sequences and manual segmentation of pork belly phantoms**. *Proc. Intl. Soc. Mag. Reson. Med.* 19, p. 2581 (2011).
28. A. Petrovic, K. Ogris, E. Hassler, K. Yen, R. Stollberger, E. Scheurer, **In-vitro Blood**. *Annual Scientific Meeting of the European Society for Magnetic Resonance in Medicine and Biology*, p. 566 (2011).
29. E. Scheurer, S. Sunitsch, R. Stollberger, A. Petrovic, **Dental age estimation: evaluation of MR sequences for the imaging of tooth development**. *Rechtsmedizin* 21(4):364 (2011).
30. A. Petrovic, A. Krauskopf, R. Stollberger, K. Yen, E. Scheurer, **In vitro Studie zur Altersbestimmung von Hämatomen mittels 3T MRT**. *Rechtsmedizin* 20(4):311 (2010).
31. E. Scheurer, A. Krauskopf, R. Stollberger, A. Petrovic, K. Yen, **In vitro Detektion kleiner Blutvolumina im subkutanen Fettgewebe mittels 3T MRT**. *Rechtsmedizin* 20(4):311 (2010).
32. A. Petrovic, Y. Dong, S. Keeling, R. Stollberger, **Smoothing and Interpolation of In-Vivo B1+ Images**. *Proc. Intl. Soc. Mag. Reson. Med.* 18, p. 2844 (2010).

# List of Figures

1.1	Temperature dependence of relaxation times $T_1$ (a), $T_2$ (b), and the relaxivities $r_1$ and $r_2$ of Gadovist (c) at 3T [5]. Interestingly, $T_2$ of fat shows a remarkably strong dependence on temperature. . . . .	6
1.2	$T_1$ and $T_2$ dependence on correlation time $\tau_c$ . $T_2$ is long for short correlation times (water) and short for solid samples. $T_1$ exhibits a minimum - it is long for fast rotating molecules but also long for solid samples (reprinted from [6]). At point <b>A</b> there is rapid molecular tumbling and the fluctuating fields average to zero. At point <b>O</b> the correlation time corresponds to the Larmor frequency and transitions between energy eigenstates is very effective. Therefore, $T_1$ exhibits a minimum at this point. . . . .	6
1.3	Comparison of different methods to stabilize the MSE echo train for a nominal refocusing FA of $150^\circ$ , $T_1 = 2000$ ms, $T_2 = 100$ ms, and echo spacing $\tau = 10$ ms: (a) CPMG vs. CP - the CPMG sequence compensates for flip angle errors whereas the CP sequence accumulates the errors resulting in a severe signal loss, (b) CPMG with crushers vs. CP with crushers - due to the eliminations of all other than the primary echo pathways both sequences yield the same result, i.e. an artificially faster decay, (c) CPMG vs. CP with an $\alpha/2 - \alpha - \alpha/2$ composite refocusing pulse - the CPMG signal is perfectly refocused, the CP signal is smooth but still deviates from mono-exponential decay, (d) XY vs. YX - both schemes can only perfectly refocus every fourth echo, and (e) and (f) the MLEV-4 and MLEV-16 phase cycling schemes (with composite pulse) perfectly refocus all echoes. . . . .	11
1.4	Comparison of different methods to stabilize the MSE echo train for a nominal refocusing FA of $120^\circ$ , $T_1 = 2000$ ms, $T_2 = 100$ ms, and echo spacing $\tau = 10$ ms: (a) CPMG vs. CP - the CPMG sequence largely compensates for flip angle errors whereas the CP sequence accumulates the errors resulting in a severe signal loss, (b) CPMG with crushers vs. CP with crushers - due to the eliminations of all other than the primary echo pathways both sequences yield the same result, i.e. an artificially faster decay, also compared to fig. 1.3(b), (c) CPMG vs. CP with an $\alpha/2 - \alpha - \alpha/2$ composite refocusing pulse - both variants cannot refocus the echoes, (d) XY vs. YX - these schemes do not seem to work for FA deviation of that size, and (e) and (f) the MLEV-4 and MLEV-16 phase cycling schemes (with composite pulse) still perform quite good, at least for every other echo. . . . .	12

List of Figures

1.5 (a) is a mono-exponential fit to a standard CPMG sequence (b) a fit to a multi-echo spin-echo sequence with crushers, and (c) a fit to multiple single-echo spin-echo images. The estimated  $T_2$  values are substantially different for all approaches. In (b) also strong  $T_2$  variations can be seen which can be attributed to  $B_{1+}$  inhomogeneities. By crushing all non-essential echo pathways, a certain amount of magnetization is lost with every refocusing pulse, depending on the flip angle. This results in strong inhomogeneity and substantially shorter  $T_2$ . In contrast, in the CPMG sequence the magnetization is not crushed but stored, and eventually contributes to the echo train, whereas with a different weighting. 13

1.6  $T_1$  and  $T_2$  changes during the aging of stationary blood. In this in-vitro study we investigated the systematic changes of the relaxation times during the degradation of whole blood samples at 3T (time axis stretched due to experimental design) [80]. . . . . 18

1.7 Severe  $B_{1+}$  inhomogeneities measured on a 3T scanner (Tim Trio, Siemens) in a homogeneous water phantom with regions of nominal flip angles confined to a thin ring. A comparison between the DA and BS methods demonstrates good agreement. . . . . 20

1.8 Strong  $B_{1+}$  inhomogeneities in the upper thigh. Left: GRE Bloch-Siegert map (8kHz off-resonant,  $700^\circ$  angle). Right: Spin echo double angle map (excitation angles  $60^\circ$  and  $120^\circ$ ). In areas of two times the nominal angle the spin echo sequence fails, as the refocusing angle is doubled to  $360^\circ$ . . . . . 20

1.9 Strong  $B_{1+}$  inhomogeneities in the upper thigh. On the left a MSE and a GRE image of the same thigh are shown. On the right the cross sections are qualitatively compared. . . . . 21

1.10 Qualitative comparison of slice profiles computed using the forward SLR algorithm for  $90^\circ$  excitation and subsequent refocusing with angles from  $45^\circ$  up to  $180^\circ$ . On the top row the actual pulse shapes are shown. (Pulse shapes were taken from vendor supplied multi-echo spin-echo sequence.) . . . . . 23

1.11 Phase accumulation scheme for free diffusion:  $\Delta_i$  correspond to individual random jumps, whereas  $x_i$  denotes the position. The accumulated phase is indicated by the blue squares. . . . . 25

1.12 Phase accumulation scheme for a multi-echo spin-echo sequence:  $\Delta_i$  correspond to individual random jumps, whereas  $x_i$  denotes the position. The accumulated phase is indicated by the colored squares. The + and - signs in the leftmost column indicate the sign reversal due to refocusing pulses. This sign reversal yields to complete cancellation of parts of the accumulated phase (marked with colored boxes) leaving only the parts shaded in light red for each echo. . . . . 28

1.13 Illustration of the effect of J-coupling on a CPMG echo train. (a) Signal vs. echo number for different echo spacing ( $\Delta\delta = 40$  Hz and  $J = 6$  Hz), (b) relative echo amplitude vs. echo spacing for different J-couplings and  $\Delta\delta = 40$  Hz (reprinted from [120]). . . . . 29

2.1 Definition of the spherical coordinates used in the calculations. Vector  $\vec{B}$  is given in terms of its length  $|B|$  and the polar and azimuthal angles  $\theta$  and  $\phi$ , respectively. . . . . 39

2.2 Equivalent description of the spin dynamics under an arbitrary magnetic field  $\vec{B}$ , (a) description by the Bloch equations and (b) equivalent description with a rotation matrix  $\mathbf{R}_{\vec{u}}(\alpha)$  around an arbitrary axis  $\vec{u} = -\vec{B}/|B|$  by an angle of  $\alpha$ .  $\alpha$  is equivalent to  $\gamma|\vec{B}|\tau$  in the Bloch picture,  $\tau$  being the pulse duration. . . . . 40

2.3 Effect of an RF pulse in the EPG algorithm demonstrated on the first configuration. 47

2.4 Schematics of the EPG shift operation. (a) The state of the EPG matrix after 4 shift operations. (b) A column of zeros is appended to the end of the EPG matrix. (c) Free precession: The top row is shifted to the right, the middle row to the left (with one more zero inserted at the end). The bottom row is left unchanged by free precession. . . . . 48

2.5 Elementary building block for a SPGR sequence. . . . . 49

2.6 Transient of SPGR signals computed with the GF approach for different off-resonance angles  $\theta = \arctan(|B_{1+}|/\Delta B)$  ( $10^\circ$  to  $70^\circ$ ) and  $M_z$  preparation (left  $K = -1$ , right  $K = 1$ ). Solid lines are with flip angle  $\alpha = 20^\circ$ , dashed lines with  $\alpha = 10^\circ$ , dotted are steady state solutions. . . . . 53

2.7 Elementary building block for a Look-Locker sequence. . . . . 53

2.8 The transversal magnetization can be split in two perpendicular parts of which one experiences a CPMG sequence (here  $M_y$  as the rotation is performed around the  $y$ -axis), and one part that experiences a CP sequence. Basically, this scenario can be found when slice-selective pulses are used, since they always produce some magnetization perpendicular to the intended direction. . . . . 55

List of Figures

2.9 Effect of refocusing pulse for  $M_x$  and  $M_y$  components. (a) before, and (b) after refocusing: lets suppose the magnetization vectors rotate counter-clockwise. For  $M_x$  the yellow shaded part is rotating faster than the blue part, and after refocusing the phase state of the yellow and blue spins is inverted, and the yellow part will eventually "catch up" with the blue for all isochromates to refocus at time  $\tau$ . Note that after refocusing, the sign of  $M_x$  is reversed. For  $M_y$ , the orange part is rotating faster, then set behind the pink shaded spins by the refocusing pulse, so that they will finally refocus along the  $y$ -axis without changing sign. . . . . 56

2.10 Imperfect refocusing in a CPMG sequence seen from the  $x$ - $z$ -plane: (a) all spins are coherent, (b) the spins dephase with time (blue), (c) the imperfect refocusing pulse is unable to rotate the "spin-fan" back to the  $x$ - $y$ -plane (red), (d) with time the spins refocus and dephase in the other direction since fast and slow spins have changed position (orange), (e) the second refocusing pulse, although imperfect, puts the spins back in the  $x$ - $y$ -plane (blue) and thereby compensates it's own imperfection. . . . . 57

2.11 Imperfect refocusing in a CP sequence seen from the  $x$ - $y$ -plane: (a) all spins are aligned with the  $x$ -axis and start to dephase (not seen), (b) the imperfect refocusing pulse is unable to put the "spin-fan" in the direction of the  $-x$ -axis, then the spins refocus und dephase again, (c) the second refocusing pulse is again not rotating enough and since there was a small gap to the  $y$ -axis before, there's now twice the gap to the  $x$ -axis. The error due to the imperfect pulse is thus accumulating. . . . . 57

2.12 Calculation of the steady state for the longitudinal magnetization. . . . . 58

2.13 Elementary bSSFP building block. . . . . 60

2.14 Evolution of the slice profile for an inversion recovery bSSFP sequence with alternating (left) and non-alternating phase of the RF pulse. In the alternating sequence the phase of the RF pulse is changed between  $\pi$  and  $-\pi$  for every second echo, whereas in the non-alternating version the RF phase stays the same throughout the echo train. . . . . 60

2.15 Transient MR signals acquired with balanced SSFP sequences (top: magnitude, bottom: phase). . . . . 61



3.1 Forward simulations of the signal decay starting at the equilibrium magnetization  $M_0$  as a function of different parameters. a,b: Signal decay according to two different signal models, i.e., mono-exponential decay (continuously decreasing curve) and GF model (curve characterized by an initial sharp bend,  $\alpha = 144^\circ$ , Gaussian slice profile) for different tissues. The influence of the refocusing flip angle (from  $18^\circ$  to  $180^\circ$ , ideal slice profile,  $T_1 = 1000$  ms,  $T_2 = 100$  ms) on the signal decay (c), influence of slice profiles versus mono-exponential decay (dotted curve) and ideal slice profile ( $T_1 = 1000$  ms,  $T_2 = 100$  ms,  $\alpha = 144^\circ$ ) (d). In (e) and (f), the effects of varying  $T_1$ , and  $T_2$ -values on the decay are illustrated ( $\alpha = 90^\circ$ , ideal slice profile) and compared with the mono-exponential decay (dotted curves). . . . . 68

3.2 Results of the Monte Carlo simulation. Estimated  $T_2$ -times are shown for the GF formalism (dark curves) and a mono-exponential model (bright curves), and are compared with true  $T_2$ -values (cross symbols). Shaded areas represent the range from lower to upper quartile. All results are from the two-parameter fit unless otherwise stated. Influence of varying flip angles assuming ideal slice profile (a), and Gaussian slice profile (b) using a two-parameter (with prior knowledge of  $B_{1+}$  and  $T_1$ ) and a four-parameter fit ( $B_{1+}$  and  $T_1$  both included in the fitting procedure). (c) Fitting results of  $B_{1+}$  (four-parameter fit). Influence of varying  $T_1$  (d),  $T_2$ -values (e), and SNR (f). . . . . 69

3.3 Data fitting in the z-domain. Real and imaginary part of transformed data (and) and corresponding fits (solid and dashed lines) in the z-domain. Simulation parameters were  $T_1 = 1000$  ms,  $T_2 = 150$  ms,  $\alpha = 144^\circ$ ,  $\tau = 10$  ms,  $SNR = 80$ , Gaussian profile, apodization factor 1.13. . . . . 70

3.4  $T_2$ -maps scaled in ms of manganese-doped water phantom. a:  $T_2$ -map calculated using the GF approach (a), "gold standard" mono-exponential fit to SE data (b), mono-exponential fit to MSE data (without first echo) (c), and  $B_{1+}$ -map scaled in % (d), 100% correspond to a flip angle of  $180^\circ$  e: Cross-sectional  $T_2$  and FA distributions, respectively, for the maps a–d. Note that in (e), two different quantities are plotted and thus two different scales are used. The solid lines correspond to  $T_2$ -values in ms, the dotted lines to nominal and actual FA in % (of the nominal angle). . . . . 73

List of Figures

3.5	Absolute deviations from a nominal flip angle of $180^\circ$ , scaled in degrees. a: Estimation by the GF fitting approach using a four-parameter fit, after filtering with a $15 \times 15$ kernel median filter, In areas of $180^\circ$ (zero deviation) the GF approach cannot accurately determine the flip angle. b: Estimation by $B_{1+}$ mapping (DA method). c: Difference image between the GF approach (a) and $B_{1+}$ mapping (b). . . . .	73
3.6	Maps of estimated $T_2$ (a,b,c, scaled in ms) and $B_{1+}$ (d) of a human brain in vivo. $T_2$ -map calculated using the GF formalism (a), calculated by mono-exponential fitting to single echo data using the method in [133] (b), and using mono-exponential fitting to MSE data (c). $B_{1+}$ map acquired with the Bloch-Siegert method, scaled in % of nominal FA. All images are median filtered with a $2 \times 2$ kernel. . . . .	74
3.7	$T_2$ -maps (a-c) and $B_{1+}$ -map (d) of a human knee joint in-vivo. (a) is the $T_2$ -map calculated with the GF formalism, (b) calculated by mono-exponential fitting to single echo data [133], and (c) by mono-exponential fitting to multi-echo data, all scaled in ms. (d) is a $B_{1+}$ acquired with the Bloch-Siegert method (scaled in % of nominal FA). All images are median filtered with a $2 \times 2$ kernel. . . . .	75
3.8	Summary of the result of an MR phantom measured with different undersampling factors. The GF approach agrees very well with the spin-echo gold standard (reprinted from [59]). . . . .	79
3.9	In vivo results of a human brain for different undersampling factors (reprinted from [59]). . . . .	80
4.1	Sequence diagram for a MESE sequence: The shaded area corresponds to the repeating sequence building blocks that stay the same from one echo to another. Phase-encoding and slice-selection gradients are omitted as they are balanced throughout the sequence. . . . .	82
4.2	Definition of coordinate system and angles for the $\vec{B}$ field used in the derivation. The same angles are used for the initial magnetization $\vec{M}[0]$ ( $\theta_e$ and $\phi_e$ ). . . . .	83
4.3	Roots and poles of $Y_\perp(z)$ in the complex plane. Poles are indicated in red, roots in orange color, respectively. The inner dashed circle corresponds to the unit circle. The outer circle was drawn at the position of the innermost pole. . . . .	88

4.4 Simulation of signal evolution for (a) excitation around x-axis, refocusing around y-axis (CPMG sequence), (b) excitation around y-axis, refocusing around x-axis (CPMG sequence), (c) excitation and refocusing around y-axis (CP sequence), (d) excitation around an axis of  $45^\circ$ , refocusing around  $-45^\circ$  (CPMG sequence with additional phase), (e) excitation around an axis of  $135^\circ$ , refocusing around x-axis (mixed CP and CPMG sequence), (f) excitation around y-axis and refocusing around an axis of  $45^\circ$  (mixed CP and CPMG sequence). . . . . 96

4.5 (a) RF waveform of excitation pulse, (b) RF waveform of refocusing pulse, (c) excitation pulse profile, (d) refocusing angle profile, (e) refocusing azimuthal angle (i.e. refocusing phase) profile, and (f) refocusing polar angle (i.e. refocusing axis) profile, all computed using forward SLR algorithm. . . . . 98

4.6 (a) Evolution of the slice profile for  $M_x$ , (b) selected  $M_x$  decay curves, (c) evolution of the slice profile for  $M_y$ , (d) selected  $M_y$  decay curves. For (b) and (d) numbers 1 correspond to the middle of the slice profile going to 4 at the edge of the profile. . . . . 99

4.7 Comparison between simulation and measurements: The top row are simulations, the bottom row the corresponding measurements. On the left hand side the signals for a CP sequence are compared, on the right hand side signals for a CPMG sequence, respectively. For each sequence type both real and imaginary part show excellent agreement between simulation and measurement. . . . . 100

4.8 Illustration of leakage effect using the DFT approach compared to the presented method for (a) blood ( $T_2 \approx 250$  ms) and (b) CSF ( $T_2 \approx 2000$  ms) for different DFT lengths. Other simulation parameters where  $M_0 = 1$  a.u.,  $T_1 = 3000$  ms,  $\tau = 8$  ms, 16 echoes. The shorter the computed DFT, the more the deviation from the actual signal decay becomes apparent. . . . . 102

5.1 RF sequence diagram for the MOMSE sequence. . . . . 111

5.2 Examples of a round phantom with  $T_1 = 103$  ms  $T_2 = 81$  ms, and a square phantom  $T_1 = 3000$  ms  $T_2 = 2500$  ms, images not scaled to a fixed scale. Echo 32 is the  $T_1$ -weighted echo. . . . . 112

5.3 Bottom row: round tap water phantom  $T_1 = 103$  ms  $T_2 = 81$  ms. Top row: square Gd-doped phantom  $T_1 = 3000$  ms  $T_2 = 2500$  ms. Sequence parameters: excitation angle  $\theta_e = 90^\circ$ , refocusing angle  $\alpha = [45^\circ, 90^\circ, 180^\circ]$ ,  $\tau = 13.2$  ms, TR=3000 ms, 32 echoes. On the right side a close-up view of the last echo is displayed. . . . . 113

5.4 Time evolution of the slice profile using a MOMSE sequence for selected echoes. Echoes 1-31 are classical CPMG echos, echo 32 is the additional  $T_1$ -echo. Solid lines are measurements, dotted lines simulations. . . . . 119

*List of Figures*

5.5	Measured signal evolution and corresponding multi-parametric fit for 3 selected phantoms acquired with refocusing angle $\alpha = 45^\circ$ . . . . .	120
6.1	Time course of the resorption of an artificially created hematoma in-vivo. PDw with fat suppression clearly gives the best contrast [148]. . . . .	127
6.2	Four stages of root channel development of the third molars used in a forensic context for age estimation [149] . . . . .	127
6.3	Comparison of MR images of the pulpa with an orthopantomogram ("gold standard", left column). The dental pulpa appears bright in PD-weighted TSE (middle column) and CISS (right column) sequences. . . . .	128
6.4	Mode of operation of the envisioned Bismuth based quadrupolar contrast agent on the left opposed to that of conventional paramagnetic contrast agents. . . .	128

# List of Tables

2.1	Time domain – z-domain correspondences . . . . .	35
2.2	Initial and steady state values for the transverse and longitudinal magnetization of a CPMG sequence computed via the z-transform. . . . .	56
2.3	Limiting cases for $F(Z)$ and $L(z)$ . . . . .	59
3.1	Comparison of original and estimated $T_2$ -values via z-domain fitting (mean $\pm$ SD)	70
3.2	Measured relaxation times for doped water phantoms and corn oil. . . . .	71
3.3	Measured $T_2$ -values for brain tissue compared to values from the literature (in ms). Additional data of the knee from one volunteer is also shown. . . . .	72
4.1	Results of the bi-exponential fitting simulations. In comparison to the ground truth median values and 25% and 75% quantiles are given for 3 different SNR values (N=200). . . . .	101
5.1	Comparison of "gold standard" sequences and MOMSE. All values are in ms.	118



# Bibliography

- [1] H.-L. M. Cheng, N. Stikov, N. R. Ghugre, and G. A. Wright, "Practical medical applications of quantitative MR relaxometry," *Journal of Magnetic Resonance Imaging*, vol. 36, no. 4, pp. 805–824, 2012. DOI: 10.1002/jmri.23718 (cit. on pp. 1, 8, 16, 17).
- [2] J. Cavanagh, N. J. Skelton, and W. J. Fairbrother, *Protein NMR Spectroscopy: Principles and Practice*, 3rd ed. Waltham, MA: Academic Press, Nov. 1, 2020, 784 pp. (cit. on pp. 2, 3, 7, 8).
- [3] E. M. Haacke, R. W. Brown, M. R. Thompson, and R. Venkatesan, *Magnetic Resonance Imaging: Physical Principles and Sequence Design*, 2nd ed. Hoboken, NJ: John Wiley & Sons, 2014 (cit. on pp. 3, 117).
- [4] M. H. Levitt, *Spin Dynamics: Basics of Nuclear Magnetic Resonance*, 2nd ed. Chichester, England ; Hoboken, NJ: John Wiley & Sons, Mar. 7, 2008, 740 pp. (cit. on pp. 4–6).
- [5] J. Krusz, A. Petrovic, R. Stollberger, and E. Scheurer, "Investigation of temperature dependence of tissue relaxation parameters for post-mortem imaging," in *Proceedings of the 21th Scientific Meeting of ISMRM*, Salt Lake City, 2013, p. 2469 (cit. on p. 6).
- [6] P. A. Boulby and F. J. Rugg-Gunn, "T<sub>2</sub>: The transverse relaxation time," in *Quantitative MRI of the Brain*, P. Tofts, Ed., John Wiley & Sons, Ltd, 2003. DOI: 10.1002/0470869526 (cit. on pp. 6, 9).
- [7] A. Abragam, *Principles of Nuclear Magnetism*, Reprint. Oxford: Oxford University Press, Oct. 27, 1983, 648 pp. (cit. on pp. 7, 8).
- [8] C. P. Slichter, *Principles of Magnetic Resonance*, 3rd ed., ser. Springer Series in Solid-State Sciences. Berlin Heidelberg: Springer-Verlag, 1990 (cit. on p. 7).
- [9] S. H. Koenig, R. D. Brown, J. F. Gibson, R. J. Ward, and T. J. Peters, "Relaxometry of ferritin solutions and the influence of the Fe<sub>3+</sub> core ions," *Magnetic Resonance in Medicine*, vol. 3, no. 5, pp. 755–767, Oct. 1986. DOI: 10.1002/mrm.1910030511 (cit. on p. 8).
- [10] A. Petrovic, E. Scheurer, and R. Stollberger, "Closed-form solution for T<sub>2</sub> mapping with nonideal refocusing of slice selective CPMG sequences," *Magnetic Resonance in Medicine*, vol. 73, no. 2, pp. 818–827, Feb. 1, 2015. DOI: 10.1002/mrm.25170 (cit. on pp. 9, 14, 63, 88, 94, 97, 101, 103, 125).

## Bibliography

- [11] S. Majumdar, S. C. Orphanoudakis, A. Gmitro, M. O'Donnell, and J. C. Gore, "Errors in the measurements of  $T_2$  using multiple-echo MRI techniques. I. effects of radiofrequency pulse imperfections.," *Magnetic Resonance in Medicine*, vol. 3, no. 3, pp. 397–417, Jun. 1986 (cit. on pp. 9, 75).
- [12] ———, "Errors in the measurements of  $T_2$  using multiple-echo MRI techniques. II. effects of static field inhomogeneity.," *Magnetic Resonance in Medicine*, vol. 3, no. 4, pp. 562–574, Aug. 1986 (cit. on p. 9).
- [13] S. Majumdar and J. C. Gore, "Effects of selective pulses on the measurement of  $T_2$  and apparent diffusion in multiecho MRI.," *Magnetic Resonance in Medicine*, vol. 4, no. 2, pp. 120–128, Feb. 1987 (cit. on pp. 9, 75).
- [14] S. Majumdar, A. Gmitro, S. C. Orphanoudakis, D. Reddy, and J. C. Gore, "An estimation and correction scheme for system imperfections in multiple-echo magnetic resonance imaging.," *Magnetic Resonance in Medicine*, vol. 4, no. 3, pp. 203–220, Mar. 1987 (cit. on pp. 9, 13).
- [15] A. P. Crawley and R. M. Henkelman, "Errors in  $T_2$  estimation using multislice multiple-echo imaging.," *Magnetic Resonance in Medicine*, vol. 4, no. 1, pp. 34–47, Jan. 1987 (cit. on pp. 9, 13).
- [16] S. T. Wong and M. S. Roos, "Effects of slice selection and diffusion on  $T_2$  measurement.," *Magnetic Resonance in Medicine*, vol. 5, no. 4, pp. 358–365, Oct. 1987 (cit. on p. 9).
- [17] J. Hennig, A. Nauerth, and H. Friedburg, "RARE imaging: A fast imaging method for clinical MR.," *Magnetic Resonance in Medicine*, vol. 3, no. 6, pp. 823–833, 1986. DOI: 10.1002/mrm.1910030602 (cit. on p. 10).
- [18] M. A. Bernstein, K. F. King, and X. J. Zhou, "RARE," in *Handbook of MRI Pulse Sequences*, Amsterdam ; Boston: Academic Press, Sep. 21, 2004 (cit. on p. 10).
- [19] J. Hennig, "Multiecho imaging sequences with low refocusing flip angles," *Journal of Magnetic Resonance*, vol. 78, pp. 397–407, 1988 (cit. on p. 10).
- [20] H. Y. Carr and E. M. Purcell, "Effects of diffusion on free precession in nuclear magnetic resonance experiments," *Physical Review*, vol. 94, no. 3, p. 630, May 1, 1954. DOI: 10.1103/PhysRev.94.630 (cit. on pp. 10, 76).
- [21] S. Meiboom and D. Gill, "Modified spin-echo method for measuring nuclear relaxation times," *Review of Scientific Instruments*, vol. 29, pp. 688–691, 1958 (cit. on p. 10).



- [22] M. H. Levitt and R. Freeman, "Compensation for pulse imperfections in NMR spin-echo experiments," *Journal of Magnetic Resonance*, vol. 43, pp. 65–80, 1981 (cit. on p. 10).
- [23] R. Freeman, S. P. Kempell, and M. H. Levitt, "Radiofrequency pulse sequences which compensate their own imperfections," *Journal of Magnetic Resonance*, vol. 38, pp. 453–479, 1980. DOI: 10.1016/j.jmr.2011.08.032 (cit. on p. 10).
- [24] A. J. Shaka, S. P. Rucker, and A. Pines, "Iterative Carr-Purcell trains," *Journal of Magnetic Resonance*, vol. 77, pp. 606–611, 1988 (cit. on p. 10).
- [25] A. A. Maudsley, "Modified Carr-Purcell-Meiboom-Gill sequence for NMR Fourier imaging applications," *Journal of Magnetic Resonance*, vol. 69, pp. 488–491, 1986 (cit. on p. 10).
- [26] J. Simbrunner and R. Stollberger, "Analysis of Carr-Purcell sequences with nonideal pulses," *Journal of Magnetic Resonance*, vol. 109, pp. 301–309, 1995 (cit. on p. 10).
- [27] Y. Zur and S. Stokar, "A phase-cycling technique for canceling spurious echoes in NMR imaging," *Journal of Magnetic Resonance*, vol. 71, pp. 212–228, 1987 (cit. on p. 10).
- [28] W. D. Foltz, J. A. Stainsby, and G. A. Wright, "T<sub>2</sub> accuracy on a whole-body imager," *Magn Reson Med*, vol. 38, no. 5, pp. 759–768, Nov. 1997 (cit. on p. 10).
- [29] C. S. Poon and R. M. Henkelman, "Practical T<sub>2</sub> quantitation for clinical applications," *Journal of Magnetic Resonance Imaging*, vol. 2, no. 5, pp. 541–553, 1992 (cit. on pp. 13, 14, 76).
- [30] J. G. Sled and G. B. Pike, "Correction for B<sub>1</sub> and B<sub>0</sub> variations in quantitative T<sub>2</sub> measurements using MRI," *Magnetic Resonance in Medicine*, vol. 43, pp. 589–593, 2000 (cit. on p. 13).
- [31] G. S. Pell, R. S. Briellmann, A. B. Waites, D. F. Abbott, D. P. Lewis, and G. D. Jackson, "Optimized clinical T<sub>2</sub> relaxometry with a standard CPMG sequence," *Journal of Magnetic Resonance Imaging*, vol. 23, no. 2, pp. 248–252, Feb. 2006. DOI: 10.1002/jmri.20490 (cit. on p. 13).
- [32] F. Mitsumori, H. Watanabe, N. Takaya, and M. Garwood, "Apparent transverse relaxation rate in human brain varies linearly with tissue iron concentration at 4.7 T," *Magnetic Resonance in Medicine*, vol. 58, no. 5, pp. 1054–1060, Nov. 2007. DOI: 10.1002/mrm.21373 (cit. on pp. 13, 17).

## Bibliography

- [33] T. J. Mosher, Y. Liu, and C. M. Torok, "Functional cartilage MRI  $T_2$  mapping: Evaluating the effect of age and training on knee cartilage response to running," *Osteoarthritis and Cartilage / OARS, Osteoarthritis Research Society*, vol. 18, no. 3, pp. 358–364, Mar. 2010. DOI: 10.1016/j.joca.2009.11.011 (cit. on p. 14).
- [34] R. M. Lebel and A. H. Wilman, "Transverse relaxometry with stimulated echo compensation," *Magnetic Resonance in Medicine*, vol. 64, no. 4, pp. 1005–1014, Jun. 2010. DOI: 10.1002/mrm.22487 (cit. on pp. 14, 72, 77).
- [35] C. Jones, Q. Xiang, K. Whittal, and A. MacKay, "Calculating  $T_2$  and  $B_1$  from decay curves collected with non- $180^\circ$  refocusing pulses," in *Proceedings of the 11th Scientific Meeting of ISMRM*, Toronto, Canada, 2003, p. 1018 (cit. on p. 14).
- [36] T. Prasloski, B. Mädler, Q.-S. Xiang, A. MacKay, and C. Jones, "Applications of stimulated echo correction to multicomponent  $T_2$  analysis," *Magnetic Resonance in Medicine*, vol. 67, no. 6, pp. 1803–1814, 2012. DOI: 10.1002/mrm.23157 (cit. on pp. 14, 30).
- [37] N. N. Lukzen and A. A. Savelov, "Analytical derivation of multiple spin echo amplitudes with arbitrary refocusing angle.," *Journal of Magnetic Resonance*, vol. 185, no. 1, pp. 71–76, Mar. 2007. DOI: 10.1016/j.jmr.2006.11.010 (cit. on pp. 14, 33, 55, 85, 86, 101).
- [38] N. N. Lukzen, M. V. Petrova, I. V. Koptuyug, A. A. Savelov, and R. Z. Sagdeev, "The generating functions formalism for the analysis of spin response to the periodic trains of RF pulses. echo sequences with arbitrary refocusing angles and resonance offsets.," *Journal of Magnetic Resonance*, vol. 196, no. 2, pp. 164–169, Feb. 2009. DOI: 10.1016/j.jmr.2008.11.008 (cit. on pp. 14, 33, 43, 49, 59, 82, 83, 85, 87, 94, 101).
- [39] N. Ben-Eliezer, D. K. Sodickson, and K. T. Block, "Rapid and accurate  $T_2$  mapping from multi-spin-echo data using bloch-simulation-based reconstruction," *Magnetic Resonance in Medicine*, vol. 73, no. 2, pp. 809–817, 2015. DOI: 10.1002/mrm.25156 (cit. on p. 14).
- [40] S. C. L. Deoni, B. K. Rutt, and T. M. Peters, "Rapid combined  $T_1$  and  $T_2$  mapping using gradient recalled acquisition in the steady state," *Magnetic Resonance in Medicine*, vol. 49, no. 3, pp. 515–526, Mar. 2003. DOI: 10.1002/mrm.10407 (cit. on p. 14).
- [41] S. C. L. Deoni, T. M. Peters, and B. K. Rutt, "High-resolution  $T_1$  and  $T_2$  mapping of the brain in a clinically acceptable time with DESPOT1 and DESPOT2," *Magnetic Resonance in Medicine*, vol. 53, no. 1, pp. 237–241, Jan. 2005. DOI: 10.1002/mrm.20314 (cit. on p. 14).

- [42] S. C. Deoni, "Transverse relaxation time ( $T_2$ ) mapping in the brain with off-resonance correction using phase-cycled steady-state free precession imaging," *Journal of Magnetic Resonance Imaging*, vol. 30, no. 2, pp. 411–417, 2009. DOI: 10.1002/jmri.21849 (cit. on pp. 14, 72, 77).
- [43] P. Schmitt, M. A. Griswold, P. M. Jakob, M. Kotas, V. Gulani, M. Flentje, and A. Haase, "Inversion recovery TrueFISP: Quantification of  $T_1$ ,  $T_2$ , and spin density," *Magnetic Resonance in Medicine*, vol. 51, no. 4, pp. 661–667, Apr. 1, 2004. DOI: 10.1002/mrm.20058 (cit. on p. 15).
- [44] P. Ehses, N. Seiberlich, D. Ma, F. A. Breuer, P. M. Jakob, M. A. Griswold, and V. Gulani, "IR TrueFISP with a golden-ratio-based radial readout: Fast quantification of  $T_1$ ,  $T_2$ , and proton density," *Magnetic Resonance in Medicine*, vol. 69, no. 1, pp. 71–81, Jan. 1, 2013. DOI: 10.1002/mrm.24225 (cit. on p. 15).
- [45] R. D. Newbould, S. T. Skare, M. T. Alley, G. E. Gold, and R. Bammer, "Three-dimensional  $T_1$ ,  $T_2$  and proton density mapping with inversion recovery balanced SSFP," *Magnetic Resonance Imaging*, vol. 28, no. 9, pp. 1374–1382, Nov. 2010. DOI: 10.1016/j.mri.2010.06.004 (cit. on p. 15).
- [46] R. Heule, C. Ganter, and O. Bieri, "Triple echo steady-state (TESS) relaxometry," *Magnetic Resonance in Medicine*, vol. 71, no. 1, pp. 230–237, Jan. 1, 2014. DOI: 10.1002/mrm.24659 (cit. on p. 15).
- [47] T.-Y. Huang, Y.-J. Liu, A. Stemmer, and B. P. Poncelet, " $T_2$  measurement of the human myocardium using a  $T_2$ -prepared transient-state trueFISP sequence," *Magnetic Resonance in Medicine*, vol. 57, no. 5, pp. 960–966, May 1, 2007. DOI: 10.1002/mrm.21208 (cit. on p. 15).
- [48] R. Deichmann, H. Adolf, U. Nöth, S. Morrissey, C. Schwarzbauer, and A. Haase, "Fast  $T_2$ -mapping with SNAPSHOT FLASH imaging," *Magnetic Resonance Imaging*, vol. 13, no. 4, pp. 633–639, Jan. 1, 1995. DOI: 10.1016/0730-725X(95)00004-Z (cit. on p. 15).
- [49] P. A. Gowland, A. Freeman, B. Issa, P. Boulby, K. R. Duncan, R. J. Moore, P. N. Baker, R. W. Bowtell, I. R. Johnson, and B. S. Worthington, "In vivo relaxation time measurements in the human placenta using echo planar imaging at 0.5 t," *Magnetic Resonance Imaging*, vol. 16, no. 3, pp. 241–247, Apr. 1, 1998. DOI: 10.1016/S0730-725X(97)00308-1 (cit. on p. 15).
- [50] X. Liu, Y. Feng, Z.-R. Lu, G. Morrell, and E.-K. Jeong, "Rapid simultaneous acquisition of  $T_1$  and  $T_2$  mapping images using multishot double spin-echo EPI and automated variations of TR and TE (ms-DSEPI-T12)," *NMR in Biomedicine*, vol. 23, no. 1, pp. 97–104, 2010. DOI: 10.1002/nbm.1440 (cit. on p. 15).

## Bibliography

- [51] D. A. Yablonskiy and E. M. Haacke, "An MRI method for measuring  $T_2$  in the presence of static and RF magnetic field inhomogeneities," *Magnetic Resonance in Medicine*, vol. 37, no. 6, pp. 872–876, 1997. DOI: 10.1002/mrm.1910370611 (cit. on p. 15).
- [52] M. Doneva, P. Börnert, H. Eggers, C. Stehning, J. Sénégas, and A. Mertins, "Compressed sensing reconstruction for magnetic resonance parameter mapping," *Magnetic Resonance in Medicine*, vol. 64, no. 4, pp. 1114–1120, Oct. 1, 2010. DOI: 10.1002/mrm.22483 (cit. on p. 15).
- [53] C. Huang, C. G. Graff, E. W. Clarkson, A. Bilgin, and M. I. Altbach, " $T_2$  mapping from highly undersampled data by reconstruction of principal component coefficient maps using compressed sensing," *Magnetic Resonance in Medicine*, vol. 67, no. 5, pp. 1355–1366, May 2012. DOI: 10.1002/mrm.23128 (cit. on p. 15).
- [54] C. Huang, A. Bilgin, T. Barr, and M. I. Altbach, " $T_2$  relaxometry with indirect echo compensation from highly undersampled data," *Magnetic Resonance in Medicine*, vol. 70, no. 4, pp. 1026–1037, Oct. 1, 2013. DOI: 10.1002/mrm.24540 (cit. on p. 15).
- [55] J. V. Velikina, A. L. Alexander, and A. Samsonov, "Accelerating MR parameter mapping using sparsity-promoting regularization in parametric dimension," *Magnetic Resonance in Medicine*, vol. 70, no. 5, pp. 1263–1273, Nov. 1, 2013. DOI: 10.1002/mrm.24577 (cit. on p. 15).
- [56] M. Uecker, T. Hohage, K. T. Block, and J. Frahm, "Image reconstruction by regularized nonlinear inversion—joint estimation of coil sensitivities and image content," *Magnetic resonance in medicine: official journal of the Society of Magnetic Resonance in Medicine / Society of Magnetic Resonance in Medicine*, vol. 60, no. 3, pp. 674–682, Sep. 2008. DOI: 10.1002/mrm.21691 (cit. on p. 15).
- [57] K. T. Block, M. Uecker, and J. Frahm, "Model-based iterative reconstruction for radial fast spin-echo MRI," *IEEE Transactions on Medical Imaging*, vol. 28, no. 11, pp. 1759–1769, Nov. 2009. DOI: 10.1109/TMI.2009.2023119 (cit. on p. 15).
- [58] T. J. Sumpf, M. Uecker, S. Boretius, and J. Frahm, "Model-based nonlinear inverse reconstruction for  $T_2$  mapping using highly undersampled spin-echo MRI," *Journal of magnetic resonance imaging: JMRI*, vol. 34, no. 2, pp. 420–428, Aug. 2011. DOI: 10.1002/jmri.22634 (cit. on pp. 15, 78).
- [59] T. J. Sumpf, A. Petrovic, M. Uecker, F. Knoll, and J. Frahm, "Fast  $T_2$  mapping with improved accuracy using undersampled spin-echo MRI and model-based reconstructions with a generating function," *IEEE Transactions on Medical Imaging*,

- vol. 33, no. 12, pp. 2213–2222, Dec. 2014. DOI: 10.1109/TMI.2014.2333370 (cit. on pp. 15, 78–80, 125).
- [60] T. Hilbert, J. Schulz, J. P. Marques, J.-P. Thiran, G. Krueger, D. G. Norris, and T. Kober, “Fast model-based  $T_2$  mapping using SAR-reduced simultaneous multislice excitation,” *Magnetic Resonance in Medicine*, vol. 0, no. 0, Jul. 4, 2019. DOI: 10.1002/mrm.27890 (cit. on p. 15).
- [61] J. Sénégas, W. Liu, H. Dahnke, H. Song, E. K. Jordan, and J. A. Frank, “Fast  $T_2$  relaxometry with an accelerated multi-echo spin-echo sequence,” *NMR in Biomedicine*, vol. 23, no. 8, pp. 958–967, Oct. 1, 2010. DOI: 10.1002/nbm.1521 (cit. on p. 15).
- [62] D. Ma, V. Gulani, N. Seiberlich, K. Liu, J. L. Sunshine, J. L. Duerk, and M. A. Griswold, “Magnetic resonance fingerprinting,” *Nature*, vol. 495, no. 7440, pp. 187–192, Mar. 14, 2013. DOI: 10.1038/nature11971 (cit. on p. 15).
- [63] I. Blystad, I. Håkansson, A. Tisell, J. Ernerudh, Ö. Smedby, P. Lundberg, and E.-M. Larsson, “Quantitative MRI for analysis of active multiple sclerosis lesions without gadolinium-based contrast agent,” *American Journal of Neuroradiology*, vol. 37, no. 1, pp. 94–100, Jan. 1, 2016. DOI: 10.3174/ajnr.A4501 (cit. on p. 16).
- [64] R.-M. Gracien, S. C. Reitz, S. M. Hof, V. Fleischer, H. Zimmermann, A. Droby, H. Steinmetz, F. Zipp, R. Deichmann, and J. C. Klein, “Changes and variability of proton density and  $T_1$  relaxation times in early multiple sclerosis: MRI markers of neuronal damage in the cerebral cortex,” *European Radiology*, vol. 26, no. 8, pp. 2578–2586, Aug. 1, 2016. DOI: 10.1007/s00330-015-4072-x (cit. on p. 16).
- [65] A. MacKay, K. Whittall, J. Adler, D. Li, D. Paty, and D. Graeb, “In vivo visualization of myelin water in brain by magnetic resonance,” *Magnetic Resonance in Medicine*, vol. 31, no. 6, pp. 673–677, Jun. 1994. DOI: 10.1002/mrm.1910310614 (cit. on p. 16).
- [66] C.-A. Julien and W.-K. Claudia, Eds., *Quantitative MRI of the Spinal Cord*, 1st ed., Academic Press, 2014 (cit. on p. 16).
- [67] S. C. Reitz, S.-M. Hof, V. Fleischer, A. Brodski, A. Gröger, R.-M. Gracien, A. Droby, H. Steinmetz, U. Ziemann, F. Zipp, R. Deichmann, and J. C. Klein, “Multi-parametric quantitative MRI of normal appearing white matter in multiple sclerosis, and the effect of disease activity on  $T_2$ ,” *Brain Imaging and Behavior*, vol. 11, no. 3, pp. 744–753, Jun. 1, 2017. DOI: 10.1007/s11682-016-9550-5 (cit. on p. 16).

## Bibliography

- [68] A. L. MacKay, I. M. Vavasour, A. Rauscher, S. H. Kolind, B. Mädler, G. R. W. Moore, A. L. Traboulsee, D. K. B. Li, and C. Laule, "MR relaxation in multiple sclerosis," *Neuroimaging Clinics of North America*, vol. 19, no. 1, pp. 1–26, Feb. 2009. doi: 10.1016/j.nic.2008.09.007 (cit. on p. 16).
- [69] S. Ropele, C. Langkammer, C. Enzinger, S. Fuchs, and F. Fazekas, "Relaxation time mapping in multiple sclerosis," *Expert Review of Neurotherapeutics*, vol. 11, no. 3, pp. 441–450, Mar. 2011. doi: 10.1586/ern.10.129 (cit. on p. 16).
- [70] I. Blystad, J. B. M. Warntjes, Ö. Smedby, P. Lundberg, E.-M. Larsson, and A. Tisell, "Quantitative MRI for analysis of peritumoral edema in malignant gliomas," *PLOS ONE*, vol. 12, no. 5, e0177135, May 23, 2017. doi: 10.1371/journal.pone.0177135 (cit. on pp. 16, 102).
- [71] S. Lescher, A. Jurcoane, A. Veit, O. Bähr, R. Deichmann, and E. Hattingen, "Quantitative T<sub>1</sub> and T<sub>2</sub> mapping in recurrent glioblastomas under bevacizumab: Earlier detection of tumor progression compared to conventional MRI," *Neuroradiology*, vol. 57, no. 1, pp. 11–20, Jan. 1, 2015. doi: 10.1007/s00234-014-1445-9 (cit. on p. 16).
- [72] L. D. DeWitt, J. P. Kistler, D. C. Miller, E. P. Richardson, and F. S. Buonanno, "NMR-neuropathologic correlation in stroke," *Stroke*, vol. 18, no. 2, pp. 342–351, Apr. 1987. doi: 10.1161/01.str.18.2.342 (cit. on p. 16).
- [73] H. Zhong, D. J. Miller, and K. L. Urish, "T<sub>2</sub> map signal variation predicts symptomatic osteoarthritis progression: Data from the osteoarthritis initiative," *Skeletal Radiology*, vol. 45, no. 7, pp. 909–913, Jul. 1, 2016. doi: 10.1007/s00256-016-2360-4 (cit. on p. 16).
- [74] G. Gambarota, A. Veltien, H. van Laarhoven, M. Philippens, A. Jonker, O. R. Mook, W. M. Frederiks, and A. Heerschap, "Measurements of T<sub>1</sub> and T<sub>2</sub> relaxation times of colon cancer metastases in rat liver at 7 T," *Magma (New York, N.Y.)*, vol. 17, no. 3, pp. 281–287, Dec. 2004. doi: 10.1007/s10334-004-0068-2 (cit. on p. 17).
- [75] A. Cieszanowski, W. Szeszkowski, M. Golebiowski, D. K. Bielecki, M. Grodzicki, and B. Pruszyński, "Discrimination of benign from malignant hepatic lesions based on their T<sub>2</sub>-relaxation times calculated from moderately T<sub>2</sub>-weighted turbo SE sequence," *European Radiology*, vol. 12, no. 9, pp. 2273–2279, Sep. 2002. doi: 10.1007/s00330-002-1366-6 (cit. on p. 17).

- [76] A. Hoang Dinh, R. Souchon, C. Melodelima, F. Bratan, F. Mège-Lechevallier, M. Colombel, and O. Rouvière, "Characterization of prostate cancer using  $T_2$  mapping at 3T: A multi-scanner study," *Diagnostic and Interventional Imaging*, vol. 96, no. 4, pp. 365–372, Apr. 1, 2015. DOI: 10.1016/j.diii.2014.11.016 (cit. on p. 17).
- [77] F. I. Yamauchi, T. Penzkofer, A. Fedorov, F. M. Fennessy, R. Chu, S. E. Maier, C. M. C. Tempany, R. V. Mulkern, and L. P. Panych, "Prostate cancer discrimination in the peripheral zone with a reduced field-of-view  $T_2$ -mapping MRI sequence," *Magnetic Resonance Imaging*, vol. 33, no. 5, pp. 525–530, Jun. 1, 2015. DOI: 10.1016/j.mri.2015.02.006 (cit. on p. 17).
- [78] L. Liu, B. Yin, K. Shek, D. Geng, Y. Lu, J. Wen, X. Kuai, and W. Peng, "Role of quantitative analysis of  $T_2$  relaxation time in differentiating benign from malignant breast lesions," *Journal of International Medical Research*, vol. 46, no. 5, pp. 1928–1935, May 1, 2018. DOI: 10.1177/0300060517721071 (cit. on p. 17).
- [79] V. Rieke and K. B. Pauly, "MR thermometry," *Journal of magnetic resonance imaging : JMRI*, vol. 27, no. 2, pp. 376–390, Feb. 2008. DOI: 10.1002/jmri.21265 (cit. on p. 17).
- [80] A. Petrovic, A. Krauskopf, E. Hassler, R. Stollberger, and E. Scheurer, "Time related changes of  $T_1$ ,  $T_2$ , and  $T_2^*$  of human blood in vitro," *Forensic Science International*, vol. 262, pp. 11–17, May 1, 2016. DOI: 10.1016/j.forsciint.2016.02.032 (cit. on pp. 17, 18, 123, 127).
- [81] K. R. Thulborn, J. C. Waterton, P. M. Matthews, and G. K. Radda, "Oxygenation dependence of the transverse relaxation time of water protons in whole blood at high field," *Biochim Biophys Acta*, vol. 714, pp. 265–270, 1982 (cit. on p. 17).
- [82] L. A. Hayman, J. J. Ford, K. H. Taber, A. Saleem, M. E. Round, and R. N. Bryan, " $T_2$  effect of hemoglobin concentration: Assessment with in vitro MR spectroscopy," *Radiology*, vol. 168, pp. 489–491, 1988 (cit. on p. 17).
- [83] R. A. Clark, A. T. Watanabe, J. William G. Bradley, and J. D. Roberts, "Acute hematomas: Effects of deoxygenation, hematocrit, and fibrin-clot formation and retraction on  $t_2$  shortening," *Radiology*, vol. 175, pp. 201–206, 1990 (cit. on p. 17).
- [84] W. M. Spees, D. A. Yablonskiy, M. C. Oswood, and J. J. H. Ackerman, "Water proton MR properties of human blood at 1.5 tesla: Magnetic susceptibility,  $T_1$ ,  $T_2$ ,  $T_2^*$ , and non-lorentzian signal behavior," *Magn Reson Med*, vol. 45, pp. 533–542, 2001 (cit. on p. 17).

## Bibliography

- [85] J. M. Zhao, C. S. Clingman, M. J. Närväinen, R. A. Kauppinen, and P. C. M. van Zijl, "Oxygenation and hematocrit dependence of transverse relaxation rates of blood at 3t.," *Magn Reson Med*, vol. 58, no. 3, pp. 592–597, Sep. 2007. DOI: 10.1002/mrm.21342 (cit. on pp. 17, 65).
- [86] P. A. Janick, D. B. Hackney, R. I. Grossman, and T. Asakura, "MR imaging of various oxidation states of intracellular and extracellular hemoglobin," *AJNR Am J Neuroradiol*, vol. 12, pp. 891–897, 1991 (cit. on p. 17).
- [87] H. Lu, C. Clingman, X. Golay, and P. C. M. van Zijl, "Determining the longitudinal relaxation time ( $T_1$ ) of blood at 3.0 tesla," *Magn Reson Med*, vol. 52, no. 3, pp. 679–682, Sep. 2004. DOI: 10.1002/mrm.20178 (cit. on pp. 17, 65).
- [88] M. J. Silvennoinen, M. I. Kettunen, and R. A. Kauppinen, "Effects of hematocrit and oxygen saturation level on blood spin-lattice relaxation," *Magnetic Resonance in Medicine*, vol. 49, pp. 568–571, 2003 (cit. on p. 17).
- [89] J. M. Gomori, R. I. Grossman, C. Yu-Ip, and T. Asakura, "NMR relaxation times of blood: Dependence on field strength, oxidation state, and cell integrity," *Journal of Computer Assisted Tomography*, vol. 11, no. 4, pp. 684–690, Aug. 1987 (cit. on p. 17).
- [90] M. D. Cohen, W. McGuire, D. A. Cory, and J. A. Smith, "MR appearance of blood and blood products: An in vitro study," *American Journal of Roentgenology*, vol. 146, pp. 1293–1297, Jun. 1986 (cit. on p. 17).
- [91] W. G. Bradley, Jr, and P. G. Schmidt, "Effect of methemoglobin formation on the MR appearance of subarachnoid hemorrhage," *Radiology*, vol. 156, pp. 99–103, 1985 (cit. on p. 17).
- [92] J. W. G. Bradley, "MR appearance of hemorrhage in the brain," *Radiology*, vol. 189, pp. 15–26, 1993 (cit. on p. 17).
- [93] P. Parizel, S. Makkat, E. V. Miert, J. V. Goethem, L. v. d. Hauwe, and A. D. Schepper, "Intracranial hemorrhage: Principles of CT and MRI interpretation," *Eur Radiol*, vol. 11, pp. 1770–1783, 2001 (cit. on p. 17).
- [94] R. Spielmann, R. Mass, C. Neumann, M. Dallek, V. Nicolas, M. Heller, and E. Bücheler, "MRT akuter Weichteilhämatome bei 1.5 T: Tierexperimentelle Ergebnisse," *Fortschr Röntgenstr*, vol. 153, no. 4, pp. 395–399, 1990 (cit. on p. 17).
- [95] J. I. Rubin, J. M. Gomori, R. I. Grossman, W. B. Gefter, and H. V. Kressel, "High-field MR imaging of extracranial hematomas," *AJR Am J Roentgenol*, vol. 148, pp. 813–817, Apr. 1987 (cit. on p. 17).



- [96] C. Langkammer, N. Krebs, W. Goessler, E. Scheurer, F. Ebner, K. Yen, F. Fazekas, and S. Ropele, "Quantitative MR imaging of brain iron: A postmortem validation study," *Radiology*, vol. 257, no. 2, pp. 455–462, Jan. 11, 2010. DOI: 10.1148/radiol.10100495 (cit. on pp. 17, 72, 77).
- [97] E. M. Haacke, N. Y. C. Cheng, M. J. House, Q. Liu, J. Neelavalli, R. J. Ogg, A. Khan, M. Ayaz, W. Kirsch, and A. Obenaus, "Imaging iron stores in the brain using magnetic resonance imaging," *Magnetic Resonance Imaging*, vol. 23, no. 1, pp. 1–25, Jan. 2005. DOI: 10.1016/j.mri.2004.10.001 (cit. on p. 17).
- [98] J. P. Kaltwasser, R. Gottschalk, K. P. Schalk, and W. Hartl, "Non-invasive quantitation of liver iron-overload by magnetic resonance imaging," *British Journal of Haematology*, vol. 74, no. 3, pp. 360–363, 1990. DOI: 10.1111/j.1365-2141.1990.tb02596.x (cit. on p. 17).
- [99] T. G. St Pierre, P. R. Clark, W. Chua-anusorn, A. J. Fleming, G. P. Jeffrey, J. K. Olynyk, P. Pootrakul, E. Robins, and R. Lindeman, "Noninvasive measurement and imaging of liver iron concentrations using proton magnetic resonance," *Blood*, vol. 105, no. 2, pp. 855–861, Jan. 15, 2005. DOI: 10.1182/blood-2004-01-0177 (cit. on p. 17).
- [100] D. J. J. Wang, M. A. Fernández-Seara, and H. Lu, "Confounding effects in arterial spin labeling," in *MR and CT Perfusion and Pharmacokinetic Imaging*, R. Bammer, Ed., Wolters Kluwer, 2016 (cit. on p. 18).
- [101] P. A. Boulby and F. J. Rugg-Gunn, "Functional and metabolic MRI," in *Quantitative MRI of the Brain*, P. Tofts, Ed., John Wiley & Sons, Ltd, 2003. DOI: 10.1002/0470869526 (cit. on p. 18).
- [102] I. Blystad, J. Warntjes, O. Smedby, A.-M. Landtblom, P. Lundberg, and E.-M. Larsson, "Synthetic MRI of the brain in a clinical setting," *Acta Radiologica*, vol. 53, no. 10, pp. 1158–1163, Dec. 1, 2012. DOI: 10.1258/ar.2012.120195 (cit. on p. 18).
- [103] P. A. Boulby and F. J. Rugg-Gunn, "The measurement process," in *Quantitative MRI of the Brain*, P. Tofts, Ed., John Wiley & Sons, Ltd, 2003. DOI: 10.1002/0470869526 (cit. on p. 19).
- [104] A. Petrovic, *Artifact Correction for In-vivo B1-Mapping in MRI: Implementation and Evaluation of Smoothing Algorithms for B1 Maps*. VDM Verlag Dr. Müller: n/a, 2010 (cit. on p. 19).

## Bibliography

- [105] R. Stollberger and P. Wach, "Imaging of the active  $B_1$  field in vivo," *Magnetic Resonance in Medicine*, vol. 35, no. 2, pp. 246–251, Feb. 1996. DOI: 10.1002/mrm.1910350217 (cit. on pp. 19, 103).
- [106] C. H. Cunningham, J. M. Pauly, and K. S. Nayak, "Saturated double-angle method for rapid  $B_1+$ ," *Magnetic Resonance in Medicine*, vol. 55, pp. 1326–1333, 2006 (cit. on p. 19).
- [107] L. I. Sacolick, F. Wiesinger, I. Hancu, and M. W. Vogel, " $B_1$  mapping by bloch-siegert shift," *Magnetic Resonance in Medicine*, vol. 63, no. 5, pp. 1315–1322, May 2010. DOI: 10.1002/mrm.22357 (cit. on pp. 19, 67, 95).
- [108] A. Lesch, M. Schlöegl, M. Holler, K. Bredies, and R. Stollberger, "Ultrafast 3d bloch-siegert  $B_1+$ -mapping using variational modeling," *Magnetic Resonance in Medicine*, vol. 81, no. 2, pp. 881–892, Feb. 1, 2019. DOI: 10.1002/mrm.27434 (cit. on p. 19).
- [109] G. R. Morell, "A phase-sensitive method of flip angle mapping," *Magnetic Resonance in Medicine*, vol. 60, pp. 889–894, 2008 (cit. on p. 20).
- [110] V. L. Yarnykh, "Actual flip-angle imaging in the pulsed steady state: A method for rapid three-dimensional mapping of the transmitted radiofrequency field," *Magnetic Resonance in Medicine*, vol. 57, pp. 192–200, 2007 (cit. on p. 20).
- [111] R. Venkatesan, W. Lin, and E. M. Haacke, "Accurate determination of spin-density and  $T_1$  in the presence of RF-field inhomogeneities and flip-angle miscalibration," *Magnetic Resonance in Medicine*, vol. 40, pp. 592–602, 1998 (cit. on p. 20).
- [112] N. G. Dowell and P. S. Tofts, "Fast, accurate, and precise mapping of the RF field in vivo using the  $180^\circ$  signal null," *Magnetic Resonance in Medicine*, vol. 58, pp. 622–630, 2007 (cit. on p. 20).
- [113] J. Pauly, P. Le Roux, D. Nishimura, and A. Macovski, "Parameter relations for the shinnar-le roux selective excitation pulse design algorithm," *IEEE Transactions on Medical Imaging*, vol. 10, pp. 53–65, 1991 (cit. on pp. 21, 22, 65, 93, 94).
- [114] E. W. Weisstein. (). Cayley-klein parameters, Wolfram MathWorld, [Online]. Available: <http://mathworld.wolfram.com/Cayley-KleinParameters.html> (visited on 07/11/2019) (cit. on p. 21).
- [115] M. A. Bernstein, K. F. King, and X. J. Zhou, *Handbook of MRI Pulse Sequences*. Amsterdam ; Boston: Academic Press, Sep. 21, 2004, 1040 pp. (cit. on p. 22).

- [116] A. Allerhand and E. Thiele, "Analysis of carr—purcell spin-echo NMR experiments on multiple-spin systems. II. the effect of chemical exchange," *The Journal of Chemical Physics*, vol. 45, no. 3, p. 902, 1966. DOI: 10.1063/1.1727703 (cit. on pp. 23, 29, 76).
- [117] A. Allerhand, "Analysis of carr—purcell spin-echo NMR experiments on multiple-spin systems. I. the effect of homonuclear coupling," *The Journal of Chemical Physics*, vol. 44, no. 1, p. 1, 1966. DOI: 10.1063/1.1726430 (cit. on pp. 23, 27, 76).
- [118] R. T. Constable, A. W. Anderson, J. Zhong, and J. C. Gore, "Factors influencing contrast in fast spin-echo MR imaging," *Magnetic resonance imaging*, vol. 10, no. 4, pp. 497–511, 1992 (cit. on pp. 27, 29, 76).
- [119] R. M. Henkelman, P. A. Hardy, J. E. Bishop, E. C. S. Poon, and D. B. Plewes, "Why fat is bright in rare and fast spin-echo imaging," *Journal of Magnetic Resonance Imaging*, vol. 2, no. 5, pp. 533–540, 1992. DOI: 10.1002/jmri.1880020511 (cit. on p. 27).
- [120] L. A. Stables, R. P. Kennan, A. W. Anderson, and J. C. Gore, "Density matrix simulations of the effects of J-coupling in spin echo and fast spin echo imaging," *Journal of Magnetic Resonance (San Diego, Calif.: 1997)*, vol. 140, no. 2, pp. 305–314, Oct. 1999. DOI: 10.1006/jmre.1998.1655 (cit. on pp. 27, 29).
- [121] A. Yahya and B. G. Fallone, " $T_2$  determination of the J-coupled methyl protons of lipids: In vivo illustration with tibial bone marrow at 3 T," *Journal of Magnetic Resonance Imaging*, vol. 31, no. 6, pp. 1514–1521, 2010. DOI: 10.1002/jmri.22195 (cit. on p. 27).
- [122] M. Gloor, K. Scheffler, and O. Bieri, "Quantitative magnetization transfer imaging using balanced SSFP," *Magnetic Resonance in Medicine*, vol. 60, no. 3, pp. 691–700, Sep. 1, 2008. DOI: 10.1002/mrm.21705 (cit. on p. 30).
- [123] F. S. Acton, *Numerical Methods that Work*. Washington, D.C: The Mathematical Association of America, 1990, 567 pp. (cit. on pp. 30, 103).
- [124] Y. Bard, *Nonlinear Parameter Estimation*. New York: Academic Press Inc, 1974, 341 pp. (cit. on p. 30).
- [125] E. I. Jury, *Theory and application of the z-transform method*. Robert E. Krieger Publishing CO., 1973 (cit. on pp. 33, 34).
- [126] A. DeMoivre, *Miscellanea analytica de seriebus et quadraturis*. London: J. Tonson & J. Watts, 1730 (cit. on p. 33).

## Bibliography

- [127] A. V. Oppenheim and R. W. Schaffer, "Transform analysis of linear time-invariant systems," in *Discrete-time signal processing*, 2nd ed., Upper Saddle River, NJ: Prentice Hall, 1999 (cit. on pp. 33, 34).
- [128] O. Föllinger, "Z-transformation," in *Laplace-, Fourier- und z-Transformation*, 7th ed., Heidelberg: Hüthig Verlag, 2000 (cit. on pp. 33, 34).
- [129] *Z-transform*, in *Wikipedia*, Mar. 21, 2019 (cit. on p. 34).
- [130] D. G. Nishimura, *Principles of Magnetic Resonance Imaging*. Stanford Univ, Feb. 11, 2010 (cit. on p. 38).
- [131] J. P. Wansapura, S. K. Holland, R. S. Dunn, and W. S. Ball, "NMR relaxation times in the human brain at 3.0 Tesla," *Journal of Magnetic Resonance Imaging*, vol. 9, pp. 531–538, 1999 (cit. on pp. 65, 72, 77).
- [132] G. E. Gold, E. Han, J. Stainsby, G. Wright, J. Brittain, and C. Beaulieu, "Musculoskeletal MRI at 3.0 T: Relaxation times and image contrast," *AJR. American Journal of Roentgenology*, vol. 183, no. 2, pp. 343–351, Aug. 2004 (cit. on p. 65).
- [133] M. S. Sussman, L. Vidarsson, J. M. Pauly, and H.-L. M. Cheng, "A technique for rapid single-echo spin-echo T<sub>2</sub> mapping," *Magn Reson Med*, 2010 (cit. on pp. 67, 74, 75).
- [134] G. J. Stanisz, E. E. Odobina, J. Pun, M. Escaravage, S. J. Graham, M. J. Bronskill, and R. M. Henkelman, "T<sub>1</sub>, T<sub>2</sub> relaxation and magnetization transfer in tissue at 3 T," *Magnetic Resonance in Medicine*, vol. 54, no. 3, pp. 507–512, 2005. DOI: 10.1002/mrm.20605 (cit. on pp. 72, 77, 102).
- [135] F. Mitsumori, H. Watanabe, and N. Takaya, "Estimation of brain iron concentration in vivo using a linear relationship between regional iron and apparent transverse relaxation rate of the tissue water at 4.7T," *Magnetic Resonance in Medicine*, vol. 62, no. 5, pp. 1326–1330, 2009. DOI: 10.1002/mrm.22097 (cit. on pp. 72, 77).
- [136] C. F. Maier, S. G. Tan, H. Hariharan, and H. G. Potter, "T<sub>2</sub> quantitation of articular cartilage at 1.5 T," *Journal of Magnetic Resonance Imaging: JMRI*, vol. 17, no. 3, pp. 358–364, Mar. 2003. DOI: 10.1002/jmri.10263 (cit. on p. 76).
- [137] A. V. Oppenheim and R. W. Schaffer, *Discrete-Time Signal Processing*, 3rd international ed. Upper Saddle River, NJ: Prentice Hall, Dec. 31, 2007, 1132 pp. (cit. on pp. 77, 89).

- [138] H. Gudbjartsson and S. Patz, "The Rician distribution of noisy MRI data," *Magnetic resonance in medicine : official journal of the Society of Magnetic Resonance in Medicine / Society of Magnetic Resonance in Medicine*, vol. 34, no. 6, pp. 910–914, Dec. 1995 (cit. on p. 78).
- [139] K. T. Block, M. Uecker, and J. Frahm, "Undersampled radial MRI with multiple coils. Iterative image reconstruction using a total variation constraint," *Magnetic Resonance in Medicine*, vol. 57, no. 6, pp. 1086–1098, Jun. 1, 2007. DOI: 10.1002/mrm.21236 (cit. on p. 78).
- [140] W. Hager and H. Zhang, "A new conjugate gradient method with guaranteed descent and an efficient line search," *SIAM Journal on Optimization*, vol. 16, no. 1, pp. 170–192, Jan. 1, 2005. DOI: 10.1137/030601880 (cit. on p. 79).
- [141] A. Petrovic, C. S. Aigner, A. Rund, and R. Stollberger, "A time domain signal equation for multi-echo spin-echo sequences with arbitrary excitation and re-focusing angle and phase," *Journal of Magnetic Resonance*, vol. 309, p. 106515, Dec. 1, 2019. DOI: 10.1016/j.jmr.2019.07.002 (cit. on pp. 81, 125).
- [142] B. Buttkus, *Spectral Analysis and Filter Theory in Applied Geophysics*. Springer Science & Business Media, Dec. 6, 2012, 665 pp. (cit. on p. 83).
- [143] M. Weigel, "Extended phase graphs: Dephasing, RF pulses, and echoes - pure and simple," *Journal of Magnetic Resonance Imaging*, vol. 41, no. 2, pp. 266–295, Feb. 1, 2015. DOI: 10.1002/jmri.24619 (cit. on p. 85).
- [144] O. Föllinger, *Laplace-, Fourier- und z-Transformation*, 7th ed. Heidelberg: Hüthig Verlag, 2000, 419 pp. (cit. on p. 86).
- [145] K. P. Whittall, A. L. Mackay, D. A. Graeb, R. A. Nugent, D. K. B. Li, and D. W. Paty, "In vivo measurement of  $T_2$  distributions and water contents in normal human brain," *Magnetic Resonance in Medicine*, vol. 37, no. 1, pp. 34–43, Jan. 1, 1997. DOI: 10.1002/mrm.1910370107 (cit. on pp. 95, 103).
- [146] J. M. Spijkerman, E. T. Petersen, J. Hendrikse, P. Luijten, and J. J. M. Zwanenburg, " $T_2$  mapping of cerebrospinal fluid: 3 T versus 7 T," *Magma (New York, N.y.)*, vol. 31, no. 3, pp. 415–424, 2018. DOI: 10.1007/s10334-017-0659-3 (cit. on p. 102).
- [147] A. Petrovic and S. Rudolf, "Simultaneous  $T_1$  and  $T_2$  mapping using a modified multi-echo spin-echo sequence (MOMSE)," in *Proc. Intl. Soc. Mag. Reson. Med 23*, Toronto, Canada, 2015, p. 1671 (cit. on pp. 111, 125).

## Bibliography

- [148] B. Neumayer, E. Hassler, A. Petrovic, T. Widek, K. Ogris, and E. Scheurer, "Age determination of soft tissue hematomas," *NMR in Biomedicine*, vol. 27, no. 11, pp. 1397–1402, 2014. DOI: 10.1002/nbm.3202 (cit. on p. 127).
- [149] T. Widek, P. Genet, H. Merkens, J. Boldt, A. Petrovic, J. Vallis, and E. Scheurer, "Dental age estimation: The chronology of mineralization and eruption of male third molars with 3t MRI," *Forensic Science International*, vol. 297, pp. 228–235, Apr. 1, 2019. DOI: 10.1016/j.forsciint.2019.02.019 (cit. on p. 127).
- [150] E. M. Hassler, K. Ogris, A. Petrovic, B. Neumayer, T. Widek, K. Yen, and E. Scheurer, "Contrast of artificial subcutaneous hematomas in MRI over time," *International Journal of Legal Medicine*, vol. 129, no. 2, pp. 317–324, Mar. 1, 2015. DOI: 10.1007/s00414-014-1124-8 (cit. on p. 127).
- [151] K. Ogris, A. Petrovic, S. Scheicher, H. Sprenger, M. Urschler, E. M. Hassler, K. Yen, and E. Scheurer, "Detection and volume estimation of artificial hematomas in the subcutaneous fatty tissue: Comparison of different MR sequences at 3.0 T," *Forensic Science, Medicine, and Pathology*, vol. 13, no. 2, pp. 135–144, Jun. 1, 2017. DOI: 10.1007/s12024-017-9847-8 (cit. on p. 127).
- [152] P. Baumann, T. Widek, H. Merkens, J. Boldt, A. Petrovic, M. Urschler, B. Kirnbauer, N. Jakse, and E. Scheurer, "Dental age estimation of living persons: Comparison of MRI with OPG," *Forensic Science International*, vol. 253, pp. 76–80, Aug. 1, 2015. DOI: 10.1016/j.forsciint.2015.06.001 (cit. on p. 127).
- [153] H. Scharfetter, A. Petrovic, H. Eggenhofer, and R. Stollberger, "A no-tune no-match wideband probe for nuclear quadrupole resonance spectroscopy in the VHF range," *Measurement Science and Technology*, vol. 25, p. 125 501, Dec. 1, 2014. DOI: 10.1088/0957-0233/25/12/125501 (cit. on p. 128).
- [154] H. Scharfetter, "An electronically tuned wideband probehead for NQR spectroscopy in the VHF range," *Journal of Magnetic Resonance*, vol. 271, pp. 90–98, 2016. DOI: 10.1016/j.jmr.2016.08.008 (cit. on p. 128).
- [155] M. Bödenler, M. Basini, M. F. Casula, E. Umut, C. Gösweiner, A. Petrovic, D. Kruk, and H. Scharfetter, "R1 dispersion contrast at high field with fast field-cycling MRI," *Journal of Magnetic Resonance*, vol. 290, pp. 68–75, May 1, 2018. DOI: 10.1016/j.jmr.2018.03.010 (cit. on p. 128).
- [156] D. Kruk, E. Masiewicz, E. Umut, A. Petrovic, R. Kargl, and H. Scharfetter, "Estimation of the magnitude of quadrupole relaxation enhancement in the context of magnetic resonance imaging contrast," *The Journal of Chemical Physics*, vol. 150, no. 18, p. 184 306, May 14, 2019. DOI: 10.1063/1.5082177 (cit. on p. 128).